N°d'ordre 2011 – ISAL – 0011 Année 2011

THÈSE

An adaptive model reduction approach for 3D fatigue crack growth in small scale yielding conditions

Présentée devant
l'Institut National des Sciences Appliquées de Lyon

pour obtenir
le GRADE DE DOCTEUR

École doctorale :
Mécanique, Énergétique, Génie Civil, Acoustique

Spécialité :
MÉCANIQUE - GÉNIE MÉCANIQUE - GÉNIE CIVIL

par

Florent GALLAND
Ingénieur INSA-Lyon

Cette thèse sera soutenue le 4 février 2011 devant la Commission d'examen

Jury

Nicolas Moës	Professeur	Président du jury
Amine Ammar	Professeur	Rapporteur
Frédéric Feyel	Professeur	Rapporteur
Francisco Chinesta	Professeur	Examinateur
Alain Combescure	Professeur	Examinateur
Sylvie Pommier	Professeur	Examinateur
Michel Rochette	Docteur	Examinateur
Anthony Gravouil	Professeur	Directeur de thèse

LaMCoS - UMR CNRS 5259 - INSA Lyon
20, avenue Albert Einstein, 69621 Villeurbanne Cedex France

Remerciements

Mes premières pensées vont bien sûr à mes directeurs de thèse Anthony Gravouil et Michel Rochette. Merci de m'avoir accueilli dans le cadre d'une véritable collaboration entre le Laboratoire de Mécanique des Contacts et des Structures (LaMCoS) de l'INSA de Lyon et l'éditeur de code de calcul ANSYS France. Les échanges ont été rendus d'autant plus facile par la proximité géographique de ces établissements ! Merci donc d'avoir fait en sorte que je puisse me concentrer uniquement sur mon travail, pour votre soutien, votre confiance et vos conseils. Comme l'a souligné Anthony lors de ma soutenance, une thèse est aussi faite de rencontres, et en voila de belles. J'aurai toujours grand plaisir à ce qu'on travaille ensemble.

Je voudrais également exprimer ma gratitude aux membres du jury. À Nicolas Moës pour avoir accepté de présider ce jury, Amine Ammar et Frédéric Feyel pour avoir accepté de relire en détail ce tapuscrit, pour leur vision d'ensemble et les commentaires bénéfiques de leurs rapports. À Sylvie Pommier, Francisco Chinesta et Alain Combescure pour l'intérêt qu'ils ont porté à mon travail. Je les remercie vivement.

Vient le tour d'Émilien Pierres, jeune Docteur du LaMCoS. Merci pour ton amitié depuis toutes ces années, tous ces échanges et tes nombreux coups de main.

Durant ces trois années de thèse, j'ai eu la chance partager le quotidien de mes collègues d'ANSYS. Je voudrais remercier tout particulièrement Cyrille Defranoux, le seul homme capable de poser des cloisons d'une main, donner un biberon de l'autre tout en discutant de l'architecture de Propamodel. Merci d'avoir partagé tout cela avec moi, et de m'avoir consacré autant de temps. De même, je n'oublie pas Emmanuel Malvesin avec qui j'ai passé énormément de temps, ainsi que Emmanuel Delor et Christelle Boichon. Je pense bien sûr sincèrement à David Roche et à Benoît Prieur pour tous ces bons moments et ces théories fumeuses mais aussi à Rémy Fernandes, François Chapuis, Anthony Lemaître, Luc Pontoire et Julien Ravoux. Merci à tous pour votre amitié.

J'ai aussi une pensée pour les doctorants et post-doctorants du LaMCoS, Jean-Charles, Aline, Lucas, Fabien, Émilien, merci pour votre accueil à chaque fois que j'allais au labo et pour toutes ces discussions.

Pour finir, je pense à ma famille, mes parents et ma soeur qui m'ont soutenu depuis toujours et sans qui je ne serais jamais arrivé là.

Enfin je remercie Anne du fond du coeur pour son amour et pour tout ce qu'elle est.

« Trying is the first step toward failure. »

— Homer Simpson, *Reality Bites*

Résumé

Il est connu depuis des décennies que la propagation des fissures de fatigue dans les matériaux élastoplastiques est très sensible à l'histoire du chargement car le comportement non-linéaire du matériau peut avoir une grande influence sur les vitesses de propagation. Cependant, le calcul brut de millions de cycles de fatigue avec des comportements matériaux non-linéaires sur des structures tridimensionnelles réalistes conduirait à des temps de calcul prohibitifs. Ainsi, nous proposons de coupler deux approches de réduction de modèle *a priori* et *a posteriori*, afin de diminuer considérablement le coût de calcul de ce type de problèmes.

Tout d'abord, considérant l'hypothèse de plasticité confinée, une stratégie de réduction de modèle *a posteriori* du comportement plastique de la structure fissurée est proposée. Le modèle réduit ainsi obtenu fournit incrémentalement l'état plastique autour du front de fissure, duquel est déduite la vitesse instantanée de la fissure. De plus, une seconde approche de réduction de modèle, *a priori* cette fois, est aussi mise en place afin d'accélérer encore plus les temps de résolution du problème global. Cette approche *a priori* consiste à construire incrémentalement — et sans calculs préalables — une base réduite spécifique à chaque cas-test, en extrayant de l'information des champs de déplacement de la structure au cours du temps et pendant la propagation éventuelle de la fissure. Ainsi, les champs de déplacement solutions de la géométrie fissurée réactualisée sont vus comme une combinaison linéaire de cette base réduite de vecteurs.

La méthode numérique considérée ici est la méthode des éléments finis. De fait, pendant la propagation de la fissure, la discrétisation spatiale du modèle doit être réactualisée afin d'être conforme avec le front de la fissure. Dans ce but, une technique spécifique de déformation de maillage est utilisée, et permet de discrétiser la géométrie variable du modèle avec des maillages de même topologie. Cette technique de déformation de maillage apparaît comme une étape clé de la stratégie de réduction de modèle.

Finalement, une approche *adaptative* est construite autour de cette stratégie. Elle permet de garantir la qualité des résultats obtenus par rapport à un critère de précision donné. La précision et l'efficacité de cette stratégie globale sont démontrées à travers de nombreux exemples bidimensionnels et tridimensionnels dans le cadre de propagation de fissure en mode I, de même que pour un exemple industriel d'une pièce fissurée d'hélicoptère.

MOTS CLÉS: Propagation de fissure 3D, Effet de refermeture, Plasticité confinée, Réduction de modèle *a priori*, Déformation de maillage, Méthode des éléments finis

Summary

It has been known for decades that fatigue crack propagation in elastic-plastic media is very sensitive to load history since the nonlinear behavior of the material can have a great influence on propagation rates. However, the raw computation of millions of fatigue cycles with nonlinear material behavior on tridimensional structures would lead to prohibitive calculation times. In this respect, we propose a global model reduction strategy, mixing both the *a posteriori* and *a priori* approaches in order to drastically decrease the computational cost of these types of problems.

First, the small scale yielding hypothesis is assumed, and an *a posteriori* model reduction of the plastic behavior of the cracked structure is performed. This reduced model provides incrementally the plastic state in the vicinity of the crack front, from which the instantaneous crack growth rate is inferred. Then an additional *a priori* model reduction technique is used to accelerate even more the time to solution of the whole problem. This *a priori* approach consists in building incrementally and without any previous calculations a reduced basis specific to the considered test-case, by extracting information from the evolving displacement field of the structure. Then the displacement solutions of the updated crack geometries are sought as linear combinations of those few basis vectors.

The numerical method chosen for this work is the finite element method. Hence, during the propagation the spatial discretization of the model has to be updated to be consistent with the evolving crack front. For this purpose, a specific mesh morphing technique is used, that enables to discretize the evolving model geometry with meshes of the same topology. This morphing method appears to be a key component of the model reduction strategy.

Finally, the whole strategy introduced above is embedded inside an *adaptive* approach, in order to ensure the quality of the results with respect to a given accuracy. The accuracy and the efficiency of this global strategy have been shown through several examples, either in bidimensional and tridimensional cases for mode I crack propagation, including the industrial example of an helicopter structure.

KEYWORDS: 3D fatigue crack growth, Crack closure effect, Small scale yielding, *a priori* model reduction, Mesh morphing, Finite element method

Contents

Introduction

The accurate prediction of the fatigue life of components or structures is of great interest for mechanical engineering applications. In this respect, it is now more and more needed to be able to simulate accurately tridimensional fatigue crack growth in complex structures. As a consequence, computational fracture mechanics has been strongly developed in recent years. An important issue is the meshing itself when the crack has to be explicitly described by the numerical method. To alleviate these types of problems, alternative methods have been proposed such as the boundary element method, where only the surface of the crack has to be meshed [MI 94, BON 95], the meshless methods [BEL 94, KRY 99] where the mesh notion does not exist and the crack is only described by the nodal weight functions values, or the methods based on the partition of the unity (among others, the generalized finite element method [STR 01, PER 09, PER 10] and the extended finite element method [MOË 99, MOË 02, SUK 08, RAN 09a]) which allow using meshes that do not conform to the crack since the discontinuity is taken into account by special shape functions. Nevertheless, the finite element method is still the more widespread numerical method in the industry, in particular because of its robustness and availability in commercial codes. For those reasons, it is the chosen numerical method for this work. Still, it is underlined that the proposed approach could have been applied to either the extended, generalized or similar finite element methods. In addition, realistic problems are submitted to complex spectrum loadings. In those cases, fatigue crack propagation in elastic-plastic media is particularly sensitive to the localized nonlinear phenomena that take place in the vicinity of the crack tip [WHE 72]. Indeed, contact and frictional effects along the crack faces as well as the confined plasticity are non-negligible issues in fatigue problems [ELG 07, PIE 10, BÉC 08]. In the finite element method framework, sophisticated material behavior laws [LEM 90, SIM 00] as well as robust contact algorithms [SIM 92] allow the very details of those effects to be captured. However, they induce a nonlinear, iterative logic in the model solving. Since in practice fatigue lives can reach millions of "cycles", this approach will lead to prohibitive calculation times and is inapplicable. In this respect, and in the context of tridimensional mode I cracks with no assumption on the crack front shape, we propose to apply the so-called general idea of *model reduction*, in order to decrease this computational cost [GAL 10a, GAL 10b].

The model reduction methods are used when many resolutions of similar problems are needed. They make use of the information contained in some solutions to make the other computations faster. Those methods can be put in two general categories: the *a posteriori* and *a priori* approaches. In the *a posteriori* approach, some preliminary computations are performed first to build a basis of a reduced subspace approximating the solution space associated with the considered problem. This is called the *offline* phase, it possibly has a high numerical cost, but it is performed only once. Then, the reduced model can be used in an *online* phase, many times, to obtain rapidly the outputs of interest, seeking them only in the reduced subspace [VER 03]. The *a priori* approach is different. There are no preliminary computations, and therefore no offline/online computational decomposition. The reduced basis is built on the fly, during the use of

the model, enriched when necessary by the information contained in appropriate solutions. Generally, these enrichment steps are performed during the first resolutions. When the basis is rich enough, it can be used to compute efficiently the solutions of the problem as linear combinations of those basis vectors [RYC 06].

In our approach, two different model reductions are successively applied. First, the small scale yielding hypothesis is assumed, and an *a posteriori* model reduction of the plastic behavior of the cracked structure is performed, by means of the Crack Tip Condensed Plasticity model. Using an elastic-plastic behavior as realistic as possible, a crack solicited in mode I is simulated, and the resulting displacement field is projected onto a suitable reduced basis. Pommier *et al.* [POM 07, HAM 07] remarked that a basis of dimension 2 is sufficient to describe accurately the elastic-plastic displacement field of a steady crack: one vector for the elastic part and a second one for the plastic part of the field. This model reduction method enables to unzoom from the finite element model. Only the elastic part of the displacement field is computed by the finite element method, the plastic state is computed apart, on this reduced basis of dimension 2. At this point, even if the nonlinear finite element computations are avoided, describing realistic spectrum loadings over millions of load steps requires millions of linear elastic computations to provide the elastic state of the structure to this reduced model. An additional *a priori* model reduction associated with those linear elastic finite element problems is then used to further accelerate the time to solution of the whole crack propagation analysis. This *a priori* approach consists in building incrementally and without any previous calculations a reduced basis specific to the considered test case, by extracting information from the evolving displacement field of the structure. Then the displacement solutions of the updated crack geometries are sought as linear combinations of those few basis vectors. If the reduced basis dimension is low, the problems to solve are then significantly smaller than the initial ones.

In order to make that model reduction more efficient, all the geometrical updates of the propagating crack are performed by means of a mesh morphing technique. This method is widely used, among others, in computer graphics animations, reliability analysis and fluid-structure interaction [ALE 02]. It enables to discretize several different geometries with meshes of the same topology, allowing the number of degrees of freedom and the connectivity to be kept unchanged all along the crack growth analysis. This is done by modifying the nodes coordinates, while keeping the element distortion as low as possible. Using such an approach enables to avoid a lot of remeshing steps, and since all the morphed meshes have the same dimension, no projections of the reduced basis shape functions on those successive meshes are needed.

This first method coupling the Crack Tip Condensed Plasticity model, a mesh morphing technique and an *a priori* reduced basis approach provides fairly encouraging results [GAL 09a, GAL 10c]. However, deciding *when* to update the numerical model to compute stress intensity factors values consistent with the growing crack configuration is not an easy task. In addition, the chosen update interval has a great influence on the final accuracy of the simulation. In this respect, an adaptive strategy overcoming that difficulty is developed, which computes iteratively the quasi-optimal update interval that ensures a given accuracy.

This typescript is outlined as follows. In a first chapter, the considered continuous reference problem is developed, along with some theoretical background on fracture mechanics. An overview of the existing numerical methods and propagation laws adapted to crack growth simulation is provided. Then, the Crack Tip Condensed Plasticity model is extensively described. In a second chapter, the mathematical fundamentals of the reduced basis approach are introduced, as well as details on how it is applied to the fracture mechanics context. The mesh morphing approach is then explained. Afterward, the general strategy and the way the basic components of the method are fitted together are presented, along with several bidimensional and tridimensional examples. A long discussion on the effect of the mesh morphing technique on the behavior

of the reduced basis approach is also provided. Finally, in a last chapter, the adaptive strategy is introduced, together with complex tridimensional examples to illustrate the capabilities of the method.

Chapter 1

Fatigue crack growth analysis: challenges and methods

Contents

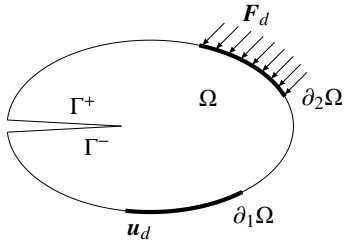

Figure 1.1 Notation used for the different parts of the domain Ω.

1 Linear elastic fracture mechanics: theoretical notions

1.1 Continuous reference problem

We present hereinafter a general definition of the reference problem. The static deformation of a linear elastic, homogeneous and isotropic cracked body is considered. Since the crack is evolving, this body defines a time-dependent domain $\Omega(t)$ (see Figure 1.1) defined on all the considered temporal interval $[0, T]$. It is worth emphasizing that from the governing equations point of view, there is no history effects between two successive configurations. Furthermore, at any given propagation step, we assume small strains and displacements. The outer boundary of the domain $\Omega(t)$ is decomposed into two complementary parts, $\partial_1\Omega(t)$ along which displacements $\boldsymbol{u}_d(t)$ are imposed and $\partial_2\Omega(t)$ along which forces $\boldsymbol{F}_d(t)$ are prescribed. The body can possibly be submitted to some volume forces $\boldsymbol{f}_d(t)$. The crack is represented by its faces $\Gamma^+(t)$ and $\Gamma^-(t)$. These two surfaces are considered free from any solicitations. The crack front is given by the intersection $\Gamma^+(t) \cap \Gamma^-(t)$. At each time, the Cauchy stress tensor field $\boldsymbol{\sigma}(t)$ and the displacement field $\boldsymbol{u}(t)$ must satisfy the local equilibrium conditions:

$$\boldsymbol{\nabla} \cdot \boldsymbol{\sigma}(t) + \boldsymbol{f}_d(t) = \boldsymbol{0} \quad \text{in } \Omega(t) \tag{1.1}$$

$$\boldsymbol{\sigma}(t) \cdot \boldsymbol{n} = \boldsymbol{F}_d(t) \quad \text{on } \partial_2\Omega(t) \tag{1.2}$$

$$\boldsymbol{\sigma}(t) \cdot \boldsymbol{n} = \boldsymbol{0} \quad \text{on } \Gamma^+(t) \text{ and } \Gamma^-(t) \tag{1.3}$$

$$\boldsymbol{u}(t) = \boldsymbol{u}_d(t) \quad \text{on } \partial_1\Omega(t) \tag{1.4}$$

where $\boldsymbol{n}$ is the outward normal vector to the boundary of the domain $\Omega(t)$. The constitutive law and the strain-displacement relationship write:

$$\boldsymbol{\sigma}(t) = \boldsymbol{C} : \boldsymbol{\varepsilon}(t) \quad \text{in } \Omega(t) \tag{1.5}$$

with:

$$\boldsymbol{\varepsilon}(t) = \frac{1}{2}\left(\boldsymbol{\nabla}\boldsymbol{u}(t) + (\boldsymbol{\nabla}\boldsymbol{u}(t))^T\right) \equiv \boldsymbol{\varepsilon}(\boldsymbol{u}(t)) \tag{1.6}$$

where $\boldsymbol{C}$ is the Hooke's tensor and $\boldsymbol{\varepsilon}(t)$ the symmetric strain tensor.

The weak form associated with the local equilibrium equations and boundary conditions is as follow:
Find $\boldsymbol{u}(t)$ in space $\mathcal{U}^{[0,T]}$ such that:

$$\int_{\Omega(t)} \boldsymbol{\varepsilon}(\boldsymbol{u}(t)) : \boldsymbol{C} : \boldsymbol{\varepsilon}(\boldsymbol{v})\, d\Omega = \int_{\Omega(t)} \boldsymbol{f}_d(t) \cdot \boldsymbol{v}\, d\Omega + \int_{\partial_1\Omega(t)} \boldsymbol{F}_d(t) \cdot \boldsymbol{v}\, ds \quad \forall t \in [0;T],\ \forall \boldsymbol{v} \in \mathcal{U}_0 \tag{1.7}$$

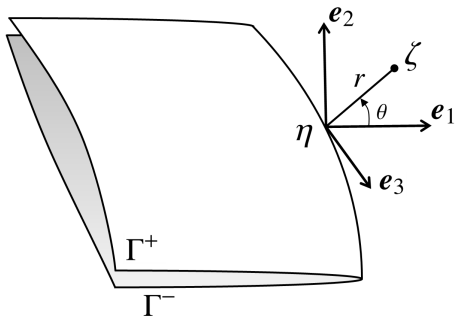

Figure 1.2 Local coordinate systems at the crack front.

where $\mathcal{U}^{[0,T]}$ is the vector space of the kinematically admissible displacement fields:

$$\mathcal{U}^{[0,T]} = \{\boldsymbol{u}(t) \in V \,|\, \boldsymbol{u}(t) = \boldsymbol{u}_d(t) \text{ on } \partial_1\Omega(t)\} \quad \forall t \in [0,T] \tag{1.8}$$

and $\mathcal{U}_0$ the vector space of the kinematically admissible virtual fields with zero prescribed displacements:

$$\mathcal{U}_0 = \{\boldsymbol{v} \in V \,|\, \boldsymbol{v} = \boldsymbol{0} \text{ on } \partial_1\Omega\} \tag{1.9}$$

notice that the exact mathematical nature of the space V is related to the regularity of the solution.

To complete this definition of the reference problem with details on the chosen numerical method for the resolution of those equations, the discretized reference problem is introduced in section 2 of chapter 2.

In addition to the mechanical reference problem, let us introduce the local coordinate system at the crack front that will be used all along this typescript. At a point η of the front, we define the origin of a Cartesian coordinate system (see Figure 1.2). The $\boldsymbol{e}_1$ vector is called the extensional vector, it stands in the local crack plane and is orthogonal to the front. The normal vector $\boldsymbol{e}_2$ is orthogonal to $\boldsymbol{e}_1$ and the triplet $(\eta, \boldsymbol{e}_1, \boldsymbol{e}_2)$ defines a plane orthogonal to the crack surface. The last vector $\boldsymbol{e}_3$ is the tangent vector to the front. In addition to this Cartesian system, a polar coordinate system (r, θ) is defined in the plane orthogonal to the front.

1.2 Global energetic approach

The Griffith energy balance approach [GRI 21] is one of the founding works of modern fracture theory. Griffith's motivation was in understanding the effects of surface scratches on fatigue. At this time, it was thought that it should be possible to estimate the fatigue limit of a scratched component by using simple criteria based either on the maximum principal stress or the maximum principal strain. Griffith showed that scratches could significantly increase the stress and strain level, however, he noted that on a shaft of 1 inch in diameter the maximum stress or strain would be the same whether the scratches where one ten-thousand or one-hundred of an inch deep provided that they were geometrically similar. This lead him to infer that a simple critical stress or strain criterion could not be used to predict fracture, so that he turned to energy concept.

The Griffith's approach consists in a global analysis of the energy balance during the crack growth process. This theory presuppose the existence of an initial crack and thus does not predict the flaw initiation. The main idea is to link the necessary energy to grow the crack $\mathrm{d}W_{crack}$ to the newly created surface area $\mathrm{d}A$ through a characteristic material parameter, the surface energy per unit area γ:

$$\mathrm{d}W_{crack} = 2\gamma \, \mathrm{d}A \tag{1.10}$$

Hence, this theory stands that the material fails not because of a maximum stress, but rather because a certain energy criterion was met. Then, following the first law of the thermodynamics, crack propagation is caused by a transfer of energy from external work and strain energy to surface energy.

Thus, on a domain Ω (see Figure 1.1), at a given time t, the first law of the thermodynamics writes [LEM 90]:

$$\frac{\partial E}{\partial t} + \frac{\partial K}{\partial t} = P_{\text{ext}} + Q - 2\gamma \frac{\partial A}{\partial t} \tag{1.11}$$

where E is the internal energy of Ω, K its kinetic energy, P_{ext} the power of the external forces and Q the heat received by the system. In addition, for a linear elastic body, the variation of internal energy can be expressed as:

$$\frac{\partial E}{\partial t} = Q + \frac{\partial W_{\text{elas}}}{\partial t} \qquad \text{with} \qquad \frac{\partial W_{\text{elas}}}{\partial t} = \int_{\Omega} \boldsymbol{\sigma} : \dot{\boldsymbol{\varepsilon}} \, \mathrm{d}\Omega \tag{1.12}$$

where W_{elas} defines the elastic energy stored in the domain. Furthermore, without volume forces, the power of the external forces is the following:

$$P_{\text{elas}} = \int_{\partial_2 \Omega} \boldsymbol{F}_d \cdot \frac{\partial \boldsymbol{u}}{\partial t} \, \mathrm{d}S \tag{1.13}$$

where the vector $\boldsymbol{F}_d$ represents the surface forces prescribed on $\partial_2\Omega$. Notice that in presence of volume forces, an additional term appears in Equation (1.13) but that does not modify the nature of the reasoning. Considering the cracked surface area A as the only single variable of the energy balance, and emphasizing the kinetic energy term, the first law of the thermodynamics can be rewritten such as:

$$\frac{\partial K}{\partial t} = \left(\int_{\partial_2 \Omega} \boldsymbol{F}_d \cdot \frac{\partial \boldsymbol{u}}{\partial t} \, \mathrm{d}S - \frac{\partial W_{\text{elas}}}{\partial t} - 2\gamma \right) \cdot \frac{\partial A}{\partial t} \tag{1.14}$$

The stability of the whole crack propagation process depends on the sign of the kinetic energy term. Considering Equation (1.14), the cracked surface area A being the only variable of the energy balance, if K increases, the process becomes unstable and the crack starts to propagate. In addition to that, the fracture process being irreversible, it comes:

$$\frac{\partial A}{\partial t} \geq 0 \tag{1.15}$$

At this point, the energy release rate G can be introduced:

$$G = \int_{\partial_2 \Omega} \boldsymbol{F}_d \cdot \frac{\partial \boldsymbol{u}}{\partial A} \, \mathrm{d}S - \frac{\partial W_{\text{elas}}}{\partial A} \tag{1.16}$$

Expressed in this form, the stability of the system depends explicitly on the value of G. In other words, the energy release rate corresponds to the rate of potential energy released during the creation of free surfaces by the fracture process. From here, the 3 following cases can be identified:

- $G < 2\gamma$: no crack propagation
- $G = 2\gamma$: *stable* crack propagation
- $G > 2\gamma$: *unstable* crack propagation.

Remark 1 *From a scalar quantity, the energy release rate G, depending only on the cracked surface area, the Griffith's theory allows determining if a crack will propagate or not. However, it does not define a complete framework for crack growth since localized tridimensional effects, as well as the propagation direction cannot be inferred from a single scalar quantity. A more detailed analysis of the local fields in the vicinity of the crack front is necessary.*

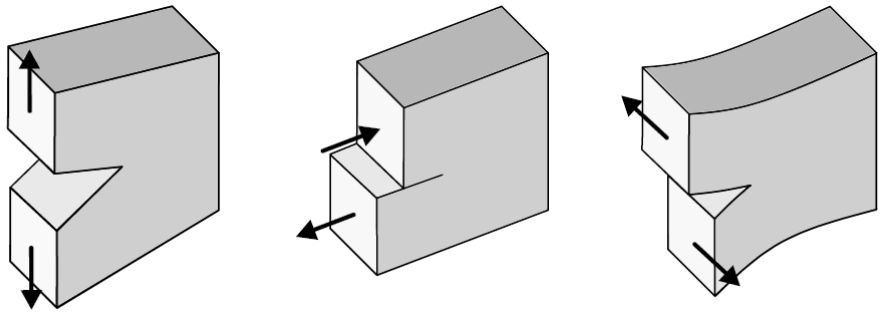

(a) mode I (b) mode II (c) mode III

Figure 1.3 The three fracture modes.

1.3 Asymptotic approach

During the fracture process, the initially sane body is progressively separated into different parts by the propagation of a crack. At the unloaded state, a crack is constituted by two coincident free surfaces of which union defines the *fracture surface*. When loaded, the displacement field of the cracked body becomes discontinuous across this fracture surface, allowing the definition of the displacement jump such as:

$$[\![\boldsymbol{u}]\!] = \boldsymbol{u}^+ - \boldsymbol{u}^- \tag{1.17}$$

From a kinematic point of view, three basic solicitation modes of the crack can be identified, and subsequently, any stress system in the vicinity of the crack tip may be expressed as a general combination of those modes (see Figure 1.3):

- mode I: opening mode, the displacements of the crack surfaces are perpendicular to the plane of the crack
- mode II: sliding mode, due to in-plane shear solicitation, the displacements of the crack surfaces is in the plane of the crack and perpendicular to the leading edge of the crack
- mode III: tearing mode, due to out-of-plane shear solicitation, crack surfaces displacements are in the plane of the crack and parallel to the crack front.

For certain crack configurations subjected to external forces, and assuming isotropic linear elastic material behavior, it is possible to derive analytical expressions for the stresses in the body. Based on the early work of Griffith, Westergaard [WES 39], Irwin [IRW 57], and Williams [WIL 57] where among the first to provide such solutions. Considering a polar coordinate system of which origin is at the crack tip (Figure 1.2), the stress field can be expressed as an infinite series, which, at the second order, writes:

$$\sigma_{ij} = \frac{K_I}{\sqrt{2\pi r}} f_{ij}^I(\theta) + \frac{K_{II}}{\sqrt{2\pi r}} f_{ij}^{II}(\theta) + \frac{K_{III}}{\sqrt{2\pi r}} f_{ij}^{III}(\theta) + T_{ij} + O(\sqrt{r}) \tag{1.18}$$

where σ_{ij} is the stress tensor, r and θ are as defined on Figure 1.2. The terms f_{ij}^n are known dimensionless functions of θ, detailed in Tables 1.1 and 1.2. The scalar constants K_n are the so-called *stress intensity factors*, usually expressed in MPa $\sqrt{\text{m}}$, and the second order term T_{ij} is known as *T-stress*.

In the series development of the stress fields, the leading term containing the stress intensity factor is proportional to $1/\sqrt{r}$. As the distance r to the crack front tends to zero, this leading term

Table 1.1 Stress and displacement fields around a crack tip for mode I and mode II (linear elastic, isotropic material behavior).

	Mode I		Mode II		T-stress
$\sigma_{11} =$	$\frac{K_I}{\sqrt{2\pi r}} \cos\left(\frac{\theta}{2}\right)\left[1 - \sin\left(\frac{\theta}{2}\right)\sin\left(\frac{3\theta}{2}\right)\right]$	$-$	$\frac{K_{II}}{\sqrt{2\pi r}} \sin\left(\frac{\theta}{2}\right)\left[2 + \cos\left(\frac{\theta}{2}\right)\cos\left(\frac{3\theta}{2}\right)\right]$	$+$	T
$\sigma_{22} =$	$\frac{K_I}{\sqrt{2\pi r}} \cos\left(\frac{\theta}{2}\right)\left[1 + \sin\left(\frac{\theta}{2}\right)\sin\left(\frac{3\theta}{2}\right)\right]$	$+$	$\frac{K_{II}}{\sqrt{2\pi r}} \sin\left(\frac{\theta}{2}\right)\cos\left(\frac{\theta}{2}\right)\cos\left(\frac{3\theta}{2}\right)$		
$\sigma_{33} =$	$\frac{K_I}{\sqrt{2\pi r}} 2\nu \cos\left(\frac{\theta}{2}\right)$	$-$	$\frac{K_{II}}{\sqrt{2\pi r}} 2\nu \sin\left(\frac{\theta}{2}\right)$	$+$	T_{33}
$\sigma_{12} =$	$\frac{K_I}{\sqrt{2\pi r}} \cos\left(\frac{\theta}{2}\right)\sin\left(\frac{\theta}{2}\right)\cos\left(\frac{3\theta}{2}\right)$	$+$	$\frac{K_{II}}{\sqrt{2\pi r}} \cos\left(\frac{\theta}{2}\right)\left[1 - \sin\left(\frac{\theta}{2}\right)\sin\left(\frac{3\theta}{2}\right)\right]$		
$u_1 =$	$\frac{K_I}{2\mu}\sqrt{\frac{r}{2\pi}} \cos\left(\frac{\theta}{2}\right)\left[\kappa - 1 + 2\sin^2\left(\frac{\theta}{2}\right)\right]$	$+$	$\frac{K_{II}}{2\mu}\sqrt{\frac{r}{2\pi}} \sin\left(\frac{\theta}{2}\right)\left[\kappa + 1 + 2\cos^2\left(\frac{\theta}{2}\right)\right]$		
$u_2 =$	$\frac{K_I}{2\mu}\sqrt{\frac{r}{2\pi}} \sin\left(\frac{\theta}{2}\right)\left[\kappa + 1 - 2\cos^2\left(\frac{\theta}{2}\right)\right]$	$-$	$\frac{K_{II}}{2\mu}\sqrt{\frac{r}{2\pi}} \cos\left(\frac{\theta}{2}\right)\left[\kappa - 1 - 2\sin^2\left(\frac{\theta}{2}\right)\right]$		

Note: ν is the Poisson's ratio, μ the shear modulus and κ the Kolosov constant.

Table 1.2 Nonzero stress and displacement fields around a crack tip for mode III (linear elastic, isotropic material behavior).

$$\sigma_{13} = -\frac{K_{III}}{\sqrt{2\pi r}} \sin\left(\frac{\theta}{2}\right)$$

$$\sigma_{23} = \frac{K_{III}}{\sqrt{2\pi r}} \cos\left(\frac{\theta}{2}\right)$$

$$u_3 = \frac{2K_{III}}{\mu}\sqrt{\frac{r}{2\pi}} \sin\left(\frac{\theta}{2}\right)$$

Note: μ is the shear modulus of the material.

approaches infinity, but the subsequent terms remain either constant, finite, or approach zero. Thus, the stress field evolution is governed by a singularity at crack tip. In addition, it can also be shown that the displacement field evolves with $\sqrt{r}$. The formal definition of the stress intensity factors is given, for the three different solicitation modes, by the following expressions:

$$K_I = \lim_{r\to 0} \sqrt{2\pi r}\, \sigma_{22}^{\theta=0} \tag{1.19}$$

$$K_{II} = \lim_{r\to 0} \sqrt{2\pi r}\, \sigma_{21}^{\theta=0} \tag{1.20}$$

$$K_{III} = \lim_{r\to 0} \sqrt{2\pi r}\, \sigma_{23}^{\theta=0} \tag{1.21}$$

Physically, the stress intensity factors somehow quantify the intensity of the stress singularity. Indeed, since the stresses at crack tip are infinite, it is quite complicated to define a propagation criterion relying on their value. For that reason, the stress intensity factors are extensively used in the fracture mechanics community.

It is worth highlighting that the leading term of the series expansion (1.18) and consequently the stress intensity factor value depend on the geometry of the considered body, the geometry of the crack and the loading of the system. However, provided that the material behavior is homogeneous isotropic, the stress intensity factor does not depend on any material parameter. On the contrary, the T-stress, second term of the series does depend on the Poisson's ratio.

In the Tables 1.1 and 1.2, ν is the Poisson's ratio of the material and μ its shear modulus. The parameter κ refers to the Kolosov constant and its value depends on the plane problem assumption that is made:

$$\kappa = \begin{cases} 3-4\nu & \text{for plane strain} \\ \dfrac{3-\nu}{1+\nu} & \text{for plane stress} \end{cases} \tag{1.22}$$

Thereby, the solution fields provided by the asymptotic development (1.18) are rigorously correct only for the special cases of plane strain and plane stress. In this respect, it is important to understand that in tridimensional problems, those 2D assumptions are only approximations of the real stress constraint state. Indeed, the stress gradients around the crack front lead to the appearance of a triaxial state of stress near the tip. In short, in the bulk of the material, the stress state is essentially plane strain. Near the free surfaces, the stress triaxiality is lower, but a state of pure plane stress exists only *at* the free surface. It has been shown that the T-stress is of specific importance to this issue, since it can be a very powerful indicator of the local constraint state around the crack front [NAK 92]: a high level of T-stress indicates a high triaxiality state, that is, close to plane strain, whereas a low T-stress level reveals a state close to plane stress.

Remark 2 *It is noteworthy that the asymptotic solutions of the stress field are not valid everywhere in the cracked structure, but only in a limited zone surrounding the crack front called K-dominance zone. Indeed, in this area, the behavior of the stress solution is totally dominated by the elastic singularity. Typically, the size of the K-dominance area should be considered to be approximatively 1/10 of the characteristic length of the crack.*

Remark 3 *In a number of situations, the asymptotic behavior of the near front fields is even more complex than the description provided above, and sometimes difficult to properly define. For instance, one can refer to the situation at a vertex on a free surface or to the front rotation and segmentation in mixed mode I+III. A very comprehensive review of the theoretical results for tridimensional cracks in linear elastic media, stress intensity factor perturbation and bifurcation criteria can be found in the Lazarus' book [LAZ 10].*

1.4 Relationship between K and G

Two main classes of scalar parameters describing the crack behavior have been introduced so far. The energy release rate, that quantifies the change in potential energy of the structure induced by an extension of the flaw, and the stress intensity factors, that characterize the stress, strains and displacement fields near the tip. Hence the energy release rate somehow describes the global behavior of the crack while the stress intensity factors are local parameters. However, in the linear elastic case, those parameters are related by a simple analytic expression. Irwin, by performing a crack closure analysis [IRW 57], provided this relation which is now referred to as the *Irwin's formula*:

$$G = \frac{K_I^2}{E^\star} + \frac{K_{II}^2}{E^\star} + \frac{K_{III}^2}{2\mu} \tag{1.23}$$

with μ the shear modulus of the material. Notice the additive contribution of the stress intensity factors K_I, K_{II}, K_{III}. The parameter $E^\star$ is a constant of which value depends on the plane problem assumption of the analysis:

$$E^\star = \begin{cases} E & \text{for plane stress} \\ \dfrac{E}{1-\nu^2} & \text{for plane strain} \end{cases} \tag{1.24}$$

where E is the Young's modulus of the material, and ν its Poisson's ratio.

Remark 4 *The relation of Equation (1.23) assumes a self-similar crack growth. Under this assumption, a planar crack remains planar and the fields around the front keep a constant shape during the propagation. This is usually not the case for mixed-mode propagation, and the crack will tends to propagate in such a way as to maximize the energy release rate. A more elaborated strategy is hence needed, for instance using an evaluation of the energy release rate as a function of the propagation direction [COT 80, LEB 99].*

1.5 Crack tip plastic zone

The elastic asymptotic analysis revealed that the stress field tends to infinity near the crack front. Obviously, no existing material can stay elastic in such conditions. Indeed, whatever the material, the geometry of the crack, and even the loading, a plastic zone will develop around the front. Consequently, the size of this plastic zone must be controlled, in order to quantify how much the stress relaxation due to the plasticity modifies the elastic solution. To stay in the framework of the linear elastic fracture mechanics, the *small scale yielding* hypothesis is commonly used. This assumption stands that if the size of the plastic zone, of characteristic length r_p, is sufficiently small compared to the K-dominance zone of the crack, the singular fields introduced in section 1.3 are still valid. In practice, the size of the K-dominance zone can be expressed in terms of a, the characteristic length of the crack, and the small scale yielding assumption is fulfilled if:

$$\frac{r_p}{a} < 3\% \tag{1.25}$$

Even in the small scale yielding case, the crack tip plastic zone has a major influence on the growth rates of fatigue cracks (see section 3).

Under fatigue or repeated loading, two different plastic zones are defined, the so-called monotonic and cyclic zones. The monotonic plastic zone appears at any time that the structure undergoes a load opening the crack. The global shape of this zone is varying between the shape of butterfly wings in plane strain conditions (in the bulk of the structure) and the shape of a bean

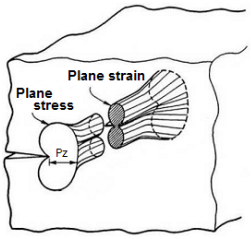

Figure 1.4 Schematic plastic zone shape at the tip a of mode I crack in a tridimensional body.

when the triaxiality state goes lower (plane stress conditions, near the free surface of the part). In addition, the crack tip yielding zone is smaller in plane strain conditions than in plane stress. An overview of the shape of this zone is presented on Figure 1.4. To estimate analytically the size of the monotonic plastic zone, Irwin considered as a first approximation that the boundary between the yielded material and the zone that remain in the elastic domain occurs when the stress predicted by the asymptotic analysis reaches the yield strength σ_y of the material. On the crack plane ($\theta = 0$), the normal stress σ_{22} for a linear elastic material is given on Table 1.1. Consequently, assuming plane stress conditions, a first order estimate of the plastic zone size expressed in terms of stress intensity factor writes:

$$r_p = \frac{1}{2\pi}\left(\frac{K_I}{\sigma_y}\right)^2 \tag{1.26}$$

Under plane strain conditions, the yielding being moderated by the triaxiality state, the Irwin plastic zone estimate is smaller by a factor of 3:

$$r_p = \frac{1}{6\pi}\left(\frac{K_I}{\sigma_y}\right)^2 \tag{1.27}$$

Remember that in reality, the global size and shape of the monotonic plastic zone depend also on the hardening of the material.

The cyclic plastic zone, sometimes called reverse plastic zone in the literature, appears during the unloading of the structure. It is embedded inside the monotonic plastic zone. The Figure 1.5 describes the crack tip deformation that occurs during single load-unload cycle. During the loading, the monotonic plastic zone arises and the crack tip blunts. When the load is removed, the surrounding material, that as remained elastic, forces the material at crack tip to conform to its original shape. As a consequence, compressive residual stresses appear inside the monotonic plastic zone. If those stresses exceed the compressive yield stress of the material, a smaller, compressive plastic zone develops close to the crack tip [MCC 91].

Remark 5 *The crack tip plastic zone shape and size highly depend on the material behavior and hardening [POM 02]. In addition, it has a great influence on the growth rates since it is at the origin of the plasticity-induced crack closure phenomenon (section 3.2). Thereby, to produce accurate results, the material non-linearities have to be taken into account during crack propagation simulations.*

1.6 Stress intensity factors computation

The computation of the stress intensity factors and of the energy release rate in arbitrary tridimensional structures has always been a challenging task. Several methods have been proposed

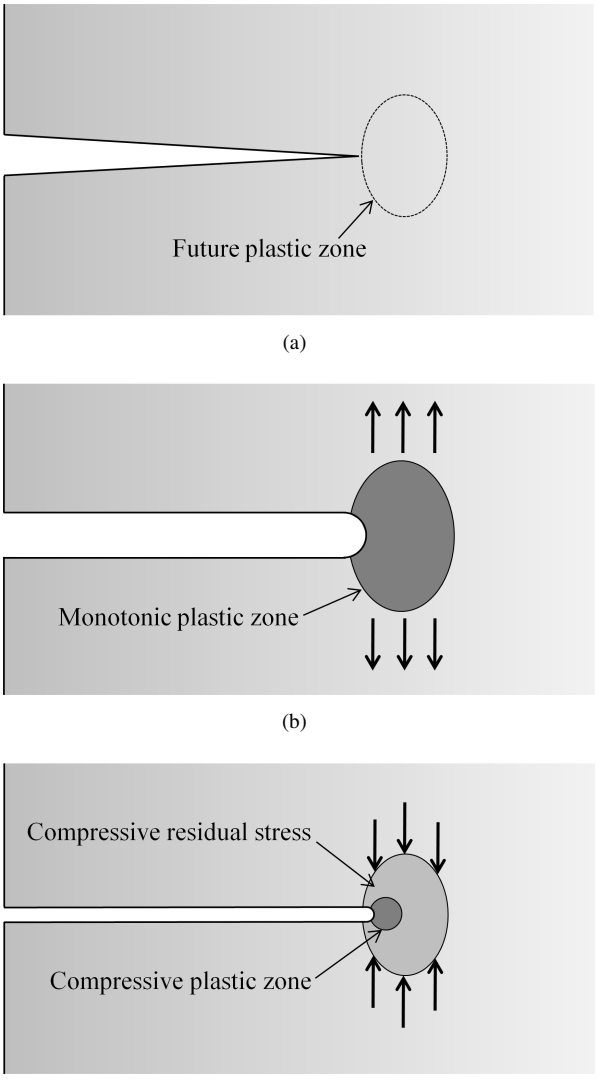

Figure 1.5 Deformation at a crack tip during a single load-unload cycle. A crack in an virgin material (a) is submitted to a tensile load resulting in tip blunting and monotonic plastic zone appearance (b). Then the load is removed and the compressive residual stresses lead to the formation of a compressive yielded zone, the cyclic plastic zone (c) [AND 05].

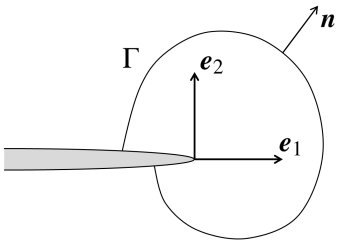

Figure 1.6 Crack tip integration contour.

over the years, such as the elemental crack advance, the stiffness derivative method [PAR 74], or the displacement matching method. The latter has been used for years in the industry, in particular because of its simplicity of implementation. It consists in projecting the nodal displacements obtained by a finite element computation on the singular solutions of Table 1.1. After that, the extraction of the stress intensity factors values is straightforward. Since the asymptotic solutions are valid only in a restricted zone near the crack tip, the nodal displacement are to be taken as close as possible to the front. Here arises the main accuracy problem of this type of approach. Indeed, in the vicinity of the crack tip, the finite element method is saturated by the singularity and does not allows to capture accurately the solution. In order to alleviate this constraint, energetic methods have been introduced and are now widely accepted as very robust and accurate techniques [DES 83]. They rely on the integration domain independence property of some class of integrals, hence allowing to use fields computed far from the crack front for the extraction of the stress intensity factors. Finally, some innovative approaches have emerged recently, using the old idea of projecting the displacement solutions onto a basis provided by a truncated Williams' expansion [WIL 57], but this time directly *during* the numerical resolution, not in a postprocessing step [LIU 04, PAS 10]. Hence the singular fields are accurately described by the basis and the computed stress intensity factors are of a fairly good quality. In this work, path independent domain integral methods were used and are presented hereinafter.

1.6.1 The *J* integral

The path independent J contour integral was first proposed by Rice in the late 1960's [RIC 68]. It is based on the energy conservation law and on the former work of Eshelby [ESH 56]. Originally, the integration domain was defined as a line for bidimensional problems and a surface for tridimensional ones. Thus, assuming the Einstein summation convention, the associated definition of the J integral writes:

$$J = -\int_{\Gamma} \boldsymbol{P}_{ij}\boldsymbol{n}_j \, \mathrm{d}\Gamma \qquad \forall\, \Gamma \tag{1.28}$$

where $\boldsymbol{n}$ is the outward normal to the integration contour Γ such as illustrated on Figure 1.6. The tensor $\boldsymbol{P}_{ij}$ is the Eshelby tensor defined as follow:

$$\boldsymbol{P}_{ij} = W\boldsymbol{\delta}_{kj} - \boldsymbol{\sigma}_{ij}\frac{\partial \boldsymbol{u}_i}{\partial \boldsymbol{x}_k} \tag{1.29}$$

in which $\boldsymbol{\delta}_{kj}$ is the Kronecker delta, $\boldsymbol{\sigma}$ and $\boldsymbol{u}$ being respectively the stress and displacement solution fields. The parameter W is the deformation energy, which, for a linear elastic material, depends on the stresses and on the deformation tensor $\boldsymbol{\varepsilon}$:

$$W = \frac{1}{2}\boldsymbol{\sigma}_{ij}\boldsymbol{\varepsilon}_{ij} \tag{1.30}$$

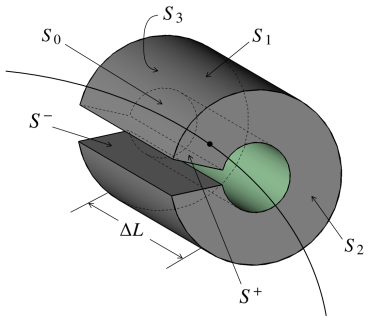

Figure 1.7 Volume integration domain around a tridimensional crack front.

The form of the integral (1.28) is not suitable for numerical analysis, since in practice, the accurate evaluation of stresses and strains along a specific contour is an awkward task. To alleviate this specific drawback, the J integral has been reformulated in the form of a domain integral. Hence, the integration domain becomes a surface in 2D and a volume in 3D. A general discussion of crack tip contour integrals and their associated domain representation is given in [MOR 87].

Consider a point η of a tridimensional crack front at which we would like to compute the J integral. A volume V is constructed, centered around the point η (see Figure 1.7). It consists of a "tube" of length ΔL, limited by its inner surface S_0, its outer surface S_1, its lateral faces S_2 and S_3, as well as the portion of crack faces S^+ and S^-. In the domain V, a virtual extension field $\boldsymbol{q}$ is defined such as:

$$\boldsymbol{q} = \alpha(\zeta) \cdot \boldsymbol{e}_1 \tag{1.31}$$

where α is a sufficiently smooth scalar field depending on the position of the current point ζ in the domain V, and fulfilling the following conditions:

$$\begin{cases} \alpha(\zeta) = 1 & \text{for } \zeta \in S_0 \\ \alpha(\zeta) = 0 & \text{for } \zeta \in S_1 \cup S_2 \cup S_3 \cup S^+ \cup S^- \end{cases} \tag{1.32}$$

With all those components, we can define a weighted average $\bar{J}$ of J over the crack front segment of length ΔL enclosed in the domain V, and rewrite the integral (1.28) in terms of a volume integral on V:

$$\bar{J} = -\int_V \left[W \boldsymbol{\delta}_{kj} - \boldsymbol{\sigma}_{ij} \frac{\partial \boldsymbol{u}_i}{\partial \boldsymbol{x}_k} \right] \frac{\partial \boldsymbol{q}_k}{\partial \boldsymbol{x}_j} \, \mathrm{d}V - \int_{S^+ + S^-} \left(\boldsymbol{\sigma}_{ij} \boldsymbol{n}_j^f \right) \frac{\partial \boldsymbol{u}_i}{\partial \boldsymbol{x}_k} \boldsymbol{q}_k \, \mathrm{d}\Gamma \tag{1.33}$$

the vector $\boldsymbol{n}^f$ being the local normal to the crack faces. If these crack faces are free of traction ($\boldsymbol{\sigma}_{ij} \cdot \boldsymbol{n}_j^f = 0$), the surface term in Equation (1.33) vanishes and the J integral reduces to the volume term.

Remark 6 *The $\boldsymbol{q}$ field does not necessary need to be defined in terms of a virtual crack extension, but attaching a physical significance to this parameter may aid in understanding. In fact, this vectorial field is merely a mathematical device that enables the generation of a domain integral.*

In addition, if thermal solicitations are present in the considered body, a supplementary correction term must be added. If thermal strains are present, the following decomposition of the total strains can be done:

$$\boldsymbol{\varepsilon}_{ij}^{total} = \boldsymbol{\varepsilon}_{ij}^{e} + \boldsymbol{\varepsilon}_{ij}^{t} \tag{1.34}$$

in which the superscripts e and t refer respectively to the elastic and thermal strains. The elastic deformation energy is then defined by

$$W^e = \frac{1}{2}\boldsymbol{\sigma}_{ij}\boldsymbol{\varepsilon}^e_{ij} \tag{1.35}$$

Finally, without surface traction and in presence of thermal strains, the J integral rewrites, computed on the volume V:

$$\bar{J} = \int_V \left\{ \left[\boldsymbol{\sigma}_{ij}\frac{\partial \boldsymbol{u}_i}{\partial \boldsymbol{x}_k} - W\boldsymbol{\delta}_{kj} \right] \frac{\partial \boldsymbol{q}_k}{\partial \boldsymbol{x}_j} + \left[\alpha\,\boldsymbol{\sigma}_{ii}\frac{\partial \Theta}{\partial \boldsymbol{x}_k} \right] \boldsymbol{q}_k \right\} \mathrm{d}V \tag{1.36}$$

where α is the coefficient of thermal expansion and Θ is the temperature relative to the strain-free conditions. Considering that the pointwise value of the J integral does not vary over the segment C of crack front enclosed in the integration domain, the integral $J(\eta)$ at the point η of the front evaluates:

$$J(\eta) = \frac{\bar{J}}{\int_C \boldsymbol{q}(\zeta)\,\mathrm{d}\zeta} \tag{1.37}$$

It has been shown that the value of the integral (1.36) is independent of the choice of the integration domain, given that it encloses the crack front, that there is no traction on the crack faces and that the crack is planar inside the integration domain. In addition, performing an analysis of the potential energy balance of a cracked body, Rice proved that, under quasistatic conditions, the J integral is equivalent to the energy release rate G:

$$J \equiv G \tag{1.38}$$

This very powerful equality allows using the J integral for practical numerical evaluation of the energy release rate. Using the Irwin's formula (1.23), the stress intensity factors can also be linked to the J integral. However, under mixed mode solicitations, this integral does not allow to differentiate the three different stress intensity factors values from the global expression of J. For this purpose, the interaction integral has been introduced.

1.6.2 The interaction integral

The so-called interaction integral [MOR 87, DES 83] is a specific integral that keeps the interesting properties of the standard J integral such as the domain independence, and that enables the extraction of the stress intensity factors from the solution fields of a crack solicited in mixed mode loading.

Let consider a cracked body at an equilibrium state. Its stress and deformation tensors $\boldsymbol{\sigma}$ an $\boldsymbol{\varepsilon}$, as well as its displacement field $\boldsymbol{u}$, fulfill the boundary conditions. A second state is then introduced. This additional state represent in fact an auxiliary, fictitious state and all its corresponding quantities will be denoted by the subscript *aux*. Applying the superposition principle, and assuming the Einstein summation convention, the J volume integral of these two states writes:

$$J^{total} = -\int_V \left[W^{total}\boldsymbol{\delta}_{kj} - \left(\boldsymbol{\sigma}_{kj} + \boldsymbol{\sigma}^{aux}_{ij}\right)\frac{\partial\left(\boldsymbol{u}_i + \boldsymbol{u}^{aux}_i\right)}{\partial \boldsymbol{x}_k} \right] \frac{\partial \boldsymbol{q}_k}{\partial \boldsymbol{x}_j}\,\mathrm{d}V \tag{1.39}$$

where the total deformation energy is given by

$$W^{total} = \frac{1}{2}\left(\boldsymbol{\sigma}_{ij} + \boldsymbol{\sigma}^{aux}_{ij}\right)\left(\boldsymbol{\varepsilon}_{ij} + \boldsymbol{\varepsilon}^{aux}_{ij}\right) \tag{1.40}$$

By reordering the terms, the total J integral can be expressed as the following sum:

$$J^{total} = J + J^{aux} + I \tag{1.41}$$

in which J and J^{aux} are the J integrals of respectively the real state and the auxiliary state, and I is the *interaction integral* of these two states:

$$I = J^{total} - J - J^{aux} \tag{1.42}$$

$$I = \int_V \left[\frac{1}{2} \left(\boldsymbol{\sigma}_{ij} \boldsymbol{\varepsilon}_{ij}^{aux} + \boldsymbol{\sigma}_{ij}^{aux} \boldsymbol{\varepsilon}_{ij} \right) \boldsymbol{\delta}_{kj} - \boldsymbol{\sigma}_{ij} \frac{\partial \boldsymbol{u}_i^{aux}}{\partial \boldsymbol{x}_k} - \boldsymbol{\sigma}_{ij}^{aux} \frac{\partial \boldsymbol{u}_i}{\partial \boldsymbol{x}_k} \right] \frac{\partial \boldsymbol{q}_k}{\partial \boldsymbol{x}_j} \, \mathrm{d}V \tag{1.43}$$

Using Hooke's law and assuming major symmetry, it can be shown that:

$$\boldsymbol{\sigma}_{ij} \boldsymbol{\varepsilon}_{ij}^{aux} = \boldsymbol{\sigma}_{ij}^{aux} \boldsymbol{\varepsilon}_{ij} \tag{1.44}$$

allowing to further simplify the integral (1.43). Finally, adding the necessary correction accounting for thermal strains [JOH 07, NAK 92], the interaction integral I rewrites:

$$I = \int_V \left\{ \left[\boldsymbol{\sigma}_{ij} \boldsymbol{\varepsilon}_{ij}^{aux} \boldsymbol{\delta}_{kj} - \boldsymbol{\sigma}_{ij} \frac{\partial \boldsymbol{u}_i^{aux}}{\partial \boldsymbol{x}_k} - \boldsymbol{\sigma}_{ij}^{aux} \frac{\partial \boldsymbol{u}_i}{\partial \boldsymbol{x}_k} \right] \frac{\partial \boldsymbol{q}_k}{\partial \boldsymbol{x}_j} + \left[\alpha \boldsymbol{\sigma}_{ii} \frac{\partial \Theta}{\partial \boldsymbol{x}_k} \right] \boldsymbol{q}_k \right\} \mathrm{d}V \tag{1.45}$$

Using the Irwin's formula (1.23), the interaction integral can be linked to the stress intensity factors corresponding to the real state and the auxiliary state:

$$I = \frac{2\left(1-\nu^2\right)}{E} \left(K_I K_I^{aux} + K_{II} K_{II}^{aux} \right) + \frac{1}{\mu} \left(K_{III} K_{III}^{aux} \right) \tag{1.46}$$

At this point, a judicious choice of the auxiliary fields before evaluating the Equation (1.45) allows extracting the stress intensity factors by a simple arithmetic procedure [GOS 02]. For instance, substituting $K_I^{aux} = 1$ and $K_{II}^{aux} = K_{III}^{aux} = 0$ into Equation (1.46) yields:

$$I = \frac{2\left(1-\nu^2\right)}{E} K_I \tag{1.47}$$

Just as for the J integral (1.36), the interaction integral (1.45) is in fact defined as a weighted average over a crack front segment C. Again, considering that the pointwise value of this integral does not vary significantly in the integration volume, the mode I stress intensity factor K_I at any point of the front enclosed in the integration domain is deduced as:

$$K_I = \frac{E}{2(1-\nu^2)} \frac{I}{\int_C \boldsymbol{q}(\zeta) \, \mathrm{d}\zeta} \tag{1.48}$$

To conclude on that point, the interaction integral provides a very practical tool for the numerical evaluation of the stress intensity factors. At the beginning of this thesis, it has been necessary to implement this method in the ANSYS solver code.

2 Numerical methods for 3D crack growth analysis

2.1 Overview

In general, the numerical simulation of crack growth is resolved in three main stages (Figure 1.8). In a first step, the structural mechanics problem is solved, that is, the partial derivative equations modeling the mechanical behavior of the cracked structure associated with the appropriate

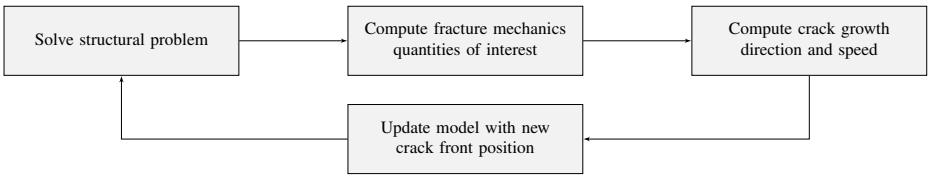

Figure 1.8 General strategy for the numerical simulation of crack propagation.

boundary conditions. This provides approximate displacement and stress fields that constitute the numerical solution of the problem. Then the fracture mechanics quantities of interest (for instance the stress intensity factors, see section 1) are computed during a second, post-processing stage. In addition, the crack growth direction and speed are computed by means of an appropriate propagation law (refer to section 3). At this point, in a third and last step, the model is updated to be consistent with the newly computed crack front position. This process is repeated iteratively until the final fracture of the structure or the crack arrest.

To deal with this type of problems, several adapted numerical method were proposed over the last thirty years. Among them, the finite element method (FEM) is a very popular numerical method for resolving structural mechanics problems. Besides the fact it is a now very robust and mature method [BEL 00, ZIE 05], its main advantages are that it can deal with very complex geometry, material behaviors and contact conditions. The size of the problem to solve depend on the mesh used to discretize the considered mechanical system. When dealing with problems of evolving geometries, such as crack growth, using a specific mesh morphing technique for the geometrical updates of the model (extensive details on that part are provided in section 4 of chapter 2) allows discretizing several different problems with meshes of the same dimension. Hence the problems to solve are of the same dimension as well, providing a straightforward coupling with reduced basis and model reduction techniques in general. For this reason, it is the chosen numerical method for this work. All the associated developments and computations were performed in the ANSYS software, taking advantage of very powerful solver and elements.

However, this powerful method faces two major drawbacks. First, the used mesh must explicitly describe the crack geometry. Since fracture mechanics is essentially a multiscale problem, significant mesh refinement is necessary in the cracked region to capture the steep gradient solutions. Basically the scale of the whole structure (some meters) can be very different from the scale of the crack (some centimeters) and even from the scale of the non-linear events localized at crack tip (some micrometers). In spite of the improvements carried out to the automated 3D meshers, such type of mesh can be difficult to achieve. The second drawback comes from the fact that the convergence of the finite element method is saturated by the singular fields around the tip and does not allow to capture accurately the solution. In this respect, a review of different methods, with their particular advantages and drawbacks is proposed in this section.

Another type of method adapted to fracture mechanics analysis is the boundary element method (BEM). This method attempts to solve the governing partial derivative equations once they have been formulated in terms of integral equations [ALI 02, BON 04]. Those equations are written on the boundaries of the considered domain, and the BEM uses the applied boundary conditions to fit boundary values into the integral equations. Hence only the boundaries of the model have to be discretized for the resolution of the equations (that is, lines in 2D and surfaces in 3D). This is the main advantage of the method: the problems to solve are in fact one dimension lower than the actual embedding space of the model. Once the integral equations are solved, in a post-processing stage, they can be used to compute numerically the solution at any point in the interior of the actual domain. This type of method has been applied in various fields, such as fluid

or electromagnetism [WRO 02], and of course fracture mechanics [BON 95, MI 94]. The main drawback stems from the fact that BEM is applicable to problems for which Green's function can be calculated (a mathematical device allowing to solve the integral equations). These specific functions are available only for some specific geometries, under mainly linear assumptions (e.g., no plasticity) placing considerable restrictions on the range of problem to which BEM can be applied. Attempts have been conducted to overcome this drawback, mainly by coupling the BEM to a FEM associated with parts of the structures far from the crack [FRA 03] or using an iterative coupling of a FEM formulation on the real considered structure but without crack, and a boundary element method on an infinite cracked body [NIK 01]. The other drawback of these method is that they usually give rise to fully populated matrices, making the storage requirement and computational time to solve the problems growing according to the square of the size of the problem. Again, methods such as the fast multipole [MAR 05, NIS 02] were introduced but their success strongly depend on the type of problem solved.

The challenging aspect of fracture mechanics lies in capturing the discontinuous displacement and singular stress fields around the crack. Indeed, in order to interpolate accurately such fields, the interpolation capabilities of standard FEM must be enhanced. In this respect, a third class of methods was developed, in which the crack is not explicitly represented by the mesh of the model. This includes, among others, the element-free or meshless methods [BEL 94], the diffuse element method, which is based on moving least square approximation [NAY 92], the reproducing kernel particle method [LIU 95], the natural element method [SUK 01] and the smoothed particle hydrodynamics method [MON 05]. In all those methods, the mesh notion does not exist in the sense that only nodal data is necessary to perform the computations. The crack is then described by appropriate weight functions nodal values [BEL 94, KRY 99].

In this same class, the methods based on the partition of unity [MEL 96] are particularly interesting for fracture mechanics applications. Among other, the generalized finite element method [STR 01, PER 09, PER 10] and the extended finite element method (XFEM) [MOË 99, MOË 02, DAU 00, SUK 08] can be mentioned. In the latter, the kinematic field of the standard finite element method is enriched by introducing additional degrees of freedom to the nodes surrounding the crack. The crack is then described implicitly by the associated specific shape functions. This method has been continuously improved over the recent years, allowing now to use nonlinear material behaviors, contact of the crack faces and multiscale approaches [ELG 07, BÉC 08, PIE 10, RAN 09a]. Coupling with experimental analysis as also been performed [RAN 09b]. The main advantage is that the mesh does not need to be modified during the crack propagation, only the enrichments are updated. Anyway, the mesh does still need to be adapted to the phenomenon that must be captured (yet much less than with the standard FEM). In addition, updating the enrichments makes the number of degrees of freedom changing during that propagation. This makes the coupling of XFEM with model reduction method less direct than with FEM.

Apart from that, it is worth mentioning approaches in which the discontinuity is not introduced at the global level by adding degrees of freedom to existing nodes around the crack, but rather at a local level, embedding the discontinuity locally in the weak form or the behavior law at the element level, so that the enhancement has no effect on the global system of equations [BOR 02]. These approaches are often referred to as strong discontinuity approaches [LAR 96, OLI 02].

2.2 Finite element method: practical remarks

During the analysis, the crack must be explicitly described in the finite element model and to provide accurate numerical results, significant mesh refinement must be performed around the leading edge of the crack. Since no existing solution was available within the ANSYS framework, an

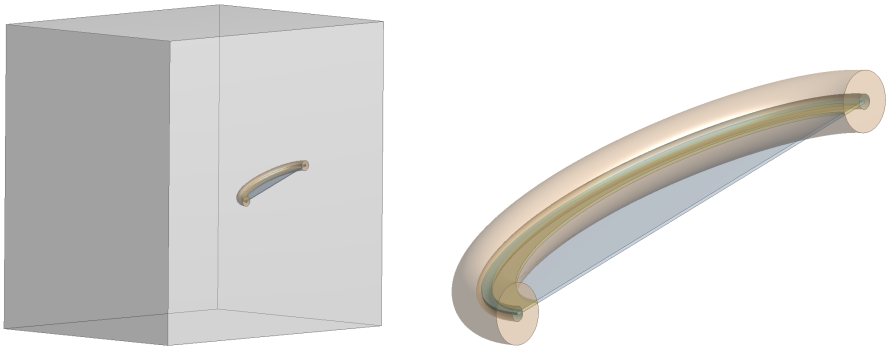

(a) (b)

Figure 1.9 Overview (a) and closeup (b) of the specific geometric configuration used to introduce the crack at the geometry level.

automatic meshing methodology has been developed. This new methodology is very general and allows to tackle complex non-planar 3D crack geometries, with arbitrary front shapes. Anyway for the explanation of the methodology proposed herein, the crack will be considered planar.

In this approach, the crack is first introduced at the geometry level, that is, before the meshing step, using a specific configuration shown on Figure 1.9. The crack front is represented by a spline, which is of a great versatility and allows to handle any type of complex crack front shape. Along this spline, two concentric toruses are swept (in light orange on the figure). In addition, three bodies with a small, finite thickness are extruded at the location of the crack plane (in blue, brown and green on the figure). At this point, the crack is not existing as such, since these bodies of finite thickness are present at the place of the crack faces. The whole geometry is then meshed, as presented on Figure 1.10. Obviously, the resulting mesh is still not representing a crack, but the extruded torus have guided the mesher to provide concentric layers of elements near the crack front. So here takes place the second step of the methodology. The closest elements to the crack tip, that is, the gray elements inside the smaller torus, are deleted and replaced by new wedge elements, joining precisely at the crack front. In addition, the brown, yellow and blue elements constituting the thin bodies at the crack plane location are also deleted. Then the nodes belonging to the newly created crack faces are moved toward the crack plane to fill the gap leaved by the elements deletion. The resulting mesh is shown on Figure 1.11, as well as an example of von Mises stress obtained on this mesh solicited by an arbitrary loading. This specific methodology has been used to mesh all the test-cases presented in this typescript.

Remark 7 *In addition to the introduced meshing methodology, an automated remeshing strategy has also been developed to test some ideas. It takes advantage of the scripting capabilities available within the ANSYS framework, combining* Python*,* JScript *and* APDL *languages. In this method, based upon the front position provided by the crack growth law, the spline constituting the crack front is merely updated and the meshing methodology is performed again on the obtained updated geometry.*

Hence as shown above, in the vicinity of the crack front, a specific radial pattern is used for the meshing. Each row of element around the tip is called a “contour”. This definition as well as the radial mesh pattern are illustrated on Figure 1.12. The first mesh contour is constituted by quadratic wedges. Since in our finite element problems the material behavior is linear elastic, in those elements the midside nodes near the crack tip are placed at the quarter point, hence follow-

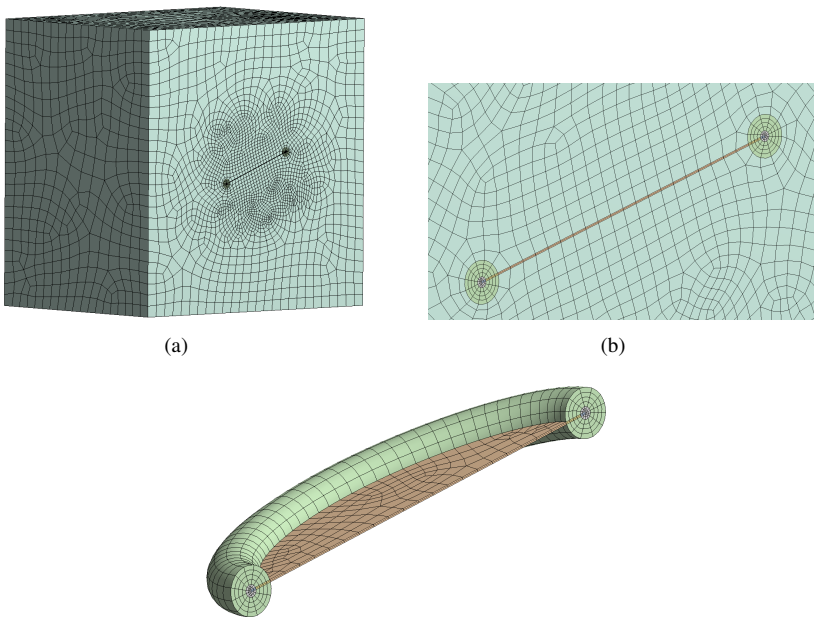

(a) (b)

(c)

Figure 1.10 Overview (a) and closeups (b) - (c) of the initial mesh of the pseudo-crack geometry.

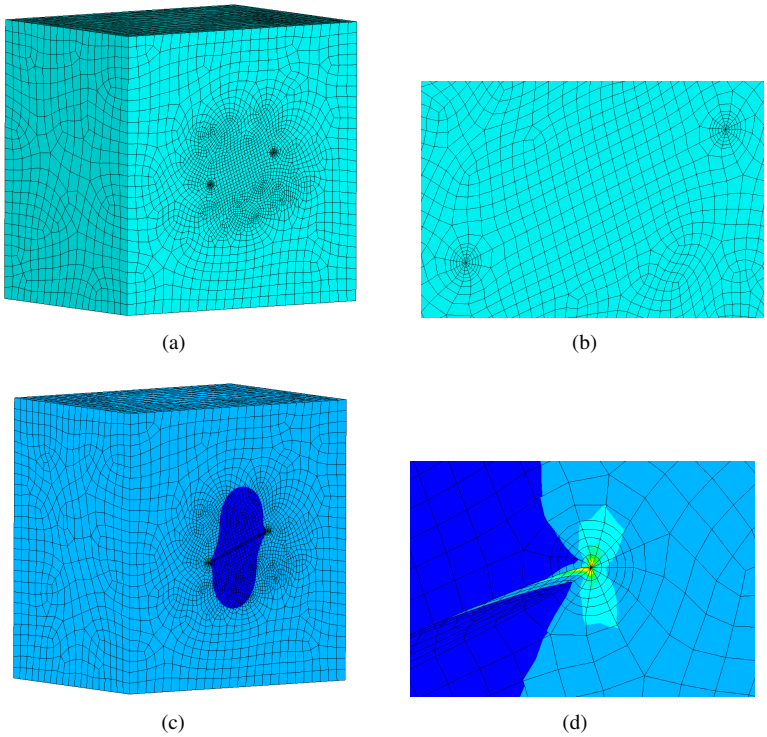

(a) (b)

(c) (d)

Figure 1.11 Overview (a) and closeup (b) of the final crack mesh. Example of von Mises stress solution obtained on that mesh for an arbitrary solicitation (c) - (d).

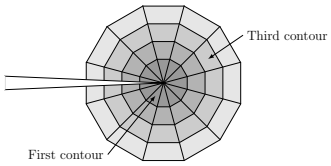

Figure 1.12 Definition of the element "contours" on a section of the specific radial mesh pattern at the crack tip.

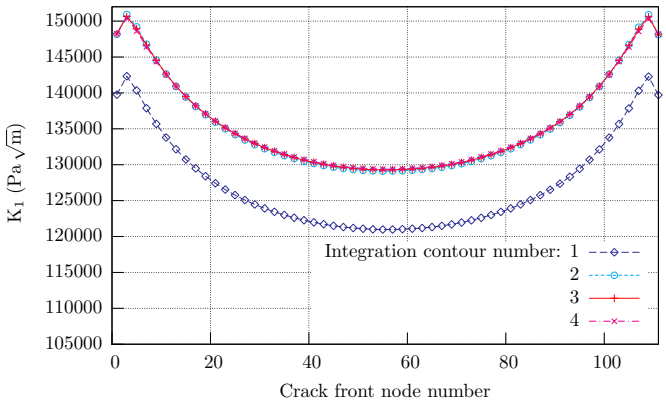

Figure 1.13 Mode 1 stress intensity factor computed on several integration contours around the crack front.

ing the Barsoum's recommendations [BAR 77]. The other contours are meshed with conventional quadratic hexahedra.

All along the crack growth, the stress intensity factors must be computed and provided to the crack growth law. They are extracted from the stress and displacement fields by means of the so-called interaction integral (see section 1.6.2). The accuracy of this type of domain integral methods, even with coarse meshes, is now well known. Nevertheless, in the context of crack evolution analysis, the validity of the results must be ensured at each propagation step. For that purpose, an indicator based on the path independence property of those integrals is used. Hence at each propagation step, the interaction integral is computed several times, using the different contours of elements around the crack front as several different integration domains. Since these integrals exhibit some path independence properties, all the obtained stress intensity factors should be the same. In practice, those properties do not hold very close of the crack tip and for bad quality meshes. Thereby, checking the invariance of the obtained stress intensity factors over the integration domains provides an indicator of the quality of the numerical solution [BUI 78]. This method is used in an automated manner, without any intervention of the user. An example is given on Figure 1.13. For a simple 3D test case, the mode I stress intensity factors obtained at each crack front node are plotted. They are computed using different integration domains. Here, the K_1 that has been computed on the first contour of elements is much lower than the others. However, when the other contours are used to evaluate the interaction integral, the obtained K_1 are quite similar, hence exhibiting the contour independence property. This permits to conclude that the stress intensity factors computed on the second, third and fourth contours can be considered of a good numerical quality. During a crack analysis solve, we would then choose to use the results of the fourth contour.

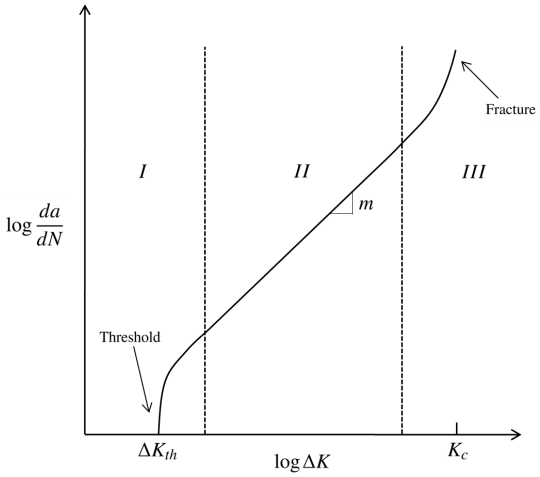

Figure 1.14 Typical fatigue crack growth behavior in metals.

3 Fatigue crack propagation: an overview

3.1 Fundamentals of fatigue crack growth

The Figure 1.14 is a schematic log-log plot of the crack growth rate $\mathrm{d}a/\mathrm{d}N$ versus ΔK, the variations of the applied stress intensity factor. The obtained sigmoidal curve contains three regions exhibiting different growth rate behavior, and due to different propagation mechanisms. At the low end, in the region I, the crack velocity decreases rapidly with decreasing ΔK until it reaches hardly detectable growth rates. On the contrary, for high ΔK values corresponding to the region III, the observed growth rates increases rapidly until the unstable, final propagation. In the linear region of the log-log plot of Figure 1.14, the crack velocity can be described by a power function of the variation of the stress intensity factor:

$$\frac{\mathrm{d}a}{\mathrm{d}N} = C\,\Delta K^m \tag{1.49}$$

where C and m are some experimentally determined material parameters. In the early 1960's, Paris and Erdogan [PAR 63] were apparently the first to discover the power-law relationship for fatigue crack growth in region II. Nowadays, this region in which stable crack growth occurs has become widely known as the *Paris regime*, as well as Equation (1.49) is now referred to as the *Paris law*.

Remark 8 *Since in practice the material constant m ranges from 2 to 6, it appears that a small error in the stress intensity factor evaluation would be greatly magnified using the Paris power law, leading to inaccurate results in terms of propagation rates. Because of this sensitivity of da/dN upon ΔK, it is essential to properly determine the numerical values of the stress intensity factors.*

Subsequently, a number of researchers have developed equations modeling the da/dN and ΔK relationship, trying to improve the Paris law. Indeed, one drawback of the initial Paris law is that the computed growth rates depends only on ΔK, consequently it is assumed that it is insensitive to the load ratio R:

$$R = \frac{K_{\max}}{K_{\min}} \tag{1.50}$$

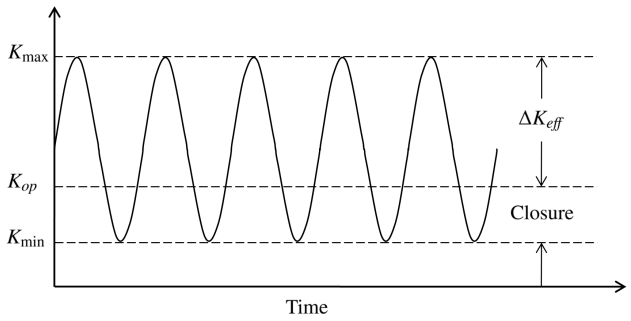

Figure 1.15 Crack closure concept during fatigue crack growth. The crack faces are in contact at low, nonetheless positive, loads. This leads to the definition of an effective stress intensity factor range ΔK_{eff}.

To cite one of those works aiming a more comprehensive relationship, Forman [FOR 67] proposed the following equation, valid for the regions II and III of the sigmoidal curve:

$$\frac{\mathrm{d}a}{\mathrm{d}N} = \frac{C\,\Delta K^m}{(1-R)\,K_c - \Delta K} \tag{1.51}$$

which can be rewritten such as:

$$\frac{\mathrm{d}a}{\mathrm{d}N} = \frac{C\,\Delta K^{m-1}}{\frac{K_c}{K_{max}} - 1} \tag{1.52}$$

Thus the crack growth rate becomes infinite as K_{max}, the maximal stress intensity factor applied to the crack, tends to K_c, the fracture toughness of the material. Note that Equation (1.51) contains an explicit dependence to the loading ratio R.

3.2 Crack closure effect

The so-called *crack closure effect* was accidentally discovered by Elber [ELB 70] in 1970. He postulated that contact between crack surfaces (that is, crack closure) occurred at loads that were low but greater than zero. Elber inferred that crack closure decreased the fatigue crack growth rate by reducing the effective stress intensity range. Indeed, it can be shown experimentally that the propagation rate of a fatigue crack under cyclic loading is not really proportional to the variations of the applied stress intensity factor ΔK, but rather to the effective stress intensity factor ΔK_{eff} experienced by the crack [ELB 71]. The closure concept is as follow: when a sample is cyclically loaded between a maximal stress intensity factor K_{max} and a minimal one K_{min}, the crack faces get in contact as soon as the applied stress intensity factor is lower than K_{op}, the value at which the crack opens. Elber then assumed that the portion of the loading cycle that is below the opening stress intensity factor K_{op} does not contribute to fatigue crack growth since the crack is closed. See Figure 1.15 for an illustration of the concept. In terms of equations, Elber defined an effective stress intensity range as follows:

$$\Delta K_{eff} \equiv K_{max} - K_{op} \tag{1.53}$$

And finally proposed a modified Paris equation:

$$\frac{\mathrm{d}a}{\mathrm{d}N} = C\Delta K_{eff}^m \tag{1.54}$$

Later on, Suresh and Ritchie [SUR 84] identified five different mechanisms for fatigue crack closure:

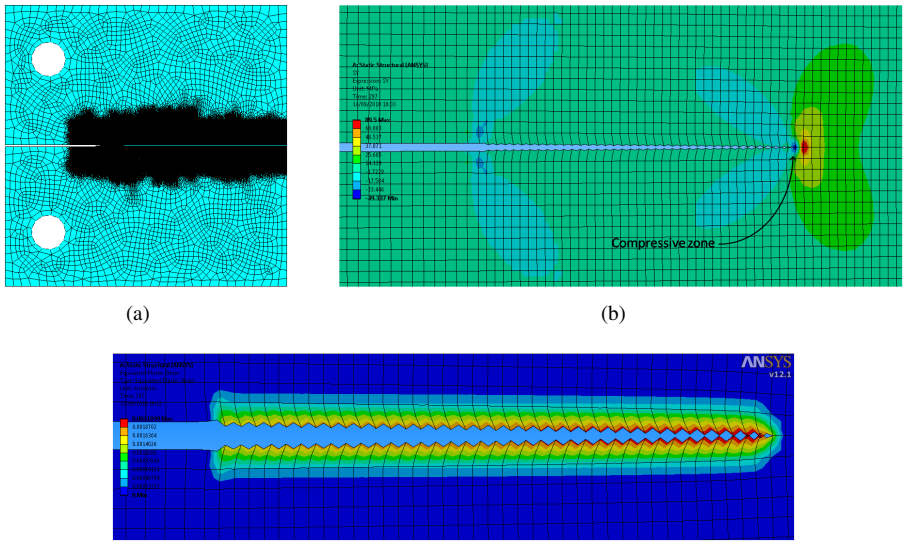

(a) (b)

(c)

Figure 1.16 Simulations of a mode I crack propagation in a 2D CT sample (a). Close-up around the crack of the resulting σ_{yy} component of the stress tensor, showing residual compression stress at crack tip (b). The residual plastic deformations and the plastic wake (c) lead to bumps on the crack faces that can contact. The results are plotted on amplified configurations.

- Plasticity-induced crack closure
- Roughness-induced crack closure
- Oxide-induced crack closure
- Closure induced by the presence of a viscous fluid between the crack faces
- Closure induced by a material transformation (e.g., phase transform) near the crack.

In the present work, we will however focus on the plasticity-induced crack closure, which is particularly sensitive to the loading history.

Since Elber's original study, numerous researchers have studied the mechanisms of plasticity-induced crack closure, whereas experimentally [JAM 85, POM 02] or using finite element computations [NEW 76, SOL 04, ELG 07]. They conclude that this phenomenon is created by the conjunction of two sources. First the localized plastic zone at the crack tip, which lead to the appearance of compressive residual stresses at low loads, making the loading cycles less efficient (Figure 1.16(b)). And secondly, since the crack grow through this plastic zone, the stress redistributions in the appearing plastic wake make contact occurring between the crack faces (see Figure 1.16(c)).

Note that the Figure 1.16 illustrating this paragraph was obtained by a 2D elastic-plastic finite element analysis of a propagating crack in a compact tension specimen inspired by the computations conducted by [ELG 07] using the extended finite element method. A very fine mesh constituted by 218495 nodes and 74407 elements is used, leading to 655485 degrees of freedom. An arbitrary isotropic bilinear elastic-plastic material behavior is employed, with properties close to those of a standard steel. The contact between the crack faces is handled by a penalty method and crack propagates by a node release technique.

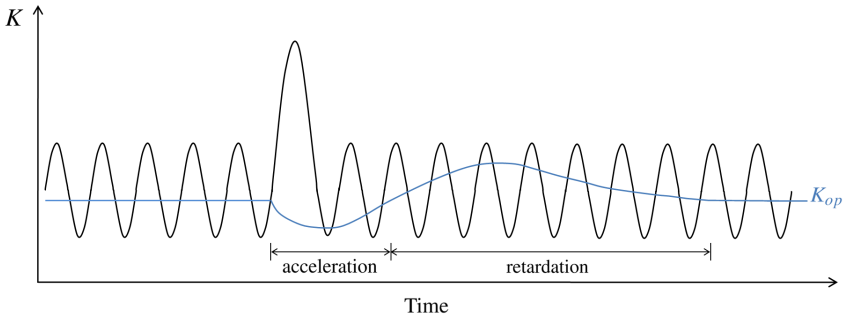

Figure 1.17 Schematic evolution of the opening level K_{op} during an overload.

Because it makes some part of the loading cycles inefficient, the crack closure effect has a great influence on the growth rates of fatigue cracks. It is tightly linked to the nonlinear elastic-plastic behavior of the material, and to the loading history. Indeed, the appliance of load variations, such as overloads or underloads, make the plastic zone evolving in a nonlinear way. Thereby, to perform accurate crack growth prediction, this effect has to be taken into account during the numerical simulations.

3.3 Fatigue crack propagation under variable amplitude loading

The growth behavior of fatigue damage has been widely studied during the last fifty years. The Paris, Forman, Walker laws and their modifications are now commonly used to compute the propagation rates. However, when fatigue cracks are submitted to complicated loading spectra with variable amplitudes, these equations become inaccurate. In those cases, the main complexity comes from the interactions between the variable stresses, their influence on the confined crack tip plastic zone and finally on the crack velocity. This causes the so-called crack closure effect to arise. To illustrate this, one can refer to the well known retardation effect after an overload. Qualitatively, this phenomenon arises because during and overload, the local crack tip plastic zone grows bigger than under nominal loading. Just after that, the compressive reverse plastic zone will be bigger as well. The resulting compressive stresses at the tip will decrease the efficiency of the subsequent loading cycles. The crack growth rates are hence decreased significantly until that the crack has propagated enough, such that its tip is far beyond the overload plastic zone. The reader can refer to section 1.5 for an extensive description of the crack tip plastic zones.

For most of the common structural materials, such as steel for instance, a *delayed retardation* is observed after an overload [BAT 97]. An illustration of the evolution of the opening level K_{op} of a crack during an overload is provided on Figure 1.17. This level corresponds in fact to the stress intensity factor that must be applied to avoid contact between the crack lips, and thus crack closure. As a consequence, the crack growth rates can be correlated with the value of K_{op}. At the beginning of the situation presented on Figure 1.17, the crack undergoes a cyclic loading. The opening level (which can also be called "closure level") is hence steady, and the crack speed is constant. During the overload itself, the opening level immediately drops down. This is because crack tip blunts much more than under nominal loading, reducing the level of crack closure. As a result, an instantaneous, yet transitory, acceleration arises. Then, the crack propagates through the residual plastic compressive stress zone made by the overload, and the opening level of the crack rises up significantly, producing the so-called delayed retardation effect. After that, the closure level goes back slowly to its initial level.

The nature of the very complex response of a crack to an overload depends on the type of

material and on the overload ratio, but also on the geometry of the sample and on the real tridimensional configuration of the crack. In addition, in order to yield accurate predictions, it is of a crucial importance that crack growth models could simulate the short transitory acceleration phase of the delayed retardations. In the case of more complicated loadings, with several overloads and underloads of different ratios, the response of the crack is even much more complex and highly non-linear. Indeed, interactions between the cycles of variable amplitude is observed. In practice, these effects have a dramatic influence on the growth rates, as they can modify the crack velocity up to a factor 4! Many researchers have therefore tried to come up with models dedicated to the prediction of propagation rates under variable amplitude loadings.

Remark 9 *The spectacular phenomenon of retardation after an overload is often used during the commissioning and testing of pressurized installations (e.g., pipes, pressure vessels). This destructive testing method consists in applying an overload, that is, a loading greater than in the nominal operating conditions. If a critical flaw already exists in the tested material, the part will be destroyed by the test. On the contrary, the installation is not destroyed and the propagation of all the non-critical defaults is retarded, and sometimes even stopped by the overload effect.*

Some of the first models dedicated to simulate crack growth under spectrum loading are based on the Wheeler [WHE 72] and on the Willenborg [WIL 71] laws. They assume that the crack retardation is due to interactions between the current crack tip plastic zone and the bigger plastic zone due to the overload. In Wheeler's model, the nominal crack growth rate, coming from a Paris law, is multiplied by a retardation function when an overload occurs. The retardation effect is maintained as long as the current crack tip plastic zone is estimated to be included inside the overload plastic zone. Though simple, this model fail to handle successive overloads, because it stands that the retardation effect arises just after the overload. This leads to strongly underestimate the growth rates when the crack is submitted to repeated overloads. The principle of the Willenborg's model, for its part, consists in using a modified, effective stress intensity factor inside a Forman law when an overload occurs. The effective stress intensity factor determination is based on considerations about the estimated size of the overload plastic zone, and the propagation distance of the crack after the overload. This model is more efficient than the Wheeler's one, since the Forman's law allows to account for load ratios effects and the computation of the effective stress intensity factor enables to handle successive overloads of various levels. However, for intense overloads, the propagation rates are highly underestimated.

More sophisticated models where then proposed, with among others the CORPUS, PREFFAS or ONERA models [NEW 97]. Those are empirical models, essentially based on one or more evolution laws of the crack closure level. One major drawback comes precisely from the empirical nature of their growth laws. They require a large test campaign to identify the numerous model parameters, and they cannot ensure to be able to predict the crack speed for configurations that were not considered during the test campaign. A third type of models are the semi-numerical models such as FASTRAN [NEW 92], and are generally based on the Dugdale strip-yield model [DUG 60]. Those models were first designed for bidimensional analysis under the assumption of plane stress. For tridimensional simulations, the level of constraint depends among others on the geometrical configuration of the crack and especially on the crack location relative to external boundaries. As a consequence, the triaxiality level varies all along the crack front. Thereby, the strip yield model was extended to plane strain conditions [NEW 81]. Unfortunately, it leads to some contradictions in the physical meaning of the model and those attempts were less successful.

Remark 10 *All the fatigue crack growth model, including the Crack Tip Condensed Plasticity model presented in the next sections, are designed for a specific range of loading. This can stem*

either from the model parameters identification process, for instance, a number of experiment conducted using specific load levels, or even from the assumptions on the underlying physical propagation mechanism that is made in the model. Indeed, the propagation mechanism are very different in the threshold region, in the Paris regime and at high stress intensity factors values. In this respect, some very interesting work has been done in trying to couple various models, each of them dedicated to a specific physical crack growth mechanism [SUN 05, SUN 09]. The combination of those different models leads to consistent predictions of the propagation rates, for the whole range of the load spectrum.

4 The Crack Tip Condensed Plasticity model

Trying to build a more general propagation law, avoiding as much as possible empirical or experimentally fitted parameters and without any finite element elastic-plastic computation during the crack growth, the Crack Tip Condensed Plasticity model (or CTCP model), was first introduced by Pommier *et al.* [POM 05]. This innovative model can be viewed as an equivalent plasticity model for the whole cracked structured, that condenses the plastic behavior of the crack in a few scalar internal variables carried by the crack front. From a given elastic stress intensity factor, it allows computing incrementally the plastic state at crack tip and deduces from that the crack advance increment. In addition, the model can accounts for any plastic hardening (for instance combinations of non-linear isotropic and kinematic hardenings), and hence simulate crack growth in material exhibiting complicated behavior such as Bauschinger effect or ratcheting. Furthermore, it requires only one single experimentally fitted material parameter α (see Equation (1.58)). Since then, the model has been extended to 3D and continually improved, in particular by taking into account the biaxiality state by means of the T-stress level, compressive loadings [POM 07] and thermal effects [RUI 06]. Recently, successful attempts were conducted to enable the model to tackle mixed mode I+II non proportional loadings [MOU 09, DEC 09, POM 09], also providing numerical devices to ease the extraction of the stress intensity factors for kinking cracks [DEC 10].

Remark 11 *The CTCP model is often referred to as* LMT model *in the literature (from the name of the laboratory where it was initially developed). Hence* Crack Tip Condensed Plasticity model *is not by any means the official name of the model, however, for the sake of clarity we decided to use it extensively in this typescript.*

4.1 Understanding the CTCP model underlying ideas: a pragmatic approach

The CTCP model is based on an analysis of the displacement field near the crack tip. On Figure 1.18, the displacement field of the superior lip of a 2D crack loaded in mode I is represented. It was obtained by finite element computations. The crack tip is located at the origin. The x-axis measures the distance r along the crack faces normalized by the crack length a, and the y-axis the vertical component $\boldsymbol{u}_y$ of the displacement field of the superior crack lip, obtained by various finite element computations. The broken light blue line represents the obtained displacement solution for a linear elastic crack $\boldsymbol{u}_y^{le}(r)$. It is in fact the very well known asymptotic solution evolving with $\sqrt{r}$, the square root of the distance to the tip (refer to section 1.3). At this point, taking the same crack submitted to an arbitrary load and using this time a non-linear elastic-plastic material behavior for the computations yields the displacement field $\boldsymbol{u}_y^{ep}(r)$ depicted in dotted blue line. The main idea of the CTCP model comes from the fact that offsetting the linear elastic displacement solution by an appropriate scalar value ρ, constant along the crack faces (in black on the

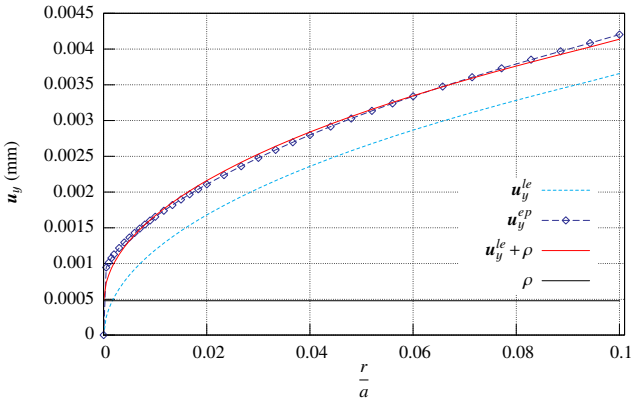

Figure 1.18 The CTCP model main idea: on a same crack, at the scale of the K-dominance zone, the vertical component of the linear elastic displacement field $\boldsymbol{u}_y^{le}(r)$ corrected by a constant scalar ρ matches with a fairly good approximation the full elastic-plastic displacement field $\boldsymbol{u}_y^{ep}(r)$.

figure), the elastic-plastic field can be matched with a fairly good correlation:

$$\boldsymbol{u}_y^{ep}(r) \approx \boldsymbol{u}_y^{le}(r) + \rho \tag{1.55}$$

This corrected field is proposed in continuous red line on the Figure 1.18. It is highlighted that this correlation is acceptable only outside the confined plastic zone, that is, not too close to the tip. In addition, it has been shown that the relative error between the full elastic-plastic displacement field and the corrected elastic one is in general about 12% [HAM 07]. In 2D mode I, the scalar correction ρ can be viewed as a representation of the plastic blunting at the tip, arising from the localized plastic deformations.

Remark 12 *The link between elastic-plastic and elastic crack tip displacement field by a constant offset is not a new idea. For steady cracks in small scale yielding conditions, in particular, this concept was already present in the Irwin's plastic correction [IRW 61] and in the Rice's description of the J-integral [RIC 68]. In both papers, it allows computing the stress intensity factors of elastic-plastic cracks just as if they were slightly longer elastic cracks. For all that, the CTCP model is a very interesting application of that observation.*

4.2 The CTCP model as an *a posteriori* model reduction

The plastic correction proposed in the previous section is valid on the crack lips, and it can also be extended to the whole displacement field around the crack tip. Although the plastic correction concept is easy to understand for the restriction of the displacement field to the lips of the crack, it is harder to see the validity of such approach applied to the full displacement field with all its components. In this respect, a more mathematical approach can be conducted, based on the model reduction framework (see section 3 of chapter 2 for details on this approach). Indeed, Hamam [HAM 06] computed the Karhunen-Loève decomposition of all the components the displacement field history during the loading of a crack. After that, he showed that the full displacement field could be reconstructed with a very good approximation using only the two first modes of its decomposition. Furthermore, it appeared that those two modes were very similar to respectively the elastic part and the plastic part of the displacement field.

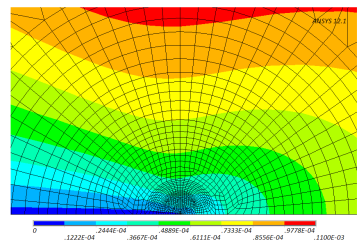

(a) x component of the linear elastic solution

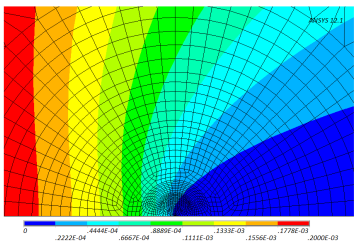

(b) y component of the linear elastic solution

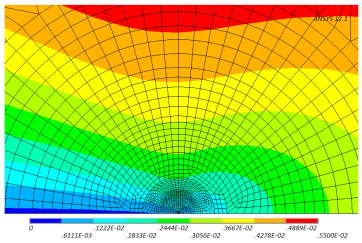

(c) x component of the first mode of the singular value decomposition

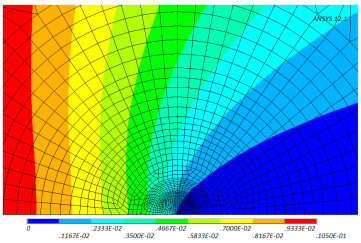

(d) y component of the first mode of the singular value decomposition

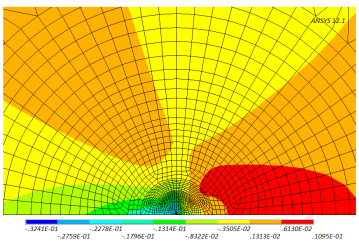

(e) x component of the second mode of the SVD

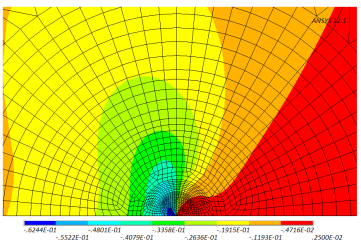

(f) y component of the second mode of the SVD

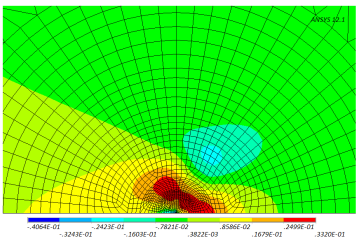

(g) x component of the third mode of the SVD

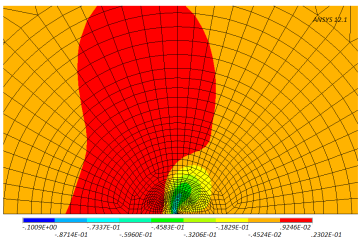

(h) y component of the third mode of the SVD

Figure 1.19 Displacement fields obtained by a linear elastic computation of a 2D crack in mode I (a) - (b), and 3 first modes of the singular value decomposition of the field history of the same crack with an elastic-plastic behavior (c) to (h). The linear elastic solution is very close to the first mode of the SVD.

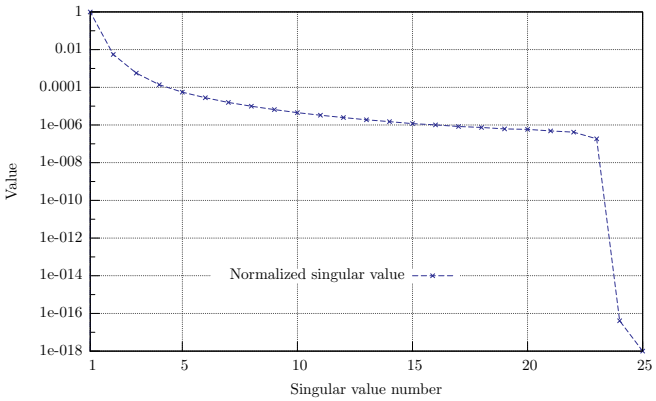

Figure 1.20 Normalized singular values of the elastic-plastic field history.

To illustrate that fact, a similar analysis is presented hereinafter. A 2D crack is solicited in mode I. The test-case used for this analysis is in fact the identification test-case described in section 4.3.2, please refer to that section for details on the finite element modeling. A first computation is conducted, using a linear elastic material and a loading corresponding to a stress intensity factor of 1 MPa $\sqrt{m}$. Then a second calculation is performed, this time with a non-linear elastic-plastic behavior, and a maximum loading of 100 MPa. This loading step is divided into 25 increments. Then a matrix containing all the 25 obtained displacement solutions is built:

$$\boldsymbol{A} = \begin{pmatrix} \boldsymbol{u}_1^1 & \boldsymbol{u}_2^1 & \cdots & \boldsymbol{u}_{25}^1 \\ \boldsymbol{u}_1^2 & \boldsymbol{u}_2^2 & \cdots & \boldsymbol{u}_{25}^2 \\ \vdots & \vdots & \ddots & \vdots \\ \boldsymbol{u}_1^N & \boldsymbol{u}_2^N & \cdots & \boldsymbol{u}_{25}^N \end{pmatrix} \tag{1.56}$$

where N is the number of degrees of freedom of the model. Finally, singular value decomposition (SVD) of this matrix is performed. This allows building, without any *a priori* knowledge, an optimal decomposition of the elastic-plastic fields in the form of Equation (1.55), that is, a series of spacial fields that not depend upon time, multiplied by temporal prefactors. Close-ups around the crack tip of the obtained displacement fields are proposed on Figures 1.19(c) to (h), as well as the result of the linear elastic computation on Figures 1.19(a) - (b). As analyzed by Hamam, the first mode of the SVD is very close from the linear elastic solution. In addition, the normalized singular values of the decomposition are plotted on Figure 1.20. The third singular value, normalized by the sum of the 15 singular values, is about 5.66×10^{-4}. This means that the whole non-linear elastic-plastic displacement field history can be reconstructed with about 0.08% of error using only linear combinations of the two first modes of the SVD. Note that this type of approach (e.g., SVD, Karhunen-Loève decomposition or Principal Component Analysis) is very well known in the model reduction framework, for instance to build reduced-basis or even estimate the dimension of a solution subspace. Similar analysis were carried on many times during this thesis, such as the ones presented in section 6 of chapter 2.

Hence the CTCP model is based on the assumption that the elastic-plastic displacement field of the crack faces near the tip (in the K-dominance region) can be projected onto a reduced basis of dimension 2: one vector describing the elastic part of the displacement field, and a second one the plastic part.

Remark 13 *It should be mentioned that Henninger* et al. *[HEN 10] recently used a different approach, trying to perform the projection of the elastic-plastic field on the Williams' series expansion of the singular elastic crack tip fields [WIL 57]. Doing so, a basis of dimension 8 is set up and the necessary plastic corrections are provided by the supersingular, yet totally elastic, terms of the expansion.*

Once the reduced basis approach has been validated on the whole displacement field, for the sake of simplicity, the projection on the reduced basis is not performed along all the directions of the space, but only along the vertical axis of the local coordinate system attached to the crack front. In that case, the elastic-plastic displacement field of the crack faces can be written as the sum of the linear elastic displacement solution of the crack and of a constant describing the plastic part of the displacement. This constant is called the plastic flow intensity factor ρ. It is an image of the plastic state at the tip. Remember that in mode I it can be viewed as a representation of the plastic blunting at the crack tip. For that reason, in the remainder of this typescript, it will be called indifferently "plastic flow intensity factor" or "plastic blunting". In order to separate time and space dependent variables, the elastic part is written as the product of a reference displacement field and an effective stress intensity factor $\widetilde{K}_I(t)$ made dimensionless by a reference stress intensity factor $\bar{K}$:

$$\boldsymbol{u}_y^{ep}(r,t) \approx \frac{\widetilde{K}_I(t)}{\bar{K}} \cdot \boldsymbol{u}_y^{le}(r) + \rho(t) \tag{1.57}$$

where r is the distance to the crack tip, $\boldsymbol{u}_y^{ep}(r,t)$ is the whole elastic-plastic displacement field of the crack faces along the local vertical axis, as calculated using the finite element method, and $\boldsymbol{u}_y^{le}(r)$ is the linear elastic displacement solution, again along the local vertical axis. It is worth emphasizing that the approximation in the model is not to split the elastic-plastic displacement solution in its elastic and plastic parts, but to assume that the plastic correction can be written as a constant along the crack faces.

At this point, the projection (1.57) is used to create a specific *a posteriori* model reduction. First, an offline phase of computations is used to build the evolution laws of the variable associated with the plastic vector as a function of the evolutions of the variable associated with the elastic vector. Then, during the online phase, the plastic state of the crack is computed incrementally from the elastic state of the crack and the plastic state at the previous time step. From a computational point of view, this operation is very efficient since it avoids non-linear finite element resolutions, only elastic solutions are needed!

Using elastic-plastic finite element computations in the ANSYS software, the projection of Equation (1.57) is performed for a given crack under a variable amplitude loading sequence. From that, the evolution of ρ against K_I^{∞}, the applied stress intensity factor, is plotted on Figure 1.21. Clearly, the relation between those two variables is non linear, and path dependent. However, in the framework of the thermodynamics of dissipative processes, an elastic-plastic model associated with these evolutions was built [POM 07]. It allows determining incrementally the value of the plastic flow intensity factor rate $d\rho$ from the current value of the model's internal variables. One of those internal variables is associated with the crack closure level, and it evolves with the loading history. It is of a special importance because schematically, if the loading level is under the crack closure threshold, there is no evolution of the plastic state of the crack and hence no plastic flow occurs: the instantaneous plastic flow rate $d\rho$ is zero. On the contrary, if the loading intensity is above that threshold, the crack tip will blunt and this will induce variations of the plastic flow. Furthermore, the propagation law of the model is explicitly based on this plastic flow rate.

Here comes the second assumption of the CTCP model, an hypothesis on the crack propagation mechanism. It assumes that the crack grows by successive plastic blunting and resharpening

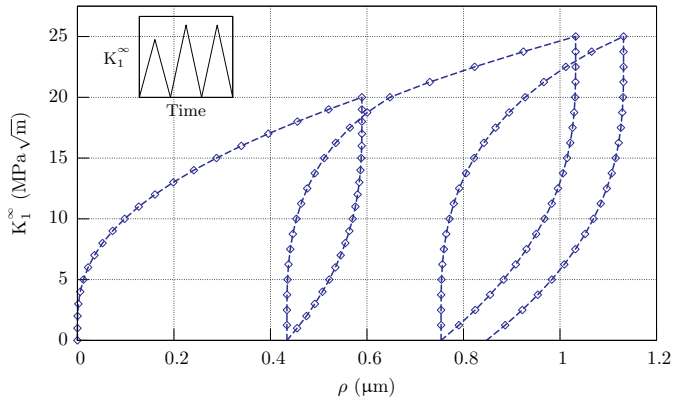

Figure 1.21 Evolutions of the plastic flow intensity factor ρ against K_I^∞ for a variable amplitude loading sequence as computed in the ANSYS software.

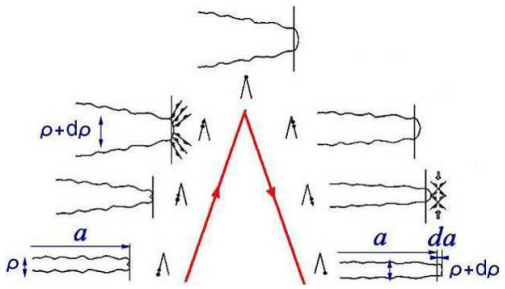

Figure 1.22 Schematic propagation mechanism by successive plastic blunting and resharpening of the crack tip [PEL 69].

of the tip, during respectively the loading phase and the unloading phase of the solicitation (see Figure 1.22 for a schematic description of this mechanism). This mechanism, proposed by Laird in 1967 [LAI 67], stands that during one loading cycle, the increment of crack advance is proportional to the radius of plastic blunting. Crack advance and plastic blunting being strongly linked, the propagation law of the model can be introduced, as a linear relationship between them:

$$\frac{\mathrm{d}a}{\mathrm{d}t} = \alpha \cdot \left| \frac{\mathrm{d}\rho}{\mathrm{d}t} \right| \tag{1.58}$$

where a is the crack advance and ρ a scalar value quantifying the amount of plastic blunting. The scalar α being for its part the only experimentally determined parameter.

Remark 14 *It is important to have in mind that the blunting-resharpening propagation mechanism comes from a "macro" point of view. The real crack growth mechanism can only be described at a more "micro" level, and for mode I solicitations in the Paris regime, it is based on dislocations arising on preferred slipping planes. Since Laird's publication, other contributors, such as Pelloux [PEL 69] and Neumann [NEU 69], provided experimental evidence of that fact. Anyway, this precision does not have any influence on the validity of the CTCP model, since it is designed to describe phenomena observable at a macro level.*

Hence the main advantage of the CTCP model is that it drastically reduces the number of degrees of freedom of the plasticity model. Using the proposed specific projection, in 2D and

mode I, they are reduced to the location of the crack tip, the applied stress intensity factor and the plastic flow intensity factor ρ. In 3D, the adopted approach consists in applying this condensed plasticity model to various points along the crack front, where the corresponding stress intensity factor must be computed. All in all, the number of degrees of freedom for the plasticity model is about a hundred, which is quite reasonable.

The implementation of the CTCP model is organized in two stages: an identification phase, during which the material parameters allowing to write the evolution laws of the internal variables are determined, and the use phase itself. In the following sections, those two steps are extensively described.

4.3 Identification of the model parameters

This stage is divided into two parts: the first one consists in performing some elastic-plastic computations using a very fine mesh, and on a fine time scale, in order to obtain the response of the elastic-plastic material behavior in the vicinity of the crack tip. The second one corresponds to the identification of the CTCP model parameters, during a post-processing stage of the previous computations.

4.3.1 Validity and use conditions of the model

The model parameters identification is conducted on a specific, well-known and simple test-case. Those constants are identified for a specific material behavior. In addition, since they depend only on this chosen material, the identified CTCP model is general and can be applied subsequently to any other test-case with the same material behavior. The only restriction concerns the applicable range of loading. Indeed, the CTCP parameters are determined for a certain range of stress intensity factor, that is, up to a certain $K^{\infty}_{\max}$. Consequently, the tensile loads to which the studied structure is likely to be submitted must be included in that range. However, it should be noted that the model will be valid whatever the compression loads that will be applied to the crack.

Concerning the chosen material law, it must contain at least one plastic hardening (either kinematic or isotropic). It is worth emphasizing that the closer to the real material behavior the law is, the more accurate the identified CTCP model will be. In this respect, a combination of both kinematic and isotropic hardenings is often preferable. The CTCP model identification being done during a post-processing step, using only the computed displacement fields, the limitation to the complexity of the elastic-plastic law is coming from the underlying finite element software.

4.3.2 Identification stage test-case

The chosen test-case for the parameters identification is a 2D plate in plane strain, containing a central crack (a so-called Griffith's crack). For symmetry reasons, only one quarter of the geometry is modeled. The dimensions of the whole plate are $200 \times 200\,\text{mm}$ and the crack length is $2a = 20\,\text{mm}$.

The loads are applied on the upper side (loading $\boldsymbol{S}_{\text{y}}$) and on the right hand side vertical face (loading $\boldsymbol{S}_{\text{x}}$). Proportional loadings such as:

$$\left|\boldsymbol{S}_{\text{x}}\right| = f\left(\left|\boldsymbol{S}_{\text{y}}\right|\right) \tag{1.59}$$

allow adjusting the biaxiality level and the T-stress (see section 4.3.5). In a first approach, let us consider:

$$\left|\boldsymbol{S}_{\text{x}}\right| = \left|\boldsymbol{S}_{\text{y}}\right| \tag{1.60}$$

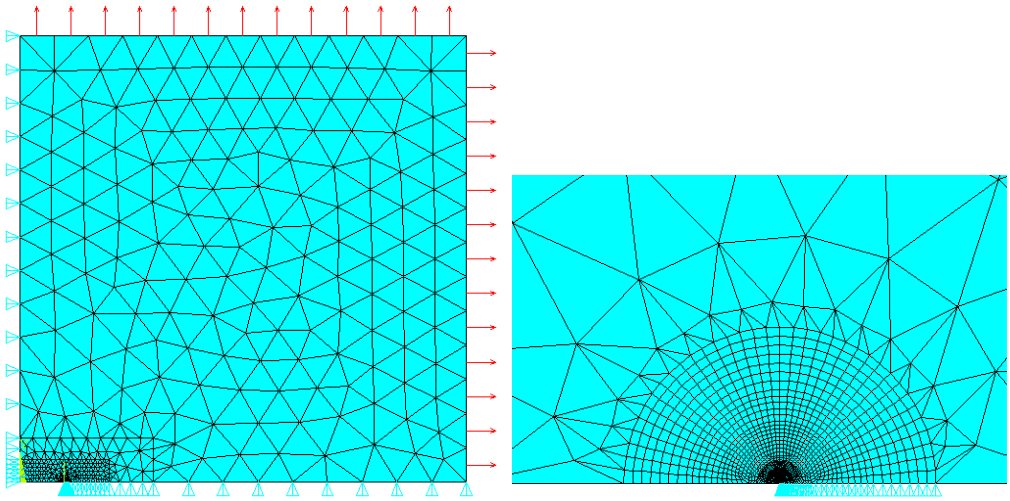

(a) Mesh and boundary conditions (b) Mixed triangles-quadrangles mesh around the crack tip

Figure 1.23 Geometry, mesh and boundary conditions of the test-case used for the identification of the CTCP model parameters.

The mesh is constituted of 3 nodes triangles and 4 nodes quadrangles, with full integration (Plane182 elements in the ANSYS software). A radial mesh is used around the crack tip, and a free mesh far from it. Significant mesh refinement has been conducted in the vicinity of the crack since the first four layers of elements measure 5 µm. All in all, 2122 elements, 1826 nodes and 3652 degrees of freedom are used (Figure 1.23).

4.3.3 Finite element computations on fine space and time scales

Linear elastic computation The first computation is a linear elastic calculation, for an applied tensile load $\boldsymbol{S}_{\mathrm{y}}$ corresponding to a nominal stress intensity factor $K_I^{nom} = 1\,\mathrm{MPa}\sqrt{m}$ (see Figure 1.24). For the geometrical configuration of the identification test-case, the load to be applied on the plate writes then:

$$\left|\boldsymbol{S}_{\mathrm{y}}\right| \equiv \sigma^{nom} = \frac{K_I^{nom}}{\sqrt{\pi a}} \approx 5,6433\,\mathrm{MPa} \tag{1.61}$$

The vertical component of the displacement field of the crack lip must be stored (since only one quarter of the plate is modeled, there is only one single crack lip). This is done only for the fields corresponding to the K-dominance zone, that is, for the first millimeter around the crack tip. The obtained displacements constitute the field $\boldsymbol{u}_y^{le}(r,\theta=\pi)_{K_{\mathrm{I}}=1}$ expressed in the local coordinate system associated with the crack tip, with $0 < r < 1\,\mathrm{mm}$.
Note: In the remainder of this typescript, it will be denoted by u^{le}.

Elastic-plastic computations on the fine time scale At this point, the whole elastic-plastic response, on the fine time scale, of a cracked structure with the studied material behavior must be extracted. The identification test-case will hence be submitted to thirty loading cycles, of maximum stress intensity factor $K_{\max}^{\infty}$ with a load ratio R = 0. Indeed, approximately thirty loading cycles are necessary to obtain a stabilized cycle plastic zone (this number of cycle obviously depends on the chosen material behavior law).

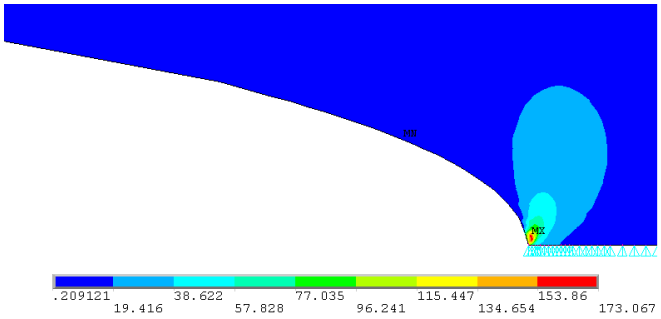

Figure 1.24 Von mises stress and displacement of the crack lip for $K_I^{\infty} = 1\text{MPa}\sqrt{m}$

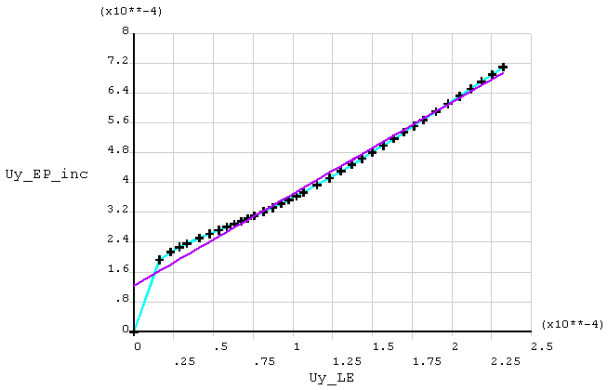

Figure 1.25 Prefactors identification in a $\delta u_n^{ep} - u^{le}$ graph (in mm).

This non-linear computation must be performed with a fine temporal discretization. The first loading and the last unloading are the most important half-cycles. Consequently, those loadings are performed using 25 time steps, while others are made using only 6 time steps. Again, the vertical component of the displacements of the crack lip are stored, for each time step. The obtained displacements constitute the field $u_{\text{y}}(r, \theta = \pi, t)$.
Note: In the following, it will be denoted by u^{ep}.

4.3.4 Implementation of the identification phase

Determination of prefactors $\widetilde{K}_{\text{I}}(t)$ and $\rho(t)$ Remember that the model CTCP consists in splitting, along the crack lip, the vertical component of the total elastic-plastic field in an elastic and a plastic part. Rewriting Equation (1.57) in a scalar form:

$$u^{ep}(r,t) \approx \frac{\widetilde{K}_I(t)}{\bar{K}} \cdot u^{le}(r) + \rho(t) \tag{1.62}$$

In addition, to ensure a good precision [POM 05], the model must be written in an *incremental* manner, in other words, the approximation of Equation (1.62) must be applied between two successive time step increments $t_{\text{n}-1}$ and t_{n}. Consequently, the total prefactors $\widetilde{K}_{\text{I}}$ and ρ are in fact

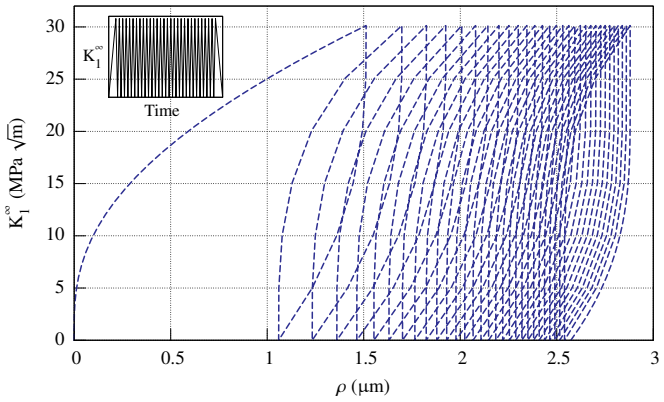

Figure 1.26 Temporal evolutions of ρ and K_{I}^{∞} during 30 cycles of cyclic loading.

the sum of all the prefactors increments:

$$\rho(t_n) = \sum_{i=0}^{n} \delta\rho_n \quad \text{and} \quad \widetilde{K}_{\mathrm{I}}(t_n) = \sum_{i=0}^{n} \delta\widetilde{K}_n, \tag{1.63}$$

$$\text{with} \quad u^{ep}(t_n, r) - u^{ep}(t_{n-1}, r) \approx \delta\widetilde{K}_n \cdot u^{\mathrm{le}}(r) + \delta\rho_n \tag{1.64}$$

Following Equation (1.64), the elastic-plastic displacement increment is a *linear* function of the elastic displacement, with $\delta\widetilde{K}_{\mathrm{n}}$ the slope of the curve and $\delta\rho_{\mathrm{n}}$ the y-intercept. Thereby, the prefactors will be identified by a linear least square method in a $\delta u_n^{ep} - u^{le}$ chart (Figure 1.25).

The prefactor $\widetilde{K}_{\mathrm{I}}$ differs in fact from the classical stress intensity factor (that will be denoted by K_{I}^{∞}). It represent the stress intensity factor actually seen by the crack, that is, the classical factor, but modified by a corrective stress intensity factor K_{I}^{sh} which allows accounting for the plastic residual stresses at crack tip. In this respect, the superscript "*sh*" stands for *shield*. In practice, K_{I}^{sh} does not exceed 12% of K_{I}^{∞}, and its evolution is linear with respect to ρ, with a slope β. It is absolutely not necessary to compute β, however, during an implementation and commissioning stage, its post-process can help to highlight some bugs. At this point, K_{I}^{sh} must be computed and its variations with respect to K_{I}^{∞} stored:

$$K_{\mathrm{I}}^{\mathrm{sh}} = \widetilde{K}_{\mathrm{I}} - K_{\mathrm{I}}^{\infty} \approx \beta \cdot \rho \tag{1.65}$$

It is now possible, for visualization purpose to plot the temporal evolutions of ρ and K_{I}^{∞}. Those evolutions and the stabilization of the hysteresis loops coming from the stabilization of the crack tip plastic zone are presented on Figure 1.26.

Identification of the parameters of the blunting law In the framework of the thermodynamics of the dissipative processes, a cyclic elastic-plastic constitutive law for the cracked structure is set up. It is the first law of the CTCP model, and is called *the blunting law.* This law allows computing incrementally the evolutions of ρ from the evolutions of K_{I}^{∞}. Indeed, on Figure 1.27, some specific zones can be identified, corresponding to the evolution of either the monotonic (denoted by M on the figure) or cyclic (C) crack tip plastic zones, and even some "elastic" zones (E) where no evolution of the plastic flow intensity factor ρ occurs (which is equivalent to say that no plastic

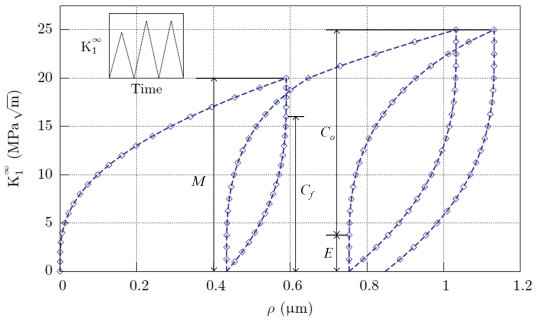

Figure 1.27 Identification of specific zones for the evolutions of ρ with respect to K_I^∞.

blunting occurs). During the loading of the crack, those zones can move or become bigger, with a strong analogy with the classical kinematic and isotropic hardening models.

In short, the model is constituted by 3 state variables: an elastic one K_I^∞ and two dissipative ones, the crack length a and the plastic flow intensity factor ρ. It appears that thermodynamic driving force φ associated with ρ is equal to the half of the energy release rate (more precisely, it is equal to the half of the Rice's J-integral [POM 07])[1]. Other internal variables are introduced, so as to define the cyclic plastic zone by its position φ_{xc} and its size $2\cdot\varphi_c$ inside the monotonic plastic zone of size φ_m and position φ_{xm}. The blunting law must provide the plastic flow intensity factor rate as a function of the loading and of the current values of the internal variables:

$$\frac{d\rho}{dt} = f(\varphi, \varphi_c, \varphi_{xc}, \varphi_m, \varphi_{xm}) \tag{1.66}$$

For that purpose, equations describing the partial derivatives of the internal variables with respect to the state variables are empirically derived:

$$\begin{cases} \dfrac{\partial\varphi_c}{\partial\rho}, \dfrac{\partial\varphi_{xc}}{\partial\rho}, \dfrac{\partial\varphi_m}{\partial\rho}, \dfrac{\partial\varphi_{xm}}{\partial\rho} \\ \dfrac{\partial\varphi_c}{\partial a}, \dfrac{\partial\varphi_{xc}}{\partial a}, \dfrac{\partial\varphi_m}{\partial a}, \dfrac{\partial\varphi_{xm}}{\partial a} \end{cases} \tag{1.67}$$

Using approximate linear or square root equations to predict these evolutions, 8 internal parameters (called a_m, b_m, a_{xm}, a_{cf}, b_{cf}, k_a, k_b and p_a)[2] are introduced. All in all, the blunting law of the CTCP model is somehow very similar to a classical elastic-plastic material behavior law with internal variables. A rigorous demonstration of the underlying thermodynamics state variables and conjugate forces can be found in [HAM 06], and is not written here. However, the process used for the identification of the model parameters is detailed in the following sections, as it was implemented in the ANSYS software.

The parameters a_m, b_m and a_{xm} are identified during the first loading. The parameters a_{cf} and b_{cf} are determined during the last unloading. Finally, the parameters k_a, k_b and p_a are identified after the last unloading (Figure 1.28).

Identification of parameters a_m, b_m, a_{cf} and b_{cf} The temporal evolutions of the plastic blunting with respect to the applied stress intensity factor are proposed on Figure 1.26. These

[1] The driving force φ is expressed in MPa$^2\cdot$m, refer to Equation (1.75).

[2] The parameters a_m, a_{xm}, a_{cf}, k_a, k_b and p_a are expressed in $^{\text{MPa}\sqrt{\text{m}}}/_{\sqrt{\mu\text{m}}}$, while the parameters b_m and b_{cf} are in MPa $\sqrt{\text{m}}$.

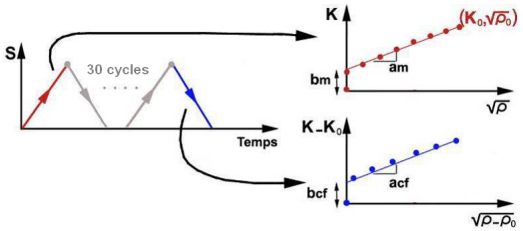

(a) Parameters a_m, b_m, a_{cf} and b_{cf}

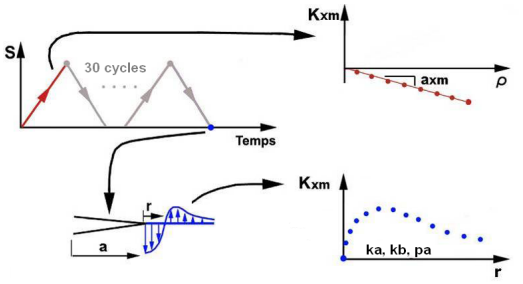

(b) Parameters a_{xm}, k_a, k_b and p_a

Figure 1.28 Identification of the blunting law parameters [HAM 06].

evolutions are modeled by linear functions of K^{∞} with respect to $\sqrt{\rho}$, and identified by a least square method in appropriate charts.

Monotonic plastic zone evolutions The parameters a_m and b_m describe the approximation of the evolutions of the monotonic plastic zone. They are identified during the first loading, since at this time, the cyclic plastic zone is not yet existing. The only elastic-plastic phenomenon occurring is thus an extension of the monotonic plastic zone. These parameters are identified in some $K^{\infty} - \sqrt{\rho}$ charts (see Figure 1.29).

Cyclic plastic zone evolutions The parameters a_{cf} and b_{cf} describe, for their part, the evolutions of the size of the cyclic plastic zone. Thereby, they are identified during the last unloading, the cyclic plastic zone being stabilized by the 30 loading cycles that has undergone the crack. Furthermore, during an unloading stage, the monotonic plastic zone does not evolves. The only elastic-plastic phenomenon occurring at this time is hence an evolution of the cyclic plastic zone. These parameters are identified in some charts, plotting $(K_0^{\infty} - K^{\infty})$ against $(\sqrt{\rho_0 - \rho})$, where K_0^{∞} and ρ_0 are respectively the values of the elastic stress intensity factor and of the plastic blunting *just before* the last unloading. An example of their determination is given in Appendix A.

Identification of parameters a_{xm}, k_a, k_b and p_a These variables are associated with the closure effect in general and in particular with its evolutions with the variations of the plastic blunting and the crack advance.

Evolutions of the contact loading with the plastic blunting If the crack does not propagate, an applied tensile loading can only blunt the crack. After that, locally the material around the tip

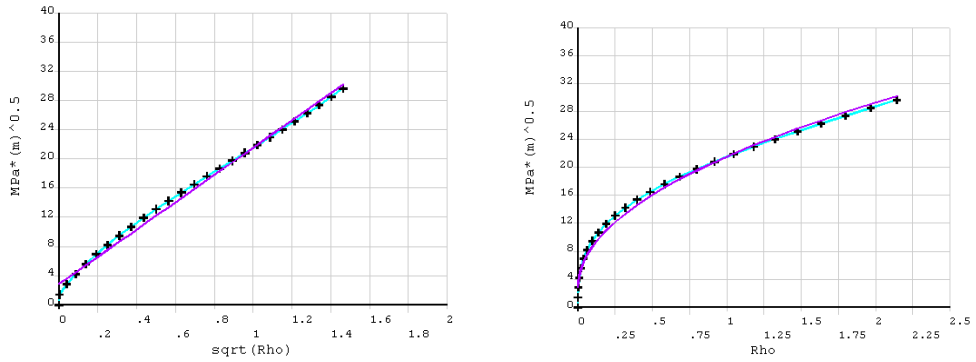

(a) Curve obtained by finite element computation (in green) and least square fit (in purple) represented in a $K_{\mathrm{I}}^{\infty} - \sqrt{\rho}$ chart

(b) In a $K_{\mathrm{I}}^{\infty} - \rho$ chart

Figure 1.29 Example of identification of the a_m and b_m parameters.

might be hardened, but for a nil external loading the crack faces cannot contact. Furthermore, the stronger the tensile loading has been, the more the crack faces are away from each other: the complete crack closure effect cannot arise. Only the part of it which is due to the plastic hardening in the vicinity of the front is present, the part which is due to the contact between the crack faces is missing.

The *contact loading* is defined as the value of the external loading to make the crack faces contact. According to the previous paragraph, the plastic blunting make the contact loading drop. Thereby, to obtain the contact of the crack lips, a compressive loading needs to be applied. On the contrary, an advance of the crack will make the contact loading rise toward the positive values. It is the competition between those two effects which will lead to a global crack closure effect, that is, to a *positive* mean contact loading.

The parameter a_{xm} controls the modeling of the evolutions of the contact loading with respect to the plastic blunting (in terms of internal variables: $\frac{\partial \varphi_{xm}}{\partial a}$). Making the elastic stress intensity factor appear, the displacement field decomposition (1.62) rewrites:

$$u^{ep}(r,t) = \frac{K_{\mathrm{I}}^{\infty}(t) + K_{\mathrm{I}}^{sh}(t)}{\bar{K}} \cdot u^{le}(r) + \rho(t) \tag{1.68}$$

Moreover, when the crack lips contact:

$$u^{ep} = 0 \tag{1.69}$$

In this case, it comes:

$$K_{\mathrm{I}}^{\infty} = K_{\mathrm{I}}^{contact} = K_{xm} = -K_{\mathrm{I}}^{sh}(\rho) - \frac{\rho}{u^{le}(r_c)} \cdot \bar{K} \tag{1.70}$$

The evolutions of the contact loading K_{xm}, written in terms of stress intensity factor, can be plotted during the first loading as a function of the plastic flow intensity factor ρ. However, the field $u^{le}(r)$ is a function of r and the parameter r_c is defined as the position of the point where, at the time of the contact, the crack faces meet each other. Hence to know K_{xm}, the parameter r_c must be known. It is quite complicated to properly identify this point. In the framework of the CTCP model, an arbitrary choice is made:

$$r_c = 1\,\mathrm{mm} \tag{1.71}$$

The evolution of K_{xm} is a line. Its slope a_{xm} is identified by the least square method, and the obtained evolution is then:

$$K_{xm} = a_{xm} \cdot \rho \tag{1.72}$$

An example of identification of the a_{xm} parameter is provided in Appendix A.

Evolutions of the contact loading with the crack advance It remains to model $\frac{\partial \varphi_{xm}}{\partial a}$ and $\frac{\partial \varphi_m}{\partial a}$, the evolutions of the internal variables associated with the monotonic plastic zone, in function of the extension of the crack, for a *fixed* plastic blunting. The blunting being set, the method consists in imagining that after the unloading of the structure, the crack propagates of a variable length through the residual stresses that exist beyond the front. This stress field will somehow pinch the crack and induce a negative stress intensity factor that will act against its opening.

This stress intensity factor is computed just as the one of a crack of length $2(a_0 + l)$ loaded on its extremities by a constant stress σ_{xm}. Here, a_0 is the initial half-length of the crack and l the variable length of propagation:

$$K_{xm} = \sigma_{xm} \sqrt{\pi\,(a_0 + l)} \left[\frac{2}{\pi} \arccos\left(\frac{a_0}{a_0 + l} \right) \right] \tag{1.73}$$

The value of the constant stress σ_{xm} is computed as the mean of the residual stresses $\sigma_{yy}^{residual}$ between a zero propagation and a propagation length l:

$$\sigma_{xm} = \frac{1}{l} \int_{r=0}^{r=l} \sigma_{yy}^{residual}(r)\,\mathrm{d}r \tag{1.74}$$

It remains to write the chosen function to model the evolutions of the internal variables related to the monotonic plastic zone with the extension of the crack expressed in terms of K_{xm}. Remember that the internal variable φ is equal to the half of the energy release rate. Using the Irwin's formula (1.23), the internal variables can be rewritten in terms of stress intensity factors. Considering plane strain:

$$\varphi = A^2 K^2 sign(K) \quad \text{with} \quad A = \sqrt{\frac{1 - \nu^2}{2E}} \tag{1.75}$$

Moreover, the chosen evolution equation is as follow:

$$\varphi_{xm}(l) = \varphi_{m0} \cdot \frac{k_b}{k_a - p_a} \cdot \left(e^{k_a \cdot l} - e^{p_a \cdot l} \right) \tag{1.76}$$

using Equation (1.75), it comes:

$$K_{xm}(l, \rho) = K_{m0}^2 \cdot \frac{k_b}{k_a - p_a} \cdot \left(e^{k_a \cdot l} - e^{p_a \cdot l} \right) \tag{1.77}$$

It remains to unfold K_{m0}. The extension of the monotonic plastic zone reads:

$$K = K_m + K_{xm} \tag{1.78}$$

At the end of the last loading, just before the last unloading, it can be written:

$$K_{\mathrm{I}_{\max}} = K_{m0} + K_{xm}(\rho) \tag{1.79}$$

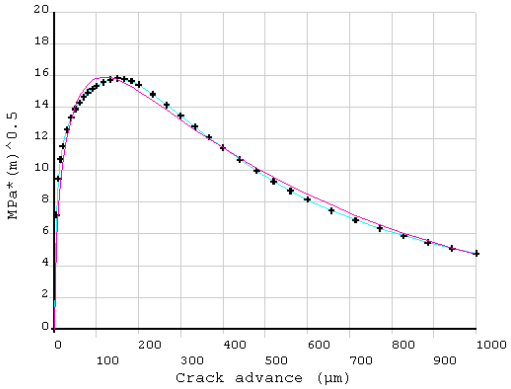

Figure 1.30 Identification of the parameters k_a, k_b and p_a by the method of the simplex of Nelder and Mead.

Rewriting Equation (1.72) into (1.79) yields:

$$K_{m0} = K_{\mathrm{I}_{\max}} - a_{xm} \cdot \rho_{\max} \tag{1.80}$$

And finally, Equation (1.77) can be rewritten such as:

$$K_{xm}(l,\rho)\big|_{\rho=\rho_{\max}} = (K^{\infty}_{\mathrm{I}_{\max}} - a_{xm} \cdot \rho_{\max})^2 \cdot \frac{k_b}{k_a - p_a} \cdot \left(e^{k_a \cdot l} - e^{p_a \cdot l}\right) \tag{1.81}$$

The parameters k_a, k_b and p_a are identified by an optimization method. The chosen numerical method is the simplex of Nelder and Mead [PRE 92], with one simple constraint to avoid trivial solutions: $k_a \neq k_b$. The main advantage of the simplex method is that it does not require to compute the gradient of the cost function. See Figure 1.30 for an example of such identification.

4.3.5 Biaxiality and *T*-stress

The model allows to account for the effects of the biaxiality of the loading by means of the T-stress level, yet staying in the assumption of proportional loadings. The height material parameters are identified for several T/K ratios, varying in a range such that it covers all the encountered values of this ratio during the simulation on the chosen test-case. Typically, for a crack propagation analysis of a compact tension sample, those ratios need to cover the range $-2 < T/K < 2$. The variations of each parameter in function of these T/K ratios are interpolated by second order polynomials which coefficients are identified by a least square method [PRE 92]. Then, during the use stage of the CTCP model, at each propagation step, the appropriate set of parameter will be chosen.

To obtain several proportional loadings corresponding to various T/K ratios a linear function linking the horizontal loading, the vertical loading and the specific biaxiality ratio must be written such as $|S_{\mathrm{x}}| = f\left(\frac{T}{K}, |S_{\mathrm{y}}|\right)$. In the case of a Griffith's crack (such as the CTCP identification test-case), the T-stress and the stress intensity factor in mode I and plane strain write:

$$K = |S_{\mathrm{y}}| \cdot \sqrt{\pi \cdot a} \quad \text{and} \quad T = |S_{\mathrm{x}}| - |S_{\mathrm{y}}| \tag{1.82}$$

where a is the half-length of the crack. Manipulating those equations, it comes:

$$|S_{\mathrm{x}}| = |S_{\mathrm{y}}| \cdot \left(\frac{T}{K} \cdot \sqrt{\pi \cdot a} + 1\right) \tag{1.83}$$

In section 4.3.2, it was supposed that $|S_x| = |S_y|$. Actually, the loading $|S_x|$ to be applied is in fact the one described by Equation (1.83), function of $|S_y|$ and a. Some examples of the variations of the parameters of the CTCP model upon the T/κ ratio modeled by second order polynomials are presented in Appendix A.

4.3.6 Parameter α of the cracking law

In general, the second law of the CTCP model is called indifferently the cracking law or the propagation law. The ninth and last parameter to be determined is the dimensionless coefficient α which allows adjusting the propagation rates of the cracking law:

$$\frac{da}{dt} = \alpha \cdot \left| \frac{d\rho}{dt} \right| \tag{1.84}$$

This parameter is the only one which is not identified numerically but experimentally. A crack propagation experiment under cyclic loading is conducted, and the same propagation is then simulated using the CTCP model, with $\alpha = 1$. After that, the Paris lines of both the experiment and the simulation are plotted in a $\log(da/dN) - \log(K)$ chart. The parameter α allows offsetting the simulated line, without modifying its slope. Hence α is chosen so as to make the simulation results match the experimental ones. In fact, the CTCP model allows simulating the slope of the Paris line, in other terms the exponent m of the Paris law (1.49), and the C coefficient is corrected by the α parameter.

4.3.7 Example of identification

A numerical identification of the CTCP model parameters has been conducted, using the methodology described above. The chosen elastic-plastic material was made as close as possible to the material used by Rami Hamam in his thesis [HAM 06], in order to compare the results. The material model considered is a rate-independent version of the nonlinear kinematic hardening model proposed by Chaboche [LEM 90], together with a Voce nonlinear isotropic hardening law. Multiple kinematic hardening models can be superposed. Doing so, the resulting kinematic back stress $\boldsymbol{X}$ is the sum of all the back stresses $\boldsymbol{X}_i$ corresponding to the n elementary models:

$$\boldsymbol{X} = \sum_{i=1}^{n} \boldsymbol{X}_i \tag{1.85}$$

Hence the evolution law for the kinematic hardening models is defined as follow:

$$\dot{\boldsymbol{X}}_i = \frac{3}{2} C_i \dot{\boldsymbol{\varepsilon}}_p - \gamma_i \boldsymbol{X} \dot{p} \tag{1.86}$$

where $\dot{\boldsymbol{\varepsilon}}_p$ is the plastic strain increment, and $\dot{\boldsymbol{X}}_i$ the back stress increment. The parameters C_i and γ_i are the material constants of the law. The coefficient C_i characterizes the rate of hardening, that is, its "speed" in a $(\sigma - \varepsilon)$ chart, and the ratio C_i/γ_i the maximum hardening amplitude. Furthermore, the equivalent plastic strain increment $\dot{p}$ is:

$$\dot{p} = \sqrt{\frac{3}{2} \cdot \mathrm{Tr}\left(\dot{\boldsymbol{\varepsilon}}_p \cdot \dot{\boldsymbol{\varepsilon}}_p\right)} \tag{1.87}$$

and the evolution law of the isotropic hardening writes:

$$R = \sigma_y + R_0\, p + Q\left(1 - e^{-bp}\right) \tag{1.88}$$

Table 1.3 Material parameters of the linear elastic part of the behavior, the nonlinear isotropic hardening and the three kinematic hardening models used for the CTCP model coefficients identification.

E (GPa)	ν	σ_y (MPa)
190	0.3	335

R_0 (MPa)	Q (MPa)	b
210	80	0.53

C_1 (MPa)	γ_1	C_2 (MPa)	γ_2	C_3 (MPa)	γ_3
50000	1000	32500	500	11397	29

Table 1.4 Identified CTCP model parameters using the elastic-plastic behavior described in Table 1.3, for a nil T/K ratio.

a_m	b_m	a_{cf}	b_{cf}	a_{xm}	p_a	k_a	k_b	α
22.85	2.25	46.33	8.19	−1.45	−0.018	0.0038	−0.0029	4

where R is the isotropic back stress, and σ_y the yield strength of the material. In a $(\sigma - \varepsilon)$ chart, the isotropic hardening behavior eventually tends to a line. Thus R_0 is the slope of the final hardening rate and the sum $(\sigma_y + Q)$ its y-intercept.

In the simulations, three kinematic hardening models are used in conjunction of the isotropic hardening model. The associated parameters are recalled in Table 1.3, E and ν being respectively the Young's modulus and the Poisson's ratio of the elastic part of the material behavior. With such behavior, the obtained CTCP parameters[3] are of the same order, yet slightly different, of those computed in [HAM 06]. They are presented in Table 1.4. Along with these variables, the second order polynomials interpolating their variations with respect to the applied T/K ratio are shown in Appendix A, together with their coefficients. Whenever the CTCP model is employed in this typescript, the utilized material parameters are the ones presented here above. In addition, the last parameter α of the cracking law is chosen to be equal to 4, such as proposed in the Hamam's thesis.

4.4 Integration of the model laws

4.4.1 General structure

The conception and the use of the CTCP model is very similar to a classical elastic-plastic law. It is in fact an elastic-plastic model equivalent to the complete model, but condensed on the crack front. These similarities become even more obvious in the way it is implemented, because it mainly consists in deducing from a loading increment the evolutions of the internal variables and the plastic state (in other words the blunting) of the crack front.

From a global point of view, the use of the CTCP model is conducted in two parts: a first step concerning the blunting law integration and then a second stage associated with the cracking law integration (see Figure 1.31). The blunting law integration allows computing from the state vector of the model at time $(n-1)$ and a loading increment expressed in terms of stress intensity

[3] Remember that the parameters a_m, a_{xm}, a_{cf}, k_a, k_b and p_a are expressed in $\text{MPa}\sqrt{\text{m}}/\sqrt{\mu\text{m}}$, while the parameters b_m and b_{cf} are in MPa $\sqrt{\text{m}}$. The last parameter α is dimensionless.

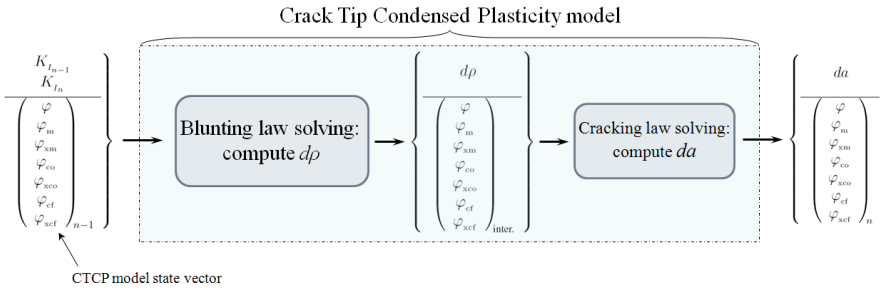

Figure 1.31 General structure of the use stage of the CTCP model.

factor, the increment of plastic flow intensity factor dρ and an intermediate state vector, partially updated. This state vector is denoted by "inter." on Figure 1.31. The integration of the cracking law itself is very simple to implement. It consists in determining the crack growth increment from the plastic flow intensity factor increment. Then the internal variables of the model that depend upon the crack advance are updated, to finally build the final state vector at time n.

Some internal variables of the model evolve then in function of both the plastic blunting and the crack advance. The chosen general structure allows uncoupling the computation of those variations. Consequently, the model integration is not iterative, but direct. It is worth noting that this two step resolution is an approximation, possible because the internal variables evolve rapidly with the plastic blunting (for variations of ρ of some 0.1 µm) but much more slowly with the crack advance (for variations of a of some 100 µm).

4.4.2 Numerical integration

The use stage of the CTCP model requires the numerical integration of the blunting and cracking laws of the crack. Some test using an implicit algorithm were first conducted by Hamam *et al.* [HAM 07]. However, a piecewise analytic integration was finally chosen. This method is very fast. To simplify the implementation, the internal variables associated with the cyclic domain were duplicated, so that it exists an *opening* cyclic domain $(\varphi_{xco};\varphi_{co})$ and a *closing* cyclic domain $\left(\varphi_{xcf};\varphi_{cf}\right)$. It should be clear that it exists actually only one single domain, to duplicate it is only a numerical trick.

From this point, all the parameters that are related with the current state of the model will be denoted by the subscript 1, whereas the parameters related to the next state, that is, mainly the parameters that must be computed by the algorithm, will be denoted by the subscript 2. Remember that the thermodynamic variable φ associated with the plastic blunting ρ is equal to the half of the energy release rate. It is a key relationship of the model. This variable represents the loading. The latter, expressed as a stress intensity factor value, must firstly be rewritten in terms of internal variable φ of the model, using Equation (1.75). Hence in function of the external applied loading φ_2 and of the current state vector of the model:

$$\left(\varphi_1,\varphi_{m_1},\varphi_{xm_1},\varphi_{co_1},\varphi_{xco_1},\varphi_{cf_1},\varphi_{xcf_1}\right)_1 \tag{1.89}$$

an algorithm chooses what *event* is happening, and therefore which evolution equations must be activated. The possible events are summarized on Figure 1.32. During a loading increment, one or more events can occur. Indeed, the initial and the final loadings do not necessarily belong to the same event zone. In this case, the loading must be subdivided and several events must be solicited. Obviously, the choice algorithm must be able to handle all the possible cases.

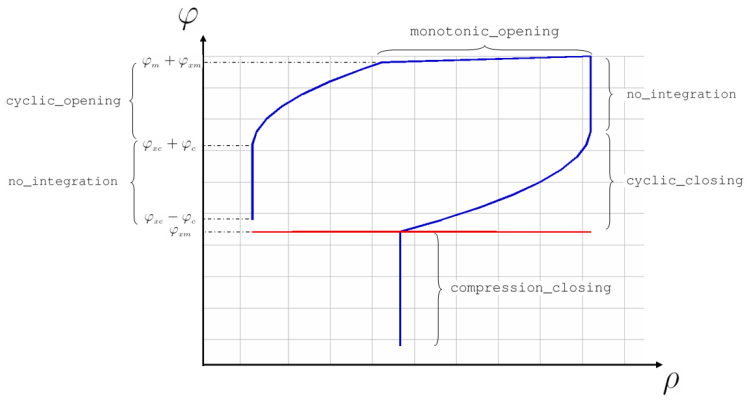

Figure 1.32 Summary of all the possible *events* occurring during a blunting cycle, identified in a $\varphi - \rho$ chart.

The equations concerning the compression phases of the crack are detailed hereinafter. The other equations, except some slight modifications, are very similar to those proposed by Rami Hamam in his thesis [HAM 06], and will only be presented.

Accounting for the compression phases As soon as the applied loading is lower than the contact loading K_{xm}, the crack lips contact, making the crack undergoing a compression loading. The crack being closed, the CTCP displacement field partitioning does not make sense and is therefore not performed anymore. Consequently, the plastic blunting ρ does not vary. However, those compression phases have an effect on the evolutions of the plastic blunting when the crack opens again.

Apparently, the cyclic elastic zone becomes then shorter, and can even disappear. Indeed, if the compression has been really strong, the crack begins to blunt as soon as it opens. In a $K_I^\infty - \sqrt{\rho}$ chart, the blunting curves undergo a mere vertical offset: the y-intercept changes, but not the slope. Furthermore, over a certain underload level, this phenomenon saturates and the y-intercept does not decrease anymore. These behaviors are described on Figure 1.33. Thereby, during the opening phase immediately following a compression phase, the plastic blunting arises at the same rate than if there had been no compression, but begins at a lower level of loading. It follows that, comparing the plastic state of two cracks undergoing the same tensile loading, the one which has been compressed just before is more blunted than the one which as not been submitted to a compression phase. In other words, the compression phases speed up the propagation.

Hamam *et al.* [HAM 07] showed that the apparent narrowing of the cyclic elastic zone is the only effect of an underload on the blunting evolutions. Moreover, this effect disappears after on cycle. To model this effect, the chosen solution consists in moving the cyclic elastic zone toward the compression loadings (that is, downward in a $K_I^\infty - \rho$ chart), without changing its size. The only internal variable which will evolve is then φ_{xco}, during the `compression_closing` event. In addition, the cyclic elastic zone must stay inside the monotonic elastic zone: this is the chosen criterion to simulate the saturation of the phenomenon.

Evolutions of the cyclic elastic domain during an unloading phase At the beginning of an unloading phase, the cyclic elastic zone is firstly crossed. The behavior of the crack is elastic, the plastic blunting does not vary, the corresponding event is `no_integration` (Figure 1.34, (1) et (2)).

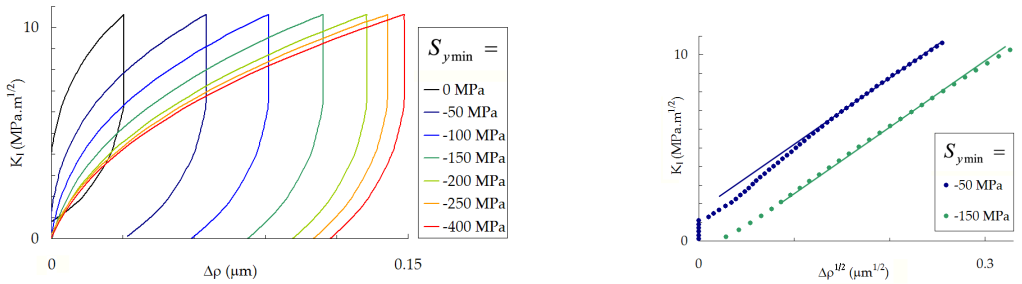

Figure 1.33 Evolutions of the plastic blunting ρ during the opening phase following a compression phase [HAM 06]. Presented for several different underload levels $|S_{ymin}|$ (a), or in a $K_I^{\infty} - \sqrt{\rho}$ chart (b). In function of the underload level, only the y-intercept changes.

After that, the cyclic plastic blunting arises, until the contact loading is reached. The cyclic elastic zone moves, following the applied loading. The associated event is `cyclic_closing` (figure 1.34, (3)). Next the crack lips contact, the plastic blunting ρ does not vary anymore, but the cyclic elastic domain keeps moving inside the monotonic elastic zone during the `compression_closing` event (figure 1.34, (4)). It is the key event to account for the compression phases. The cyclic elastic zone can move entirely under the contact loading, and even entirely in the negative loadings. The expression of this displacement writes, in terms of internal variables:

$$\varphi_{xc} = \varphi_2 + \varphi_c \tag{1.90}$$

Finally, as soon as the lower bound of the cyclic elastic zone reaches the lower bound of the monotonic elastic zone, nothing more happens. This criterion to stop writes, in terms of loading:

$$\varphi = \varphi_{xm} - \varphi_m \tag{1.91}$$

and its associated event is called `no_integration` (figure 1.34, (5)). During the loading following this compression, the plastic blunting will begin only when the applied loading will be greater than the *blunting threshold*, which corresponds to the higher of this two values: the contact loading or the upper bound of the cyclic elastic domain.

Plastic blunting evolution equations during a loading following a compression phase
The plastic blunting evolution equations during a loading following a compression phase are based on those used during an unloading. It was chosen to model the evolutions of ρ in the cyclic plastic zone by a function such as $K_I^{\infty} = f(\sqrt{\Delta\rho})$. For an unloading phase:

$$K_0 - K_1 = a_{cf} \cdot \sqrt{\rho_0 - \rho_1} + b_{cf} \tag{1.92}$$

remember that the constants a_{cf} and b_{cf} are material parameters of the model, they are determined during the identification stage of the CTCP model, during an unloading. If the minimum loading reached was greater than the loading leading to the contact of the lips (the so-called contact loading), there was no compression of the crack. It is the simplest case, and it corresponds to the Figure 1.35(a). During a loading in such conditions, the equation that model the behavior of ρ can be deduced from the unloading equation (1.92), where K_{reload} is the loading from which begins

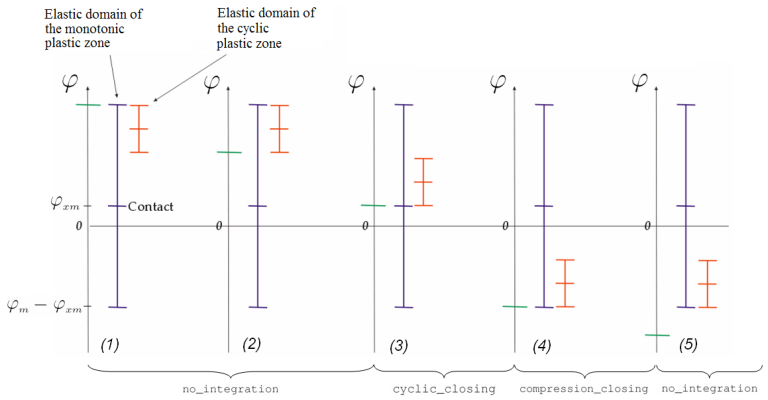

Figure 1.34 Evolutions of the position of the cyclic and monotonic elastic domains during an unloading of the crack.

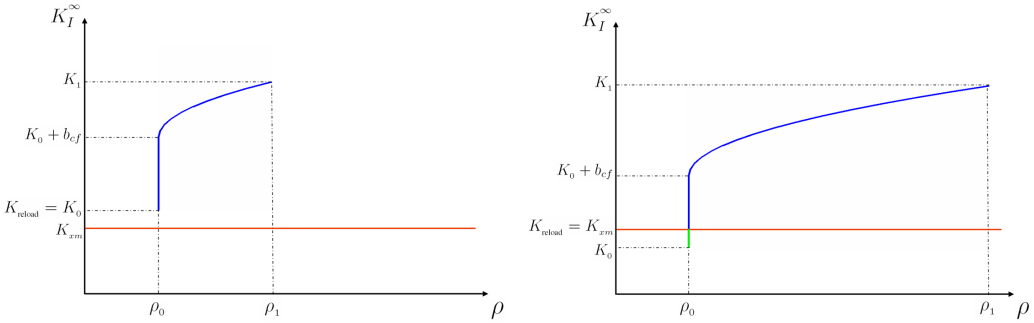

Figure 1.35 Behavior of the plastic blunting ρ during loading without (a) or with (b) preliminary underloads.

the reloading. In this case it is equal to the minimum loading reached and to the lower bound K_0 of the cyclic elastic domain:

$$K_1 - K_{reload} = a_{cf} \cdot \sqrt{\rho_1 - \rho_0} + b_{cf} \tag{1.93}$$

On the contrary, in the case of a loading occurring just after a compression of the crack, this equation is no more valid. Indeed, the `compression_closing` event has been activated, the location K_{xc} of the cyclic elastic domain has moved with the compression loading when it went under the contact loading. As a consequence, K_{reload} does not fulfill the same conditions than in the previous case. it is now equal to the loading at which the opening of the lips begin, in other words the contact loading K_{xm}. It should be noted that the actual dimension of the cyclic elastic zone $2\varphi_c$ has not changed. However, its *apparent* dimension has been reduced by a value equivalent to the light green part of the curve on Figure 1.35(b). Thus, in the case of a loading consecutive to an underload, the plastic blunting evolution equation, which begins at K_{reload}, writes:

$$K_1 - K_{reload} = a_{cf} \cdot \sqrt{\rho_1 - \rho_0} + \left(\left(K_0 + b_{cf}\right) - K_{reload}\right) \tag{1.94}$$

Using Equation (1.75), and replacing K_{reload} by its value:

$$K_{reload} = K_{xm} = \frac{\sqrt{\varphi_{xm}}}{A} \cdot sign(\varphi_{xm}) \tag{1.95}$$

Similarly, $K_0 + b_{cf}$ is the upper bound of the cyclic elastic zone, which writes:

$$K_0 + b_{cf} = \frac{\sqrt{\varphi_{xc} + \varphi_c}}{A} \cdot sign(\varphi_{xc} + \varphi_c) \tag{1.96}$$

Rewriting the Equations (1.95) and (1.96) in Equation (1.94) yields the complete expression of the blunting evolution equation after a compression phase:

$$K_1 - K_{reload} = a_{cf} \cdot \sqrt{\rho_1 - \rho_0} + \left(\frac{\sqrt{\varphi_{xc} + \varphi_c}}{A} \cdot sign(\varphi_{xc} + \varphi_c) - \frac{\sqrt{\varphi_{xm}}}{A} \cdot sign(\varphi_{xm}) \right) \tag{1.97}$$

This expression is valid even if the cyclic elastic domain goes entirely under the contact loading of the lips or in the negative values of loading.

The y-intercept of Equation (1.97) is an expression of several internal variables. This expression is built with the values of those variables at the end of the compression phase. However, during a reload, these values will be updated and hence will evolve. In this respect, the y-intercept must be stored in an additional variable b_{comp} at the end of the compression phase:

$$\begin{aligned} K_1 - K_{reload} &= a_{cf} \cdot \sqrt{\rho_1 - \rho_0} + b_{comp} \\ \text{with:} \quad b_{comp} &= \left(\frac{\sqrt{\varphi_{xc} + \varphi_c}}{A} \cdot sign(\varphi_{xc} + \varphi_c) - \frac{\sqrt{\varphi_{xm}}}{A} \cdot sign(\varphi_{xm}) \right) \end{aligned} \tag{1.98}$$

To illustrate this, the y-intercept b to be used for the plastic blunting evolutions during a loading is as follows:

$$b = \begin{cases} b_{comp} & \text{if there was an underload} \\ b_{cf} & \text{otherwise} \end{cases} \tag{1.99}$$

Details on the expression of K_{reload} based on the internal variables The size of the cyclic elastic zone is updated at the end of the unloading (`cyclic_closing`), before the compression, using the expression:

$$\varphi_c = \frac{A^2 b_{cf}}{2} \cdot \left(2 \cdot \frac{\sqrt{\varphi_2}}{A} + b_{cf} \right) \tag{1.100}$$

where φ_2 is the applied external loading, and thus represents the minimum loading reached. Doing so, the size of the cyclic elastic domain φ_c keeps implicitly track of the minimum loading reached. In terms of the stress intensity factors, this loading is in fact K_{reload}. Therefore, it exists an equation that allows expressing K_{reload} from the internal variables during a reloading. The Equations (1.75) and (1.100) enable to write:

$$\varphi_c = \frac{A^2 b_{cf}}{2} \left(2K_{reload} + b_{cf} \right) \tag{1.101}$$

and finally:

$$K_{reload} = \frac{\varphi_c}{A^2 b_{cf}} - \frac{b_{cf}}{2} \tag{1.102}$$

The Equation (1.102) will be used as an expression of K_{reload} based on the internal variables for the analytic integration of the blunting evolutions equations, when there was no compression phase. It is the chosen solution in [HAM 06].

In a first analysis, this solution seems also to be valid if there has been a compressive phase, since it represents the minimum loading reached during the closing cyclic plasticity phase (`cyclic_closing` event), in this case φ_{xm}. Since the size of the cyclic elastic domain φ_c is not updated during a compression loading, it remains constant until the reloading. However, the split resolution of the blunting and cracking laws (see section 4.4.1), makes that the internal variable φ_{xm} is updated with the advance increment *just after* the end of the `cyclic_closing` event, during which φ_c is computed. The expression (1.102) is in this case no more valid, it does not give a correct information on the value of φ_{xm} since this variable has changed. In addition, during a loading, the opening of the crack must arise very precisely at the contact loading. Thereby, if the crack has undergone an underload, the expression (1.95) is finally used to define K_{reload} from the internal variables.

To illustrate this, K_{reload} writes, based on the internal variables:

$$K_{reload} = \begin{cases} \frac{\sqrt{\varphi_{xm}}}{A} \cdot sign(\varphi_{xm}) & \text{if there was an underload} \\ \frac{\varphi_c}{A^2 b_{cf}} - \frac{b_{cf}}{2} & \text{otherwise} \end{cases} \tag{1.103}$$

Analytic integration of the blunting equations during a loading phase To implement the evolution equations of ρ for the cyclic plastic zone, their analytic integration must be computed. The y-intercept b and the expressions of K_{reload} are different depending on whether there was a compression phase or not. For all that, the reasoning is conducted using the general form of the equations, which remains the same for both cases. During a loading phase, the plastic blunting evolution equations can then be written for both an initial configuration (denoted by the subscript 1) and a final configuration (subscript 2):

$$\begin{aligned} K_1 - K_{reload} &= a_{cf} \cdot \sqrt{\rho_1 - \rho_0} + b \\ K_2 - K_{reload} &= a_{cf} \cdot \sqrt{\rho_2 - \rho_0} + b \end{aligned} \tag{1.104}$$

from which the expression of $\mathrm{d}\rho$ can be deduced:

$$\mathrm{d}\rho = \rho_2 - \rho_1 = \left(\frac{K_2 - K_{reload} - b}{a_{cf}} \right)^2 - \left(\frac{K_1 - K_{reload} - b}{a_{cf}} \right)^2 \tag{1.105}$$

Expressing K_1 and K_2 in terms of internal variables (Equation (1.75)), and replacing b and K_{reload} by their values (respectively Equations (1.99) and (1.103)), the expressions of ρ_2 are obtained, in function of the state vector of the CTCP model at time t_1, if there was a compression loading or not:

– *If there was an underload:*

$$\rho_2 = \frac{1}{a_{cf}^2} \cdot \left[\left(\frac{\sqrt{\varphi_2}}{A} - \frac{\sqrt{\varphi_{xm}}}{A} \cdot sign(\varphi_{xm}) - b_{comp} \right)^2 - \left(\frac{\sqrt{\varphi_1}}{A} - \frac{\sqrt{\varphi_{xm}}}{A} \cdot sign(\varphi_{xm}) - b_{comp} \right)^2 \right] + \rho_1 \tag{1.106}$$

– *Otherwise:*

$$\rho_2 = \frac{1}{a_{cf}^2} \cdot \left[\left(\frac{\sqrt{\varphi_2}}{A} - \frac{\varphi_c}{A^2 b_{cf}} - \frac{b_{cf}}{2} \right)^2 - \left(\frac{\sqrt{\varphi_1}}{A} - \frac{\varphi_c}{A^2 b_{cf}} - \frac{b_{cf}}{2} \right)^2 \right] + \rho_1 \tag{1.107}$$

For the implementation, there must be a flag that indicates during the loading if there was a compression phase.

Internal variables initialization – initial values At the beginning of the first loading, nothing is plastic yet, the structure is still fully elastic. Thus this first loading is starting by an elastic opening of the crack. It corresponds in fact to the crossing of both the cyclic and monotonic elastic zones, which are at this time superimposed. Then, the material enters in its plastic domain, giving birth to the monotonic plastic zone directly, without passing trough the cyclic plastic zone, which will be created during the first unloading.

The internal variables must hence describe a plastic threshold corresponding to the upper bound of the monotonic elastic zone which was determined during the identification stage of the CTCP model, during the first loading. The equation that models the plastic blunting evolution during the first loading is as follows:

$$K = a_m \cdot \sqrt{\rho} + b_m \tag{1.108}$$

The y-intercept b_m, material parameter of the model, represents the size of the initial elastic zone, and its lower bound is the nil loading $\varphi_0 \equiv K_0 \equiv 0$. These size and position of the elastic zone must be assigned to both domains, cyclic and monotonic, since they are initially superimposed. Hence the internal variables must all be initialized to 0, except:

$$\begin{cases} \varphi_m = A^2 b_m^2 \\ \varphi_{xco} = \dfrac{A^2 b_m^2}{2} \\ \varphi_{co} = \dfrac{A^2 b_m^2}{2} \end{cases} \tag{1.109}$$

CTCP model implementation All the equations to implement are presented in this section. The state vector at time t_1:

$$\left(\varphi_1, \varphi_{m_1}, \varphi_{xm_1}, \varphi_{co_1}, \varphi_{xco_1}, \varphi_{cf_1}, \varphi_{xcf_1}\right)_1 \tag{1.110}$$

is assumed to be entirely known, while the one at time t_2 is to be determined. The variables φ_1 and φ_2 represent the applied loading at respectively times t_1 and t_2 (Equation (1.75)). The conditions on these variables allowing to determine which event must be activated are detailed. Only the cases in which φ_1 and φ_2 belong to a same event are described. In practice, if the loading increment makes that the two variables belong to different events, it is in fact too large and it must be envisaged to subdivide it internally. Since the compression phases are taken into account, the cyclic elastic zone can move entirely under the contact loading φ_{xm} of the crack lips. During a loading stage, the plastic blunting must occur when the loading will be greater than the blunting threshold, which corresponds to the greater of either the contact loading or the upper bound of the cyclic elastic domain. The first thing to do is thus to initialize a "blunting threshold" variable, which is absolutely not an additional internal variable, but rather a device used to ease the implementation. It is denoted $\varphi_{blunting}$ to remind that it always contains an internal variable:

$$\varphi_{blunting} = \max\left(\varphi_{xm}; \varphi_{xco} + \varphi_{co}\right) \tag{1.111}$$

1. **Opening phase —** $\Delta\varphi = \varphi_2 - \varphi_1 > 0$

   (a) *Domain in which the crack is closed:* $\left(\varphi_1;\varphi_2\right) < \varphi_{xm_1}$
   The loading initial and final values φ_1 and φ_2 are lower than the contact loading, there is no equation to integrate. The chosen event is `no_integration`. In practice, this case is the same than the case in which the loading increment is entirely contained inside the cyclic elastic domain, since they lead to the same event. The only implemented test consists hence in checking if the loading increment is contained inside the cyclic elastic domain.

   (b) *Cyclic elastic domain:* $\left(\varphi_1;\varphi_2\right) < \varphi_{\text{blunting}}$
   The loading initial and final values φ_1 and φ_2 are lower than the blunting threshold, there is no equation to integrate. The chosen event is `no_integration`.

   (c) *Cyclic plastic domain:* $\varphi_{\text{blunting}} \leq \left(\varphi_1;\varphi_2\right) < \varphi_{xm} + \varphi_m$
   The loading initial and final values φ_1 and φ_2 are contained inside the cyclic plastic zone, that is to say that they are greater than the blunting threshold but lower than the monotonic plastic threshold. The corresponding event is `cyclic_opening`. The equations to integrate are:

$$\rho_2 = \frac{1}{a_{cf}^2}\cdot\left[\left(\frac{\sqrt{\varphi_2}}{A} - K_{\text{reload}} - b\right)^2 - \left(\frac{\sqrt{\varphi_1}}{A} - K_{\text{reload}} - b\right)^2\right] + \rho_1 \quad \text{with:}$$

$$\left(K_{\text{reload}}\,;\,b\right) = \begin{cases} \left(\frac{\sqrt{\varphi_{xm}}}{A}\cdot sign\left(\varphi_{xm}\right)\,;\,b_{comp}\right) & \text{if there was an underload} \\ \left(\frac{\varphi_c}{A^2 b_{cf}} - \frac{b_{cf}}{2}\,;\,b_{cf}\right) & \text{otherwise} \end{cases} \tag{1.112}$$

$$\varphi_{co_2} = \varphi_{co_1} \tag{1.113}$$

$$\varphi_{xco_2} = \varphi_2 - \varphi_{co_2} \tag{1.114}$$

$$\varphi_{cf_2} = \frac{A^2 b_{cf}}{2}\cdot\left(2\cdot\frac{\sqrt{\varphi_2}}{A} - b_{cf}\right) \tag{1.115}$$

$$\varphi_{xcf_2} = \varphi_2 - \varphi_{cf_2} \tag{1.116}$$

   (d) *Monotonic plastic domain:* $\varphi_{xm} + \varphi_m \leq \left(\varphi_1;\varphi_2\right)$
   The loading initial and final values φ_1 and φ_2 are greater than the monotonic plastic threshold, hence this plastic zone extends. The corresponding event is `monotonic_opening`. The equations to integrate are:

$$\rho_2 = \left(\frac{\frac{\sqrt{\varphi_2}}{A} - b_m}{a_m}\right)^2 - \left(\frac{\frac{\sqrt{\varphi_1}}{A} - b_m}{a_m}\right)^2 + \rho_1 \tag{1.117}$$

$$\varphi_{cf_2} = \frac{A^2 b_{cf}}{2} \cdot \left(2 \cdot \frac{\sqrt{\varphi_2}}{A} - b_{cf} \right) \tag{1.118}$$

$$\varphi_{xcf_2} = \varphi_2 - \varphi_{cf_2} \tag{1.119}$$

$$\varphi_{xm_2} = A^2 \cdot \underbrace{\left(\frac{\sqrt{\varphi_{xm_1}}}{A} \cdot sign\left(\varphi_{xm_1}\right) + a_{xm} \cdot \mathrm{d}\rho \right)}_{\alpha} \cdot sign(\alpha) \quad \text{with} \quad \mathrm{d}\rho = \rho_2 - \rho_1 \tag{1.120}$$

$$\varphi_{m_2} = \varphi_2 - \varphi_{xm_2} \tag{1.121}$$

2. **Closing phase —** $\Delta\varphi < 0$

   (a) *Cyclic elastic domain:* $\left(\varphi_1 ; \varphi_2\right) > \varphi_{xcf} - \varphi_{cf}$
   The loading initial and final values φ_1 and φ_2 belong to the cyclic elastic zone, there is no equation to integrate. The chosen event is `no_integration`.

   (b) *Cyclic plastic domain:* $\varphi_{xcf} - \varphi_{cf} \geq \left(\varphi_1 ; \varphi_2\right) > \varphi_{xm}$
   The loading initial and final values φ_1 and φ_2 belong to the cyclic plastic domain, in other terms they are lower than the lower bound of the cyclic elastic zone, but greater than the loading for which the crack lips contact (the so-called contact loading). The corresponding event is `cyclic_opening`. The equations to integrate are:

$$\rho_2 = \frac{1}{a_{cf}^2} \cdot \left[\left(\frac{\varphi_{cf}}{A^2 b_{cf}} - \frac{b_{cf}}{2} - \frac{\sqrt{\varphi_1}}{A} \right)^2 - \left(\frac{\varphi_{cf}}{A^2 b_{cf}} - \frac{b_{cf}}{2} - \frac{\sqrt{\varphi_2}}{A} \right)^2 \right] + \rho_1 \tag{1.122}$$

$$\varphi_{cf_2} = \varphi_{cf_1} \tag{1.123}$$

$$\varphi_{xcf_2} = \varphi_2 + \varphi_{cf_2} \tag{1.124}$$

$$\varphi_{co_2} = \frac{A^2 b_{cf}}{2} \cdot \left(2 \cdot \frac{\sqrt{\varphi_2}}{A} + b_{cf} \right) \tag{1.125}$$

$$\varphi_{xco_2} = \varphi_2 + \varphi_{co_2} \tag{1.126}$$

Remark 15 *In any case, between a cyclic plastic phase during a loading and a compression phase during an unloading, an unloading cyclic plastic phase happens. It is taken advantage of this phase to reinitialize the flag which indicates, during a loading stage, that a compression phase has happened (see section 4.4.2). Indeed, a compression stage has an influence only on the loading phase that immediately follows it, its effect totally disappears during the next unloading.*

(c) *Compression loading domain:* $\varphi_{xm} \geq \left(\varphi_1 ; \varphi_2\right)$

When the applied loading becomes lower than the contact loading, the plastic blunting does not evolve anymore but the cyclic elastic zone moves. The variable b_{comp} is also updated. The corresponding event is `compression_closing`. The evolution equations are then:

$$\varphi_{co_2} = \varphi_{co_1} \tag{1.127}$$

$$\varphi_{xco_2} = \varphi_2 + \varphi_{co_2} \tag{1.128}$$

$$b_{comp} = b_{cf} + \left(\left(\frac{\sqrt{\varphi_{xc} - \varphi_c}}{A} \cdot sign\left(\varphi_{xc} - \varphi_c\right) \right) - \frac{\sqrt{\varphi_{xm}}}{A} \cdot sign\left(\varphi_{xm}\right) \right) \tag{1.129}$$

Remark 16 *During a compression phase, the flag which, during the following loading, indicates that a compression load was applied must be set on (see section 4.4.2).*

3. **Propagation —** $\mathrm{d}\rho \neq 0$

At this point, the blunting law integration, that is, the integration of the variations of the internal variables with respect to the evolutions of the plastic blunting ρ, is totally done. The cracking law itself must now be integrated, as well as the evolutions of the internal variables, this time with respect to the crack advance a. The crack propagation occurs if and only if there is a variation of the plastic blunting. This function is thus used only if the statement $\mathrm{d}\rho \neq 0$ is true.

(a) *Propagation law:*

The propagation law is used to determine the crack advance increment $\mathrm{d}a$ by unit length of crack front from the plastic blunting increment $\mathrm{d}\rho$:

$$\mathrm{d}a = \alpha \cdot |\mathrm{d}\rho| \tag{1.130}$$

(b) *Update of the internal variables depending on the crack advance:*

Once the crack advance increment has been computed, the internal variables which depend upon the crack length can be updated:

$$\varphi_{m_2} = \varphi_{m_1} \cdot e^{p_a \cdot \mathrm{d}a} \tag{1.131}$$

$$\varphi_{xm_2} = \left(\varphi_{xm_1} + \varphi_{m_1} \cdot c_{pos}\right) \cdot e^{k_a \cdot \mathrm{d}a} - \varphi_{m_2} \cdot c_{pos} \quad \text{with} \quad c_{pos} = \frac{k_b}{k_a - p_a} \tag{1.132}$$

4.4.3 Examples

To illustrate the equations detailed in the previous section, the results of some simulations conducted with the CTCP model are presented hereinafter. A first example is given on Figure 1.36. In a preliminary phase, the parameters of the constitutive law of the model have been numerically identified. A realistic elastic-plastic behavior composed of a non-linear isotropic hardening and two non-linear kinematic hardening models (Chaboche law) has been used (refer to section 4.3.7).

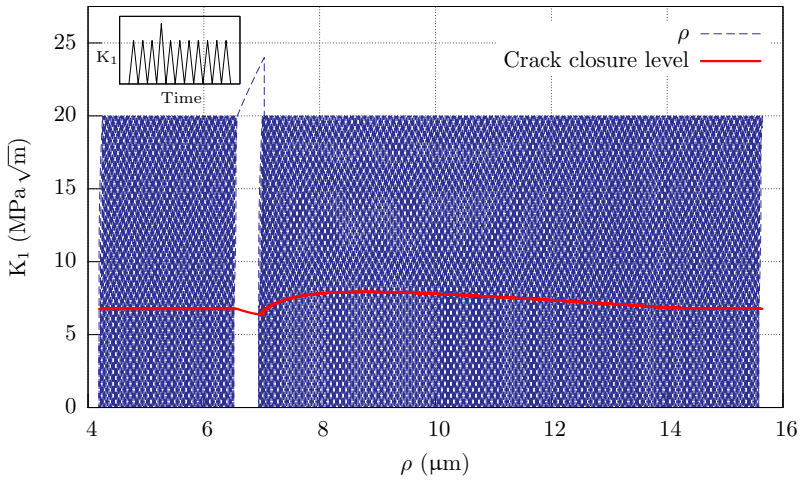

Figure 1.36 Plastic flow intensity factor ρ and crack closure level evolutions under a single overload simulated with the CTCP model as implemented in the ANSYS software.

A 2D, mode I crack is then simulated. Recall that during the simulations, only linear elastic computations are conducted by the finite element method, the material non-linearities are taken into account at the CTCP model level. The simulated crack is submitted to a cyclic loading which corresponds to a stress intensity factor oscillating between 0 and 20 MPa $\sqrt{\text{m}}$. At a certain time, a single overload of 24 Mpa $\sqrt{\text{m}}$ is introduced. This represents an overload of 1.2 times the nominal load. For the chosen material behavior, under those levels of loading the crack is in the Paris regime. The evolutions of the computed plastic flow intensity factor ρ and of the associated crack closure level are plotted (see Figure 1.36). This closure level corresponds in fact to the internal variable φ_{xm} of the CTCP model, expressed here as K_{xm} in terms of stress intensity factors by means of the relation (1.75). The plastic flow evolutions have basically the same hysteresis shape than those represented on Figure 1.21, but here, because of the scale of the figure, they appear really shrunk.

During the first part of this simulation, the prescribed loading is cyclic. The resulting evolutions of the plastic flow are very regular and the crack closure level is steady. The crack velocity is therefore constant, and is equivalent to the growth rate that would be evaluated from a Paris law. Then, the crack undergoes the overload. Immediately, the plastic flow goes up and the hysteretic nature of the evolutions of ρ can be noticed. At the same time, the crack closure level drops down. The results of this is a transitory acceleration of the crack. After that, the crack closure level rises up significantly: crack retardation occurs. To finish, the closure level slowly goes back to its original value. At the end, the crack speed is again steady, equivalent to the Paris law speed, and there is no trace of the overload. This behavior is precisely in accordance with what is described in the literature [BAT 97], and very specific effects such as the transitory speedup of the crack are well observed.

Two other simulations are proposed on Figure 1.37. The material behavior chosen for those simulations is totally artificial, it is designed to generate a very fast evolution of the internal variables. As a consequence, a zoom on a specific event (typically an overload Figure 1.37(a) or an underload (b)) reveals the hysteresis curves of the evolutions of the plastic flow intensity factor ρ. During the simulation of Figure 1.37(b), the crack is submitted to a cyclic loading oscillating between 7 and 20 MPa $\sqrt{\text{m}}$ until that the closure level is constant. Again, this closure level, in red on the figure, corresponds to the internal variable φ_{xm} of the CTCP model, expressed as K_{xm} in

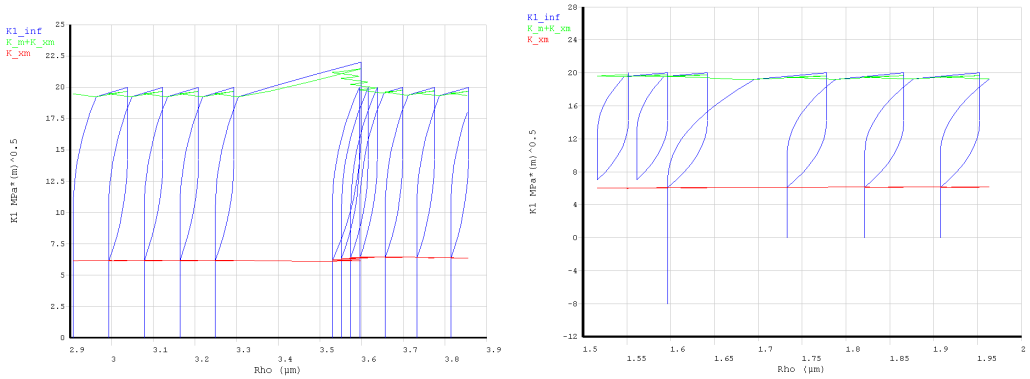

(a) Response to an overload of factor $F = 1,1$

(b) Response to an underload of factor $F = -0,4$

Figure 1.37 Crack Tip Condensed Plasticity model simulations of some typical loadings.

terms of stress intensity factors by means of the relation (1.75). At a certain time (corresponding to a value of ρ of approximately 1.6 µm), an underload of -8 MPa $\sqrt{\text{m}}$ is applied to the crack. This underload represents -0.4 times the nominal load. When the crack opens again, it is clear that the plastic blunting (in blue on the figure) arises as soon as the loading is greater than the closure level. Indeed, the compression has been so strong that the cyclic opening elastic zone has totally disappeared. However, it reappears as soon as the next cycle begins. After that strong overload, all the subsequent cycles are submitted to loadings oscillating between 0 and 20 MPa $\sqrt{\text{m}}$, leading to a slight compression of the crack. In those cases, the cyclic elastic zone is apparently shortened by the compression but it is still there.

Finally, a last simulation under complex spectrum loading is presented. The CTCP model parameters are those identified in section 4.3.7, and the loading describes a specific spectrum varying between 4 and 25.5 MPa $\sqrt{\text{m}}$. The resulting evolutions of the crack closure level (the internal variable φ_{xm} of the CTCP model) are plotted along with whether the plastic flow intensity factor evolutions (Figure 1.38(a)), or the external loading evolutions (Figure 1.38(b)). First the crack closure level reaches progressively its nominal level (approximatively around time step 5000 on Figure 1.38(b)). Then, the variations of the loading have a clear influence on the closure level, making transitory accelerations similar to the one observed in the first example of this section (Figure 1.36) when overload phenomena occur, and other very complex, yet smoother, evolutions during the cyclic parts of the loading. Indeed, the incremental logic of the CTCP model allows the history and the interactions between the loading cycles to be preserved, enabling to observe changes in the crack closure level which would have been hardly predictable by a propagation law based on cycle extraction. For instance, the block of loading located between the time step 37500 and 42500 is lower than the previous block, however, the closure level is raising inside this zone of loading, in spite of what is commonly observed.

The obtained crack growth is also presented on Figure 1.39(a). Definitely the growth rates are irregular, varying in function of the applied loading. A closeup of the crack growth evolution around the time step 25400 is proposed on Figure 1.39(b). The variations of the growth rates are observable even very locally, cycle by cycle. During this analysis, 51016 time steps were simulated. Since each cycle of the loading is discretized by 32 time steps, this simulation corresponds to 1563 cycles. The final crack growth being 1133.1 µm, the overall mean growth rate is 0.725 µm per cycle.

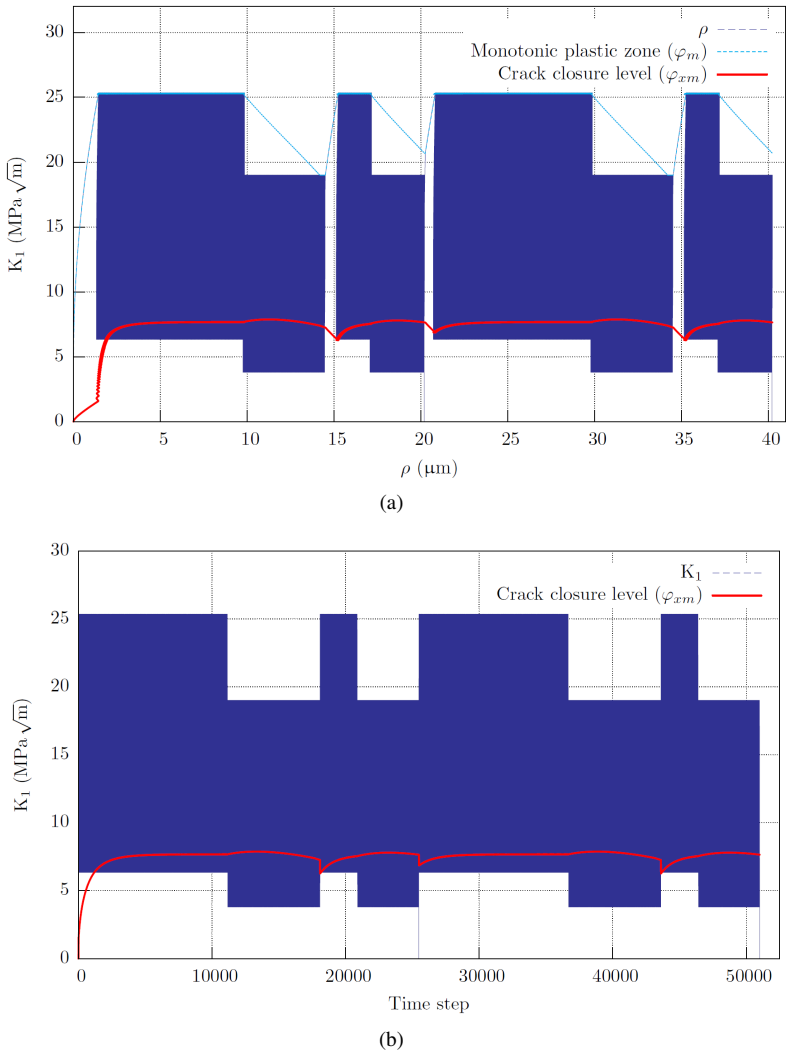

Figure 1.38 Crack Tip Condensed Plasticity model simulation of a specific spectrum loading. The crack closure evolutions are presented along with the evolutions of the plastic flow intensity factor (a) and the evolutions of the external loading (b).

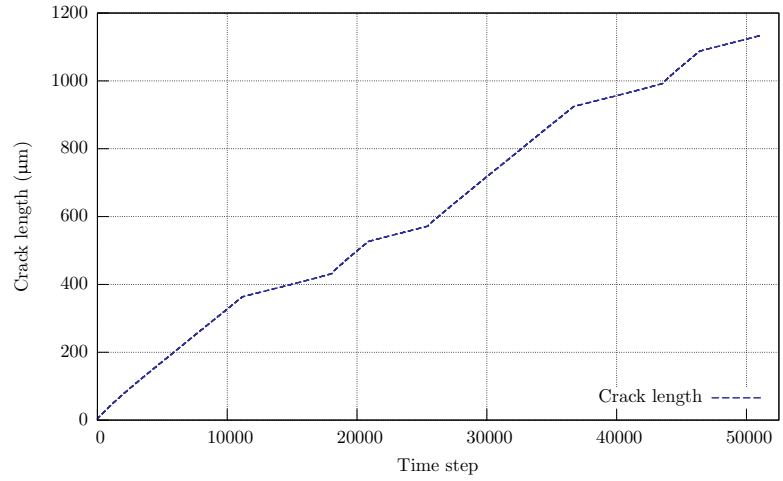

(a)

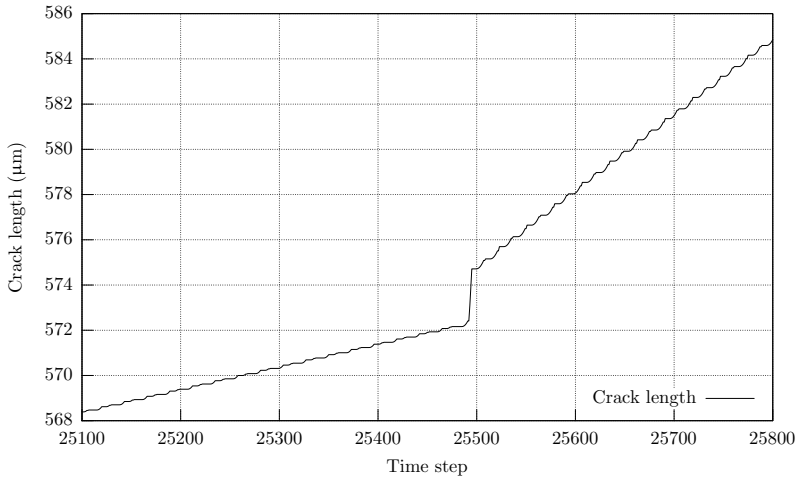

(b)

Figure 1.39 Crack growth in function of time obtained by the Crack Tip Condensed Plasticity model simulation of 1563 cycles of a specific spectrum loading (a). Closeup around the time step 25400 (b).

Chapter 2

A computational strategy for 3D fatigue crack growth in small scale yielding conditions

Contents

1 Objectives

Using the Crack Tip Condensed Plasticity model introduced in the first chapter, fast computation of the crack tip confined plasticity effects on the propagation rates is now possible, provided that the elastic stress intensity factor for the considered tridimensional structure is available. In this respect, simulating a high number of fatigue cycles will lead to solving as many linear elastic problems, with evolving geometry, in order to compute the stress intensity factors. Obviously, the required calculation time for this is prohibitive. At this point, the use of an additional acceleration technique based on an *a priori* model reduction approach will considerably decrease the computational cost of those numerous linear elastic calculations. The chosen numerical methods and strategy are extensively described in this chapter, along with bidimensional and tridimensional examples.

2 Discretized reference problem

Now that the objective of this work are clear, let us introduce the discretized problem corresponding to the reference problem of section 1.1. We recall that the static deformation of a linear elastic, homogeneous and isotropic cracked body under small strain and displacement assumptions is considered. Since the crack is evolving, this body defines a time-dependent domain $\Omega(t)$ (see Figure 1.1) defined on all the temporal study interval $[0,T]$.

For this evolution problem, additionally to the displacement field $\boldsymbol{u}(t)$, an extra unknown $\dot{\boldsymbol{a}}$ is used to represent the velocity of the crack. The propagation law is then used to determine this crack speed as well as the updated front position from the stress state of the structure, written in terms of stress intensity factors K_i. Thereby, at each time t, along with the usual displacement and stress fields, we have to solve for the crack growth rate at each node of the front:

$$\dot{\boldsymbol{a}}\Big(\boldsymbol{x}_f(t), K_i\Big(\boldsymbol{x}_f, t\Big), t\Big) \qquad \forall t \in [0,T] \tag{2.1}$$

where $\boldsymbol{x}_f(t)$ contains the spatial coordinates of the front.

For the numerical resolution, the space discretization is performed using finite elements. Again, it is worth highlighting that since the crack is growing, the discretization of the problem changes with time. However, the whole evolution problem can be viewed as a set of ordered, successive linear elastic problems. The only dependence between them is from a geometrical point of view. As a consequence, there is no need to project any field on the evolving meshes. In addition to that, the time is also discretized. The time stepping is chosen fine enough to describe accurately the spectrum loading prescribed to the structure. Therefore, at any discrete time step t_k, for a model involving N degrees of freedom, its N nodal displacements $(q_i^{t_k})_{i=1,\dots,N}$ are connected to the displacement field by the finite element shape functions $\boldsymbol{N}_i^{t_k}$ such that:

$$\boldsymbol{u}_{t_k}(\boldsymbol{x}) = \sum_{i=1}^{N} \boldsymbol{N}_i^{t_k}(\boldsymbol{x}) \cdot q_i^{t_k} \qquad \forall t_k \in [t_0 \dots t_T] \tag{2.2}$$

where $\boldsymbol{x} = [x,y,z]$ is the coordinate vector of any point of the time-dependent domain Ω_{t_k}. Then, with matrix notations, the finite element approximation writes:

$$\boldsymbol{K}_{t_k} \cdot \boldsymbol{u}_{t_k} = \boldsymbol{F}_{t_k} \qquad \forall t_k \in [t_0 \dots t_T] \tag{2.3}$$

where we define the stiffness matrix $\boldsymbol{K}_{t_k}$, which accounts for the prescribed displacements, and the generalized forces $\boldsymbol{F}_{t_k}$ in the usual manner according to the finite element method. These quantities can obviously evolve along the simulation according to the modifications of the domain with the crack propagation.

3 Reduced basis approach: decreasing the computational cost during the propagation

3.1 Model reduction techniques: principle

The model reduction techniques are all arising from a same motivation: reducing the cost of some numerical computations. This cost can be imputed to several different causes, ranging from the *curse of dimensionality* when trying to solve problems in high dimensions (such as the Shrödinger equation for instance [AMM 08]), to transient or multiscale problems [LAD 09]. In this respect, a number of techniques were developed, each of them adapted to a specific class of problems. Among others, one can mention the submodeling approach, in which the result obtained during a first FEM analysis with a coarse mesh are projected as boundary conditions of a refined mesh of a region of interest, providing a more accurate solution on this region at a cheap cost; or even dynamic reduction methods such as the well-known Craig and Bampton's component mode synthesis [CRA 68]. Another emerging model reduction strategy if the Proper Generalized Decomposition [AMM 10, GON 10]. It is based on a separated representation of the variables of the model. Hence this method is specifically well-suited to solve problems in very high-dimensional spaces, since the complexity no more scales with n^d, were n is the number of degrees of freedom and d the dimension of the problem, but rather with $n \times d$!

The last wide variety of model reduction techniques are the methods based on reduced solution subspaces considerations, the so-called *reduced basis methods* [VER 03, MAD 02]. These approaches are particularly adapted to transient and evolution problems in general, that is, where a time or pseudo-time is involved in the analysis. Indeed, considering a time-dependent problem that is to be solved using the finite element method, let us introduce some notations, similar to those used in the previous section. Let denote by $\boldsymbol{u}(\boldsymbol{x},t)$ the solution of the partial differential equations associated with the structural problem set on a bounded spatial domain $\Omega \subset \mathbb{R}^d$ and on a closed temporal domain $\mathcal{T} \subset \mathbb{R}$. At each instant t, the solution $\boldsymbol{u}(\boldsymbol{x},t)$ belongs to $\mathcal{U}$, a functional space adapted to the considered partial differential equations (refer to section 1.1 of chapter 1 for a description of this space). Using a first Galerkin projection, the problem can actually be written in a discrete weak form suitable for a finite element resolution:
Find $\boldsymbol{u}_n(t)$ in space $\mathcal{U}_n$ such that:

$$\mathcal{A}(\boldsymbol{u}_n(t), \boldsymbol{v}_n; t) = g(\boldsymbol{v}_n) \qquad \forall \boldsymbol{v}_n \in \mathcal{U}_n \tag{2.4}$$

where the space $\mathcal{U}_n$ is a subset of the functional space $\mathcal{U}$ and the subscript n is related to the number of degrees of freedom of the discretization and to the dimension of $\mathcal{U}_n$. The functional g is a linear form of $\mathcal{U}_n'$, the dual space of $\mathcal{U}_n$. For its part, $\mathcal{A}(\cdot,\cdot;t)$ is a symmetric bilinear form continuous and coercive on $\mathcal{U}_n$, uniformly with respect to the parameter t. Thus it exists two positive constants β and γ such that:

$$\begin{aligned} &\mathcal{A}(\boldsymbol{u}_n, \boldsymbol{v}_n; t) \leq \beta \|\boldsymbol{u}_n\|_{\mathcal{U}_n} \|\boldsymbol{v}_n\|_{\mathcal{U}_n} \qquad \forall \boldsymbol{u}_n, \boldsymbol{v}_n \in \mathcal{U}_n \\ &\mathcal{A}(\boldsymbol{u}_n, \boldsymbol{u}_n; t) \geq \gamma \|\boldsymbol{u}_n\|^2_{\mathcal{U}_n} \end{aligned} \tag{2.5}$$

If the dependency of the solution $\boldsymbol{u}(t)$ with respect to the time parameter t is sufficiently regular, a model reduction by a reduced basis method can be envisaged. It consists in using an *a priori* knowledge of a reduced solution space U_r, much smaller than the initial space $\mathcal{U}_n$, in which the solution of the problem (2.4) can be sought. These methods lie in fact on the assumption that the solutions of the problem are not distributed in an infinite dimensional space, but rather, they are belonging to a low dimensional solution manifold that can be approximated locally by a very low dimensional vector space.

Generally, a specific difficulty stands in the definition of an appropriate reduced space of solution in order to capture the studied phenomenon. In the context of reduced basis methods, a usual strategy is to define it such as:

$$U_r = \text{Span}\{\boldsymbol{u}_n(t_k),\ k = 1,\ldots,r\} \tag{2.6}$$

where the $\boldsymbol{u}_n(t_k)$ are the solution vectors of the discrete problem at r different times t_k of the considered temporal interval. The $\boldsymbol{u}_n(t_k)$ are called solution *snapshots*. Using a second Galerkin procedure, the reduced problem to solve is then:
Find $\boldsymbol{u}_r(t)$ in space U_r such that:

$$\mathcal{A}(\boldsymbol{u}_r(t), \boldsymbol{v}_r; t) = g(\boldsymbol{v}_r) \qquad \forall \boldsymbol{v}_r \in U_r \tag{2.7}$$

It is noteworthy that in this reduced problem, the test functions $\boldsymbol{v}_r$ are no more the usual finite element test functions, but rather new functions, whose support can be the entire domain Ω or a part of it, which are spanning the reduced solution space U_r. The most often, an orthonormal basis of U_r is chosen. This basis constitutes then a *reduced basis* for the initial problem (2.4). Details on the generation of such a basis for a given U_r are proposed in section 3.2. In addition, the reduced problem (2.7) is consistent under the conditions (2.5). Indeed, the Lax-Milgram theorem [LAX 54] states that a unique solution $\boldsymbol{u}_r(t)$ exists in U_r. Furthermore, the Cea's lemma [CEA 64] provides the following bound for this approximation:

$$\|\boldsymbol{u}(t) - \boldsymbol{u}_r(t)\|_{U_r} \leq \sqrt{\frac{\beta}{\gamma}} \inf_{\boldsymbol{v}_r \in U_r} \|\boldsymbol{u}(t) - \boldsymbol{v}_r\|_{U_r} \tag{2.8}$$

The relevancy of such approaches stands in the fact that in many cases, the right hand side of this upper bound can be made very small. The real thing that cannot be known *a priori* is the necessary dimension of U_r to approximate the complete solution space. The smaller this dimension, the more efficient the reduced basis technique. As a matter of fact, this dimension will be small if the set

$$S(\mathcal{T}) = \{\boldsymbol{u}_n(t) \mid t \in \mathcal{T}\} \tag{2.9}$$

of all the solutions behaves well. At this point, in order to clarify in which sense the good behavior of the set $S(\mathcal{T})$ should be understood, we can follow Maday [MAD 06] and introduce the notion of n-width of Kolmogorov [KOL 36, PIN 85].

Definition 1 *Let F be a subset of $\mathcal{U}$ and Y_n a generic n-dimensional subspace of $\mathcal{U}$. The angle of F from Y_n is*

$$E(F; Y_n) = \sup_{x \in F} \inf_{y \in Y_n} \|x - y\|_{\mathcal{U}} \tag{2.10}$$

The Kolmogorov n-width *of F in $\mathcal{U}$ is given by*

$$\begin{aligned} d_n(F, \mathcal{U}) &= \inf\{E(F; Y_n) : Y_n \text{ a } n\text{-dimensional subspace of } \mathcal{U}\} \\ &= \inf_{Y_n} \sup_{x \in F} \inf_{y \in Y_n} \|x - y\|_{\mathcal{U}} \end{aligned} \tag{2.11}$$

The n-width of the space F hence measures the extent to which it can be approximated by a n-dimensional subspace of $\mathcal{U}$. For a given dimension n of the approximating space, the smaller the Kolmogorov n-width, the better the approximation. The reduced basis will thus be efficient if, choosing $F = S(\mathcal{T})$, the set of solutions can be approximated accurately by a subspace of *low* dimension. The main reason for which the Kolmogorov n-width may tend to zero

as n tends to infinity is the quality of the dependency of the solution to the variations of the parameter t. Indeed, if the solution is so regular that analyticity exists in this dependency, exponential convergence can be achieved. In other words, the solutions of $S(\mathcal{T})$ must reside on a low-dimensional *smooth* manifold. However, for a large class of problems this is not the case. Applied to them, the model reduction techniques will not reduce significantly the computational cost of the resolution!

The above definition hence formalizes the fact that on some kind of problems, the model reduction approaches cannot be applied. Without special treatment, the crack propagation problem falls in that class. Fortunately, even when the Kolmogorov n-width is large in a first analysis, mathematical devices can sometimes be used to reduce it. In this thesis, the specific response to this problem was to use a mesh morphing technique to handle the geometrical updates of the model during the simulations. This topic is extensively detailed in section 7, providing an illustrating example along with an explanation.

In the following section, some classical methods for building an orthonormal basis approximating the subspace spanned by a set of vector are recalled.

Remark 17 *It is very important to understand that, in order to apply successfully a reduced basis technique to a specific kind of problem, the dependency of the solution with respect to the* parameter variations *should be smooth. However, the solutions fields can exhibit a limited regularity with respect to the* spatial coordinates*. In other words, only the variations of the solution fields, not the solutions themselves have to be smooth. This particular feature make the reduced basis applicable to a wide range of problems.*

Remark 18 *Note that for the sake of clarity, the previous reasoning was conducted using a problem on a fixed domain Ω that does not depend upon time. In the specific context of crack propagation, this is not true and an evolving domain $\Omega(t)$ must be considered. Anyway, the reasoning still holds provided that appropriate solution spaces $\mathcal{U}_n$ and $\mathcal{U}_r$ are chosen. Again, the naive approach in that case would lead to a large dimension r of the reduced solution space and in this work, a mesh morphing technique is employed to overcome that fact (section 4). Doing so, since the mesh morphing technique induces a distortion of the elements, special attention is paid to keep a sufficient mesh quality in order to preserve the coercivity of the stiffness matrix.*

3.2 Approximating linear space

Suppose that we have access to n state variables, such as for instance numerical solutions of an analysis (degrees of freedom, data at Gauss points), or even experimental data (answers to a survey, strain probe, gray level of the pixels of a picture). Now suppose that we can get this information at m different times, or for m different experimental conditions or random parameters values. We hence get m vectors of size n, called snapshots and constituting the set $\{\boldsymbol{u_i}\}_{i=1}^{m}$. These vectors span a vector space $\mathbb{R}^m$. The objective now is to approximate it by another vector space of lower dimension r. In other words, find a set of ordered orthonormal basis vectors $\{\boldsymbol{\phi}_i\}_{i=1}^{r}$ such that it approximates a random vector $\boldsymbol{x}$ which takes its value in $\mathbb{R}^n$ as:

$$\boldsymbol{x} \approx \check{\boldsymbol{x}}_r = \sum_{i=1}^{r} \alpha_i \cdot \boldsymbol{\phi}_i \tag{2.12}$$

Of course the representation (2.12) is not unique, and the number r of shape functions $\boldsymbol{\phi}_i$ required to obtain a correct approximation of $\boldsymbol{x}$ can be large. A very useful process to obtain an orthonormal basis of the subspace spanned by a vector set is the Gram-Schmidt algorithm,

detailed in the following section. However, it can be even more interesting to find a basis such that the approximation at rank p, hence using p basis vectors, is the best approximation at rank p, in the sense of a given norm. Of course, to be interesting, p should be lower than n. To build a basis like this, the problem to solve is in fact to find $\{\boldsymbol{\phi}_i\}_{i=1}^{r}$ that minimizes the mean square projection error of the snapshots:

$$P_{err} = \frac{1}{m} \cdot \sum_{i=1}^{m} \left\| \boldsymbol{u}_i - \sum_{j=1}^{r} \alpha_j \cdot \boldsymbol{\phi}_j \right\|^2 \tag{2.13}$$

Given the chosen accuracy, this ensures to use the minimal number of basis vectors for the approximation (2.12). Using such a basis, this approximation is then called the *proper orthogonal decomposition* (POD) of $\boldsymbol{x}$ truncated at the order r.

The first works on the proper orthogonal decomposition date back to the very early 1900's, with the research of Pearson [PEA 01]. It was originally developed in the field of statistics, aiming to express collections of multidimensional data using only some relevant, reduced dimensions to simplify the analysis. Since then, the POD concept has been applied to an impressive number of different fields such as for instance statistical analysis, data mining, image processing (and specifically image compression), mechanical engineering, and biomedical engineering. In fact, it is intimately connected to model reduction in the broad sense. Since almost all technological fields are dealing with an overwhelming quantity of data, in spite of the progress of the computer hardware, people were logically attracted by reducing their processing costs, explaining the widespread use of such techniques.

Consequently, three main methods emerged to build a POD in the discrete case, namely the principal component analysis (PCA), the Karhunen-Loève decomposition (KLD) and the singular value decomposition (SVD). They are in fact equivalent and yield similar results [LIA 02]. They are all described in the next sections.

3.2.1 Gram-Schmidt process

The Gram-Schmidt process is named for Jørgen Pedersen Gram and Erhard Schmidt [GRA 84]. It is a method to orthonormalize a set of vectors in an inner product space. Taking a set $\{\boldsymbol{u}_i\}_{i=1}^{m}$ of vectors of $\mathbb{R}^n$, it generates an orthogonal set $\{\boldsymbol{\phi}_i\}_{i=1}^{m}$ that spans the same successive vector spaces:

$$F_j = \text{Span}\left\{\boldsymbol{\phi}_1 \cdots \boldsymbol{\phi}_j\right\} = \text{Span}\left\{\boldsymbol{u}_1 \cdots \boldsymbol{u}_j\right\} \quad \forall j < m \tag{2.14}$$

The main step of the algorithm consists in subtracting to the vector $\boldsymbol{u}_{j+1}$ its orthogonal projection on the space F_j. Let us first introduce the projection operator along the direction $\boldsymbol{u}$ by:

$$\text{proj}_{\boldsymbol{v}}(\boldsymbol{u}) = \frac{\langle \boldsymbol{v}, \boldsymbol{u} \rangle}{\langle \boldsymbol{v}, \boldsymbol{v} \rangle} \cdot \boldsymbol{v} \tag{2.15}$$

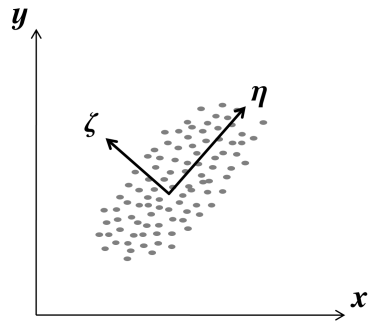

Figure 2.1 Schematic principal component analysis of a dataset. The computed directions $\boldsymbol{\eta}$ and $\boldsymbol{\zeta}$ are those which maximize the variance of the data, originally expressed in terms of $\boldsymbol{x}$ and $\boldsymbol{y}$.

where $\langle \cdot, \cdot \rangle$ denotes the inner product in $\mathbb{R}^n$. The algorithm writes then:

$$\begin{aligned}
\boldsymbol{v}_1 &= \boldsymbol{u}_1, \quad & \boldsymbol{\phi}_1 &= \frac{\boldsymbol{v}_1}{\|\boldsymbol{v}_1\|} \\
\boldsymbol{v}_2 &= \boldsymbol{u}_2 - \mathrm{proj}_{\boldsymbol{v}_1}(\boldsymbol{u}_2), \quad & \boldsymbol{\phi}_2 &= \frac{\boldsymbol{v}_2}{\|\boldsymbol{v}_2\|} \\
\boldsymbol{v}_3 &= \boldsymbol{u}_3 - \mathrm{proj}_{\boldsymbol{v}_1}(\boldsymbol{u}_3) - \mathrm{proj}_{\boldsymbol{v}_2}(\boldsymbol{u}_3), \quad & \boldsymbol{\phi}_3 &= \frac{\boldsymbol{v}_3}{\|\boldsymbol{v}_3\|} \\
&\vdots & &\vdots \\
\boldsymbol{v}_m &= \boldsymbol{u}_m - \sum_{j=1}^{m-1} \mathrm{proj}_{\boldsymbol{v}_j}(\boldsymbol{u}_m), \quad & \boldsymbol{\phi}_m &= \frac{\boldsymbol{v}_m}{\|\boldsymbol{v}_m\|}
\end{aligned} \tag{2.16}$$

In order to truncate the obtained basis at an order r, a criterion on the norm of the obtained basis vector $\boldsymbol{\phi}_r$ is set up. Indeed, during the process the norm of $\boldsymbol{\phi}_r$ is an indicator of how well the basis constituted by the set of orthonormal vectors $\{\boldsymbol{\phi}_i\}_{i=1}^{r-1}$ describes the initial set $\{\boldsymbol{u}_i\}_{i=1}^{m}$ since it indicates how much "information" this extra vector adds to the basis. In short, the smaller the norm, the better the approximation.

It is highly emphasized that the Gram-Schmidt process does not necessarily yield the POD of a given set of vector, in the sense that the obtained orthonormal basis may not be optimal in the general case. However, it is a very practical tool since it can be applied in an incremental manner, allowing to enrich easily the basis with additional vectors. This is of a special interest in the context of solving evolution problems since the data coming from the solution vectors will be got, precisely, incrementally all along the computations.

Remark 19 *In practice, for numerical stability reasons, the* stabilized *Gram-Schmidt algorithm is implemented, which is slightly different. Anyway, a Gram-Schmidt process should always be called twice on the set of vector that must be orthogonalized. Indeed, this is a specific requirement in order to obtain accurate numerical results.*

3.2.2 PCA and KLD

The principal component analysis (PCA) [PEA 01, HOT 33] and the Karhunen-Loève decomposition (KLD) [KAR 43, LOÈ 55] are quite similar, both in their definition and in the way they

are computed. From a statistical viewpoint, they aim at building an orthonormal basis that maximizes the variance of all the data along its directions. An artificial illustrating example is provided on Figure 2.1. Qualitatively, the computed directions $\boldsymbol{\eta}$ and $\boldsymbol{\zeta}$ are those which contain the most information about the data, originally expressed in terms of $\boldsymbol{x}$ and $\boldsymbol{y}$. Suppose that the set of snapshots $\{\boldsymbol{u_i}\}_{i=1}^m$ is arranged in a matrix $\boldsymbol{A}$ such as:

$$\boldsymbol{A} = \begin{pmatrix} \boldsymbol{u}_1^1 & \boldsymbol{u}_2^1 & \cdots & \boldsymbol{u}_m^1 \\ \boldsymbol{u}_1^2 & \boldsymbol{u}_2^2 & \cdots & \boldsymbol{u}_m^2 \\ \vdots & \vdots & \ddots & \vdots \\ \boldsymbol{u}_1^n & \boldsymbol{u}_2^n & \cdots & \boldsymbol{u}_m^n \end{pmatrix} \tag{2.17}$$

Then the *covariance* matrix is defined such as:

$$\boldsymbol{C} = \boldsymbol{A}\boldsymbol{A}^T \tag{2.18}$$

The characteristics of this matrix are directly linked to the linear dependency of the snapshots among themselves. Indeed, a fully populated covariance matrix indicates very correlated snapshots whereas a sparse one signalizes dependent entries. After that, computing the proper orthogonal decomposition of the snapshots by whether the PCA or KLD method consist in solving the following eigenvalue problem:

$$\boldsymbol{C}\boldsymbol{\phi}_i = \lambda_i \boldsymbol{\phi}_i \tag{2.19}$$

The orthonormal basis constituted by the set of vector $\{\boldsymbol{\phi}_i\}_{i=1}^m$ is the proper orthogonal decomposition.

Note that the matrix $\boldsymbol{C}$ is of dimension $n \times n$. Depending on the number of state variables n compared to the number of instants m, it can be interesting to solve the following modified problem, which is of *smaller* dimension $m \times m$, using the so-called snapshot POD method [SIR 87]:

$$\begin{cases} \left(\boldsymbol{A}^T\boldsymbol{A}\right)\boldsymbol{v}_i = \xi_i \boldsymbol{v}_i \\ \boldsymbol{\phi}_i = \dfrac{1}{\sqrt{\xi_i}} \boldsymbol{A}\boldsymbol{v}_i \end{cases} \tag{2.20}$$

3.2.3 SVD

The singular value decomposition (SVD) is a powerful matrix factorization technique. It was introduced almost simultaneously by Beltrami and Jordan in the 1870's and extended to complex rectangular matrices by Ekardt and Young in 1939. This method can be viewed as an extension of the eigenvalue decomposition for non-square matrices.

Computing the SVD of the matrix $\boldsymbol{A}$ (2.17) of dimensions $n \times m$ consists in computing its factorization under the form:

$$\boldsymbol{A} = \boldsymbol{U}\boldsymbol{\Sigma}\boldsymbol{V}^T \tag{2.21}$$

where the superscript T indicates matrix transpose, and

- $\boldsymbol{U}$, orthogonal matrix of dimension $n \times n$, contains the left singular vectors of $\boldsymbol{A}$. The columns of $\boldsymbol{U}$ constitute in fact an orthonormal basis of the row space of $\boldsymbol{A}$. In the present case, they are homogeneous to a *spatial* basis of the data contained in $\boldsymbol{A}$.
- $\boldsymbol{V}$, orthogonal matrix of dimension $m \times m$, contains the right singular vectors of $\boldsymbol{A}$. Symmetrically to the matrix $\boldsymbol{U}$, The columns of $\boldsymbol{V}$ constitute an orthonormal basis of the column space of $\boldsymbol{A}$. In the present case, they are hence homogeneous to a *temporal* basis of the data contained in $\boldsymbol{A}$.

- $\boldsymbol{\Sigma}$, diagonal matrix of dimension $n \times m$, contains $p = \min(n,m)$ nonnegative numbers σ which are called the singular values of $\boldsymbol{A}$ and are arranged, by convention, in decreasing order.

There is a strong link between the singular value decomposition and the principal component analysis of a matrix. Indeed, starting from the SVD of matrix $\boldsymbol{A}$, it comes:

$$\begin{aligned} \boldsymbol{A}\boldsymbol{A}^T &= \left(\boldsymbol{U}\boldsymbol{\Sigma}\boldsymbol{V}^T\right)\left(\boldsymbol{V}\boldsymbol{\Sigma}^T\boldsymbol{U}^T\right) \\ &= \boldsymbol{U}\boldsymbol{\Sigma}\boldsymbol{V}^T\boldsymbol{V}\boldsymbol{\Sigma}^T\boldsymbol{U}^T \end{aligned} \tag{2.22}$$

The matrix $\boldsymbol{V}$ being an orthogonal matrix $\boldsymbol{V}^T\boldsymbol{V}$ is identity, and $\boldsymbol{\Sigma}$ being a diagonal matrix:

$$\begin{aligned} \boldsymbol{A}\boldsymbol{A}^T &= \boldsymbol{U}\boldsymbol{\Sigma}^T\boldsymbol{\Sigma}\boldsymbol{U}^T \\ &= \boldsymbol{U}\boldsymbol{\Sigma}^2\boldsymbol{U}^T \end{aligned} \tag{2.23}$$

where we recognize the eigenvalue decomposition of $\boldsymbol{A}\boldsymbol{A}^T$. Furthermore, the relation between the singular values σ_i and the PCA eigenvalues λ_i of $\boldsymbol{A}$ can then be deduced:

$$\lambda_i = \sigma_i^2 \tag{2.24}$$

A similar reasoning can be conducted with $\boldsymbol{A}^T\boldsymbol{A}$.

Now suppose that the truncated projection described in Equation (2.12) is performed using the r first columns of $\boldsymbol{U}$, or similarly the r eigenvectors $\boldsymbol{\phi}_i$ of the PCA corresponding to the r greatest eigenvalues $\{\lambda_i\}_{i=1}^r$. A very interesting theorem [LIA 02] stands that these basis vectors constitute an optimal basis, which was the desired result, and also that the minimum error induced by the projection is equal to the square summation of the $m-r$ remaining singular values of the matrix $\boldsymbol{A}$. This provides a truncation criterion to choose, with respect to a given desired error, how many basis vectors should be retained. It directly stems that observing the decreasing rate of the singular values gives a clear idea of how much the information contained in the matrix $\boldsymbol{A}$ will compress, in a general sense. This approach can be employed during a preliminary phase to estimate roughly the Kolmogorov n-width of a set of vector and thus the pertinence of applying a reduced basis method to it. Such kind of analysis is proposed several times in this typescript.

The computational cost of a singular value decomposition can be high, depending of course on the size of the matrix that must be decomposed. Therefore, in practice, variants of the SVD exist and among them, a very useful one is the *Thin SVD*, in which only the m first columns of $\boldsymbol{U}$ are computed. If $m \ll n$, it provides a significant reduction of the cost of the SVD computation. This situation arises quite often in numerical model reduction, since it corresponds to less snapshots vectors than degrees of freedom.

Remark 20 *The singular value decomposition is a quite generic process and can be adapted to vectors or functions varying with respect to time, coordinates, and basically any kind of parameters. It can also be used to compute low rank approximation of matrices. For instance in the context of image processing, it is often used to "compress" pictures, that is, from an initial picture, build one of a slightly lower quality but with a lower storage size. Such a process is provided on Figure 2.2, together with the normalized singular values of the initial image and various reconstructed images of different orders.*

3.3 The *a posteriori* and *a priori* distinction

The model reduction techniques are classified in two main categories, the so-called *a posteriori* and *a priori* strategies. Choosing to use a method from whether the first or the second category mainly depends on the type of application that is envisaged.

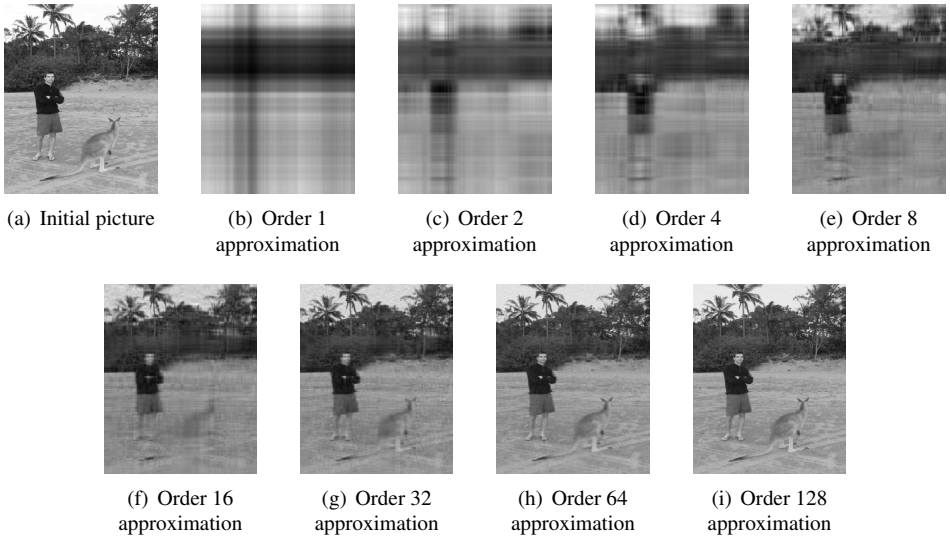

(a) Initial picture (b) Order 1 approximation (c) Order 2 approximation (d) Order 4 approximation (e) Order 8 approximation

(f) Order 16 approximation (g) Order 32 approximation (h) Order 64 approximation (i) Order 128 approximation

Figure 2.2 Image reconstructed from its truncated singular value decomposition.

3.3.1 *a posteriori* model reduction

The principle of the *a posteriori* method consists in defining explicitly a set of parameters and their variation ranges when setting up the problem. For instance, in the case of stochastic applications, these might be some random parameters, or different temporal loading for the case of evolution problems, or even geometric parameters for the domain evolution problems. Then, in a first *offline* phase, several solutions of the problem are computed for certain, well chosen, values of the parameters. The obtained vectors constitute the solution *snapshots*. These preliminary calculations are conducted by means classical resolution methods and are generally much time consuming. Hence this first offline phase can be considered as a learning phase for the process, since the reduced basis is extracted from the obtained solutions snapshots by computing their POD. After that, in an *online* phase, the solutions for new values of the input parameters are computed as linear combinations of the basis vectors. This second process is very efficient provided that the dimension of the reduced basis is low. Fortunately, it is the case for several applications, if the parameters values for the offline computations were sufficiently well chosen. This selection is thus of a great importance for the efficiency of the whole method, and can be conducted randomly, or by a *greedy* strategy [BUF 09].

This type of methods is particularly adapted to the "many queries" context, and when the offline / online decomposition is acceptable. Consequently, they are widely used in the framework of reanalysis, parametric studies, optimization, response surface building and even real-time simulations [NIR 10].

3.3.2 *a priori* model reduction

The *a priori* methods, for their part, propose a more versatile approach. The offline / online decomposition is no more necessary, and the actual reduced computations can be started without any *a priori* knowledge of the solutions characteristics. Indeed, the solution snapshots are build on the fly, during the computations. At this point, various strategies can be used to obtain those

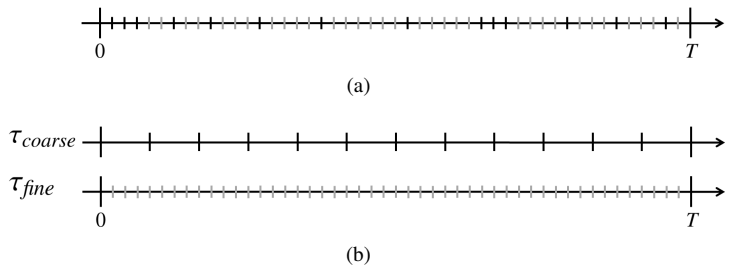

Figure 2.3 Schematic definition of the snapshots for the *a priori* model reductions. The iterative construction strategy (a) and the multiple timescale method (b).

snapshots. Two of them are briefly described in the following.

A first method consists in trying to solve the reduced problem (that is, seeking the solutions as linear combinations of the basis vectors) at each time step. An error is then computed, for instance based on an equilibrium residual, to determine if the basis contains sufficient information to describe the sought solution. If this is the case, nothing special to do then, the solution is found and the computations can go on to the next time step. However, if the error criterion is not fulfilled, a classical solve of the model is performed and the basis is enriched with the additional snapshot obtained. A schematic illustration of this approach is shown on Figure 2.3(a), where the gray time steps correspond to reduced resolutions whereas the black ones represent the full solves enriching the basis. This method can be viewed as an iterative construction of the basis, enriched only when it is needed [RYC 06, RYC 05a]. The first strategy proposed in this typescript is based on that approach (see section 5 of chapter 2).

A second method consists in starting by solving approximately the whole problem. For instance, for an evolution problem, a coarse time grid would be initially used, providing the snapshots at a reasonable cost. Then, a second, refined time grid, adapted to the problem is used to obtain the final solution, using the POD obtained from the coarse problem to speedup the computations. A schematic representation of this latter approach is provided on Figure 2.3(b). This method can be considered as a multiple timescale method. The second strategy proposed in this typescript (section 1 of chapter 3) is coupling this type of time adaptive method with an iterative construction of the reduced basis.

These *a priori* methods, though very versatile, exhibit some limitations. Indeed, it is very difficult to know *a priori* the number of snapshots required to built an efficient basis. More generally, estimating if the envisaged application will behave well with respect to a reduced basis approach is a complex task. A short discussion on this point can be found in section 7.2 of this chapter.

3.4 Application to crack propagation analysis

The reduced basis strategies were first introduced in the late 1970s for nonlinear structural analysis [NOO 80], and subsequently developed over the last twenty years, especially in circuit modeling and structural dynamics analysis [BAR 95, MAD 02]. In the fracture mechanics context, the *a posteriori* model reduction approach (i.e., with an offline / online decomposition) as already been used to compute efficiently the stress intensity factors for some academic problems [HUY 07]. This class of approach is based on the fact that there is a parametric dependence

of the solution to a set of explicitly defined variables [VER 03]. It is therefore necessary to clearly identify these parameters and their variation ranges when setting up the problem. Then, preliminary computations using classical resolution methods are conducted to build a reduced basis. In the case of a small number of parameters, (for instance in 2D, the crack length and maybe some geometrical variables), this approach is very convenient. However when this number increases, the amount of "snapshots" required to span the parameters space and then to build the reduced basis increases dramatically, and so does the computational cost of the problem. Therefore, in the framework of 3D applications, (in the context of this typescript, mode I cracks with no assumption on the crack front shape), this strategy will not be effective since numerous parameters would be necessary to describe the front shape evolutions.

In this respect, we propose to use a more general *a priori* approach together with the considered crack growth simulations, which avoid the definition of any parameters and thus does not depend explicitly on their number [GAL 10b]. This type of strategy, aiming to build reduced models without any *a priori* knowledge of the solutions of the problems has been widely studied recently, and applied to transient thermal resolutions [RYC 05a], nonlinear dynamics [KRY 01] and nonlinear material behavior [RYC 09], or in association with LATIN solvers [LAD 09], meshless techniques [RYC 06] and boundary element methods [RYC 05b]. However, only a few attempts were made to tackle problems on domains with moving boundaries such as involved in a growing crack analysis. These studies pointed out reduced basis projection and mesh morphing issues (see examples provided in [RYC 09, RYC 06]).

Let us define the considered 3D crack propagation problem as a set of linear elastic problems, one for each propagation step. They are all slightly different, due to the modification of the crack geometry during the propagation. The reduced basis approach used here holds that the displacement solution fields of this set of problems are not some arbitrary members of an infinite-dimensional solution space but rather that they belong locally to a low-dimensional manifold induced by the smoothness of the propagation [VER 03]. Indeed, the crack geometry at each propagation step is deduced from its configuration at the previous step, by means of the propagation law. Fortunately, from one step to the following, the geometric modifications are slight, provided that the time step is sufficiently short. So, one can assume that the current geometry still contains some characteristics of the previous steps. In other terms, a reduced basis approximation space $Q^\star$ for the solution subspace can be built as:

$$Q^\star = \text{Span}\{\boldsymbol{u}_{t_n}, 1 \leq n \leq r\} \tag{2.25}$$

where $\boldsymbol{u}_{t_n}$ are vectors, linear elastic displacement solutions of n successive propagation steps, and hence r is the dimension of the approximation space. For the reduced basis itself, we generate r orthonormal shape functions $\boldsymbol{\phi}_n$ from the "snapshots" vectors $\boldsymbol{u}_{t_n}$. The finite element problem involving N degrees of freedom, the dimension of the shape functions is then $N \times 1$. For that step, one can use a Gramm-Schmidt process, orthogonalizing the snapshots with respect to the inner product, or, better, extract an optimal orthonormal basis by means of a truncated Karhunen-Loève expansion. Thus the orthonormalized reduced basis approximation space writes:

$$Q = \text{Span}\{\boldsymbol{\phi}_n, 1 \leq n \leq r\} \tag{2.26}$$

If the associated basis is rich enough, the displacement solution at a later propagation step t_k can be written, within an acceptable error range, as a linear combination of these orthonormal shape functions:

$$\boldsymbol{u}_{t_k} \approx \sum_{n=1}^{r} \lambda_n \cdot \boldsymbol{\phi}_n \qquad \text{with} \quad k \geq r+1 \tag{2.27}$$

the gain in computational time is straightforward: only the $r = \dim(Q)$ parameters λ_n have to be computed, there is no need for a whole equilibrium solve. The dimension of the reduced basis Q is then of a key importance, because the gain in CPU time is directly related to it: the smaller $\dim(Q)$, the faster the computations.

We can then introduce the reduction matrix $\mathbf{\Phi}$, which defines a linear mapping from the classical, detailed finite element space onto the reduced subspace Q:

$$\mathbf{\Phi} = \begin{pmatrix} \boldsymbol{\phi}_1^1 & \boldsymbol{\phi}_2^1 & \cdots & \boldsymbol{\phi}_r^1 \\ \boldsymbol{\phi}_1^2 & \boldsymbol{\phi}_2^2 & \cdots & \boldsymbol{\phi}_r^2 \\ \vdots & \vdots & \ddots & \vdots \\ \boldsymbol{\phi}_1^N & \boldsymbol{\phi}_2^N & \cdots & \boldsymbol{\phi}_r^N \end{pmatrix} \tag{2.28}$$

The reduced displacement vector $\tilde{\boldsymbol{u}}_{t_k}$, projection of the detailed nodal displacement vector onto the reduced solution subspace is thereby defined. The matrix $\mathbf{\Phi}$ being an orthogonal matrix by definition, it writes:

$$\tilde{\boldsymbol{u}}_{t_k} = \mathbf{\Phi}^T \boldsymbol{u}_{t_k} \tag{2.29}$$

Finally, at any appropriate time step t_k, the projected problem is deduced from the detailed finite element problem of Equation (2.3):

$$\left[\mathbf{\Phi}^T \boldsymbol{K}_{t_k} \mathbf{\Phi}\right] \cdot \tilde{\boldsymbol{u}}_{t_k} = \mathbf{\Phi}^T \boldsymbol{F}_{t_k} \qquad \forall t_k \in [t_{r+1} \dots t_T] \tag{2.30}$$

Solving this reduced problem amounts to seek an approximate solution of the finite element problem in the reduced subspace. In order to check if the approximate displacement field respects the balance condition, a force residual $\boldsymbol{R}_{t_k}$ is classically defined as the difference between the internal and external generalized forces:

$$\boldsymbol{R}_{t_k} = \boldsymbol{K}_{t_k} \cdot (\mathbf{\Phi} \cdot \tilde{\boldsymbol{u}}_{t_k}) - \boldsymbol{F}_{t_k} \tag{2.31}$$

Hence an approximate solution is convenient if the following quality criterion is satisfied:

$$\| \boldsymbol{R}_{t_k} \|_2 \leq \varepsilon \cdot \| \boldsymbol{F}_{t_k} \|_2 \tag{2.32}$$

where $\| . \|_2$ is the usual Euclidean norm on $\mathbb{R}^N$ and ε a sufficiently small scalar constant. Should the opposite occur, the full finite element problem must be solved classically and the reduced basis enriched by an additional shape function.

As a matter of fact, the system of equations (2.30) is of low order, the dimension of the matrix $\left[\mathbf{\Phi}^T \boldsymbol{K}_{t_k} \mathbf{\Phi}\right]$ being $r \times r$, the vectors $\tilde{\boldsymbol{u}}_{t_k}$ and $\mathbf{\Phi}^T \boldsymbol{F}_{t_k}$ being $r \times 1$. Again, in order to provide interesting computational time reductions, the dimension r of the reduced solution subspace Q must be much smaller than N, the size of the initial problem.

In addition, to make this model reduction approach even more efficient, we take advantage of a methodology very similar to the *hyper-reduction* technique proposed by Ryckelynck [RYC 05a]. This strategy consists in reducing the number of control variables used to solve the projected problem (2.30). The hyper-reduced problem is set up only on a restricted part of the degrees of freedom $\boldsymbol{u}_{t_k}^\star$ selected as:

$$\boldsymbol{u}_{t_k}^\star = \boldsymbol{P}\, \boldsymbol{u}_{t_k} \tag{2.33}$$

where the matrix $\boldsymbol{P}$ contains zeros excepted a one on some lines, and the parameters of the linear combination (2.27) are computed only on a reduced integration domain $\Omega_{t_k}^\star$, restriction of the standard domain Ω_{t_k} to the domain containing the hyper-reduced degrees of freedom. Obviously,

the selection of relevant hyper-reduced degrees of freedom and the construction of the associated domain $\Omega^{\star}_{t_k}$ depend on each particular problem. Many details on these points can be found in [RYC 05a]. In practice, the hyper-reduction is used on every reduced basis example provided in this typescript. The general implementation of the reduced basis approach and more specifically the basis generation are detailed in section 5.

4 The mesh morphing technique

The mesh morphing techniques are widely used in computer graphics animations, reliability and parametric analysis [ALE 02]. They aim at transforming a given source shape, represented by a mesh, into a target shape. Consequently, they allow discretizing several different geometries with meshes of the same topology, keeping the number of nodes, and the connectivity the same. The morphing itself is done by modifying the nodes coordinates, while keeping the element distortion as low as possible.

Several mesh morphing methods have been introduced in the past, one of the most well-known being the spring analogy [BLO 00]. Additional effort was made to improve the robustness of this early method, leading to the torsional spring analogy approach [DEG 02]. Another popular method is the so-called Free-Form Deformation (FFD). It was originally created for computer aided geometric design, and recently applied to shape optimization in aeronautical design [SAM 04]. Although different variations exist, the most widely used deformation technique is the lattice-based FFD, which was introduced by Sederberg and Parry [SED 86]. The mesh to be morphed is embedded inside parallelepiped lattices. Any point of the mesh has local coordinates in the lattice coordinate system. After the lattices are modified according to the chosen transformation, the new positions of the mesh nodes are computed using a $\mathbb{R}^3$ to $\mathbb{R}^3$ mapping based on trivariate Bernstein polynomials. A major drawback of the FFD lies in the fact that the deformation control is over the lattices control point rather than over the deformed model. Unfortunately, this does not provide easy nor accurate control of the morphed mesh and of the resulting element quality.

For the crack growth applications, the most appropriate methods are those based on the computation of harmonic mappings. They aim at building a smooth mapping from the initial to the final configuration, optimal in the sense that it minimizes a distortion measure. In order to be general, this measure should be *intrinsic* in the differential geometry sense, that is, it must respect some basic properties such as rotation and translation invariance, continuity and additivity. Historically, trying to compute minimal surfaces with fixed boundaries (that is, a solution to the so-called problem of Plateau), Radó [RAD 30] and Douglas [DOU 31] had first the idea not to minimize the area functional directly but to minimize the Dirichlet energy associated with the surface expression. Subsequently, the discrete version of the harmonic energy was given by Pinkall and Polthier [PIN 93]. The obtained expression is a quadratic form, thus its minimization leads to solving a linear system of equations. After that, Desbrun *et al.* [DES 02] constructed free-boundary harmonic maps in the context of parametric surfaces, and proposed an application to texture mapping. They noticed that the Dirichlet energy is somehow a measure of the local area extension induced by the mapping process and that it allows to build angle-preserving mappings. In addition, it fulfills the essential requirement of being intrinsic to the surface.

Inspired by these works, we derived an application of the Dirichlet operator to deformations involving surface and volumetric meshes, that is, for mappings between 2-manifolds and 3-manifolds. The main difference between our approach and the former works is that we minimize the Dirichlet energy of the mesh perturbation, allowing not to compute a minimal surface, but rather to find a minimal deformation. It is worth pointing out that finite element meshes are

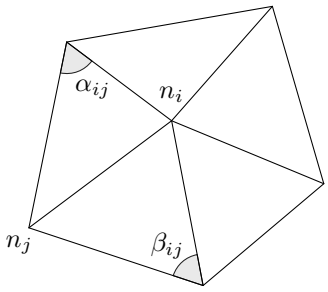

Figure 2.4 The 1-ring neighborhood of a node n_i.

volumetric and consequently, in this context, the morphing process must ensure the element quality even in the bulk of the model. In spite of that, much less work has been actually carried out in volumetric mapping compared to the surface case, including 3D surface mapping. However, a very interesting volumetric approach was introduced by Wang *et al.* [WAN 04].

A last noteworthy mesh deformation technique, stemming from the harmonic mappings, is the method based on the biharmonic operator [HEL 03]. This operator enables additional controls on the deformed mesh, since for the resolution of fourth-order partial differential equations, two conditions can be specified on each boundaries of the mesh. This allows for instance both the node positions and the normal mesh spacing to be imposed along a boundary, leading to morphed mesh of better quality. However, this goes along with a significant increase in the computational cost of the morphing resolution.

4.1 Surface case

From a continuous viewpoint, an optimal, harmonic map is the deformation function u among all the deformation functions mapping from the initial domain Ω_i to the final domain Ω_f that minimizes the Dirichlet energy [GAL 10a]:

$$E_D(u) = \frac{1}{2}\int_{\Omega_i} \| \nabla u \|^2 \tag{2.34}$$

Notice that if the considered domains are surfaces, the gradient operator and the norm must be interpreted in the Riemannian geometry sense.

In the following, we will consider the surface case and denote by $\boldsymbol{U}$ the global perturbation vector which contains the discretized version of the deformation function u at each node. In addition, the vector $\boldsymbol{u}_i$ will represent the displacement associated with a particular node n_i during the transformation. The Dirichlet energy of the transformation $\boldsymbol{U}$ on the discretized domain is the following quadratic form:

$$E_D(\boldsymbol{U}) = \frac{1}{4}\sum_{(n_i,n_j)\in\mathcal{E}} \Big(\cot\alpha_{ij} + \cot\beta_{ij}\Big)\Big(\boldsymbol{u}_i - \boldsymbol{u}_j\Big)^2 \tag{2.35}$$

where $\mathcal{E}$ is the set of edges of the mesh, and the angles α_{ij} and β_{ij} are the opposite left angles to the current edge (n_i, n_j) such as described on Figure 2.4.

The optimal mapping is obtained when the Dirichlet energy is minimum. This operator being quadratic, minimizing $E_D(\boldsymbol{U})$ has a unique solution:

$$\nabla E_D(\boldsymbol{U}) = 0 \tag{2.36}$$

which corresponds to a set of conditions explicitly given by differentiating the Equation (2.35):

$$\frac{\partial E_D}{\partial \boldsymbol{u}_i}(\boldsymbol{U}) = \frac{1}{2} \sum_{j \in \mathcal{N}(i)} \Big(\cot \alpha_{ij} + \cot \beta_{ij}\Big)\Big(\boldsymbol{u}_i - \boldsymbol{u}_j\Big) = 0 \tag{2.37}$$

where $\mathcal{N}(i)$ is the set of edges connected to the node n_i and $\boldsymbol{u}_j$ the perturbation at the node u_j. Finally, adding some Lagrange multipliers to take into account potential additional constraints, the matrix formulations of the Dirichlet energy writes:

$$E_D(\boldsymbol{U}, \boldsymbol{\lambda}) = \frac{1}{2} \boldsymbol{U}^T \boldsymbol{E}\, \boldsymbol{U} + \boldsymbol{\lambda}^T \left(\boldsymbol{L}\boldsymbol{U} - \boldsymbol{U}_0\right) \tag{2.38}$$

Leading to solve the following sparse linear system:

$$\begin{bmatrix} \boldsymbol{E} & \boldsymbol{L}^T \\ \boldsymbol{L} & \boldsymbol{0} \end{bmatrix} \begin{bmatrix} \boldsymbol{U} \\ \boldsymbol{\lambda} \end{bmatrix} = \begin{bmatrix} \boldsymbol{0} \\ \boldsymbol{U}_0 \end{bmatrix} \tag{2.39}$$

where $\boldsymbol{E}$ is a symmetric sparse matrix whose coefficients represent the quadratic form (2.35). The vector of unknowns $\boldsymbol{U}$ contains the mesh perturbations to solve for and $\boldsymbol{U}_0$ is the vector of the fixed input perturbations. In other terms it constitutes the minimal boundary conditions of the problem. The vector $\boldsymbol{\lambda}$ is used to take into account the Lagrange multipliers, thus $\boldsymbol{L}$ and $\boldsymbol{L}^T$ are the associated coupling terms.

As a remark, notice that in the expression (2.35), the terms implying the perturbations at one given node n_i only involve the perturbations defined at the nodes n_j of its 1-ring neighborhood (see Figure 2.4). For the numerical resolution of the harmonic mapping, it is an important property since it is the reason for the sparsity of the linear system (2.39).

Remark 21 *The discretized Dirichlet energy is here expressed for triangles and tetrahedra. In practice, the mesh can be constituted of the following types of finite elements: triangles, quadrangles, tetrahedra, hexahedra, pyramids and wedges. In particular, meshing a complex geometry containing a crack can involves* all *those element types. Hence strategies must then be envisaged to subdivide the elements into triangles or tetrahedra in order to compute morphing solutions on such complex meshes.*

Remark 22 *In the case of quadratic elements, a simplification consists in computing the morphing solution on a linearized mesh and then put back the midside nodes at the middle of all the elements edges. The main drawback is that it compels to use straight sided elements during the meshing, increasing the necessary number of element to describe the geometry, meanwhile, it really decreases the complexity and the computational cost of the morphing resolution.*

4.2 Volume case

The formal problem to solve is in fact finding the three components u_i of the smooth vectorial deformation function

$$\boldsymbol{u} = [u_1\ u_2\ u_3]^T \tag{2.40}$$

such that:

$$\begin{cases} \boldsymbol{\nabla}^2 \boldsymbol{u} = \boldsymbol{0} & \text{in } \Omega_i \\ \boldsymbol{u} = \bar{\boldsymbol{u}} & \text{on } \partial\Omega_i \end{cases} \tag{2.41}$$

where the vector Laplacian is defined, in Cartesian coordinates as the Laplacian of each of the components, and where $\bar{\boldsymbol{u}}$ represents the sufficient boundary conditions, some prescribed displacements on the boundaries of the domain. Similarly to the surface case, this problem can be

solved indirectly by minimizing the Dirichlet energy (2.34) of the transformation. However, from a mathematical viewpoint the volume case is somehow easier than the surface case because the domain of study being the classical Euclidean space, the norm and gradient operators do not have to be redefined.

Besides the interesting geometrical properties of the morphing function solution of the diffusion problem (2.41), an interesting feature is that the three components u_i of the deformation function $\boldsymbol{u}$ are independent and thus can be considered separately. This is one of the main differences between this approach and the techniques based on the equation of the linear elasticity, that have been used for years [STE 03]. Indeed, for these strategies, the deformation problems are coupled, leading to solve one large problem. In the present case, keeping similar notations than in the surface case, the Dirichlet energy of the component u_i summed on each element of the volume mesh writes:

$$E_D(u_i) = \frac{1}{2} \sum_{k=1}^{n_e} \int_{\Omega_{e_k}} \| \nabla u_i(\boldsymbol{x}) \|^2 \, \mathrm{d}\boldsymbol{x} \tag{2.42}$$

where the scalar n_e is the total number of elements and the integration domain Ω_{e_k} the current element. The vector $\boldsymbol{x}$ represents the current point in the integration domain, and its coordinates are expressed in the global Cartesian coordinate system. Hence in the volume case, three different *uncoupled* minimization problems have to be solved to find the morphing function, one problem for each direction of the space.

In order to apply this strategy to a volume mesh, the objective is then to express the *discrete* version of the gradient of the morphing fonction ∇u_i. In other terms, express the gradient of the morphing function in terms of nodal values, in the isoparametric element of reference. To this end, let us use some classical finite element devices. Let τ be the bijective mapping from the coordinates $\boldsymbol{\xi}$ in the element of reference to the global Cartesian coordinates $\boldsymbol{x}$ in the real element such that:

$$\begin{array}{rccc} \tau: & \mathbb{R}^3 & \longrightarrow & \mathbb{R}^3 \\ & \boldsymbol{\xi} & \longmapsto & \boldsymbol{x} \end{array} \tag{2.43}$$

Hence the inverse $\boldsymbol{J}_\tau^{-1}$ of the Jacobian matrix of this mapping allows $\nabla \tilde{u}_i$, the deformation function expressed at points written in the local coordinate system of the element to be introduced:

$$\nabla^T u_i(\boldsymbol{x}) = \nabla^T \tilde{u}_i(\boldsymbol{\xi}) \cdot \boldsymbol{J}_\tau^{-1} \tag{2.44}$$

Then, let $\boldsymbol{B}$ be the matrix containing the partial derivatives of the element shape functions and $\boldsymbol{U}_i$ the vector containing the nodal values of the perturbation along the direction $\boldsymbol{e}_i$ for the nodes of the current element. Hence $\boldsymbol{U}_i$ is a small vector dimensioned at the number of nodes of the considered element. The gradient of the deformation function at any point $\boldsymbol{\xi}$ of the reference element can be expressed as:

$$\nabla \tilde{u}_i(\boldsymbol{\xi}) = \boldsymbol{B} \cdot \boldsymbol{U}_i \tag{2.45}$$

From that equation comes the expression of the gradient of the morphing function, in terms of nodal values:

$$\nabla^T u_i(\tau(\boldsymbol{\xi})) = \boldsymbol{U}_i^T \cdot \boldsymbol{B}^T \cdot \boldsymbol{J}_\tau^{-1} \tag{2.46}$$

It stems:

$$\begin{aligned} \| \nabla u_i(\boldsymbol{x}) \|^2 &= \nabla^T u_i(\tau(\boldsymbol{\xi})) \cdot \nabla u_i(\tau(\boldsymbol{\xi})) \\ &= \boldsymbol{U}_i^T \cdot \boldsymbol{B}^T \cdot \boldsymbol{J}_\tau^{-1} \cdot \boldsymbol{J}_\tau^{-1^T} \cdot \boldsymbol{B} \cdot \boldsymbol{U}_i \\ &= \boldsymbol{U}_i^T \cdot \boldsymbol{B}^T \cdot \boldsymbol{P} \cdot \boldsymbol{B} \cdot \boldsymbol{U}_i \end{aligned} \tag{2.47}$$

where the 3×3, symmetric matrix $\boldsymbol{P} = \boldsymbol{J}_\tau^{-1} \cdot \boldsymbol{J}_\tau^{-1^T}$ is only a notation introduced to simplify the equations. Starting from Equation (2.42) and using a classical change of variables to the local coordinate system of the element of reference:

$$E_D(u_i) = \frac{1}{2} \sum_{k=1}^{n_e} \int_{\tau^{-1}\left(\Omega_{e_k}\right)} \| \nabla u_i(\tau(\boldsymbol{\xi})) \|^2 \cdot \det\left(\boldsymbol{J}_\tau^{-1}\right) \cdot \mathrm{d}\boldsymbol{\xi} \tag{2.48}$$

And finally, the discrete version of the Dirichlet energy (2.42) comes:

$$\begin{aligned} E_D(u_i) &= \frac{1}{2} \sum_{k=1}^{n_e} \boldsymbol{U}_i^T \cdot \left[\int_{\tau^{-1}\left(\Omega_{e_k}\right)} \boldsymbol{B}^T \cdot \boldsymbol{P} \cdot \boldsymbol{B} \cdot \det\left(\boldsymbol{J}_\tau^{-1}\right) \cdot \mathrm{d}\boldsymbol{\xi} \right] \cdot \boldsymbol{U}_i \\ &= \frac{1}{2} \sum_{k=1}^{n_e} \boldsymbol{U}_i^T \cdot \boldsymbol{E} \cdot \boldsymbol{U}_i \end{aligned} \tag{2.49}$$

where $\boldsymbol{E}$ is a square matrix dimensioned at the number of nodes of the current element. In practice, the integration over the elements is performed using a Gauss quadrature. Notice that all the matrices and vectors involved in Equation (2.49) depend upon the considered element, and thus are computed for each of them. Including the sum on the elements inside the matrices, the previous equation can be further condensed in:

$$E_D(u_i) = \frac{1}{2} \boldsymbol{U}_i^T \cdot \boldsymbol{E} \cdot \boldsymbol{U}_i \tag{2.50}$$

where the vector $\boldsymbol{U}_i$ and the square matrix $\boldsymbol{E}$ are now dimensioned to the total number of nodes in the mesh. To obtain the optimal deformation function along the direction $\boldsymbol{e}_i$ the Dirichlet energy must be minimized. This operator being quadratic, the unique solution of that minimization is:

$$\nabla E_D(u_i) = 0 \tag{2.51}$$

which finally amounts to solve the following linear system:

$$\boldsymbol{E} \cdot \boldsymbol{U}_i = \boldsymbol{C}_i \tag{2.52}$$

where the vector $\boldsymbol{C}_i$ comes from the prescribed displacements along the direction $\boldsymbol{e}_i$, boundary conditions of the problem. Similarly, the lines and rows corresponding to those prescribed displacements are removed from the matrix $\boldsymbol{E}$ and from the vector $\boldsymbol{U}_i$.

4.3 Mesh morphing applied to fracture mechanics

Once the mesh morphing methodology is formally exposed, let us introduce some basic ideas related to its application to fracture mechanics problems. We define the *skin mesh* of our 3D, volumetric mesh, as the collection of element facets corresponding to the external boundaries of the model. This collection also defines the initial *faceted geometry* of the cracked model. In addition, this cracked geometry can be viewed as the superposition of an uncracked, healthy component to which the crack is added. As a matter of fact, during its growth the crack does not alter the healthy part of the geometry. In other terms, all along the propagation, the external boundaries of the model are not modified. Consequently, during the morphing process, the nodes may not be allowed to move freely, but rather constrained to slide on their topological support in order to preserve the model geometry. For instance, a node belonging to a given face or edge in the initial geometry must stay on this same entity for all the subsequent morphed configurations.

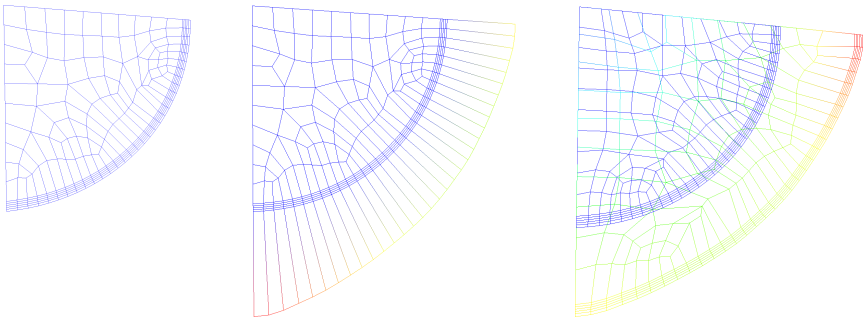

(a) (b) (c)

Figure 2.5 Example of skin mesh morphing. Initial crack plane mesh (a), initialization of the mesh perturbation corresponding to a crack growth increment (b) and resulting, smoothed crack plane mesh superposed with the initial mesh (c).

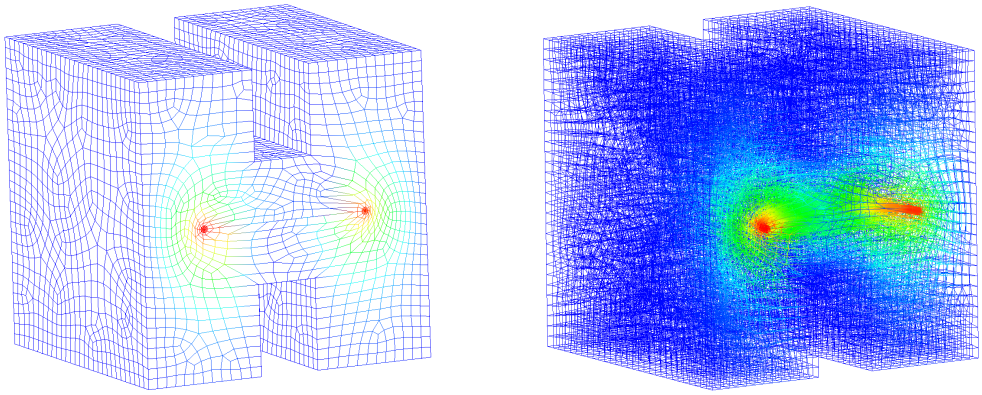

(a) (b)

Figure 2.6 Morphing of a 3D model: smoothed skin mesh (a) and volumetric mesh (b).

The morphing process is then tightly linked not only to the mesh but also to some geometrical considerations.

Here, the morphing of the 3D model is performed in two distinct steps: first handle the skin mesh, then take care of the volumetric mesh. In the first step, the target geometry is built, constituted by the faceted geometry modified conforming to the crack growth increment. The shape modifications are thereby only coming from the crack leading edge. These are the minimal boundary conditions to initialize the morphing of the skin mesh. The minimization of the element distortion is performed through the resolution of a first linear system similar to the one of Equation (2.39). As previously said, this constitutes in fact a conformal mapping, and it ensures the smoothness of the mesh deformation by minimizing the local area extension during the transformation. The additional boundary conditions forcing the nodes to stay and slide on their topological support are defined using Lagrange multipliers. An example of skin mesh morphing is depicted on Figure 2.5. The color chart represents the nodal displacements during the morphing

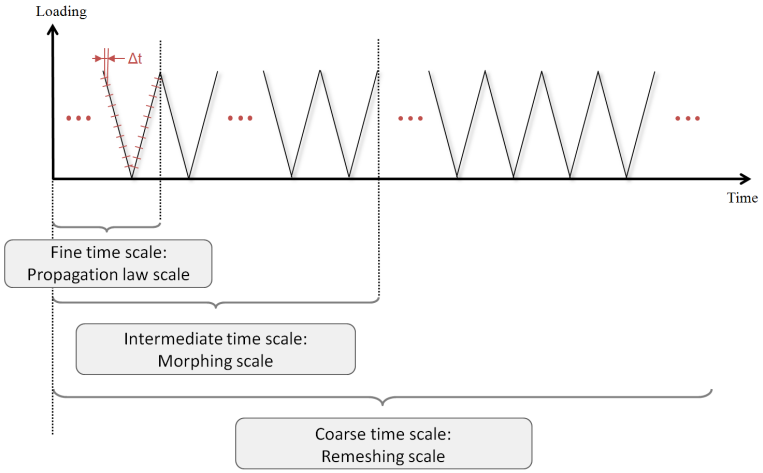

Figure 2.7 The different time scales of the strategy.

process. In a second step, once the skin mesh is morphed, the volumetric mesh can be smoothed. For this purpose, another linear system of equation is solved, associated with a tridimensional version of the Dirichlet operator (several details are provided in [WAN 04]). The configuration of the skin mesh around the volumetric mesh constitutes the boundary conditions for this resolution. On Figure 2.6, an example of the full process is shown. The smoothed skin mesh of a 3D model is used to initialize its volumetric morphing.

The clear advantages is the robustness of the method. In comparison to remeshing strategies, which involve several mesh sizing and controls, there is no user defined parameter in the mesh morphing context. Moreover, using meshes with the same number of nodes and providing mappings of the nodes from one configuration to another are some of the key features for the efficiency of the *a priori* model reduction approach described in the previous section. Among others, a constant number of nodes means a constant number of degrees of freedom, making straightforward the reduced basis matrix operations (for instance the building of the set of Equation (2.26)). In addition, the fastness of the successive morphing solves used for 3D crack growth simulations can be greatly improved. Indeed, since the morphing process is based on the resolution of partial differential equations, a suitable model reduction approach, similar to the one used for the structural problems, can be set up. A recent work explores this perspective, in the context of fluid-structure interactions [BOG 10]. This constitutes one of the future enhancements of the method.

5 Coupling the methods: general strategy

From a global point of view, the method is constituted by four main components. The first one is the *a posteriori* reduced model that handles the plastic part of the behavior of the cracked structure. At any given time step, the CTCP model computes efficiently the plastic state of the crack and its propagation distance from a given stress intensity factor (see section 4). As a consequence, only linear elastic computations have to be performed by the finite element method during the crack growth analysis. The second component of the strategy is the *a priori* model reduction associated with those successive linear elastic finite element problems. Then the third component is the mesh morphing technique that handles the geometrical updates of the model according to the crack front modifications during the propagation. Mesh morphing is a robust and

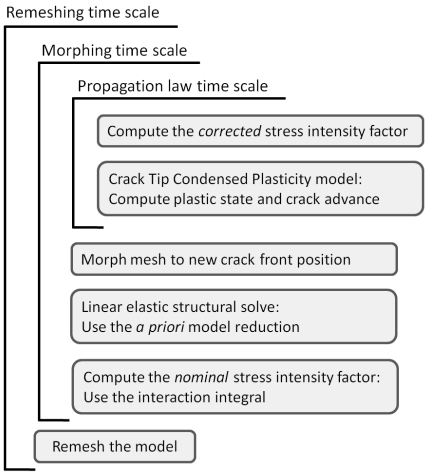

Figure 2.8 General pseudo-algorithm of the strategy.

efficient method, however during the mesh transformation process, modifying the nodes coordinates inevitably induces some distortion of the elements. Indeed, the mesh quality decreases for the large propagation ranges. This is why, at some points, the remeshing of the model cannot be avoided. These remeshing steps constitute the fourth and last component of the proposed method.

In the implementation of the global strategy, each of those components is associated with a certain time scale, as depicted on Figure 2.7. The atomic time measure is the *time step*. The spectrum loading for a given analysis is then described by a succession of time steps. Each pseudo-cycle of the loading can be sampled by, for instance, 10 time steps. Here takes place the fine time scale of the strategy, the *propagation law scale*. The CTCP model, which constitutes the propagation law of the strategy, is used on that scale. The second time scale is called the *morphing scale*. The *a priori* model reduction used to decrease the computational cost of the finite element problems, as well as the mesh morphing strategy are associated with that intermediate time scale. Finally, the remeshing steps that occurs occasionally are associated with the coarse time scale, naturally called the *remeshing scale*.

Remark 23 *When the finite element model is remeshed, the crack front is geometrically the same than just before the remeshing step, but the number and the positions of nodes that describe it may have changed. In this respect, the internal variables of the CTCP model corresponding to the new nodes must be interpolated from their values on the old nodes. In practice, this unidimensional interpolation does not introduce much error on the variable values.*

Once the time system outlined, the global algorithm can be introduced (see Figure 2.8 for an illustration). Indeed, each of the three time scales corresponds to a different time loop of the algorithm that allows coupling the components of the method. After an initialization phase, a nominal mode I stress intensity factor (SIF) is computed. For that step, a linear elastic finite element problem corresponding to the current crack configuration is set up. It is solved, submitted to a nominal load, and the corresponding nominal SIF is extracted by means of the interaction integral method presented in section 1.6. Here, at the propagation law time scale, a loop on the time steps is conducted. The model being linear, the nominal SIF is multiplied by a suitable constant to describe the spectrum loading prescribed to the structure. The obtained corrected SIF is given as an input to the CTCP model (in terms of φ_2, refer to section 4.4.2 of chapter 2), which incrementally com-

putes the plastic state at crack tip and deduces the crack advance. It is emphasized that during this process, there is neither updating nor solving of the finite element model. In fact, it is considered that for a short crack propagation around the current crack position, the nominal SIF variation is too small to be captured by an update of the finite element model. Since in practice, one time step corresponds to a crack advance of only a few micrometers, the computation of the crack growth corresponding to several time steps can be conducted with a constant nominal SIF. This explains the separation of the different time scales, and the link between time and spatial scales through the propagation rates.

At some point, when the crack has grown enough, the current nominal SIF must be updated. This decision can be based on geometrical considerations, for instance a criterion on the propagation distance regarding the crack tip element size, or even on more numerical aspects like building a local derivative of the SIF value with respect to the propagation distance. In this respect, the mesh is morphed in order to be consistent with the newly computed crack front position. The updated finite element model is solved and a modified nominal SIF is extracted. These are basically the operations handled at the morphing time scale. The reader's attention is put on the fact that this decision of updating the finite element model is quite empirical and thus does not provide any guarantee on the final result of the crack propagation simulation. Indeed, estimating if the finite element model has been updated often enough is a complicated task. In this respect, an adaptive strategy overcoming that difficulty is presented in section 1 of chapter 3.

In addition to that, the *a priori* model reduction logic is applied to the resolution of the successive finite element problems. So, at the early stage of the propagation, the solutions of the finite element problems are computed in the usual way by either a sparse or a preconditioned conjugate gradient solver, and the mode I stress intensity factors are extracted from the obtained solution fields. At the same time, the corresponding displacement solution vectors are stored and orthogonalized to build the reduced basis shape functions, following the methodology described in section 3. Once this reduced basis is rich enough to span the solution subspace, the displacement solution vectors are no more computed exactly by means of a classic solver, but rather approximated as linear combinations of the reduced basis shape functions, using the projection proposed in Equation (2.27). The stress intensity factors are then computed using those approximate solution vectors. As a consequence, if the successive displacement solution vectors are contained in a low-dimensional subspace, and hence that the reduced basis happens to be of a low dimension, the computational complexity of each time step decreases drastically.

As mentioned above, the mesh morphing technique is a key component of the method, however it induces distortion of the finite element mesh. In addition, the applicability and the efficiency of the model reduction technique highly depend on the quality of the computed mesh. Thereby, the validity of the finite element computations must be ensured at each step. For that purpose, in conjunction with mesh metrics, the indicator on the domain invariance of the interaction integral proposed in section 2.2 of chapter 1 is extensively used.

Furthermore, it is worth highlighting that the proposed methodology, although it is presented here on examples of crack loaded in mode I only, can be extended to mixed mode solicitations. Under such solicitations, a growing crack bifurcates and does not stay in its initial plane. In this case, the main complexity would come from the morphing of the finite element mesh onto complicated, kinked geometries. If the crack does not bifurcate too often, such as under mixed mode, yet proportional loading for instance, this morphing difficulty can be overcome. After that, there is no specific difficulty in applying the model reduction method to this type of computations. All the same, the efficiency of such reduced basis approaches might probably be lower than in the mode I case, because in those more complex cases, the approximate solution subspace may be of a higher dimension. Anyway, the additional cost brought by the use of the proposed model reduction technique on problems for which it is not efficient is marginal. In this respect, attempts

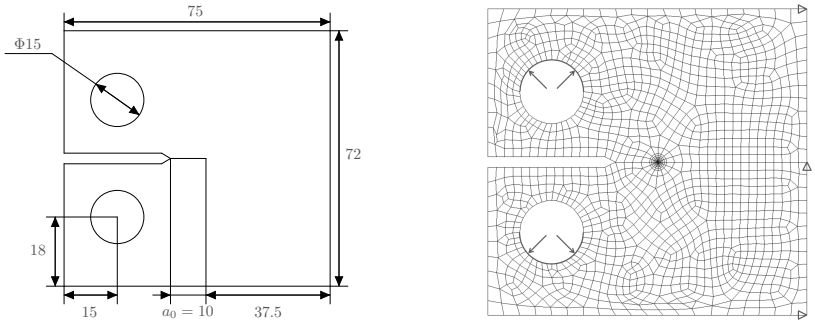

Figure 2.9 Normalized CT sample geometry in millimeters (a) and the associated finite element model (mesh and boundary conditions) (b).

of applying it on any type of crack propagation computation can always been envisaged.

The complete methodology, mainly constituted by the equivalent CTCP model, the mesh morphing technique and the reduced basis approach, has been fully implemented in the commercial finite element software ANSYS. Results on the accuracy of the *a priori* model reduction strategy, as well as estimations of the dimensions of relevant reduced solution subspaces and several details on the management of the reduced basis are presented in the next section, for both 2D and 3D test cases.

6 Examples

6.1 Stress intensity factors computation using the reduced basis: 2D CT sample

The main objective of this example is to demonstrate the usability and the accuracy of the reduced basis methods applied to fracture mechanics. The reader's attention is put on the fact that the methodology used here is not in any way the one described in section 3. However, the relevance of the reduced basis techniques in crack growth analysis is emphasized in this example by showing that the subspace containing the solutions of such an evolution problem is of relatively low dimension [GAL 09b].

The considered problem is a crack growing in a normalized Compact Tension (CT) test specimen. The dimensions of the sample presented on Figure 2.9(a) are extracted from the ASTM E 399 standard [AST 09]. The thickness B of the specimen is of 30 mm. The sample is modeled by a 2D finite element analysis under plane strain assumption. The model is discretized with quadratic quadrangles and triangles, leading to solve for 9132 degrees of freedom. In order to prevent rigid body motion, 3 degrees of freedom are fixed (see Figure 2.9(b)). The sample is loaded by traction forces F of 450 N in both pin holes. The corresponding pressure load P to be prescribed to the finite element model is assumed to be uniform and is computed such as:

$$P = \frac{F}{\Phi \cdot B} \tag{2.53}$$

where Φ is the diameter of the pin holes. The chosen material behavior is linear elastic, with a Poisson's ratio of 0.3 and a Young's modulus of 210 GPa.

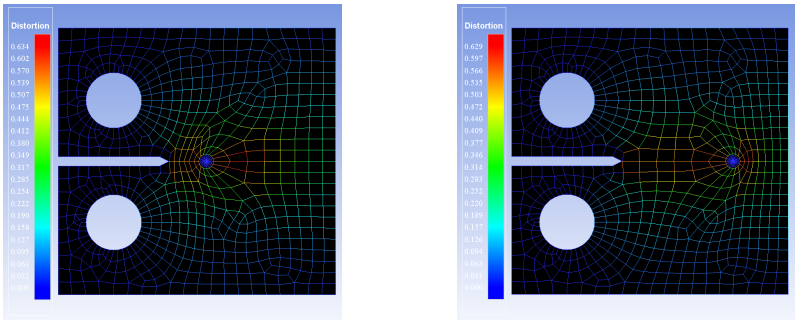

(a) (b)

Figure 2.10 Element distortion metric of the shortest (a) and longest (b) morphed mesh of the compact tension specimen.

The simulation consists in building a reduced basis of the crack growing from 10 mm to 30 mm. All along that propagation, the geometrical updates are handled by a mesh morphing technique. The evolving geometry of a 2D crack propagating in mode I is easily predictable since it depends in fact on only one parameter: the crack length. For this reason, the mesh morphing of this test-case is computed in advance, in a preliminary analysis. It is highlighted that pre-computation of the morphing solution is possible only for this type of very simple test-cases. Indeed, this procedure is applied to this preliminary example for demonstration purpose only, and a more general one will be used for the tridimensional examples (see sections 6.2 and 6.3). For that purpose, the CT sample is first meshed with a crack length of 20 mm and then this initial mesh is morphed to be able to span every crack length between 10 mm and 30 mm. During those mesh modifications, special attention is paid to minimize the distortion of the elements surrounding the crack tip, in order to ensure the accuracy of the finite element resolutions. To illustrate that point, a measure of the distortion between the initial, non morphed mesh and the morphed mesh for the shortest and longest crack lengths is presented on Figure 2.10. Once the morphing is ready, a few displacement solution vectors are computed for different crack lengths, by a standard sparse solver. Those vectors are orthogonalized and stored to build the reduced basis shape functions. In this example, 4 displacement vectors are used, constituting a reduced basis of dimension 4. They correspond to the following crack lengths: 10 mm, 16.66 mm, 23.33 mm and 30 mm. After that, the displacement solution vectors are no more computed exactly by means of a classic solver, but rather approximated as linear combinations of the reduced basis shape functions, using the projection proposed in Equation (2.27). As a consequence, the computational complexity of each resolution decreases drastically.

During the propagation, the interaction energy integral method presented in section 1.6 is used to compute the mode I stress intensity factor from the approximate solution fields. An analytic formula, function of the geometry and of the loading, is also available to compute the mode I stress intensity factor K_1 of a CT sample [BUI 78]:

$$K_1 = \frac{F}{B\sqrt{W}} \frac{2+a/W}{\sqrt{1-a/W}} \left[0.886 + 4.64\left(\frac{a}{W}\right) - 13.32\left(\frac{a}{W}\right)^2 + 14.72\left(\frac{a}{W}\right)^3 - 5.6\left(\frac{a}{W}\right)^4\right] \tag{2.54}$$

where a is the crack length and W the specimen width. In order to assess the accuracy of the pro-

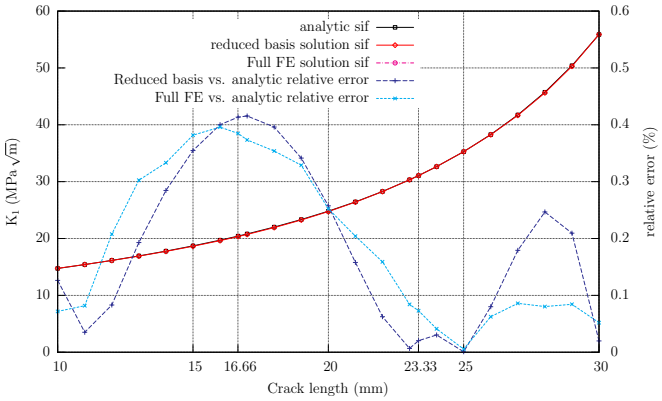

Figure 2.11 Comparison of the mode I stress intensity factor computed for various crack lengths, either numerically or analytically, and associated relative error.

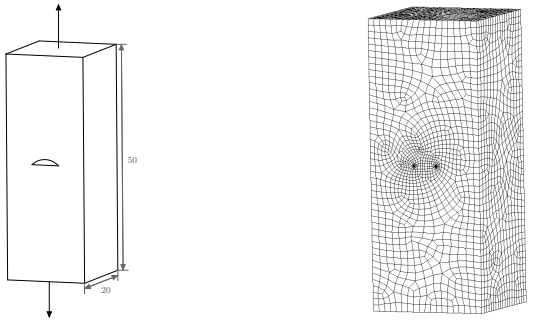

(a) (b)

Figure 2.12 Geometry of the cracked tension sample in millimeters (a) and the associated finite element mesh (b).

posed reduced basis approach, a comparison between the mode I stress intensity factor computed from the approximate solution vectors and the analytical solutions from the ASTM standard is shown on Figure 2.11. The stress intensity factor obtained from the complete, classical finite element resolutions is proposed as well. Since all these results are very similar, the associated curves are mostly superimposed. Compared to the analytical solution, the numerical results, computed either with the reduced basis approach or with full finite element resolutions yield relative errors of the same order.

All in all, the reduced basis of dimension 4 allowed keeping the relative error on the stress intensity factors under 0.42%. To conclude, the *a priori* model reduction allowed performing only 4 full finite element resolutions for that crack propagation analysis, hence providing substantial computational complexity reduction.

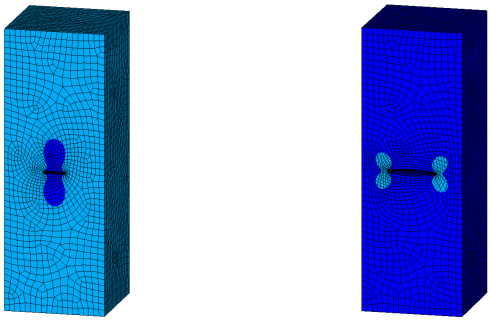

(a) (b)

Figure 2.13 Von Mises stress solution of the surface crack in a tension sample for the initial (a) and final (b) propagation step.

6.2 Surface crack in a 3D tension sample

On this first tridimensional problem, the global strategy of coupling an *a posteriori* reduced order model of the localized non-linear effects at the crack tip and an *a priori* reduced basis approach for the evolving linear displacement fields in the structure is tested. For this purpose, a surface crack is introduced in a beam of square cross-section under tension. The beam height is of 50 mm and its sides lengths and widths are of 20 mm. A tension pressure P of 100 MPa is applied on the top and bottom faces of the sample. The initial crack is semicircular of diameter 4 mm, and it is solicited in mode I (see Figure 2.12 for details). The sample is discretized with a quadratic mesh, constituted approximately of 2/3 of hexahedra and 1/3 of tetrahedra, pyramids and wedges. In particular, quadratic wedges and hexahedra are used around the crack front in a specific radial mesh pattern and a layer of pyramids make the transition between hexahedral and tetrahedral elements. The first contour of element around the front has a characteristic size of 65 µm. To prevent rigid body motion, 6 appropriate degrees of freedom are fixed in the plane of the crack, and the whole model is constituted of 239406 degrees of freedom. At the finite element level, the material behavior is linear elastic, with a Poisson's ratio of 0.3 and a Young's modulus of 200 GPa. From the finite element resolutions, a nominal mode I stress intensity factor is computed. Since the model is linear, this nominal stress intensity factor is multiplied by a suitable constant to simulate a cyclic loading of the sample, oscillating between 0 and 680 MPa.

The main objective here is to estimate the size of the reduced basis for a 3D test-case. The crack propagates according to the crack tip condensed plasticity model laws, providing realistic geometric configurations of the front. Indeed, the crack front does not stay circular along the propagation, but rather tends to an elliptical shape. Indeed, solicited in pure mode I, all along the propagation, the crack will grow in its initial plane. However, the crack front is absolutely free to deform, and hence will not remain circular but rather tend to an elliptical shape. The displacement fields and the stress intensity factors are updated at each time that the maximum propagation along the front reaches 50 µm. The geometry itself is updated using mesh morphing techniques, to avoid remeshing. The mesh morphing allowed to increase the characteristic crack length to up to 2.6 times its initial value. The initial and final configurations of the tension sample are presented on Figure 2.13, and close-ups of the corresponding morphed mesh around the crack front are shown on Figure 2.14, on which the color chart refers to the usual von Mises equivalent stress. The *a priori* model reduction is not used as such in that example. Indeed, at each finite

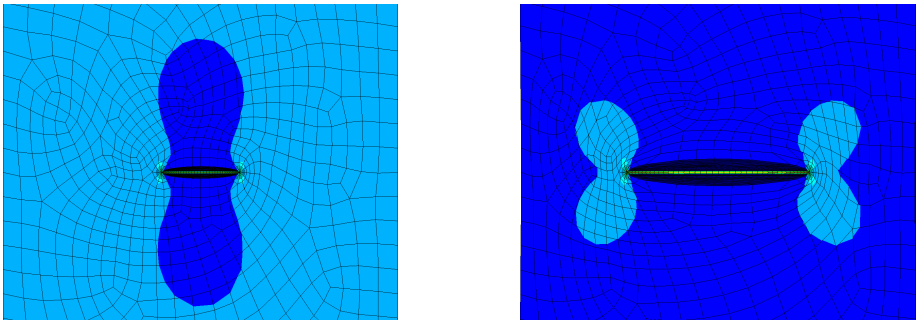

(a) (b)

Figure 2.14 Close-ups of the initial (a) and final (b) morphed mesh around the crack front of the tension sample.

element update, the problem is solved by a preconditioned conjugate gradient solver.

All along the crack propagation, which represents 26435 loading cycles and 528700 time steps, 60 updates of the finite element model are conducted. To estimate the dimension of the subspace spanned by these solutions, the singular value decomposition of the matrix constituted by this set of vector is computed. This amounts to estimating the dimension of the reduced solution subspace, and hence of the reduced basis associated with that test-case. The singular values of that decomposition are normalized by the sum of the 60 obtained values, and plotted on Figure 2.15. As a matter of fact, they are decreasing fast since the sixth normalized value is less than 10^{-5}. Furthermore, considering the sum of the five first normalized singular values, it comes that a basis constituted by the five first singular vector will contain 99.99929% of the information contained in the 60 singular vectors.

It is emphasized that building a basis of the reduced solution subspace by singular value decomposition of the set of displacement vectors corresponding to the whole crack propagation range constitutes an *a posteriori* model reduction. Moreover, an efficient approach should take into account the notion of temporal history and sequentiality introduced by the propagation phenomenon. In this respect, matching the methodology described in section 3, an *a priori* reduced basis is set up.

To demonstrate that the main characteristics of the solutions fields can be captured from the early stage of the propagation, the five first computed solution displacement vectors $(\boldsymbol{u}_{t_n})_{n=1,\dots,5}$ are incrementally normalized and orthogonalized by a Gram-Schmidt procedure. This allows building an orthonormal basis of dimension 5 of the subspace spanned by these vectors. For illustration purpose, the process was extended to the whole set of 60 vectors and the Euclidean norm of the obtained shape functions $\boldsymbol{\zeta}_i$ are plotted on Figure 2.15. The rapid decrease of these norms can be noticed. In a second step, each solution vector is projected on the reduced basis of dimension 5. The obtained projection constitutes an approximate displacement vector $\tilde{\boldsymbol{u}}_{t_k}$ such as:

$$\tilde{\boldsymbol{u}}_{t_k} = \sum_{i=1}^{5} \lambda_i \cdot \boldsymbol{\zeta}_i \tag{2.55}$$

Finally, a projection error η_k is computed, as the relative error between the exact displacement

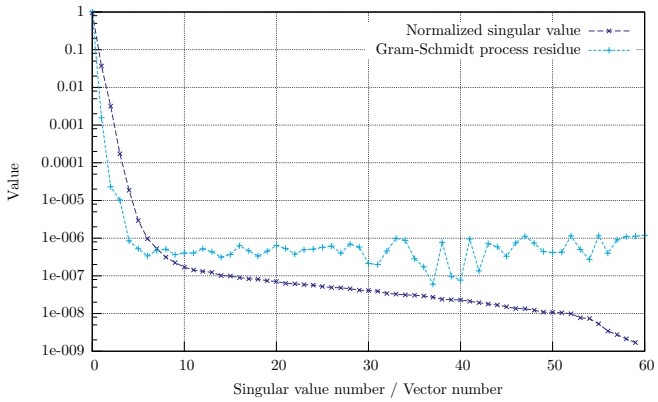

Figure 2.15 Normalized singular values of the set of 60 successive displacement solution vectors and residual of the Gram-Schmidt process during their orthogonalization.

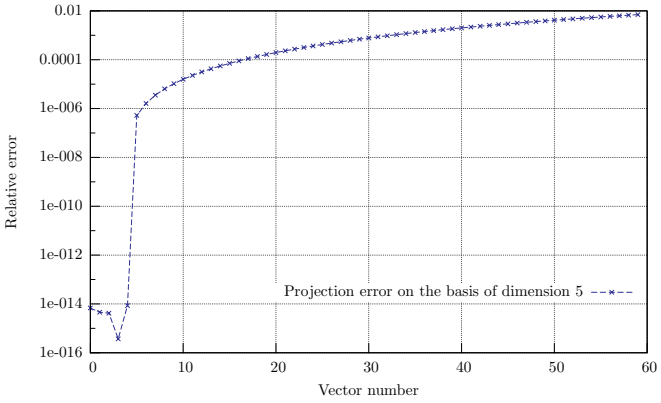

Figure 2.16 Global relative error between the exact displacement solution and its approximate counterpart in the basis built on the 5 first solution vectors.

solution and its approximate counterpart:

$$\eta_k = \frac{\| \boldsymbol{u}_{t_k} - \tilde{\boldsymbol{u}}_{t_k} \|_2}{\| \boldsymbol{u}_{t_k} \|_2} \tag{2.56}$$

the chosen norm being the Euclidean norm. The projection error for the 60 solution vectors are plotted on Figure 2.16. Obviously, the errors corresponding to the five first vectors are very small, less than 10^{-14} because the vectors are contained in the considered reduced solution subspace. Then, the error climbs up smoothly from 5.23×10^{-7} for the sixth vector to 7.03×10^{-3} for the sixtieth and last vector. Thereby, the displacement solution, all along the propagation range, can be represented with less than 0.7% of error by a basis built on the 5 first solution vectors. In this respect, we can reasonably expect the relevant reduced basis for this particular test case to be of a very low dimension.

It is worth highlighting that one of the essential conditions to make the *a priori* model reduction efficient, and in practice build reduced basis of low dimensions, is the use of mesh morphing techniques for the geometrical updates. Indeed, it allows to take advantage of the very power-

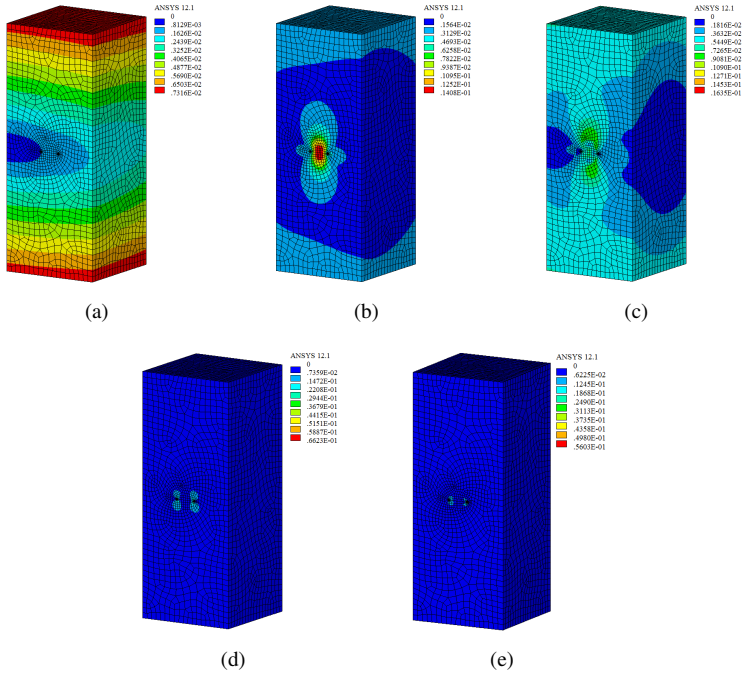

Figure 2.17 The five first orthogonalized solution displacement vectors of the tension sample, projected on the initial mesh.

ful "self-similarity" property of the cracks in linear elastic media. Since the displacement field around the leading edge of a crack always takes the same well known singular form, it can always be projected onto the surrounding of another crack front, of the same topology but with different length and shape. A second important condition for the efficiency of the reduced basis approach is a property which can be called *spatial scales separability*. Indeed, at least two different spatial scales coexist in a cracked model: the global scale of the structure and the local scale of the crack. For a considered application, in order to behave well with respect to the model reduction approach, those scales need to be *separable*. In other words, the modifications of the global displacement field induced by the propagating crack must remain localized around the front, so that the global behavior of the structure can be captured by a very few shape functions. It is typically the behavior of the tension sample considered here. To illustrate this, the five first shape functions built with this test-case are shown on Figure 2.17. Remember that the displacement fields are computed on different meshes, according to the crack propagation. Here, the shape functions are presented projected on the initial mesh although only the first one was computed on this mesh. Clearly, the three first shape functions capture the global form of the displacement fields, whereas the subsequent ones (for instance the fourth one here) allow to enhance the precision of the reduced basis by describing local modes close to the crack front. In general, the higher the order of a shape function, the more localized on the front its mode. Those points about the morphing as an essential component of the method and the spatial scale separability are extensively discussed in section 7.

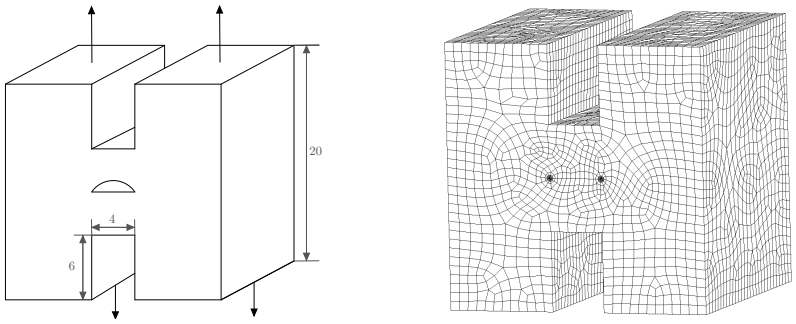

(a) (b)

Figure 2.18 Geometry of the "H" block in millimeters (a) and the associated finite element mesh (b).

6.3 Surface crack in a 3D "H" block

The purpose of this case is to test the whole strategy on more complicated problems, tridimensional geometries which induce modifications of the global shape of the crack front during its growth. Indeed, if the front shape really evolves from one propagation step to another, meaning that the crack is not growing by some kind of homothetic transformations, the displacement solution fields in the part will evolve as well. This is precisely what is likely to happen in an industrial problem. However, in that type of analysis, one can wonder if the data contained in the successive displacement solution vectors will compress well and hence if the *a priori* model reduction will be efficient. Conclusions on that point are presented hereinafter.

The crack is grown in a solid block whom section recalls the form of the letter "H". The model is symmetric and a pressure P of 100 MPa is applied on the four horizontal planes of the top and the bottom of the part (Figure 2.18). An initial semicircular crack of diameter 4 mm is introduced in a symmetry plane of the block, in such a way that it is solicited in mode I. The geometry of this test-case, somehow artificial, was chosen because the cuts of the "H" make a non uniform stress configuration around the crack, leading to a fast evolution of the front shape along the propagation. The external height, width and length of the specimen are of 20 mm. The sample is discretized with a quadratic hexahedral mesh containing approximately 30 % of quadratic tetrahedra, pyramids and wedges. The whole model represents 288204 degrees of freedom. To prevent rigid body motion, 6 appropriate degrees of freedom are fixed in the plane of the crack. At the finite element level, the material behavior is linear elastic, with a Poisson's ratio of 0.3 and a Young's modulus of 200 GPa. As in the cracked tension sample example (see section 6.2), a nominal mode I stress intensity factor is computed from the finite element resolutions. Again, since the model is linear, this nominal stress intensity factor is multiplied by a suitable constant to simulate a cyclic loading of the block, oscillating between 0 and 700 MPa.

The simulation consists in growing the crack following the growth rates provided by the crack tip condensed plasticity model laws. A number of 77906 loading cycles and 1558120 time steps are simulated. The finite element model is updated by our mesh morphing technique at each time that the maximum propagation along the front reaches 50 μm. This leads to handle 65 updates. The mesh morphing allowed to increase the characteristic crack length to up to almost 2.7 times its initial value. For illustrating purpose, we present the von Mises stress results computed on the initial and final configurations of the model (Figure 2.19(a)-(b)), as well as a superposition of the

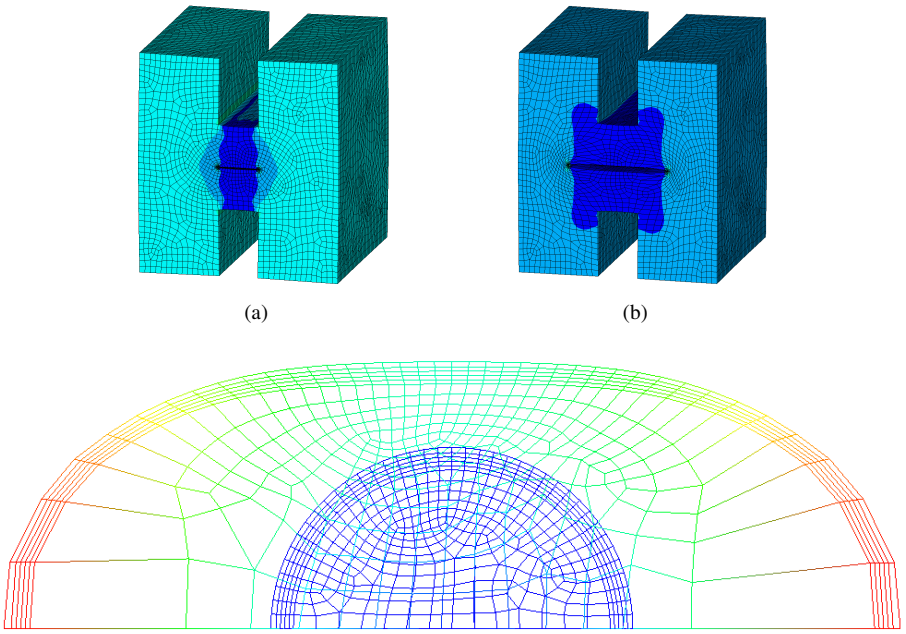

(a) (b)

(c)

Figure 2.19 Von Mises stress results computed on the initial (a) and final (b) configurations of the model, and superposition of the corresponding crack plane meshes (c).

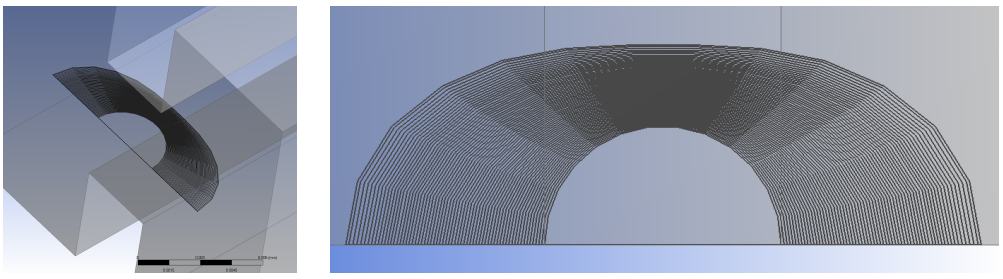

(a) (b)

Figure 2.20 Successive crack front configurations obtained during the simulation.

initial and final crack plane meshes (Figure 2.19(c)). On that last figure, the color chart represents the nodal displacement during the morphing process. The initial crack plane mesh is totally blue since it has not undergone any modification. Although the crack front shape really evolves during the simulation, the high quality of the radial mesh around the front is preserved. In addition, the successive crack front configurations obtained during the simulation are shown in Figure 2.20.

At each update of finite element model, the interaction integral method presented in section 1.6 is used to compute the mode I stress intensity factor from the solution fields. In addition to that, the *a priori* model reduction logic is applied. The solution of the initial finite element problem, corresponding to the first time step, is computed classically by a preconditioned conjugate gradient solver. For all the subsequent macro cycles, the displacement solution vectors are approximated as linear combinations of the reduced basis shape functions, using the projection proposed in Equation (2.27). A force residual is computed as described in Equation (2.31) to check if the approximate solution fulfills the chosen quality criterion.

On Figure 2.21(a), the history of those residuals is shown. The precision ε of the force convergence criterion is set to 10^{-3}. Every time that the residual is higher than this criterion, the reduced basis is considered to be incomplete. Consequently, the full finite element problem is solved by a classical solver and from the obtained solution, an additional shape function is built and added to the basis. This enriched basis allows to compute acceptable solutions for a few of the subsequent macro cycles, until another unconverged step, at which the basis is enriched again. To illustrate that process, the size of the problems solved all along the analysis are plotted on Figure 2.21(b). When a full solve is needed, the problems are large, more precisely they are of the dimension of the full finite element problem. On the contrary, if the solution can be found in the reduced basis, they are quite small, that is, of the dimension of the reduced basis. In these cases, the model reduction makes sense. Obviously, the data presented on this figure is only a rough picture of the real computational times, because it does not include all the algebraic operations used to build the reduced problem (for instance the matrix-vector products described in Equation (2.30)). However, it gives a clear idea of the efficiency of the reduced basis approach for this type of problems.

To conclude, for the specific problem of the cracked "H" block, the proposed global model reduction strategy allowed to perform only 20 full resolutions of linear elastic finite element problems, representing a little less than $1/3$ of the 65 different problems used to compute the crack propagation corresponding to 77906 loading cycles, taking into account the nonlinear crack closure effects.

7 Model reduction and fracture mechanics: discussion around the mesh morphing technique

7.1 The mesh morphing technique as a key component

In order to understand why the mesh morphing technique is a key component of the reduced basis method when applied to crack propagation analysis, let us begin by an illustrating example. The objective is to perform a crack growth simulation in a simple test-case, in which the geometrical updates are handled by two different techniques: a method which is equivalent to remeshing and the mesh morphing strategy. Then, in a post-processing step, the minimal size of an appropriate reduced basis for the simulation will be computed, for both geometrical updates methods.

The chosen test-case is a 3D block in the middle of which a planar crack with a straight front is inserted (see Figure 2.22(a)). The block length is of 100 mm, its height 100 mm and its depth 80 mm. The initial crack length is 35 mm. The crack will be solicited in pure mode I since

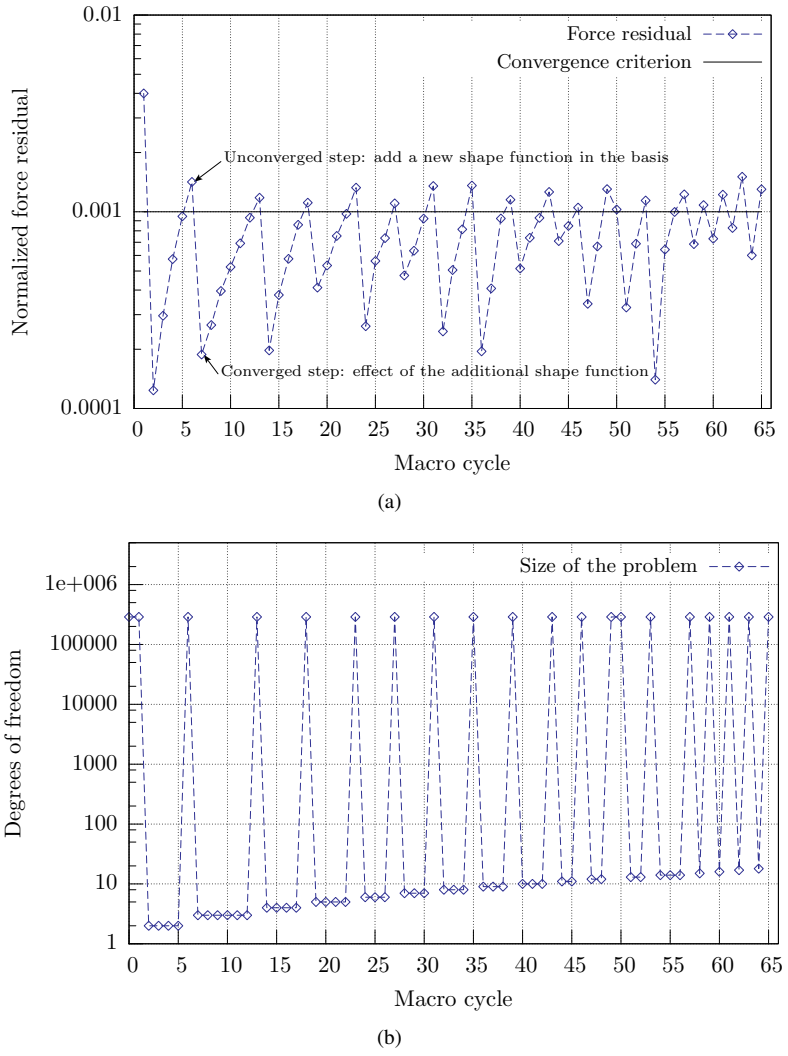

Figure 2.21 History of the residuals computed with the reduced basis (a) and of the size of the problems solved (b) for the 65 macro cycles on the “H” block sample.

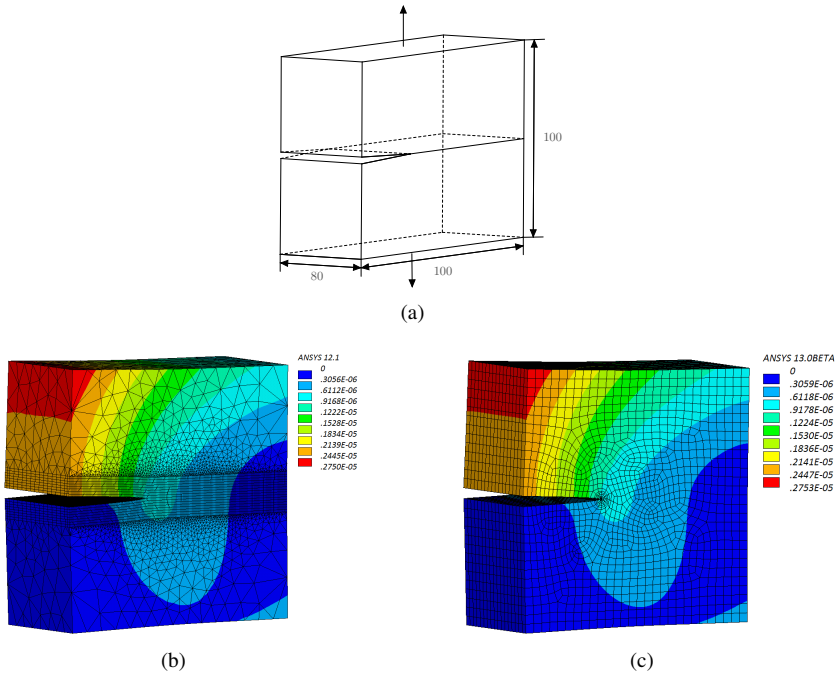

Figure 2.22 Geometry, in millimeters, of the Tada's crack configuration (a). Norm of the displacement solution of the initial configuration on the meshes corresponding whether to the node release technique (b) or to the mesh morphing technique (c).

tensile loading is applied on both the upper and lower faces of the block, by means of a 1 MPa pressure. In addition, to prevent rigid body motion, 6 degrees of freedom are blocked in the crack plane. This configuration is sometimes called the "Tada's crack" in the literature. In the simulation, 40 propagation steps are performed. Between each of them, the crack is grown by a fixed value, constant along the front, of 1.5 mm. As a consequence, the crack front remains a straight line all along the simulation, and the final crack length is of 95 mm. It is highlighted that this simulation is very artificial, and that the chosen propagation has no physical meaning. Again, the objective is to propose a very simple 3D propagation analysis.

In the first analysis, at the geometrical level, the cracked block is divided in two parts, symmetric with respect to the crack plane. Both are discretized with a free tetrahedral mesh far from the crack plane and a structured hexahedral mesh with significant refinement near that plane since the smaller edge length of the elements in that zone is 0.5 mm. All the chosen elements use quadratic shape functions. The two parts are linked together by bonded contact conditions on the crack plane. These conditions are handled by a penalty algorithm and applied only on the part of the surface corresponding to the crack plane in order to create the flaw. Consequently, the crack front nodes are the nodes on which the contact conditions start to be applied. See Figure 2.22(b) for an intuitive, visual explanation of the technique. All in all, this model is constituted by 166 114 elements, 399 833 nodes and finally 1 199 499 degrees of freedom. To grow the crack, the contact conditions are progressively released on the nodes of the front, "unbuttoning" the nodes. This technique will be referred to as the *node release technique* in the remaining of this section. This specific technique was chosen because it is absolutely equivalent to a remeshing approach, with the advantage that the number of nodes is kept constant all along the simulation.

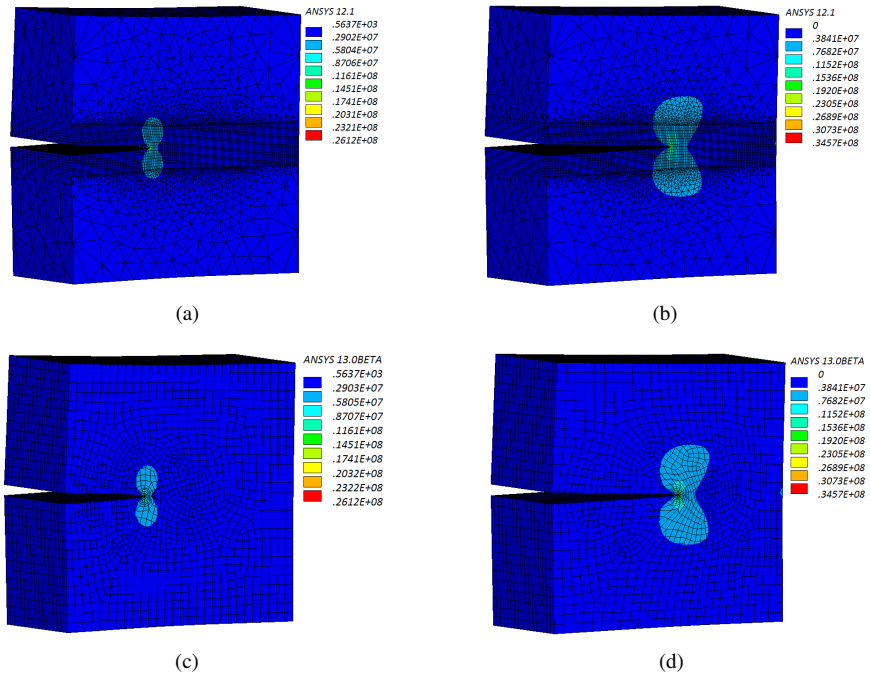

Figure 2.23 Von Mises stress obtained during the crack growth simulation. Results are presented for both the initial and final configurations on the models using the node release technique (a) – (b) and the morphing technique (c) – (d).

In the second analysis, the model is discretized using quadratic elements: a free hexahedral mesh far from the crack and a radial refined mesh around the front. The first row of elements at crack tip is constituted by quadratic wedges with a smaller edge length of 0.5 mm. This version of the test-case is constituted by 21 573 elements, 89 974 nodes and finally 269 922 degrees of freedom. By the way, this type of meshing is far more efficient than the previous one since the same crack tip refinement can be achieved with four times less degrees of freedom. During the simulation, this mesh will be deformed using the mesh morphing technique to make the crack propagate. The norm of the displacement solution computed on the morphing mesh and corresponding to the initial crack configuration is presented on Figure 2.22(c).

For each of the 40 propagation steps of the simulation, the numerical solution to the mechanical problem is solved using a preconditioned conjugate gradient solver. The obtained von Mises stresses are presented on Figure 2.23, for the initial and final configurations of the propagation and for both approaches (node release technique and morphing strategy). An important feature of this analysis is that clearly, the same mechanical solution is obtained with both methods. The obtained displacement solutions are then stored in two snapshot matrices, one associated with the set $\left\{\boldsymbol{u}_i^{nr}\right\}_{i=1}^{40}$ of solutions corresponding to the node release technique, and another one associated with the set $\left\{\boldsymbol{u}_i^{mo}\right\}_{i=1}^{40}$ corresponding to the morphing strategy. Those snapshot matrices are made

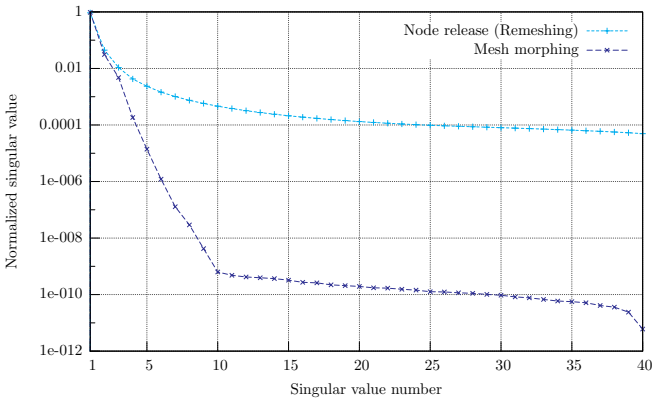

Figure 2.24 Normalized singular values of the set of 40 successive displacement solution vectors for the Tada's crack problem.

following the general form:

$$\boldsymbol{A} = \begin{pmatrix} \boldsymbol{u}_1^1 & \boldsymbol{u}_2^1 & \cdots & \boldsymbol{u}_m^1 \\ \boldsymbol{u}_1^2 & \boldsymbol{u}_2^2 & \cdots & \boldsymbol{u}_m^2 \\ \vdots & \vdots & \ddots & \vdots \\ \boldsymbol{u}_1^n & \boldsymbol{u}_2^n & \cdots & \boldsymbol{u}_m^n \end{pmatrix} \tag{2.57}$$

where the constant n would be the number of degrees of freedom of the model, dimensioned here to 3 times the number of nodes, and m would be the number of snapshots, in the present case, 40. Since with the two chosen methods the models are discretized with a constant number of degrees of freedom all along the propagation, this step is straightforward. Once this is done, the singular value decompositions of both matrices are computed.

The obtained singular values are plotted on Figure 2.24. They are all normalized by the sum of the 40 singular values. Looking at the decreasing rate of the singular values, it is clear that the two curves behave very differently. The singular values associated with the node release approach are decreasing slowly, then stagnating around 10^{-4}. That means that the information contained in the set $\{\boldsymbol{u}_i^{nr}\}_{i=1}^{40}$ does not compress well. Indeed, the lower bound of the Kolmogorov k-width, as well as the minimal error induced by the reconstruction of the solutions using a truncated basis at order k is related to the sum of the $(m-k)$ singular values of order greater than k. Consequently, for this simulation, approximating the set of solutions by a low dimensional linear subspace will not be possible without a significant loss of accuracy: a classical reduced basis approach will not work. On the contrary, the singular values which are associated with the morphing technique are decreasing very fast since for instance the ninth singular value is less than 10^{-8}. Hence the displacement solution vectors associated with morphing technique can be approximated with a fairly good accuracy as linear combinations of a few basis vectors! This result finally encourages to apply a reduced basis approach to this type of problems.

Let us introduce some explanations about the spectacular effect of the mesh morphing on this problem. First of all, keep in mind that the regularity of the solution in the parameter dependency, here the crack length, is a primordial feature so that the k-width decreases fast as k increases. When computing solutions, and by extension reduced basis shape functions, on a spatially discretized problem, the obtained vectors are in the first place associated with the *nodes*. In a second time, of course this mesh is representing a geometry and its underlying topology. In fracture me-

chanics problems, relatively to the topology, there are basically three types of nodes: the nodes which are beyond the crack front, and which "see" the tip stress singularity coming, the nodes constituting the crack front itself, which undergo a singular behavior and finally the nodes in the rear part of the crack, which are in a zone where the stress singularity is relaxed. The displacement fields characteristics of each of these three node types are very different. With the node release technique, the solutions, and consequently the reduced basis shape functions, are computed on meshes with different topology since at each propagation step, the crack tip nodes contact conditions are released. As a consequence, during the propagation, the nodes status changes: nodes that are beyond the crack at the beginning become step by step crack front nodes and end in the rear of the crack. Those strong and abrupt changes ruin the regularity hypothesis, and finally the solution space cannot be approximated by a low dimensional subspace. In fact, the node release technique associates to tightly the solution vectors with the configuration (i.e., geometry and topology) that was valid at the time that they were computed.

By opposition, the mesh morphing approach allows to preprocess the solution vectors, making them look much more similar. In fact, by definition the mesh morphing constitutes a stepwise mapping ψ of the nodes coordinates, from an original domain Ω_o to the current domain Ω_c:

$$\begin{array}{rccc} \psi: & \mathbb{R}^{3n} & \longrightarrow & \mathbb{R}^{3n} \\ & \boldsymbol{x}_o & \longmapsto & \boldsymbol{x}_c \end{array} \tag{2.58}$$

where the vectors $\boldsymbol{x}_o$ and $\boldsymbol{x}_c$ are the nodes coordinates in respectively the original and current configuration. However, what is less intuitive is that, because the displacement solution vectors $\boldsymbol{u}_i$ are expressed in terms of *nodal values*, the morphing also provides naturally non-linear mappings χ_i of these vectors from the original configuration on which they were computed to the current configuration:

$$\boldsymbol{u}_i^c = \chi_i\left(\boldsymbol{u}_i^o\right) \tag{2.59}$$

the vectors $\boldsymbol{u}_i^o$ and $\boldsymbol{u}_i^c$ being the same displacement solution vectors, expressed respectively in the original and current configurations. Doing so, the displacement solution vectors and by extension the reduced basis shape function are always expressed in a relevant coordinate system. For instance, the singular fields around the crack tip are in fact expressed in the local coordinate system that is moving with the crack front, whereas they were expressed in the global Cartesian coordinate system with the node release approach. This approach has proved to be efficient for a number of problems, however, it has to face some limitations which are presented in section 7.2.

The proposed mesh morphing approach allows to artificially smooth the solution manifold, so that it can be approximated by a linear vector space, however it does not guarantee the low dimension of that subspace. Indeed, a smart preprocessing and model reduction technique can help to reveal the most hidden characteristics of a data set, however, no matter how smart it is, the reduction will be efficient only if the *intrinsic* dimension of that set is low. Fortunately, a very powerful "self-similarity" property exists for cracks in linear elastic media, and this approach allows to take advantage of it. Indeed, the displacement field around the leading edge of a crack is complex relatively to the spatial coordinates, but it always takes the same well known singular form (refer to section 1.3 of chapter 1), making its evolutions with respect to time quite smooth. Consequently, it is possible to express this singular field as a linear combination of a few basis vectors. Against all expectations, fracture mechanics in linear elastic media hence appears to be a good candidate to reduced basis approaches! The mappings χ_i defined above are then projecting the computed solutions $\boldsymbol{u}_i^o$ onto the surrounding of another crack front, of the same topology but with different length and shape, building artificial solutions similar to the expected one.

Conducting preprocessing actions to make the solutions look alike as already been pointed out as a very efficient technique to diminish the Kolmogorov n-width in various papers. It was applied

to quantum chemistry, in which the solutions present some singularities at the position of the nuclei. To build the reduced basis, the solutions were expressed somehow "centered" around these nuclei [CAN 07]. A similar strategy was also performed in the context of parameterized domains, solving for the steady Stokes problem. The solutions were mapped to a reference domain in order to compute the reduced basis shape functions properly [LØV 06].

From a general point of view, coupling a classical model reduction approach and the morphing technique constitutes in fact a *nonlinear dimensionality reduction* technique [LEE 07, FOD 02]. Indeed, it is somehow similar to the so-called Kernel PCA strategy [SCH 97]: the snapshots are obtained in an observation space, in which they cannot be approximated by a low dimensional linear subspace. Then in a second time they are mapped to a feature space in which a classical PCA is conducted more successfully. The nonlinear dimensionality reduction (NLDR) techniques, also called manifold learning methods, are innovative tools widely used in the fields of data analysis, data mining and machine learning. They aim at providing a way to understand and reveal the structure of complex data sets. Indeed, it is clear that sometimes the traditional methods such as PCA do not success in unfolding the intrinsic dimension of a set because they are based on linear models. On the contrary, the NLDR methods are relatively recent since they emerged in the late 1990's, and treat the data in a nonlinear way, opening new possibilities. To the best of our knowledge, for the moment, those methods have not been applied as such in the field of reduced basis and model reduction. In this respect they might deserve to be studied a little more.

To finish with this comparison of the node release technique versus the morphing approach, some of the obtained SVD modes are presented on Figure 2.25 for the node release approach and on Figure 2.26 for the mesh morphing technique. Remember that the displacement fields were computed on different meshes, according to the crack propagation. Here, the shape functions are presented projected on the initial mesh although only the first one was computed on this mesh. As a matter of fact, for both techniques, the very first modes of the SVD are able to capture the global characteristics of the displacement solutions corresponding to the whole propagation simulation. After that, the subsequent modes are providing more local information about the crack tip fields. In general, the higher the order of a shape function, the more localized on the front its mode. It is apparent that the higher order shape functions obtained on the model which uses the mesh morphing technique contain more artifacts and perturbations than the corresponding shape functions of the model with the node release strategy. However, in the present situation, this does not constitute a real problem since the SVD modes to which they are associated correspond, in the morphing case, to singular values that are less than 10^{-7}. This means that those shape functions would have a very low influence on the solutions that would be computed using their associated reduced basis, and even that, in practice, they would probably not be retained in the reduced basis. Nonetheless, some hints to explain this phenomenon will be introduced in the next section.

7.2 Limitations

To illustrate the type of limitations that have to be faced, let us introduce a new illustrating test-case. It is very similar to the one presented in section 6.2, except that this time, the surface crack is introduced in a 3D beam of *circular* cross-section (see Figure 2.27). This beam height is of 50 mm and the diameter of its section is of 10 mm. It is put under tensile loading by means of pressure of 180 MPa is applied on both its top and bottom faces. The initial crack is semicircular of diameter 4 mm, and it is thus solicited in mode I. The sample is discretized using a quadratic mesh of 268 746 degrees of freedom. At this point, the crack is grown using the CTCP model and the morphing technique. The finite element model is update at each time that the maximum propagation along the crack front reaches 100 µm, leading to compute 20 propagation steps. The displacement solutions and von Mises stresses obtained on the initial and final configurations of

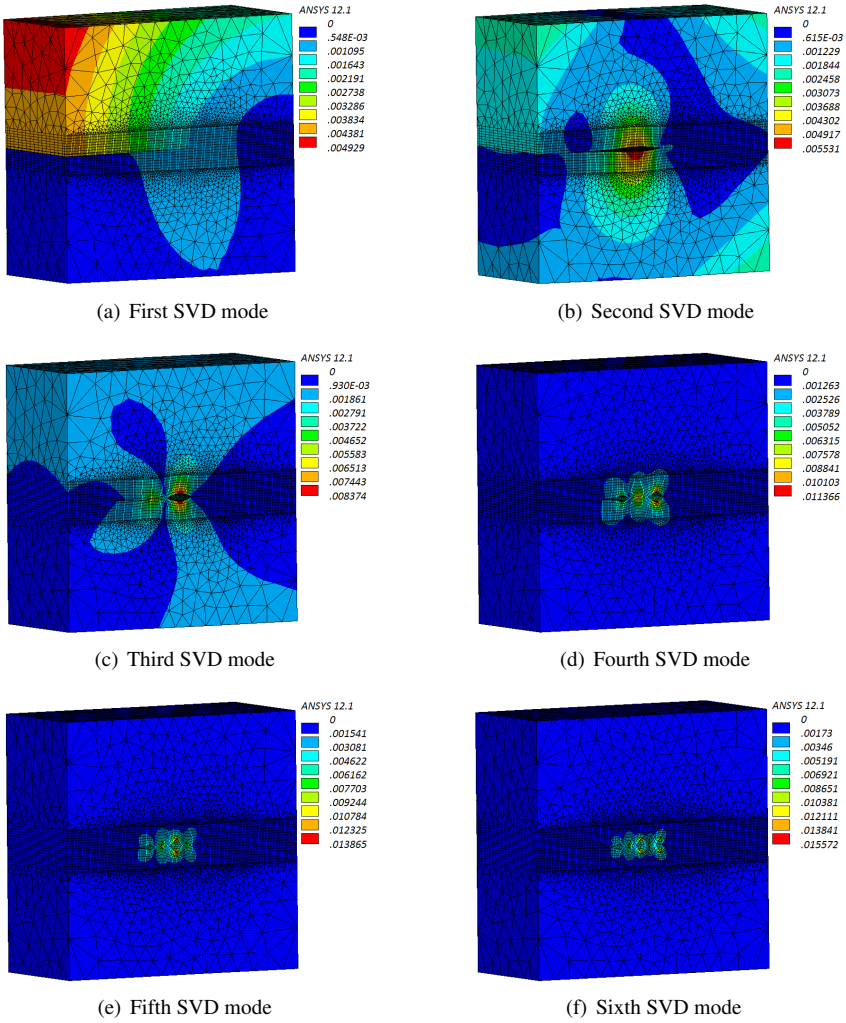

(a) First SVD mode

(b) Second SVD mode

(c) Third SVD mode

(d) Fourth SVD mode

(e) Fifth SVD mode

(f) Sixth SVD mode

Figure 2.25 Six first modes of the singular value decomposition of the displacement solution vectors computed with the node release approach.

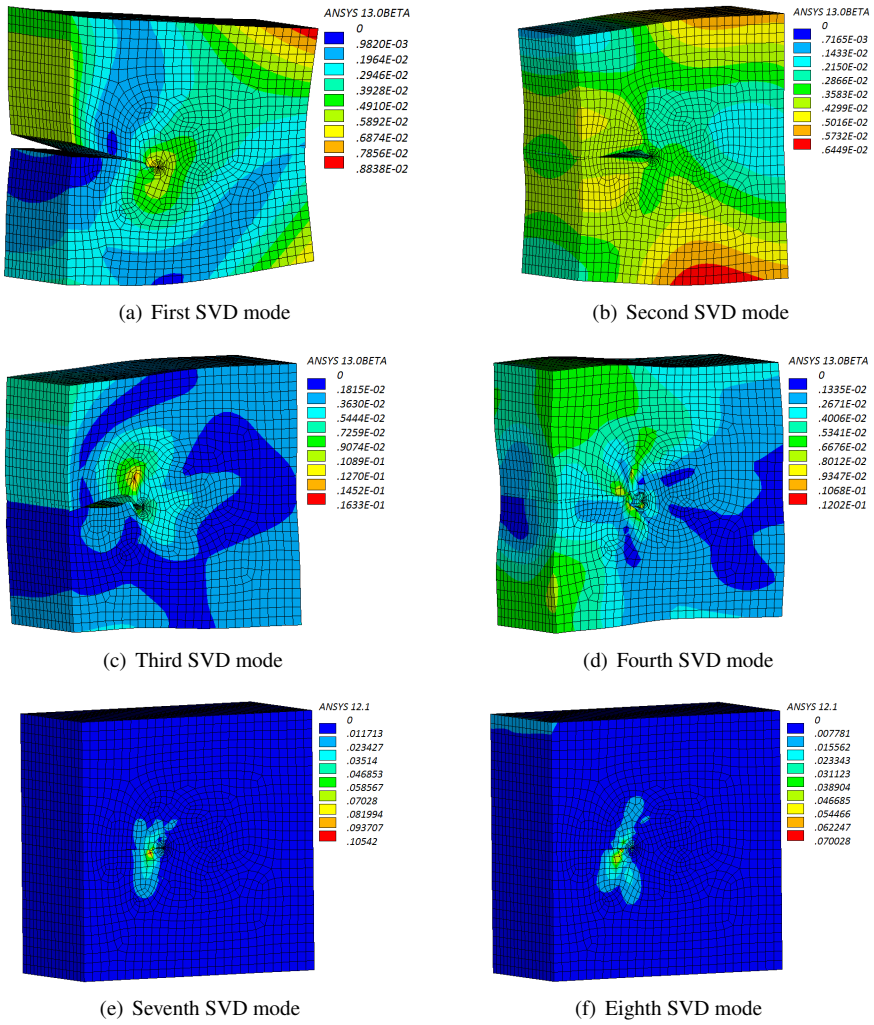

(a) First SVD mode

(b) Second SVD mode

(c) Third SVD mode

(d) Fourth SVD mode

(e) Seventh SVD mode

(f) Eighth SVD mode

Figure 2.26 Some of the first modes of the singular value decomposition of the displacement solution vectors computed with the mesh morphing technique. The modes are presented projected on the initial mesh.

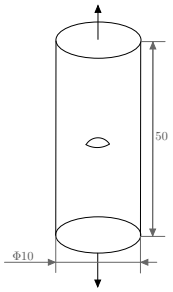

Figure 2.27 Geometry, in millimeters, of the crack in a cylindrical sample.

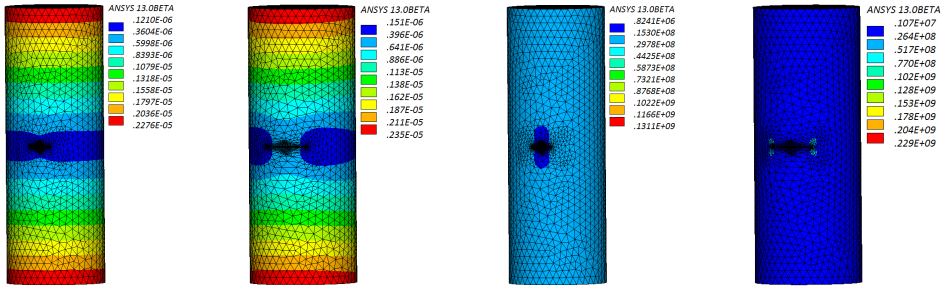

(a) (b) (c) (d)

Figure 2.28 Norm of the displacement solution for respectively the initial (a) and final (b) configurations, and associated von Mises stresses (c) – (d).

this cylindrical tension sample are provided on Figure 2.28(a). The same results are also presented on the cross-section of the sample located on the crack plane Figure 2.30.

As a matter of fact, the general shape of the solution fields on initial and final configurations are fairly similar, and anyway not much different that the initial and final fields of the rectangular tension sample are (section 6.2). Consequently, one would reasonably infer that the intrinsic dimension of the solution manifold for that cylindrical beam test-case should not be much higher than the one of the rectangular sample. For all that, the singular value decomposition of the cylindrical sample snapshot matrix is computed, and an orthonormalization of the snapshots is conducted by means of a Gram-Schmidt process as well. The resulting normalized singular values, and the norm of the Gram-Schmidt basis vectors are plotted on Figure 2.29. As a matter of fact, the singular values are stagnating around 10^{-5}, and the norm of the Gram-Schmidt shape functions around 10^{-4}, meaning that the information contained in those snapshots cannot be compressed, nor approximated by a space of low dimension. A visual manifestation of this phenomenon can also be provided, plotting the shape functions resulting from the Gram-Schmidt process (see Figure 2.31). The vectors are presented projected on the initial mesh. The shape functions do not localize around the crack front, as it was the case for all the previous test-cases presented in this typescript. Rather, they are quite irregular and artifacts appear, enriching the basis in zones far from the crack.

A first hint to explain these deceptive results is coming from the analysis of the non-linear mappings χ_i of Equation (2.59). Those are the straightforward mappings provided by the mesh morphing allowing to map the displacement solution vectors, and by extension the reduced basis

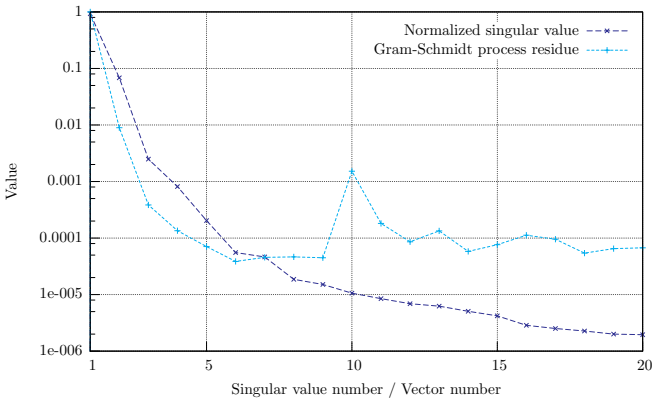

Figure 2.29 Normalized singular values of the set of 20 successive displacement solution vectors and residual of the Gram-Schmidt process during their orthogonalization.

shape functions as well, from the configuration on which they were computed to the current configuration of the cracked sample. In fact, this mapping approach is very simple since it only consists in letting the nodal values of the solution vectors be expressed without any modification on all the successive deformed meshes. However, its major drawback is that it does not ensure that the mapped field exhibit the *same characteristics* as the initial ones. To put it another way, it does not preserve important features such as the divergence or the orientation of the vector field with respect to the external boundaries of the studied body. Indeed, the solution fields of a specific geometric configuration Ω_o belong to its associated solution space $\mathcal{U}(\Omega_o)$. An efficient mapping should hence guarantee that the transformed fields to the current configuration Ω_c are projected onto its associated solution space $\mathcal{U}(\Omega_c)$, which is not the case with the method proposed in this typescript. A solution to alleviate this type of difficulty is to choose a more appropriate, yet more complex mapping, such as for instance a mapping based on the Piola transformation, as it has been pointed out in a some papers [LØV 06, DEP 10]. However, it has also been shown that computing precisely a discrete Piola transformation is particularly complex.

A second hint appears through a refined analysis of the solution displacement fields evolutions along the propagation. For that purpose, several vector plots of these displacement fields are provided on Figure 2.32. They are presented on the cross-section of the sample located on the crack plane, and the size of the plotted vectors is scaling with the magnitude of the displacement fields. First, the displacement solution of initial crack configuration is plotted on its corresponding mesh (see Figure 2.32(a)). The displacement vectors are mainly pointing toward the center of the sample. This is basically the expected behavior of a cylindrical sample under tension with a small crack or even without any crack. Indeed, because of the Poisson effect, the displacement field is not oriented only along the longitudinal direction, but also toward the center of the specimen. In the symmetry plane of the sample, only the radial component is visible. After that, the same initial displacement field is *mapped* to the final crack configuration and shown on the final mesh (Figure 2.32(b)). In spite of the naive mapping that has been used, the initial field can be easily recognized. This mapped vector constitute in fact the first of the shape function that would be used in a reduced basis approach to compute the displacement solution of the final configuration as a linear combination of the previous solution vectors. Finally, the displacement solution corresponding to the final crack position is presented on the final mesh on Figure 2.32(c). Clearly, the characteristics of the shape function of Figure 2.32(b) is not matching those of the final solution

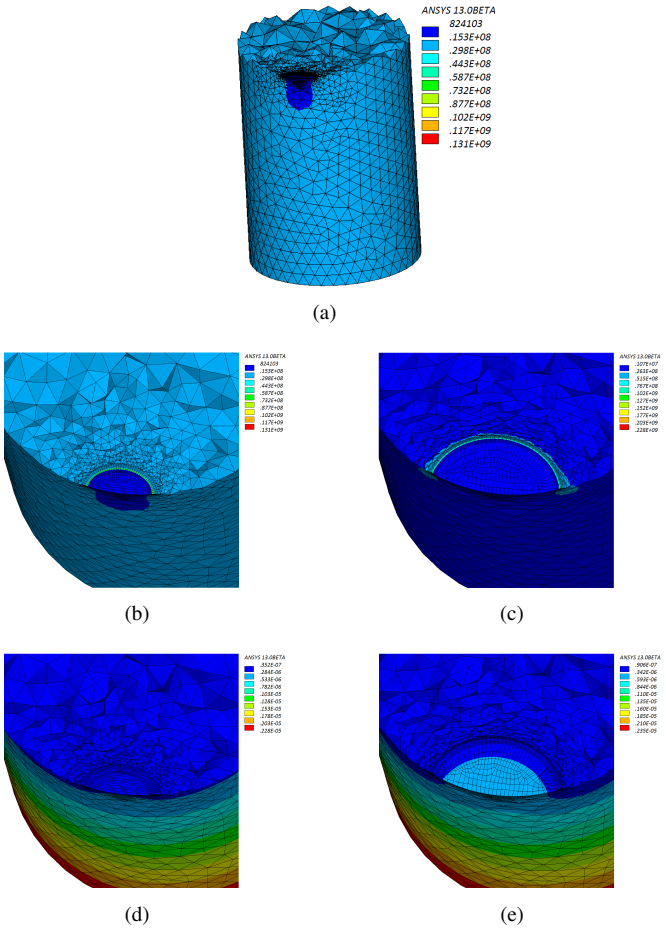

Figure 2.30 Intensity of the von Mises stresses for respectively the initial (a) – (b) and final (c) configurations, and norm of the displacement solution (d) – (e). The results are presented on the cross-section of the sample located on the crack plane.

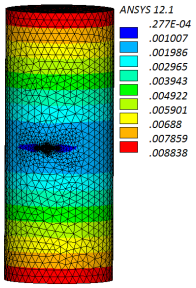

(a) First shape function

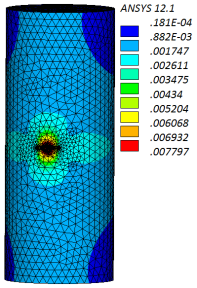

(b) Second shape function

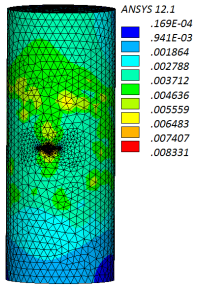

(c) Third shape function

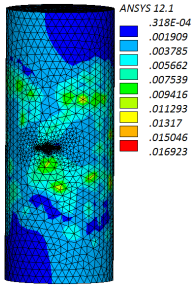

(d) Fourth shape function

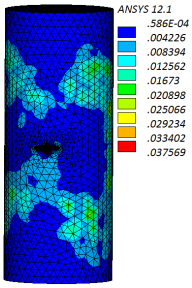

(e) Fifth shape function

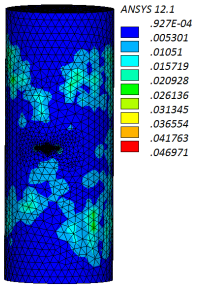

(f) Sixth shape function

Figure 2.31 First shape functions obtained by applying a Gram-Schmidt process on the displacement solution vectors of the round bar test-case. The shape functions are presented projected on the initial mesh.

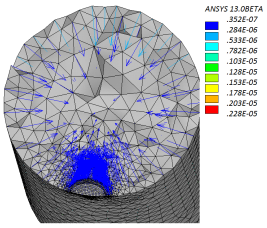

(a)

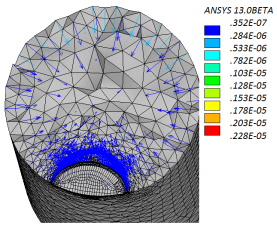

(b)

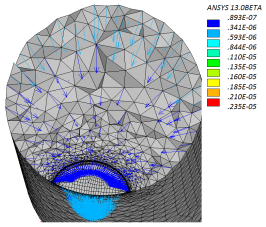

(c)

Figure 2.32 Displacement vectors presented on the cross-section of the sample located on the crack plane. The size of the vectors is scaling with the magnitude of the displacement. Initial solution presented on the initial crack configuration (a). Initial solution *mapped* to the final configuration (b). Final solution presented on its corresponding final crack configuration (c).

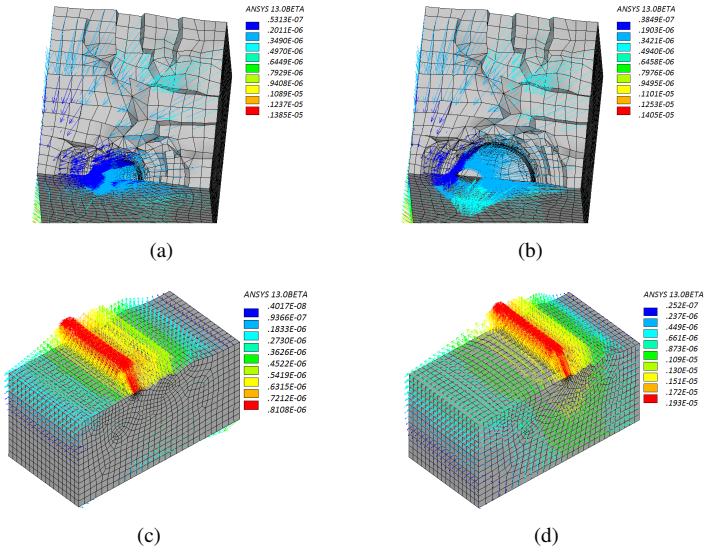

Figure 2.33 Displacement vectors presented on the cross-section of the samples located on the crack plane. The size of the vectors is scaling with the magnitude of the displacement. The results are presented for both the rectangular tension sample test-case, and the Tada's crack case. First, the initial solutions are presented on their corresponding initial crack configurations (a) – (c), then the final solutions are shown on their corresponding final configurations (b) – (d).

field. Indeed, the grown crack had an effect on the whole displacement field distribution, and the vectors are no more pointing toward the center of the sample, but rather toward the crack itself. In fact, during its propagation, the crack had a *large scale* effect on the solution field. The evolving crack generates a global effect on the structure. This means that, in this problem, there is no "separability" of the scale of the structure and the scale of the crack. The reduced basis method is hence perturbed by this observation.

In fact, reaching the latter conclusion would have been a trivial task if it would have sufficed to compare a characteristic length of the crack to a characteristic dimension of the structure (the cylinder radius for instance) in order to predict the reduced basis bad behavior. Obviously, the larger the crack compared to the scale of the structure, the larger its perturbation effects. Unfortunately, this is not that evident to classify the problems that will behave bad with respect to a reduced basis approach (such as the cyclindrical sample) from those which will behave well. Indeed, the other test-cases presented in this typescript (namely the rectangular tension sample of section 6.2 and the Tada's crack of section 7.1) behave well even with a ratio *crack size*/*structure size* comparable or higher than the one of the cylindrical sample. To illustrate that point, a similar analysis of the solution displacement fields has been conducted for those test-cases. Hence, on Figure 2.33, the initial displacement field presented on the initial configuration, as well as the final field on the final configuration are plotted, for both the rectangular tension sample and the Tada's crack. The fields of the rectangular tension sample are rather difficult to grasp because they are pointing toward a node fixed to avoid rigid body motion during the computations. However, as a matter of fact, the crack become large, but the solution fields do not evolve very much during the propagation. Considering the Tada's crack field evolutions, again it is very clear that all along the propagation, the obtained displacement field remain very similar.

To conclude on that point, the statement on the good or bad behavior of a specific test-case with respect to the reduced basis approach should be qualified because the proposed reduced basis method exhibit some convergence properties. In other words, it always exist a *small enough* propagation range in which the method will be efficient. In addition, the extra cost brought by the use of the proposed model reduction technique on problems for which it is not efficient is marginal. In this respect, attempts of applying it on any type of crack propagation computation can always been envisaged. Finally, indicators allowing to estimate *a priori* the quality of the behavior of a test-case with respect to a reduced basis approach would be really handy, and it could be an interesting perspective for future work.

7.3 Some perspectives with or without using mesh morphing

Recently, some innovative works have emerged around the long known Williams' series expansion of the crack tip singular fields [WIL 57]. Basically, these approaches consist in projecting the near tip displacement field of a crack onto the basis provided by a truncated Williams' expansion. This has been done in the context of elastic-plastic experimental cracks [HEN 10], and in the framework of enriched finite element methods by means of specific crack tip enrichments [LIU 04], or by means of local analytic patches glued to the rest of the structure whether by partitioning the energy within an overlapping zone (Arlequin method) [RÉT 10] or by an integral matching technique (Mortar framework) [PAS 10]. In the latter approach, the truncated Williams' basis constitutes a reduced subspace in which the crack tip displacement field is sought during the resolution of the mechanical problem. It has been shown that the obtained approximation is of a fairly good quality. Furthermore, the stress intensity factors being some coefficients of the series expansion, this type of method enables their direct evaluation, without any postprocessing step. The link with the reduced basis strategy proposed in this typescript is clear. Indeed, one can imagine to build a multiscale reduced basis, with some shape functions capturing specifically the phenomena associated with the global scale of the structure, and some other describing the local behavior of the crack, hence adapted to its local scale. For that purpose, the global shape functions would be obtained by some finite element computations, whereas a good candidate for the local functions seems to be these analytic Williams' series. Such an approach would enable to introduce an identified physical content into the reduced basis framework. This point of view is encouraged by the behavior of the reduced basis shape functions provided along with the examples of this typescript. Undeniably, for the cases in which reduced basis approach performs well, the two spatial scales mentioned above appear when the shape functions localize around the crack front.

Another perspective for this work might be trying to avoid the use of the mesh morphing technique. Indeed, in the current approach, it is undoubtedly of a key importance. However, looking at the shape functions associated with the Tada's crack problem modeled by the node release approach reveals interesting features. These shape functions, obtained by a Gram-Schmidt orthonormalization process on the computed snapshots, are plotted on Figure 2.34. Since an incremental orthonormalization technique has been used, the first shape function is in fact the initial displacement solution vector which has only been normalized. As a matter of fact, the second shape function is already localizing strongly on the crack front. Finally, all the subsequent vectors consist in an extremely local information at the location of the crack front and a nil displacement elsewhere. A close-up of the third shape function is proposed on Figure 2.35. An appropriate plotting scale is chosen to provide a understandable deformation. The nodes corresponding to the location of the crack front at the third propagation step (the step associated with the obtained shape function) undergo a vertical displacement similar to an opening of the crack. The adjacent nodes at the rear of the crack are moved so that the crack faces interpenetrate. Besides being very

local, the shape functions are very similar. This second feature allows to envisage a model reduction technique *without* the use of the mesh morphing, and the coupling with methods adapted to crack propagation, such as the extended finite element method for instance [MOË 02]. Indeed, once the first fully localized shape function (thus the third shape function here) is obtained by a detailed computation, all the subsequent ones could have been built by mapping the small local zone containing the information onto the surrounding of the moving crack, in other terms, express this local information in the moving local basis linked to the crack front. Moreover, the first shape functions could have been used to describe the global behavior of the structure. The advantage of using the extended finite element method is that no remeshing is involved, so that the global shape functions would not have to be mapped onto various meshes during the propagation. As a final remark, this envisaged strategy is absolutely not straightforward, because a some issues would have to be solved. For instance, prescribing the correct displacement to the enriched crack nodes. However, it might be an interesting path for future work.

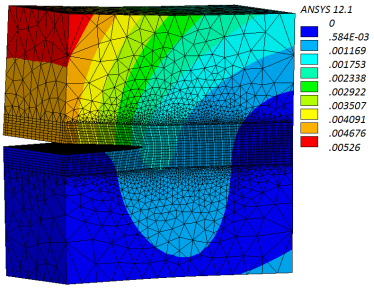

(a) First shape function

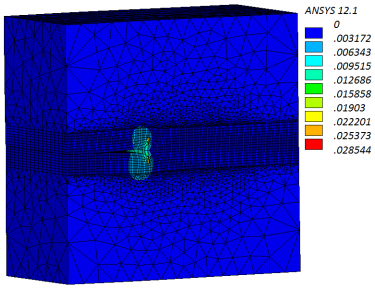

(b) Second shape function

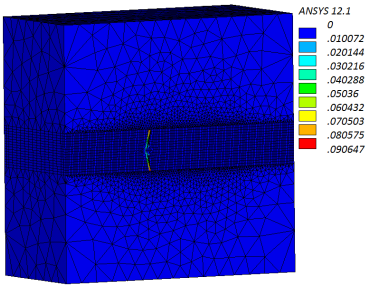

(c) Third shape function

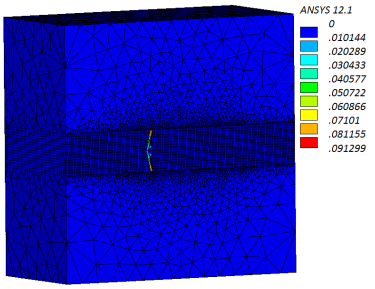

(d) Fourth shape function

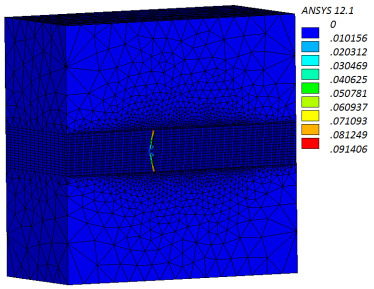

(e) Fifth shape function

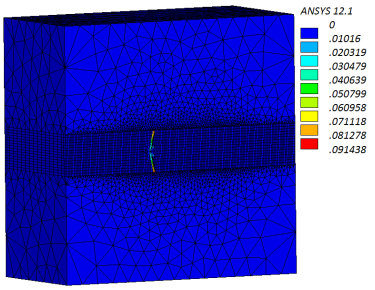

(f) Sixth shape function

Figure 2.34 Six first shape functions obtained by applying a Gram-Schmidt process on the displacement solution vectors computed with the node release approach. Notice that the shape functions four to six, yet very similar, are different since the perturbation is not located around the same node.

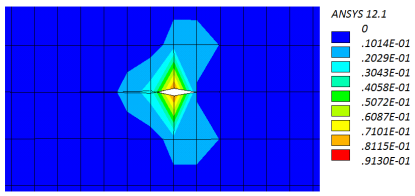

Figure 2.35 Close-up of the third shape function obtained by applying a Gram-Schmidt process on the displacement solution vectors computed with the node release approach. The pictured area corresponds to the nodes near the crack front location at the third propagation step of the simulation.

Chapter 3

An adaptive, multi-time scale strategy with model reduction technique for 3D fatigue crack growth

Contents

1 The adaptive strategy

1.1 Introduction

The crack growth simulation strategy proposed in section 5 of chapter 2 allows the coupling of four main components. Namely, the CTCP model to compute the crack propagation rates, the reduced basis method to speedup the numerous linear elastic calculations necessary to the simulation, the mesh morphing technique for the geometrical updates of the finite element problems and finally a remeshing technique used when the mesh is too distorted by the morphing process. Those components are coupled via three different time scales, each of them corresponding to a different time loop in the algorithm.

Remind that on the propagation law time scale, the incremental computation of the crack propagation by the equivalent plasticity model does not take into account the evolutions of the stress intensity factor due to the modification of the sample geometry. However, at some point, when the crack has grown enough, the nominal SIF must be updated. For that purpose, the finite element model is updated by a morphing process and a new resolution is conducted. The major difficulty of this first strategy is to decide *when* this update must be performed, based on the crack growth provided by the CTCP model. Indeed, the frequency at which the SIF is refreshed has a great influence on the propagation results. Update the finite element model too rarely and the computed growth is false, usually underestimated, which is not working in favor of the structure's integrity. On the contrary, update it too often and the computational times become overwhelming. Typically, any type of fatigue crack growth simulation is facing the same problem. In the fatigue community, an heuristic consists in updating a crack each time that the propagation length is up to 10 % of the previous crack length. Unfortunately, besides the complexity of properly defining a crack length in 3D, it does not provide any guarantee on the accuracy of the obtained result, especially when the cracked sample geometry is complex, inducing irregular variations of the SIF, or when variable amplitude loading is applied, inducing irregular propagation rates. In this respect, a specific *adaptive strategy* is proposed hereinafter to overcome that difficulty.

The computational strategy of section 5, chapter 2, is basically an incremental method in the sense that it computes successive crack front positions, the time step being continuously incremented. The adaptive approach, for its part, consists in taking this incremental strategy and to wrap around it the notion of *adaptive pass*. First, let us call the time interval between two successive updates of the finite element model an *update interval*. Then an adaptive pass is in fact a crack growth analysis using the incremental strategy, with an associated starting time for the computation and a fixed update interval. Hence in the global adaptive strategy, different resolutions of the crack growth analysis are conducted, using several adaptive passes, each of them having an update interval equal to the half of the one in the previous pass. Doing so, the results in the successive passes are increasingly accurate. The process is then stopped when it converges, that is, when the results in the current pass are similar to those of the previous pass.

1.2 Process initialization

The first step of the method is thus to run an initialization process, in order to compute the number of time steps corresponding to the maximal propagation distance that the morphing technique can handle with an acceptable distortion of the mesh. For that purpose, the nominal stress intensity factor is computed for the initial crack configuration and the crack growth is computed by means of the CTCP model for an arbitrary number of time step, for instance 2^{16}. The CTCP model being quite fast, this takes only a few seconds. Based upon the computed crack growth, and considering as a rule of thumb that the morpher can double the characteristic length of the crack, the maximal

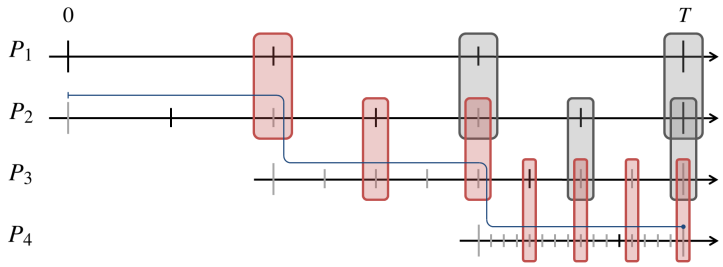

Figure 3.1 Schematic representation of the adaptive strategy. Four different adaptive passes are needed to complete the computations. The gray rectangles correspond to checked, but unconverged solutions, while the red ones correspond to the converged solutions. In addition, a black time step correspond to a full finite element resolution enriching the reduced basis, whereas a gray one means that a reduced solve has been possible. The blue curve indicates the solutions eventually used to postprocess the analysis.

number of time step is roughly estimated. Once this is done, the crack propagation simulation can begin by the first adaptive pass. This pass will cover the time interval starting from the initial time step (for instance zero for a new analysis), to the final, maximal time step that has just been computed. During the computations inside an adaptive pass, the full incremental strategy is employed, including the reduced basis approach. So the obtained displacement solutions are used to enrich the reduced basis. A schematic representation of the method is provided on Figure 3.1, where the gray time steps correspond to reduced resolutions whereas the black ones represent the full solves enriching the basis. Four adaptive passes are needed to complete the computations. The first one is denoted by P_1.

Remark 24 *For the computations, the maximal number of time step is in fact rounded down to the nearest power of two. Indeed, the powers of two having the advantage of always being divisible by two, this enables the time interval covered by an adaptive pass to be the half of the time interval of its previous pass. Hence the time interval covered by an adaptive pass is* always *a power of two.*

When the first adaptive pass is finished, the mesh and the internal variables of the CTCP model are reinitialized to their initial configurations, and the second adaptive pass is started (denoted by P_2 on Figure 3.1). This second pass begins at the initial time step and covers the entire time study interval, just as the first pass. However, the update interval is chosen to be the half of the one in the first pass. This process goes on, creating new passes with decreasing update intervals until that the convergence of the process is achieved. For that purpose, this convergence must be checked at two different levels, that is, both locally during the current pass, and globally at the end of the pass. This checking strategy is extensively described in the next section.

1.3 Checking the convergence

The convergence of the process is checked at the finite element level, between the current and the previous adaptive pass, whenever possible. Precisely, this can be achieved when the finite element resolution in the current pass corresponds to the same time step as a resolution in the previous pass. Considering that the update interval in the current pass is the half of the one in the previous pass, the correspondence arises at each time that the current solve number n in the adaptive pass is an even number. If it is the case, the obtained finite element displacement solutions of both

resolutions must be compared. In this respect, various criteria were tested and finally, a classical residual proved to be efficient. The convergence criterion is then:

$$\frac{\left\| \boldsymbol{u}_{previous} - \boldsymbol{u}_{current} \right\|}{\| \boldsymbol{u}_{current} \|} \leq \varepsilon \tag{3.1}$$

in which the chosen norm can be whether the Euclidean or the infinite norm. In practice, the chosen criterion ε is 10^{-4}. A visual explanation is provided on Figure 3.1, where the gray rectangles correspond to checked, but unconverged solutions, while the red ones correspond to the converged solutions.

If, at a given time step, the result in the current pass is *locally* converged with respect to the result in the previous pass, all the necessary data for a restart at this time step is saved. This includes the mesh configuration and all the internal variables of the CTCP model. Moreover, at the end of the current pass, if and only if all the local convergence are achieved, the convergence at the last time step is checked to determine if the process is *fully* converged. If it is not, a new adaptive pass is set up, starting at the time step corresponding to *the last local convergence*. Thereby this new adaptive pass will not start at the initial time step but at a latter one. However, its update interval will still be the half of the previous one and the pass will end at the final time step. This type of configuration corresponds to the passes P_3 and P_4 described on Figure 3.1.

1.4 Finalizing the analysis

From an implementation viewpoint, during the analysis, the finite element solutions, the CTCP model internal variables, the postprocessing and restart data are stored in objects representing the state of the analysis at a given time that can be called *temporal states*. Furthermore, these temporal state objects are stored in objects representing the adaptive passes, which are gathered in a collection. Hence at the end of the computations, the relevant postprocessing data corresponding to the converged configurations is distributed inside all the adaptive passes objects. Then the last step of the method is to retrieve this data and to present it to the end-user. For that purpose, the process run through the collection of adaptive passes, and for each of them, extract the data corresponding to the temporal states at all the time instants that are before the last local convergence in the pass. These temporal states are highlighted by a blue curve on Figure 3.1.

1.5 Short discussion

The main idea of the adaptive method is thereby to provide automatically the quasi-optimal time interval to update the finite element model for a given accuracy. The found update interval is only quasi-optimal because the update interval in the converged adaptive pass is in fact twice shorter than the actual optimal update interval. Nonetheless, in spite of that limitation, the guarantee on the accuracy that this adaptive method provides is an interesting feature. Computing several adaptive passes, looking for the correct update interval, leads to solve many more finite element problems than if the appropriate update interval have been correctly guessed at the first adaptive pass. However, remind that the adaptive strategy is coupled with the reduced basis approach. As a consequence, the first resolutions in the first adaptive passes contribute to build the reduced basis, and finally the computational cost of the subsequent calculations is drastically reduced, so that the overall analysis cost is kept under control. See Figure 3.1, in which the repartition of black and gray time step correspond to the repartition of respectively the full and reduced finite element resolutions. Furthermore, in some cases, the reduced basis dimension is even lower with this construction method. Indeed, since the update intervals are coarse in the first adaptive passes, the solution displacement vectors that are used to build the basis are very different from

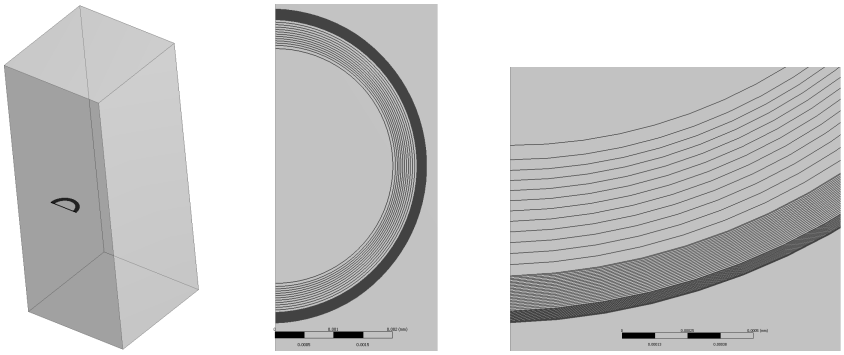

(a) (b) (c)

Figure 3.2 Overview (a) and closeups (b) – (c) of the front positions obtained at the end of the adaptive computations. The update interval is quasi-optimal, varying along the propagation as computed by the method, and ensures the chosen accuracy.

one to another. Thus they somehow contain more information than those which would have been provided by the incremental method with a short update interval. In addition, it must be noticed that the CTCP model integration is also quite fast, and it is a second very important condition to avoid the uncontrolled increase of the computational times. In the following sections, two examples of use of this adaptive method are presented.

2 Examples

2.1 Rectangular tension sample

A crack propagation analysis has been conducted on the rectangular tension sample of section 6.2 of chapter 1, using this time the adaptive strategy presented above. The sample geometry, crack configuration, mesh and boundary conditions were kept unchanged from the incremental analysis. However, the loading has been slightly modified to simulate a cyclic solicitation oscillating between 0 and 900 MPa. At the beginning of the analysis, the initialization phase determines the maximum number of time steps for which the crack grown by means of the mesh morphing method. Then the propagation is conducted for this number rounded down to the nearest power of two. So in the present case, the crack has been grown during 32768 time steps. To complete the computations with a convergence criterion ε of 10^{-4}, a total of 9 different adaptive passes were necessary. In short, this leaded to solve 107 finite element problems, among which only 7 full solves were necessary to build the reduced basis, all the 100 other resolutions took only a few seconds each to be performed! It is also underlined that the update interval in the ninth pass is $2^9 = 512$ times smaller than the update interval of the first pass, providing a significant increase in terms of accuracy. The final front positions obtained at the end of the adaptive computations, once the finalization of the analysis has been conducted following the methodology described in section 1.4, are depicted on Figure 3.2. The suitable update increment between two successive front was entirely computed by the method, and it evolves during the computations. Indeed, the rate of variation of the stress intensity factor in function of the crack length increases with the size of the crack. Consequently, to keep a correct accuracy, the update increment determined by the

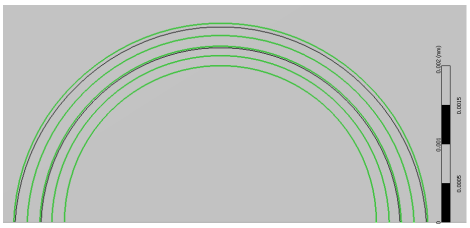

(a) First and second passes

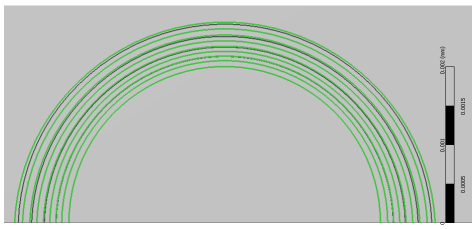

(b) Second and third passes

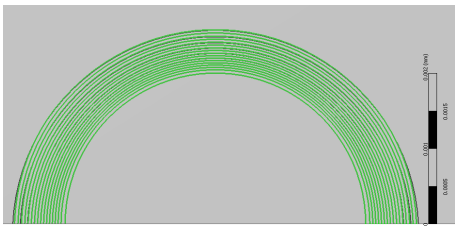

(c) Third and fourth passes

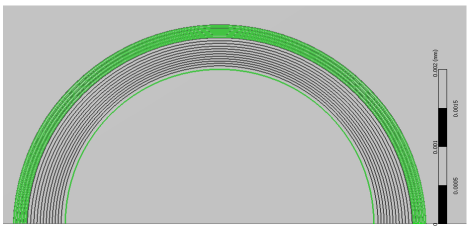

(d) Fourth and fifth passes

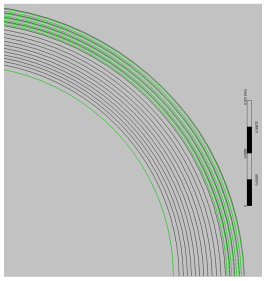

(e) Closeup of the fourth and fifth passes

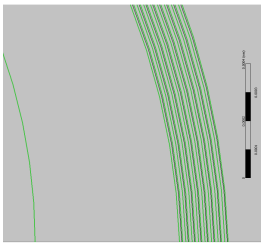

(f) Fifth and sixth passes

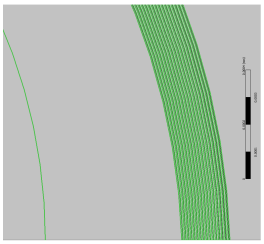

(g) Sixth and seventh passes

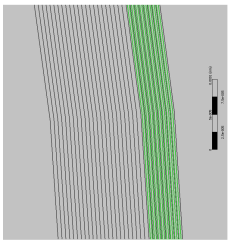

(h) Seventh and eighth passes

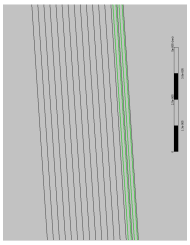

(i) Eighth and ninth passes

Figure 3.3 Computed crack front positions along the 9 different adaptive passes. The passes are compared by pairs, and the fronts corresponding to the former pass are depicted in black, while the fronts of the latter one are in green. For instance on (a), the fronts of the first pass are in black, and the fronts of the second one in green.

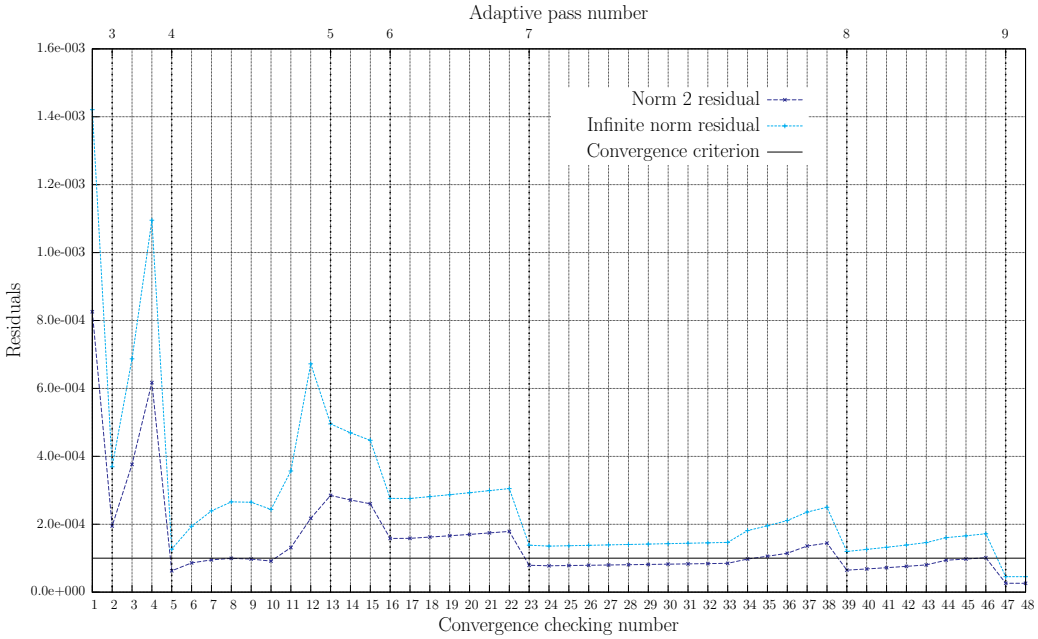

Figure 3.4 History of the check of the adaptive passes convergence all along the analysis. The vertical dotted lines represent the creation of the successive passes during the computations.

adaptive method decreases along the analysis.

In order to comment the adaptive computations, some postprocessing data is necessary. First, on Figure 3.3, the front positions obtained during each of the 9 adaptive passes are presented. The passes are compared by pairs, and the fronts corresponding to the former pass are depicted in black, while the fronts of the latter one are in green. For instance on Figure 3.3(a) the fronts of the first pass are in black, and the fronts of the second one in green. In the first pass, the 32768 computed time steps are reached in two finite element updates, corresponding to the two black fronts of the figure. Hence the update interval for this pass is 16384 time steps. Notice that the black front corresponding to the initial configuration is not visible since it is perfectly superimposed with the first green front. For the second pass, the update interval is divide by two, yielding 8192 time steps and 4 finite element problem updates. As a matter of fact, the fronts of the second pass that can be compared with fronts of the first pass (that is, the third and fifth green fronts) are slightly different from them. This difference is easily captured by the convergence check that is performed between the displacement solutions corresponding to those fronts (see section 1.3). Indeed, the history of the adaptive passes convergence checks is provided on Figure 3.4, and this first check corresponds to the first point of the curve, which is far above the 10^{-4} convergence criterion. The vertical dotted lines on the figure represent the instants of creation of the successive adaptive passes. In the current method, the Euclidean norm is used to compute the residual, however, the evolutions of a residual computed with the infinite norm is also provided. In spite of an offset, it exhibits the same general behavior than the Euclidean norm residual.

After that, the third adaptive pass is created, and it can be compared with the second one on Figure 3.3(b). Again, all the residuals comparing the third adaptive pass to the second one remain unconverged (convergence checks 2 to 4 on Figure 3.4). So the fourth pass is created, and finally, the residual comparing this pass to the third one partially converged from the check number 5

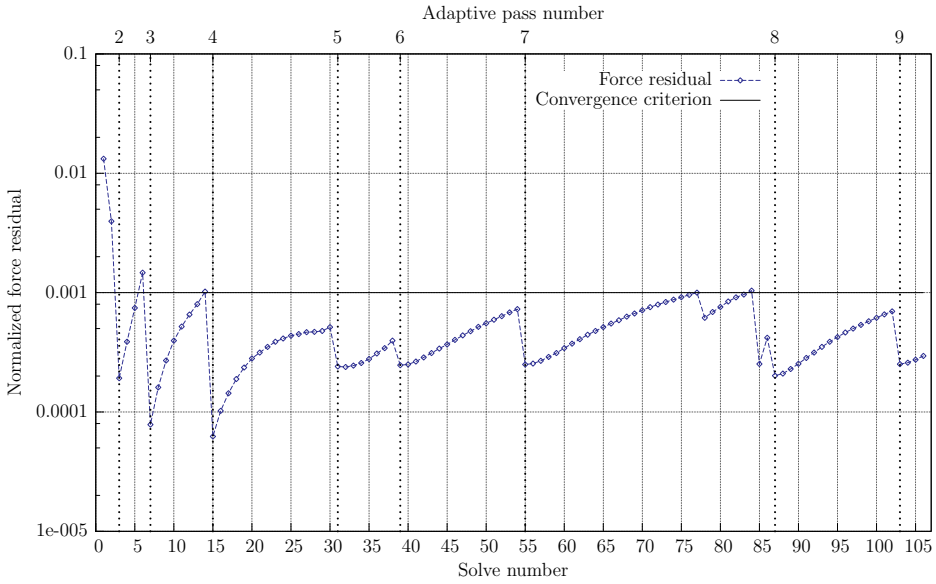

Figure 3.5 History of the reduced basis residuals.

to 10. At this point, the fifth pass is initiated and it does not start from the initial time step but rather from the last converged step of the fourth pass, in other terms, the step 25600. This can be viewed on Figure 3.3(d). After that, the sixth to ninth passes are created, following the same procedure until that the full convergence is reached.

For all the finite element resolutions, the reduced basis approach is used, so that the solution is first sought as a linear combination of the basis vectors, and then a force residual is computed to check if the computed approximate displacement vector fulfills the chosen quality criterion, here 10^{-3}. The history of those residuals is shown on the Figure 3.5. Again, the vertical dotted lines on the figure represent the instants of creation of the successive adaptive passes. The test-case behaved very well with respect to the reduced basis strategy, a very small reduced basis of dimension 7 was necessary to complete the computations. For visualization purpose, the 7 shape functions of the basis are provided on Figure 3.6.

As a final remark, it can be noticed that it was fairly obvious that the update interval chosen for the first adaptive pass would be to large to yield accurate results. Indeed, this was done mainly for demonstration purpose, and for real computations, an educated guess can be considered to choose more subtly this interval.

2.2 Industrial application: crack in a helicopter part

As a last example, a crack propagation analysis using the adaptive method is conducted on a realistic, complex industrial part. This test-case is inspired by an helicopter round-robin, initiated by the helicopter community in 2002 to benchmark the ability of predicting fatigue crack growth life in a complex tridimensional component under spectrum loading. During the round-robin, the geometry, material behavior and some loading spectra were given to the participants. Then the simulation results were collected and compared to experimental data. In general, the predicted crack path compared fairly well with the test data, as well as the propagation rates during the early stages of crack growth, but the component life was strongly underestimated at the end of

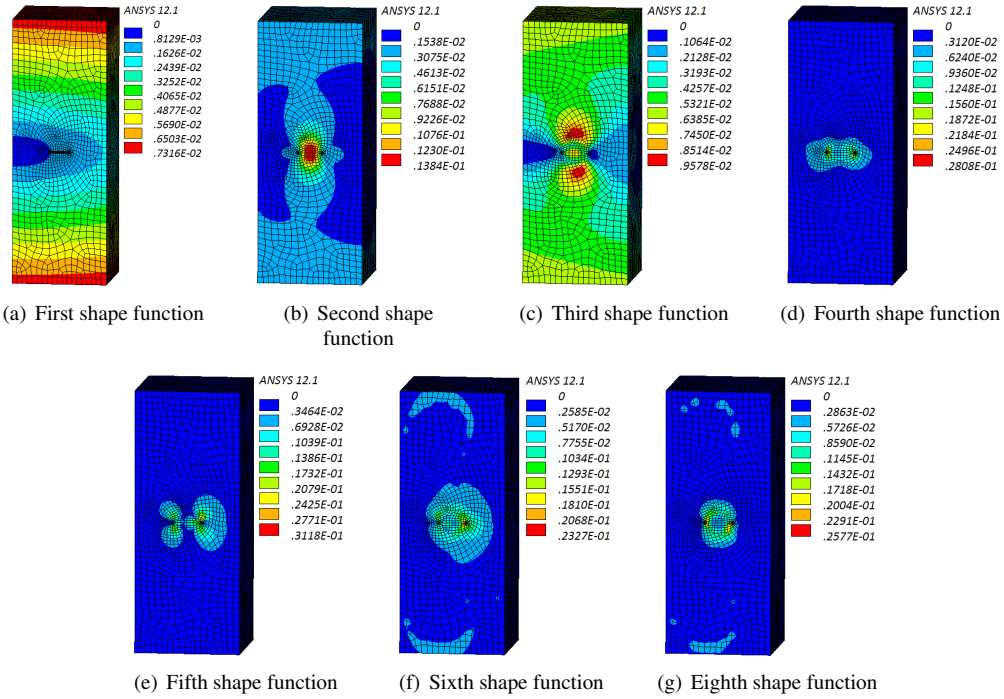

(a) First shape function (b) Second shape function (c) Third shape function (d) Fourth shape function

(e) Fifth shape function (f) Sixth shape function (g) Eighth shape function

Figure 3.6 The seven shape functions used in the adaptive computations of the rectangular tension sample.

the simulations [NEW 06, TIO 09].

In the present work, the global geometry of the sample is exactly the same as in the initial round-robin, a flanged plate with a central hole. Refer to Figure 3.7, reprinted from [NEW 06] for an overview and all the dimensions. Originally, the component was made of the 7010 aluminium alloy. This is not the case here, and the steel for which the CTCP model parameters were identified is used instead (see section 4.3.7 of chapter 1). In addition, the crack growth is predicted from a semi-circular surface defect on the inner face of the large central hole. The initial size of the crack is taken to be of a radius of 0.25 mm. A cyclic loading, oscillating between 0 and 412 360 N is applied as pressures on the six pin-holes at the extremities of the sample. In this configuration, the crack is submitted to pure mode I loading conditions, and is submitted to a maximal stress intensity factor of approximately 20 Mpa $\sqrt{\text{m}}$. During its growth, it will hence stay in its initial plane but as usual, the front shape is free to evolve. It indeed changes from the semi-circular initial shape to a slightly more semi-elliptical configuration.

The full model is discretized with a quadratic mesh constituted of 584 403 degrees of freedom. The mesh is divided into two different parts, a first one corresponding to a zone of interest around the crack, in gray on Figure 3.8, and another one for the rest of the model, in brown on the figure. During the simulation, the finite element resolutions are performed on the whole model, however, the morphing process is perform only locally around the crack, in the previously described zone of interest. An example of morphing result is provided on Figure 3.9, where the color chart represents the nodal displacement intensity.

In order to prevent rigid body motion, 6 appropriate degrees of freedom are fixed. This induces some local stress singularities and for this reason, the elements connected to the those

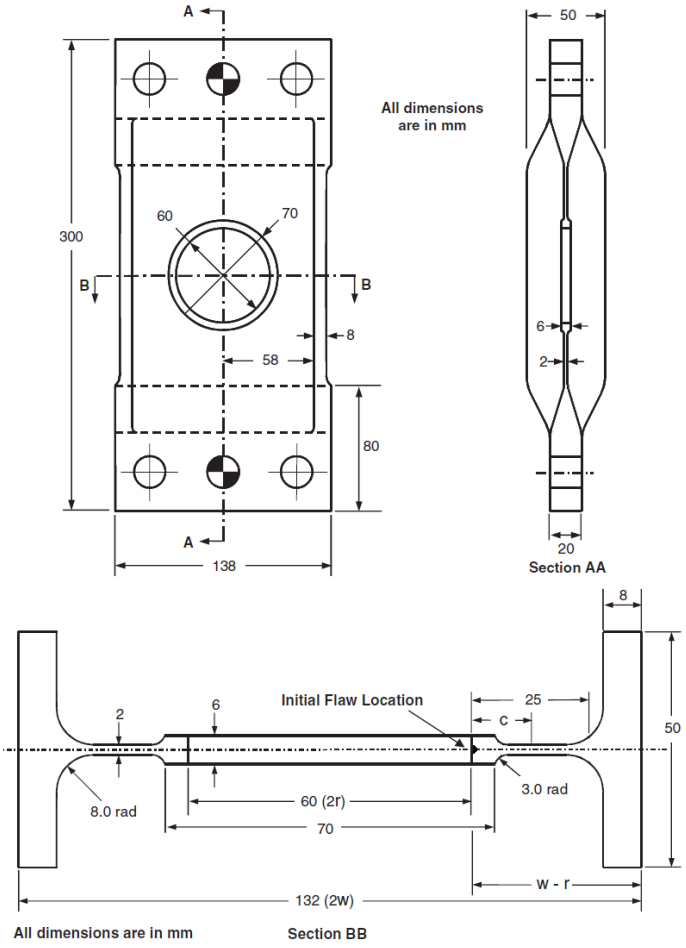

Figure 3.7 Helicopter round robin crack configuration. Reprinted from [NEW 06].

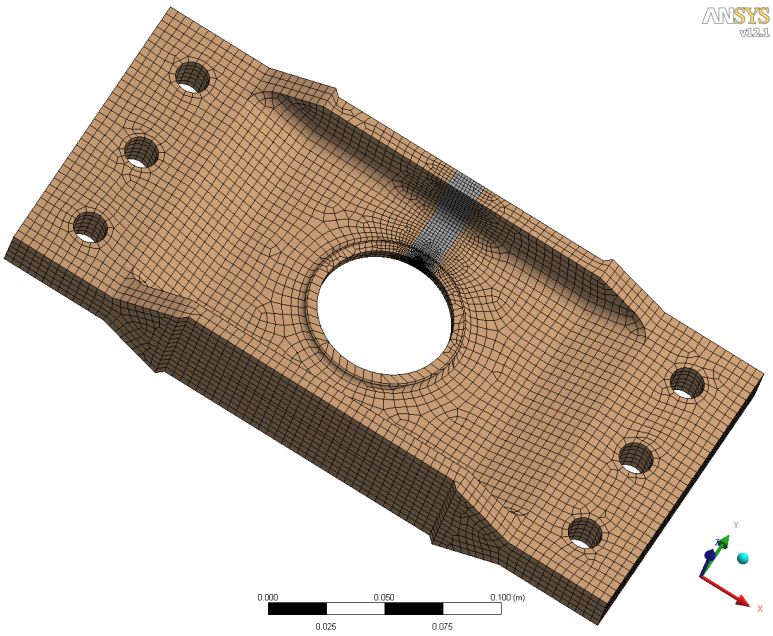

Figure 3.8 Mesh of the whole helicopter round-robin test-case.

degrees of freedom are excluded from the postprocess. On Figure 3.10, several results of displacement solution and von Mises stress chart are presented, for both the initial and the final crack configurations. Those figures allow to comprehend finely how the whole model is set up.

For this test-case, the maximum number of time step reachable by the morphing technique was automatically determined to be 4096. Then, an initial guess was performed to determine the number of update intervals of the first pass. Indeed, in the previous rectangular tension sample example, this pass was constituted of only two update intervals, and obviously that it is not enough to perform accurate computations. So here, in the first pass, the number of update intervals was chosen to be height. With a convergence criterion $\varepsilon_a = 2.5 \times 10^{-5}$, the whole analysis converges after three adaptive passes. The converged, final crack front positions obtained at the end of the computations are depicted on Figures 3.11(a) – (b). The fronts histories along the different adaptive passes are also proposed. On Figure 3.11(c), the three last crack front configurations obtained at the end of the first pass appear perturbed. The explanation comes from the fact that the CTCP model is highly nonlinear, and hence the predicted crack growth rates are very sensitive to small variations of the stress intensity factor values. Furthermore, those variations will lead to more visible perturbations on the front configurations when the update interval is large. This is why these perturbations are clearly identifiable on the first adaptive pass and totally disappear on the subsequent ones.

Some postprocess data more specific to fracture mechanics is also given. Hence the mode I stress intensity factors corresponding to the crack front history obtained at the end of the computations are plotted on Figure 3.12. Moreover, the associated mean crack growth is shown on Figure 3.13, as a function of time.

In addition, the history of the adaptive pass convergence checks is depicted on Figure 3.14. This approach leaded to perform 45 finite element resolutions, among which only 16 are associated to a full solve, leading to substantial CPU time reduction. The history of the force residuals,

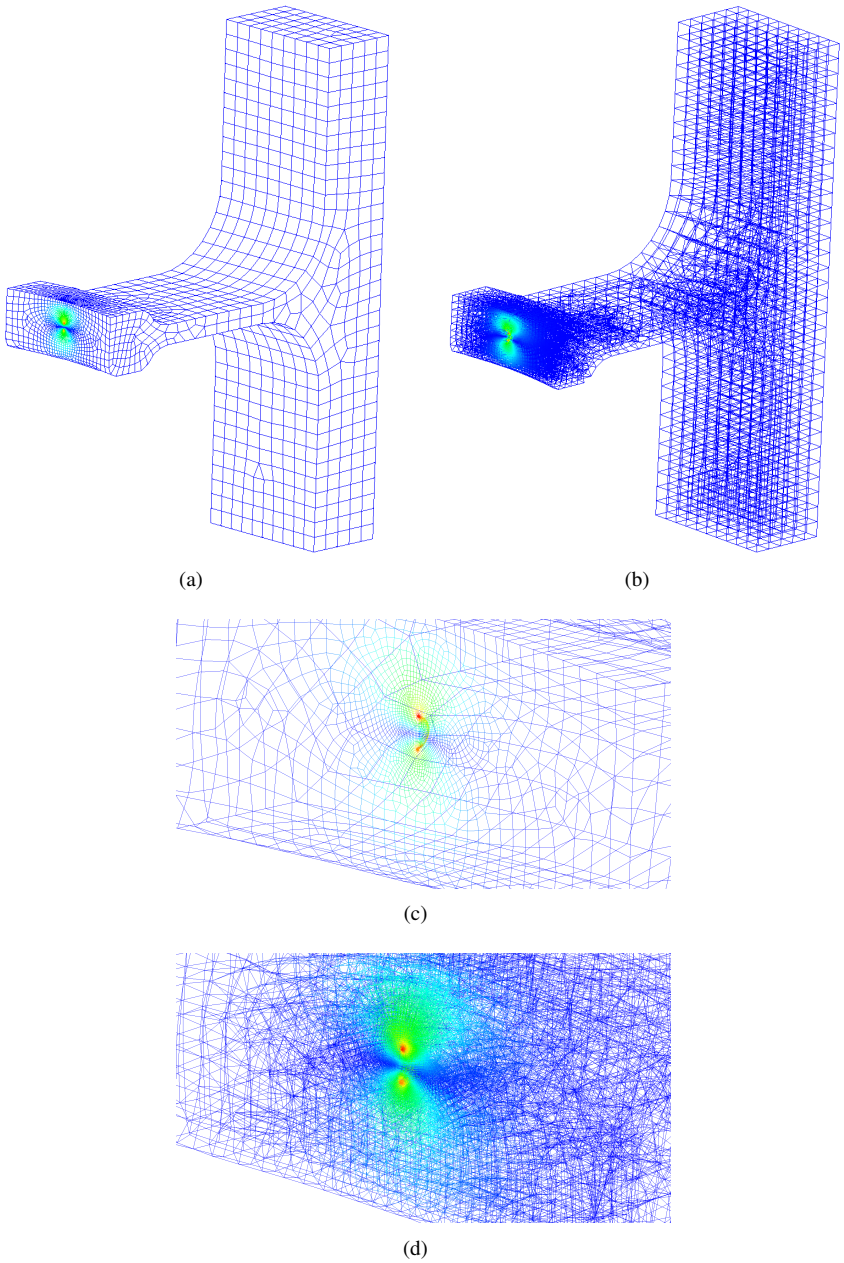

Figure 3.9 Example of mesh morphing results for the helicopter round-robin test-case. The morphing is performed locally in an interest zone around the crack. Overview and closeups are presented for both the skin mesh (a) – (c) and the volume mesh morphing (b) – (d).

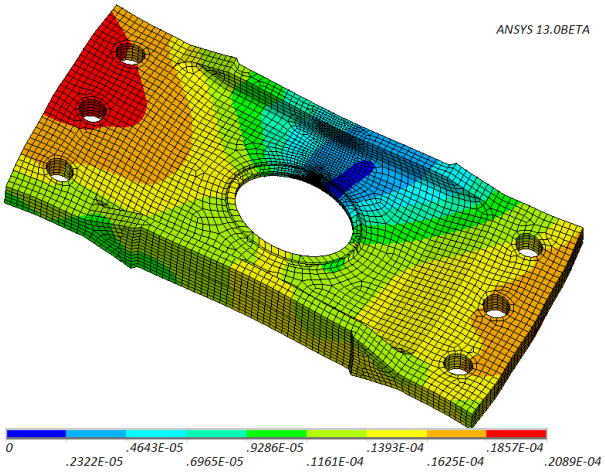

(a)

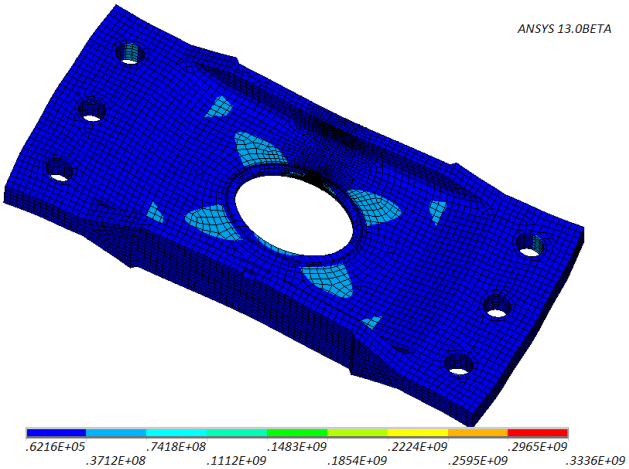

(b)

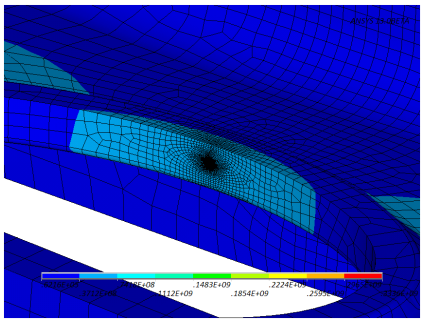

(c)

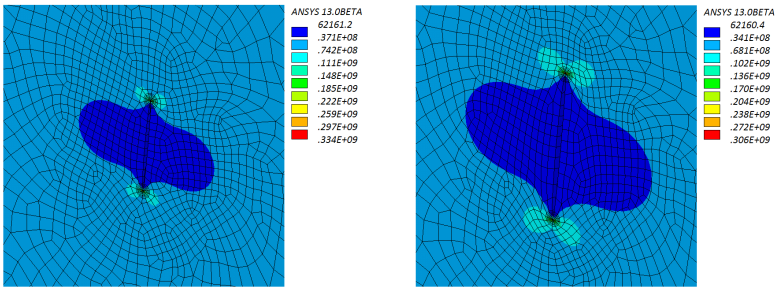

(d) (e)

Figure 3.10 Displacement solution and von Mises stress results for the initial ((a) to (d)) and the final configurations (e).

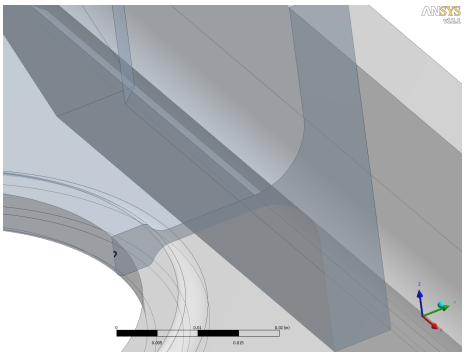

(a) Overview of the final fronts

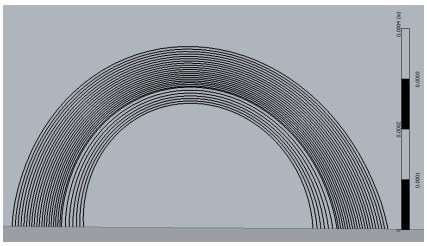

(b) Closeup of the final fronts

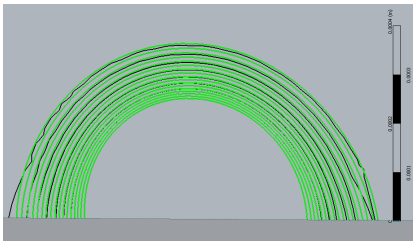

(c) Closeup of the first and second passes

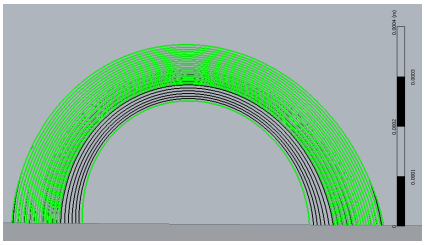

(d) Closeup of the second and third passes

Figure 3.11 Overview (a) and closeups (b) of the front positions obtained at the end of the adaptive computations performed on the helicopter round robin problem. Computed crack front positions along the 3 different adaptive passes 3.11(c) – 3.11(d). The passes are compared by pairs, and the fronts corresponding to the former pass are depicted in black, while the fronts of the latter one are in green.

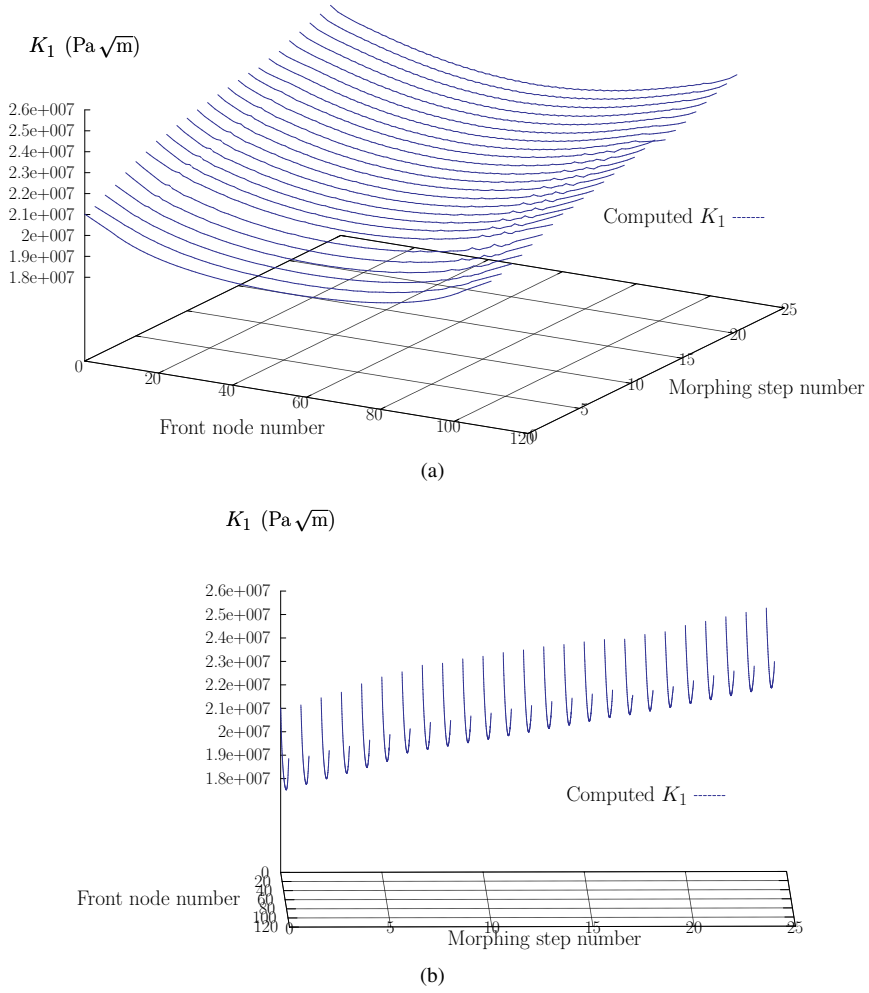

Figure 3.12 Mode I Stress intensity factor values computed along the fronts corresponding to the converged propagation solution obtained at the end of the analysis.

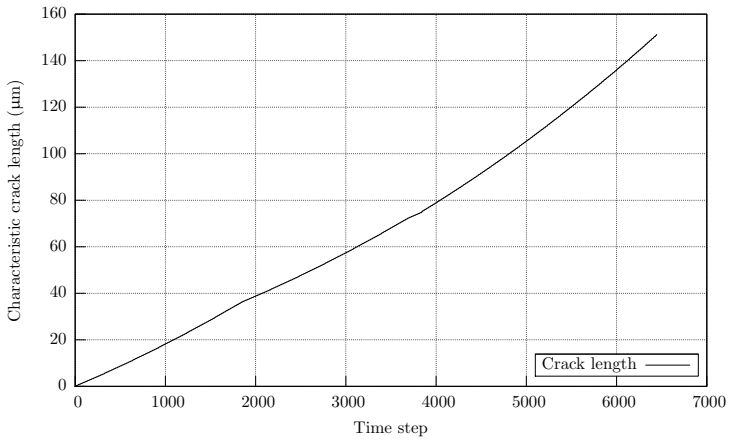

Figure 3.13 Mean crack growth corresponding to the converged propagation solution obtained at the end of the analysis.

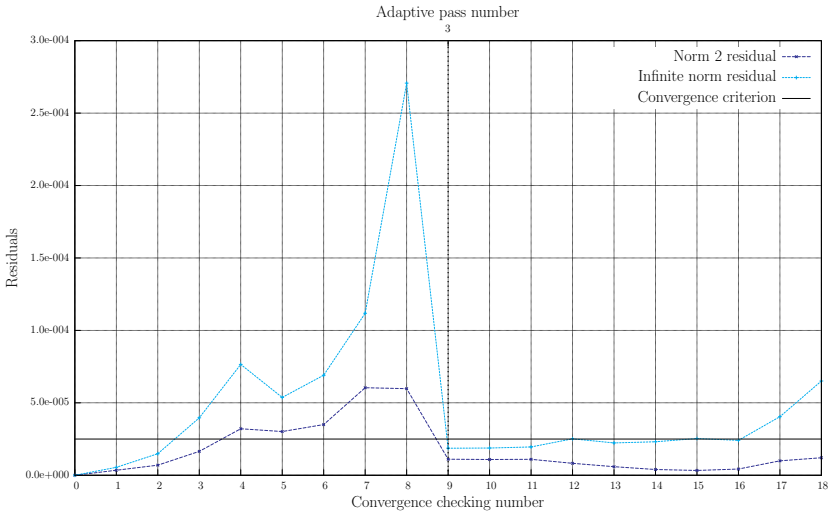

Figure 3.14 History of the check of the adaptive passes convergence all along the helicopter round robin analysis. The vertical dotted lines represent the creation of the successive passes during the computations.

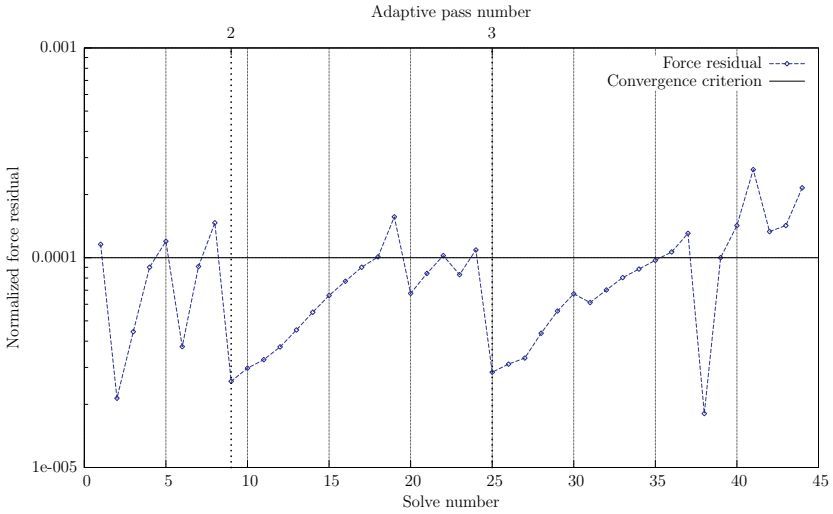

Figure 3.15 History of the reduced basis residuals of the helicopter round robin simulation.

compared to the chosen reduced basis convergence criterion $\varepsilon_r = 10^{-4}$, is plotted on Figure 3.15.

It is enhanced that the crack is very small compared to the overall dimensions of the part. Hence the spatial scale separability between the structure and the crack is particularly striking in this case. Indeed, the global displacement of the structure is totally captured by the first shape function of the reduced basis, as shown on Figure 3.16. In the subsequent basis vector, all the information is very localized around the crack. As introduced in section 3.4 of chapter 2, an hyper-reduction method is used, so that the reduced problem is solved not on the entire model, but only on a limited subset of degrees of freedom. An automatic logic allows to choose which degree of freedom to use, based on the displacement field for instance. The elements connected to those degrees of freedom are plotted on Figure 3.17, and the scale separability is also visible there, since additionally to some degrees of freedom associated to the boundary conditions, they are mainly concentrated in the cracked zone.

As in the previous example, the adaptive strategy finally allowed to perform a tridimensional fatigue crack propagation analysis taking into account the crack closure effects and ensuring a chosen accuracy for the final results, within reduced computation times.

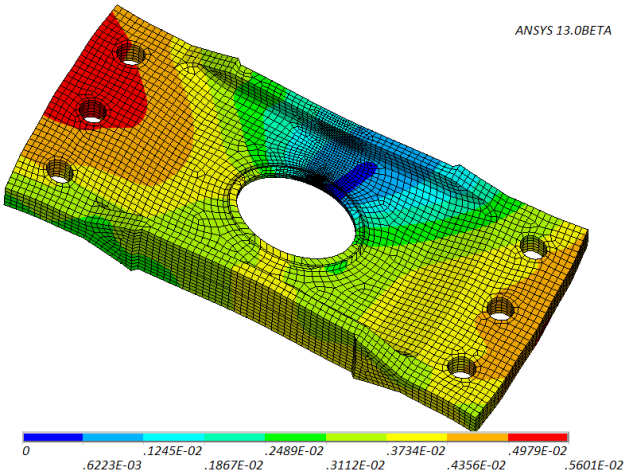

(a) First shape function

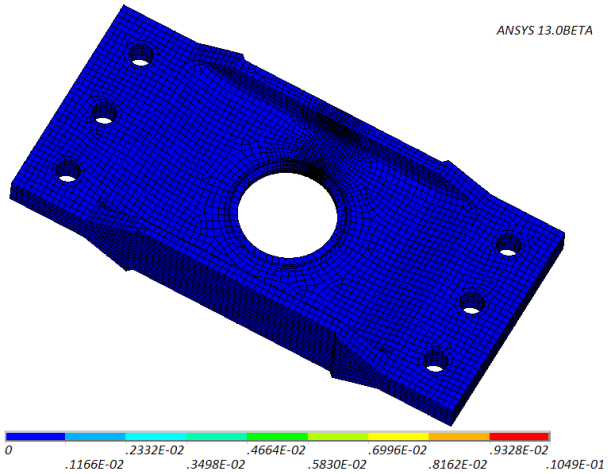

(b) Second shape function

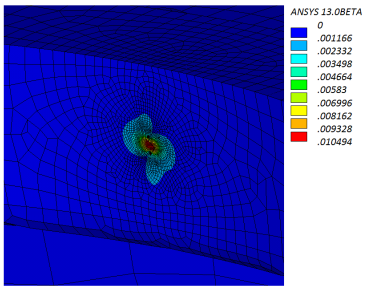

(c) Closeup of the second shape function

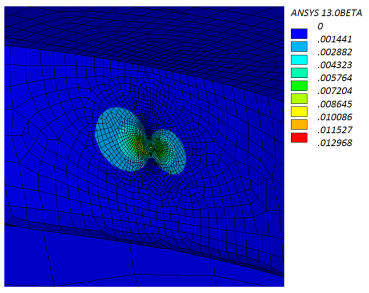

(d) Close up of the third shape function

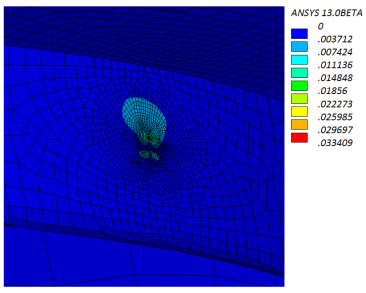

(e) Closeup of the fourth shape function

Figure 3.16 The fourth first shape functions used in the adaptive computations of the helicopter round robin.

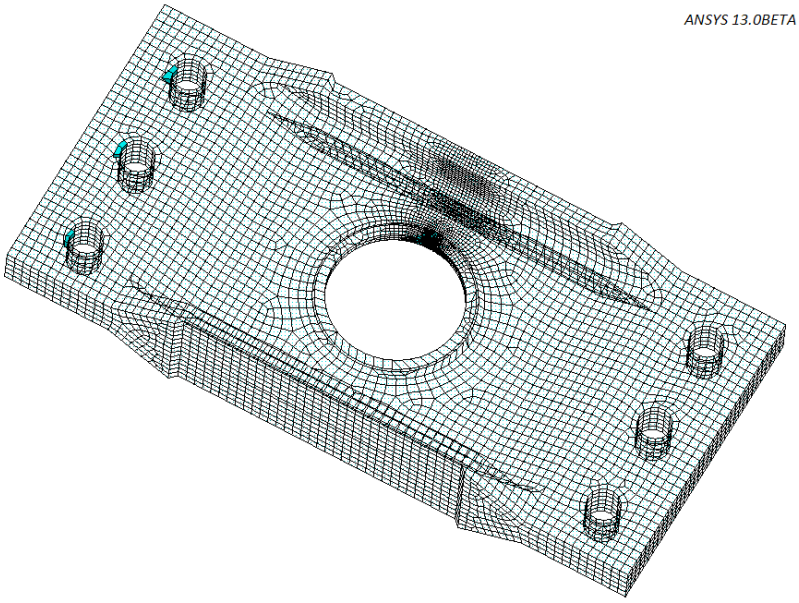

(a)

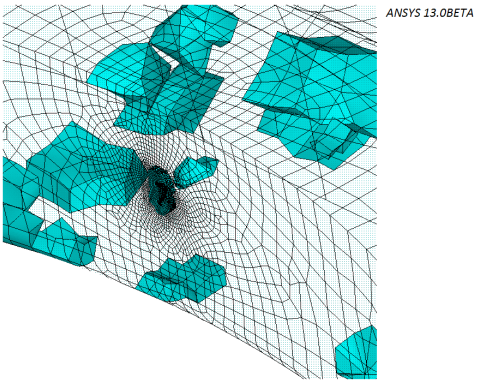

(b)

Figure 3.17 Elements connected to the degrees of freedom used in the hyper-reduction method. Additionally to some degrees of freedom connected to the boundary conditions (a) (in green in the top left corner), they are mainly located around the crack front (b).

Conclusion and future work

The work presented herein has initially started off from two main statements. First that in order to provide accurate predictions, the plasticity-induced crack closure effects must be taken into account during fatigue crack growth simulations, and secondly that those analysis must be conducted within reasonable computation times. Considering tridimensional fatigue crack propagation in complex, industrial structures, the naive approach consisting in using a finite element method to compute each fatigue loading cycle with a nonlinear elastic-plastic material behavior would lead to prohibitive computation times. In this respect, a global model reduction approach has been proposed, coupling an *a posteriori* model reduction, namely the crack tip condensed plasticity (or CTCP) model, together with an efficient acceleration technique based on an *a priori* reduced modeling approach in the ANSYS finite element software. During the crack propagation, the geometrical updates are handled by a specific mesh morphing technique. This component is of a key importance for the efficiency of the model reduction approach since it allows to take advantage of the "self-similarity" property of the singular fields around elastic crack tips. Furthermore, the CTCP model allows the closure effects appearing during fatigue crack growth under spectrum loading to be accounted for, without any tridimensional elastic-plastic calculations in the bulk. Combining such a model with an additional reduced basis acceleration technique can considerably decrease the computational cost of tridimensional fatigue crack growth analysis in standard finite element codes dedicated to complex engineering applications.

Additionally, the accuracy of the computed crack growth has been broached. As a matter of fact, the finite element model providing the stress intensity factors to the CTCP model does not need to be updated and solved at every time step. Indeed, the crack advance corresponding to one single time step would be very small and the induced perturbation on the displacement solution would not be captured by the finite element resolution. However, choosing *when* the finite element model should be updated, based on the crack growth provided by the CTCP model is a complicated task. In this respect, a specific *adaptive strategy* has been proposed to overcome that difficulty. The adaptive strategy provides automatically the quasi-optimal time interval to update the finite element model with respect to a given accuracy. This quasi-optimality is ensured for the whole computation since the computed time interval can vary all along the propagation. The accuracy and the efficiency of this global strategy have been shown through several preliminary examples, either in bidimensional and tridimensional cases for mode I crack propagation, including the industrial example of an helicopter structure.

It has been pointed out that using a mesh morphing technique to perform the geometrical updates of the model allows to preprocess the reduced basis shape functions, which are consequently expressed in the moving local basis linked to the crack front. It appears that this specific basis is adapted to express the local singular fields of the linear elastic fracture mechanics, and it allows to artificially smooth the manifold to which the solutions of the propagation problem belong. Consequently, this manifold can be approximated by a linear subspace. However, this preprocessing step does not guarantee that this linear subspace would be of a low dimension.

Fortunately, the "self-similarity" of the local crack singular fields provides that necessary condition. Hence, fracture mechanics in linear elastic media appeared to be a good candidate to model reduction techniques.

The previous remark leads directly to the limitation of the method. Indeed, the whole strategy stands on the *spatial scales separability* property of the problem. It has been shown several times that at least two specific spatial scales exist in such problems, a first one associated to the global scale of the structure and a second one linked to the local scale of the crack. Thus considering that those scales are mainly separable consists in considering that the perturbations of the global shape of the solution fields induced by the growing crack are small. A clear visual manifestation of this phenomenon comes when looking at the shape functions constituting the reduced basis of a problem that behaves well. The global characteristics of the solution fields are easily captured in a few shape functions, and the subsequent ones are dedicated to provide localized information around the crack. The most often, this approach is consistent, however some cases revealed to behave differently. Anyway, the statement on the good or bad behavior of a specific test-case with respect to the reduced basis approach should be qualified because the proposed reduced basis method exhibit some convergence properties. In other words, it always exists a *small enough* propagation range in which the method will be efficient. In addition, the extra cost brought by the use of the proposed model reduction technique on problems for which it is not efficient is marginal. In this respect, attempts of applying it on any type of crack propagation computation can always been envisaged.

Thereby, a number of perspectives are open for future work. First of all, setting up indicators that would estimate *a priori* the quality of the behavior of a given application with respect to the reduced basis approach, based on the initial solution fields for instance. A second perspective would be linked to recent work that has emerged around the Williams' series expansion of the crack tip singular fields [PAS 10, RÉT 10]. Indeed, a multiscale reduced basis could be envisaged, with finite element based shape functions capturing specifically the phenomena associated to the global scale of the structure and some other, for instance based on the Williams' series expansion, dedicated to the local behavior of the crack. Additionally, this might simplify the quality checking of the solution obtained by the reduced basis method, and the choice of an appropriate convergence criterion. A last perspective for this work might be trying to avoid the use of the mesh morphing technique, consequently envisage to couple a reduced basis approach with numerical method adapted to crack propagation computations, such as the enriched methods in general [SUK 08, PER 10]. Indeed, compared to the finite element method, those enriched methods present the advantage that no remeshing is involved, so that the possible global shape functions would not have to be mapped onto various meshes during the propagation.

Finally, in the near future, the stress intensity factor computation can be greatly improved in the ANSYS software. Indeed, the integration domain of the path independent integrals is the finite elements themselves, making the computations sensitive to the mesh quality. Using an external integration domain, fitted around the finite element can be a choice solution. In addition, the fastness of the successive morphing solves used for 3D crack growth simulations can be improved as well. Since the morphing process is based on the resolution of partial differential equations, a suitable model reduction approach, similar to the one used for the structural problems, can be set up. A recent work explores this perspective, in the context of fluid-structure interactions [BOG 10]. This may constitute one of the future enhancements of the method, together with attempts to use the global strategy in mixed mode crack growth under proportional loadings.

Appendix A

Figures and examples

Some figures representing the identification of the CTCP blunting law parameters are shown hereinafter. Examples of the second order polynomial interpolation of the variations of these parameters with respect to the T/K ratio are given as well, together with the corresponding polynomials.

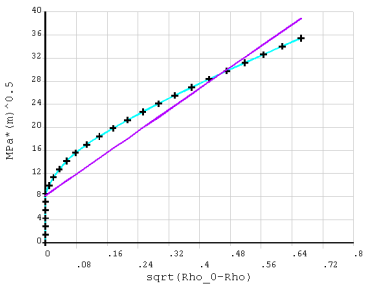

(a) Curve obtained by finite element computation (in green) and least square fit (in purple) represented in a $(K_0^{\infty} - K^{\infty}) - (\sqrt{\rho_0 - \rho})$ chart.

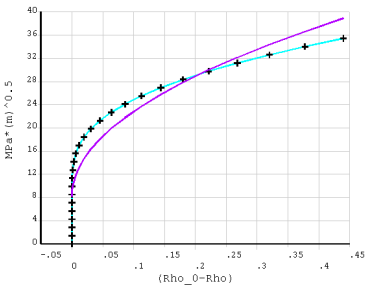

(b) In a $(K_0^{\infty} - K^{\infty}) - (\rho_0 - \rho)$ chart.

Figure A.1 Example of identification of the a_{cf} and b_{cf} parameters.

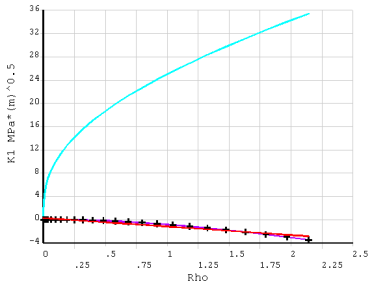

Figure A.2 Example of identification of the a_{xm} parameter in a $K_{\mathrm{I}}^{\infty} - \rho$ chart.

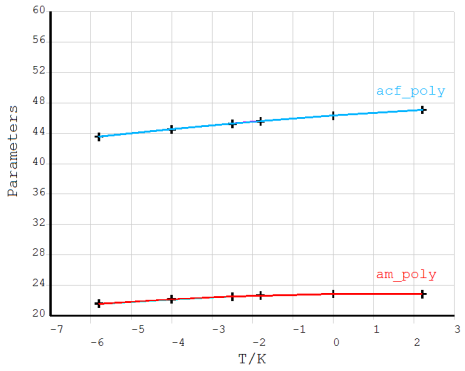

(a) $a_m = -0.0268 \cdot (T/K)^2 + 0.00566 \cdot (T/K) - 0.0186$
$a_{cf} = -6.91 \cdot 10^{-7} \cdot (T/K)^2 + 4.39 \cdot 10^{-6} \cdot (T/K) + 0.0193$

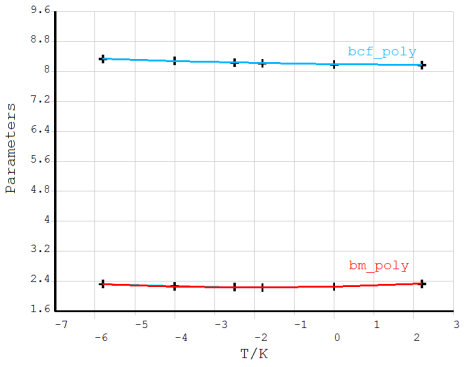

(b)
$b_m = -0.00186 \cdot (T/K)^2 - 0.0193 \cdot (T/K) - 1.743 \cdot 10^{-5}$
$b_{cf} = 0.0634 \cdot (T/K)^2 + 0.0211 \cdot (T/K) + 0.386$

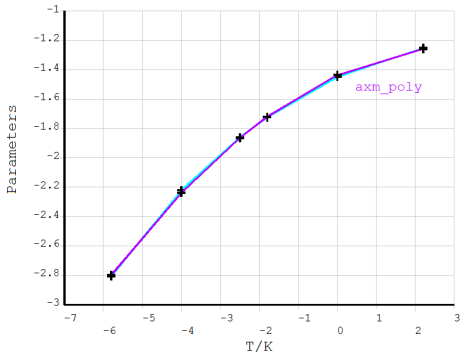

(c) $a_{xm} = -0.0138 \cdot (T/K)^2 + 0.123 \cdot (T/K) - 2.157 \cdot 10^{-4}$

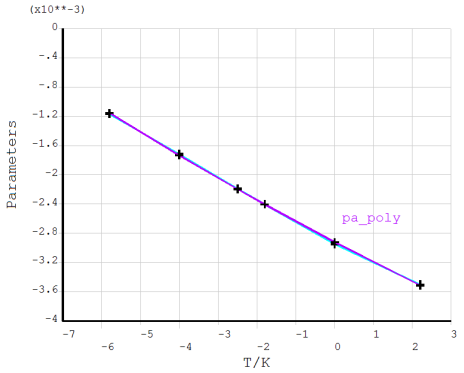

(d)
$p_a = 1.816 \cdot 10^{-4} \cdot (T/K)^2 - 2.793 \cdot 10^{-4} \cdot (T/K) - 0.123$

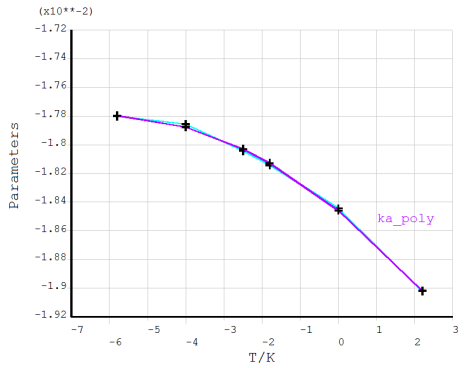

(e) $k_a = 22.836 \cdot (T/K)^2 + 2.253 \cdot (T/K) + 46.315$

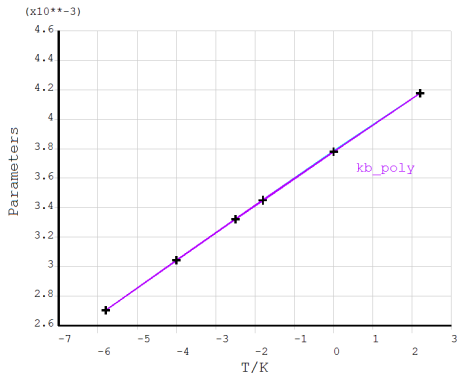

(f) $k_b = 8.192 \cdot (T/K)^2 - 1.435 \cdot (T/K) - 0.0184$

Figure A.3 Examples of the second order polynomial interpolation of the variations of the CTCP parameters with respect to the T/K ratio. The polynomial equations are presented in legend.

Bibliography

[ALE 02] Alexa M.
Recent advances in mesh morphing. *Computer graphics forum*, vol. 21, n° 2, 2002, p. 173–196.

[ALI 02] Aliabadi M.
The boundary element method. Volume 2, Applications in solids and structures. Wiley, 2002.

[AMM 08] Ammar A., Chinesta F.
Circumventing curse of dimensionality in the solution of highly multidimensional models encountered in quantum mechanics using meshfree finite sums decomposition. *Meshfree Methods for Partial Differential Equations IV*, vol. 65, 2008, p. 1–17.

[AMM 10] Ammar A.
The proper generalized decomposition: a powerful tool for model reduction. *International Journal of Material Forming*, vol. 3, n° 2, 2010, p. 89–102.

[AND 05] Anderson T.
Fracture mechanics: fundamentals and applications. CRC, 2005.

[AST 09] ASTM
Standard E 399-90: Standard test method for plane-strain fracture toughness of metallic materials. *Annual Book of ASTM Standards*, vol. 3, 2009, p. 443–473.

[BAR 77] Barsoum R.
Triangular quarter-point elements as elastic and perfectly-plastic crack tip elements. *International Journal for Numerical Methods in Engineering*, vol. 11, n° 1, 1977, p. 85–98.

[BAR 95] Barrett A., Reddien G.
On the reduced basis method. *Zeitschrift für Angewandte Mathematik und Mechanik*, vol. 75, n° 7, 1995, p. 543–549.

[BAT 97] Bathias C., Baïlon J.
La Fatigue des Matériaux et des Structures. Hermès, 1997.

[BÉC 08] Béchet É., Moës N., Wohlmuth B.
A stable Lagrange multiplier space for stiff interface conditions within the extended finite element method. *International Journal for Numerical Methods in Engineering*, vol. 78, n° 8, 2008, p. 931–954.

[BEL 94] Belytschko T., Lu Y., Gu L. et al.
Element-free Galerkin methods. *International Journal for Numerical Methods in Engineering*, vol. 37, n° 2, 1994, p. 229–256.

[BEL 00] Belytschko T., Liu W., Moran B.
Nonlinear finite element analysis for continua and structures. Wiley New York, 2000.

[BLO 00] Blom F.
Considerations on the spring analogy. *International Journal for Numerical Methods in Fluids*, vol. 32, n° 6, 2000, p. 647–668.

[BOG 10] Bogaers A.
MEng dissertation, Reduced order modeling techniques for mesh movement as applied to fluid structure interactions. Thèse de doctorat, University of Pretoria, Pretoria, 2010.

[BON 95] Bonnet M., Xiao H.
Computation of energy release rate using material differentiation of elastic BIE for 3-D elastic fracture. *Engineering Analysis with Boundary Elements*, vol. 15, n° 2, 1995, p. 137–150.

[BON 04] Bonnet M.
Boundary integral equation methods for elastic and plastic problems. *Encyclopedia of Computational Mechanics*, vol. 2, 2004.

[BOR 02] Borja R.
Finite element simulation of strain localization with large deformation: capturing strong discontinuity using a Petrov–Galerkin multiscale formulation. *Computer Methods in Applied Mechanics and Engineering*, vol. 191, 2002, p. 2949–2978.

[BUF 09] Buffa A., Maday Y., Patera A., PrudŠhomme C., G. T.
A priori convergence of the greedy algorithm for the parametrized reduced basis. *Mathematical Modelling and Numerical Analysis*, 2009.

[BUI 78] Bui H., Germain P.
Mécanique de la rupture fragile. Masson Paris, 1978.

[CAN 07] Cancès E., Le Bris C., Nguyen N., Maday Y., Patera A., Pau G.
Feasibility and competitiveness of a reduced basis approach for rapid electronic structure calculations in quantum chemistry. *Proceedings of the Workshop for High-dimensional Partial Differential Equations in Science and Engineering (Montreal)*, vol. 41, 2007, p. 15–57.

[CEA 64] Cea J.
Approximation variationnelle des problèmes aux limites. *Annales de l'Institut Fourier*, vol. 14, n° 2, 1964, p. 345–444.

[COT 80] Cotterell B., Rice J.
Slightly curved or kinked cracks. *International Journal of Fracture*, vol. 16, n° 2, 1980, p. 155–169.

[CRA 68] Craig R., Bampton M.
Coupling of structures for dynamic analysis. *AIAA Journal*, vol. 6, n° 7, 1968, p. 1313–1316.

[DAU 00] Daux C., Moes N., Dolbow J., Sukumar N., Belytschko T.
Arbitrary branched and intersecting cracks with the extended finite element method. *International Journal for Numerical Methods in Engineering*, vol. 48, 2000, p. 1741–1760.

[DEC 09] Decreuse P., Pommier S., Gentot L., Pattofatto S.
History effect in fatigue crack growth under mixed-mode loading conditions. *International Journal of Fatigue*, vol. 31, n° 11-12, 2009, p. 1733–1741.

[DEC 10] Decreuse P.-Y.
Fissuration en mode mixte I+II non proportionnel – Approche expérimentale et modélisation de la plasticité. Thèse de doctorat, École Normale Supérieure de Cachan, 2010.

[DEG 02] Degand C., Farhat C.
A three-dimensional torsional spring analogy method for unstructured dynamic meshes. *Computers and Structures*, vol. 80, n° 3-4, 2002, p. 305–316.

[DEP 10] Deparis S., Løvgren A.
Stabilized reduced basis approximation of incompressible three-dimensional Navier–Stokes equations in parametrized deformed domains. rapport, 2010, École Polytechnique Fédérale de Lausanne.

[DES 83] Destuynder P., Lescure S., Djaoua M.
Some remarks on elastic fracture mechanics. *Journal de Mécanique Théorique et Appliquée*, vol. 2, n° 1, 1983, p. 113–135.

[DES 02] Desbrun M., Meyer M., Alliez P.
Intrinsic parameterizations of surface meshes. *Computer Graphics Forum*, vol. 21, n° 3, 2002, p. 209–218.

[DOU 31] Douglas J.
Solution of the problem of Plateau. *Transactions of the American Mathematical Society*, vol. 33, 1931, p. 263–321.

[DUG 60] Dugdale D.
Yielding of steel sheets containing slits. *Journal of Mechanics Physics of Solids*, vol. 8, 1960, p. 100–104.

[ELB 70] Elber W.
Fatigue crack closure under cyclic tension. *Engineering Fracture Mechanics*, vol. 2, n° 1, 1970, p. 37–44.

[ELB 71] Elber W.
The significance of crack closure. *ASTM STP*, vol. 486, 1971, p. 230–242.

[ELG 07] Elguedj T., Gravouil A., Combescure A.
A mixed augmented Lagrangian-extended finite element method for modelling elastic-plastic fatigue crack growth with unilateral contact. *International Journal for Numerical Methods in Engineering*, vol. 71, n° 13, 2007, p. 1569–1597.

[ESH 56] Eshelby J.
The continuum theory of lattice defects. *Solid State Physics*, vol. 3, 1956, p. 79–144.

[FOD 02] Fodor I.
A survey of dimension reduction techniques. rapport, 2002, US DOE Office of Scientific and Technical Information.

[FOR 67] Forman R., Kearney V., Engle R.
Numerical analysis of crack propagation in cyclic-loaded structures. *Journal of Basic Engineering*, vol. 89, n° 3, 1967, p. 459–464.

[FRA 03] Frangi A., Novati G.
BEM–FEM coupling for 3D fracture mechanics applications. *Computational Mechanics*, vol. 32, 2003, p. 415-422, Springer Berlin / Heidelberg.

[GAL 09a] Galland F., Gravouil A., Rochette M., Perrin S.
A crack tip condensed plasticity model coupled with acceleration techniques based on reduced order model approach for 3D crack growth. *Proceedings of the* 12^{th} *International Conference on Fracture*, Ottawa, Canada, 2009.

[GAL 09b] Galland F., Gravouil A., Rochette M., Perrin S.
A global model reduction approach for fatigue crack growth with confined plasticity. *Proceedings of Fatigue Design*, Paris, France, 2009 CETIM.

[GAL 10a] Galland F., Gravouil A., Malvesin E., Rochette M.
A global model reduction approach for 3D fatigue crack growth with confined plasticity. *Computer Methods in Applied Mechanics and Engineering*, 2010. doi:10.1016/j.cma.2010.08.018.

[GAL 10b] Galland F., Gravouil A., Rochette M.
A global/local model reduction approach dedicated to 3D fatigue crack growth with crack closure effect. *IOP Conference Series: Materials Science and Engineering*, vol. 10 IOP Publishing, 2010.

[GAL 10c] Galland F., Gravouil A., Rochette M., Perrin S.
A global model reduction approach for 3D fatigue crack growth with confined plasticity. *Proceedings of the European Conference on Computational Mechanics*, Paris, France, 2010 ECCOMAS.

[GON 10] González D., Ammar A., Chinesta F., Cueto E.
Recent advances on the use of separated representations. *International Journal for Numerical Methods in Engineering*, vol. 81, n° 5, 2010, p. 637–659.

[GOS 02] Gosz M., Moran B.
An interaction energy integral method for computation of mixed-mode stress intensity factors along non-planar crack fronts in three dimensions. *Engineering Fracture Mechanics*, vol. 69, n° 3, 2002, p. 299–319.

[GRA 84] Gram J.
Undersøgelser angaaende Maengden af Primtal under en given Graeense. *Det K. Videnskabernes Selskab*, vol. 2, 1884, p. 183–308.

[GRI 21] Griffith A.
The Phenomena of Rupture and Flow in Solids. *Philosophical Transactions of the Royal Society of London. Series A, Containing Papers of a Mathematical or Physical Character*, vol. 221, 1921, p. 163–198.

[HAM 06] Hamam R.
Simulation de la propagation des fissures par fatigue dans les toiles des roues de train sous chargement à amplitude variable. Thèse de doctorat, École Normale Supérieure de Cachan, 2006.

[HAM 07] Hamam R., Pommier S., Bumbieler F.
Variable amplitude fatigue crack growth, experimental results and modeling. *International Journal of Fatigue*, vol. 29, n° 9-11, 2007, p. 1634–1646.

[HEL 03] Helenbrook B.
Mesh deformation using the biharmonic operator. *International Journal for Numerical Methods in Engineering*, vol. 56, n° 7, 2003, p. 1007–1021.

[HEN 10] Henninger C., Roux S., Hild F.
Enriched kinematic fields of cracked structures. *International Journal of Solids and Structures*, vol. 47, n° 24, 2010.

[HOT 33] Hotelling H.
Analysis of a complex of statistical variables into principal components. *Journal of educational psychology*, vol. 24, n° 6, 1933, p. 417–441.

[HUY 07] Huynh D., Patera A.
Reduced basis approximation and *a posteriori* error estimation for stress intensity factors. *International Journal for Numerical Methods in Engineering*, vol. 72, n° 10, 2007, p. 1219–1259.

[IRW 57] Irwin G.
Analysis of stresses and strains near the end of a crack traversing a plate. *Journal of Applied Mechanics*, vol. 24, 1957, p. 361–364.

[IRW 61] Irwin G.
Plastic zone near a crack and fracture toughness. *Sagamore Research Conference Proceedings*, vol. 4 Syracuse University Research Institute, Syracuse NY, 1961, p. 63–78.

[JAM 85] James M., Knott J.
An assessment of crack closure and the extent of the short crack regime in Q1N (HY80) steel. *Fatigue & Fracture of Engineering Materials & Structures*, vol. 8, n° 2, 1985, p. 177–191.

[JOH 07] Johnson J., Qu J.
An interaction integral method for computing mixed mode stress intensity factors for curved bimaterial interface cracks in non-uniform temperature fields. *Engineering Fracture Mechanics*, vol. 74, n° 14, 2007, p. 2282–2291.

[KAR 43] Karhunen K.
Uber lineare methoden für wahrscheinigkeitsrechnung. *Annales of Academic Science Fennicae Series A1 Mathematical Physics*, vol. 37, 1943, p. 3–79.

[KOL 36] Kolmogoroff A.
Uber die beste Annaherung von Funktionen einer gegebenen Funktionenklasse. *Annals of Mathematics*, vol. 37, n° 1, 1936, p. 107–110.

[KRY 99] KRYSL P., BELYTSCHKO T.
The element free Galerkin method for dynamic propagation of arbitrary 3-D cracks. *International Journal for Numerical Methods in Engineering*, vol. 44, n° 6, 1999, p. 767–800.

[KRY 01] KRYSL P., LALL S., MARSDEN J.
Dimensional model reduction in non-linear finite element dynamics of solids and structures. *International Journal for Numerical Methods in Engineering*, vol. 51, 2001, p. 479–504.

[LAD 09] LADEVÈZE P., PASSIEUX J., NÉRON D.
The LATIN multiscale computational method and the Proper Generalized Decomposition. *Computer Methods in Applied Mechanics and Engineering*, vol. 199, n° 21-22, 2009, p. 1287–1296.

[LAI 67] LAIRD C.
The influence of metallurgical structure on the mechanisms of fatigue crack propagation. *Fatigue Crack Propagation, ASTM STP NO 415. 1967, 131-180*, 1967.

[LAR 96] LARSSON R., RUNESSON K., STURE S.
Embedded localization band in undrained soil based on regularized strong discontinuity-theory and FE-analysis. *International Journal of Solids and Structures*, vol. 33, n° 20, 1996, p. 3081–3102.

[LAX 54] LAX P., MILGRAM A.
Parabolic equations. *Annals in Mathematics Studies*, vol. 33, 1954, p. 167–190.

[LAZ 10] LAZARUS V.
Three-dimensional linear elastic fracture mechanics: from theory to practice. Habilitation à Diriger des Recherches de l'Université Pierre et Marie Curie (UPMC Univ Paris 6), 2010.

[LEB 99] LEBLOND J.
Crack paths in three-dimensional elastic solids. I: two-term expansion of the stress intensity factors–application to crack path stability in hydraulic fracturing. *International Journal of Solids and Structures*, vol. 36, n° 1, 1999, p. 79–103.

[LEE 07] LEE J., VERLEYSEN M.
Nonlinear dimensionality reduction. Springer Verlag, 2007.

[LEM 90] LEMAITRE J., CHABOCHE J.
Mechanics of Solid Materials. Cambridge University Press, 1990.

[LIA 02] LIANG Y., LEE H., LIM S., LIN W., LEE K., WU C.
Proper orthogonal decomposition and its applications – Part I: theory. *Journal of Sound and Vibration*, vol. 252, n° 3, 2002, p. 527–544.

[LIU 95] LIU W., JUN S., ZHANG Y.
Reproducing kernel particle methods. *International Journal for Numerical Methods in Fluids*, vol. 20, n° 8-9, 1995, p. 1081–1106.

[LIU 04] LIU X., XIAO Q., KARIHALOO B.
XFEM for direct evaluation of mixed mode SIFs in homogeneous and bi-materials. *International Journal for Numerical Methods in Engineering*, vol. 59, n° 8, 2004, p. 1103–1118.

[LOÈ 55] LOÈVE M.
Probability theory. Foundations. Random sequences. Toronto, Van Nostrand, 1955.

[LØV 06] LØVGREN A., MADAY Y., RØNQUIST E.
A reduced basis element method for the steady Stokes problem: Application to hierarchical flow systems. *Modeling Identification and Control*, vol. 27, n° 2, 2006, Page 79.

[MAD 02] MADAY Y., PATERA A., TURINICI G.
A Priori Convergence Theory for Reduced-Basis Approximations of Single-Parameter Elliptic Partial Differential Equations. *Journal of Scientific Computing*, vol. 17, n° 1, 2002, p. 437–446.

[MAD 06] MADAY Y.
Reduced basis method for the rapid and reliable solution of partial differential equations. *Proceedings of International Conference of Mathematicians, Madrid. European Mathematical Society Eds*, 2006.

[MAR 05] Margonari M., Bonnet M.
Fast multipole method applied to elastostatic BEM-FEM coupling. *Computers & Structures*, vol. 83, n° 10-11, 2005, p. 700–717.

[MCC 91] McClung R.
Crack closure and plastic zone sizes in fatigue. *Fatigue & Fracture of Engineering Materials & Structures*, vol. 14, n° 4, 1991, p. 455–468.

[MEL 96] Melenk J., Babuka I.
The partition of unity finite element method: basic theory and applications. *Computer methods in applied mechanics and engineering*, vol. 139, n° 1-4, 1996, p. 289–314.

[MI 94] Mi Y., Aliabadi M.
Three-dimensional crack growth simulation using BEM. *Computers & Structures*, vol. 52, n° 5, 1994, p. 871–878.

[MOË 99] Moës N., Dolbow J., Belytschko T.
A finite element method for crack growth without remeshing. *International Journal for Numerical Methods in Engineering*, vol. 46, n° 1, 1999, p. 131–150.

[MOË 02] Moës N., Gravouil A., Belytschko T.
Non-planar 3D crack growth by the extended finite element and level sets — Part I: Mechanical model. *International Journal for Numerical Methods in Engineering*, vol. 53, 2002, p. 2549–2568.

[MON 05] Monaghan J.
Smoothed particle hydrodynamics. *Reports on Progress in Physics*, vol. 68, 2005, Page 1703.

[MOR 87] Moran B., Shih C.
Crack tip and associated domain integrals from momentum and energy balance. *Engineering Fracture Mechanics*, vol. 27, n° 6, 1987, p. 615–642.

[MOU 09] de Moura Pinho R., Pommier S., Longuet A., Mary C., Vogel F.
A multiaxial endurance criterion for LCF/HCF complex cycles. *Proceedings of Fatigue Design*, Paris, France, 2009 CETIM.

[NAK 92] Nakamura T., Parks D.
Determination of elastic T-stress along three-dimensional crack fronts using an interaction integral. *International Journal of Solids and Structures*, vol. 29, n° 13, 1992, p. 1597–1611.

[NAY 92] Nayroles B., Touzot G., Villon P.
Generalizing the finite element method: diffuse approximation and diffuse elements. *Computational mechanics*, vol. 10, n° 5, 1992, p. 307–318.

[NEU 69] Neumann P.
Coarse slip model of fatigue. *Acta Metallurgica*, vol. 17, n° 9, 1969, p. 1219–1225.

[NEW 76] Newman J.
A finite element analysis of fatigue crack closure. *ASTM special technical publication*, vol. 590, 1976, p. 281–301, American Society for Testing and Materials.

[NEW 81] Newman Jr J.
A crack closure model for predicting fatigue crack growth under aircraft spectrum loading. *Methods and Models for Predicting Fatigue Crack Growth Under Random loading- ASTM STP 748* Astm Intl, 1981, p. 53–84.

[NEW 92] Newman Jr J.
FASTRAN-2: A fatigue crack growth structural analysis program. *NASA STI/Recon Technical Report N*, vol. 92, 1992, Page 30964.

[NEW 97] Newman Jr J.
The merging of fatigue and fracture mechanics concepts: a historical perspective. *Fatigue and fracture mechanics*, vol. 28, 1997, Page 3, ASTM International.

[NEW 06] Newman J., Irving P., Lin J., Le D.
Crack growth predictions in a complex helicopter component under spectrum loading. *Fatigue & fracture of engineering materials & structures*, vol. 29, n° 11, 2006, p. 949–958.

[NIK 01] Nikishkov G. A. S.
SGBEM-FEM alternating method for analyzing 3D non-planar cracks and their growth in structural components. *CMES-Computer Modeling in Engineering and Sciences*, vol. 2, n° 3, 2001, p. 401–422.

[NIR 10] Niroomandi S., Alfaro I., Cueto E., Chinesta F.
Accounting for large deformations in real-time simulations of soft tissues based on reduced-order models. *Computer Methods and Programs in Biomedicine*, 2010. doi:10.1016/j.cmpb.2010.06.012.

[NIS 02] Nishimura N.
Fast multipole accelerated boundary integral equation methods. *Applied Mechanics Reviews*, vol. 55, 2002, Page 299.

[NOO 80] Noor A., Peters J.
Reduced basis technique for nonlinear analysis of structures. *AIAA Journal*, vol. 18, n° 4, 1980, p. 455–462.

[OLI 02] Oliver J., Huespe A., Pulido M., Chaves E.
From continuum mechanics to fracture mechanics: the strong discontinuity approach. *Engineering Fracture Mechanics*, vol. 69, n° 2, 2002, p. 113–136.

[PAR 63] Paris P E. F.
A critical analysis of crack propagation laws. *Journal of Basic Engineering*, vol. 85, n° 4, 1963, p. 528–534.

[PAR 74] Parks D.
A stiffness derivative finite element technique for determination of crack tip stress intensity factors. *International Journal of Fracture*, vol. 10, n° 4, 1974, p. 487–502.

[PAS 10] Passieux J., Gravouil A., Réthoré J., Baietto M. C.
Direct estimation of generalized stress intensity factors using a three-scale concurrent multigrid X-FEM. *International Journal for Numerical Methods in Engineering*, 2010. doi:10.1002/nme.3037.

[PEA 01] Pearson K.
On lines and planes of closest fit to systems of points in space. *Philosophical Magazine Series 6*, vol. 2, n° 11, 1901, p. 559–572.

[PEL 69] Pelloux R.
Mechanisms of formation of ductile fatigue striations. *ASM Trans. Quart.*, vol. 62, n° 1, 1969, p. 281–285.

[PER 09] Pereira J., Duarte C., Guoy D., Jiao X.
Hp-Generalized FEM and crack surface representation for non-planar 3-D cracks. *International Journal for Numerical Methods in Engineering*, vol. 77, n° 5, 2009, p. 601–633.

[PER 10] Pereira J., Duarte C., Jiao X.
Three-dimensional crack growth with hp-generalized finite element and face offsetting methods. *Computational Mechanics*, vol. 46, n° 3, 2010, p. 431–453.

[PIE 10] Pierrès E., Baietto M., Gravouil A.
A two-scale extended finite element method for modelling 3D crack growth with interfacial contact. *Computer Methods in Applied Mechanics and Engineering*, vol. 199, n° 17-20, 2010, p. 1165–1177.

[PIN 85] Pinkus A.
n-widths in Approximation Theory. Springer, Berlin, 1985.

[PIN 93] Pinkall U., Polthier K.
Computing discrete minimal surfaces and their conjugates. *Experimental mathematics*, vol. 2, n° 1, 1993, p. 15–36.

[POM 02] Pommier S.
Plane strain crack closure and cyclic hardening. *Engineering Fracture Mechanics*, vol. 69, n° 1, 2002, p. 25–44.

[POM 05] Pommier S., Risbet M.
Time-derivative equations for fatigue crack growth in metals. *International Journal of Fracture*, vol. 131, n° 1, 2005, p. 79–106.

[POM 07] Pommier S., Hamam R.
Incremental model for fatigue crack growth based on a displacement partitioning hypothesis of mode I elastic-plastic displacement fields. *Fatigue and Fracture of Engineering Materials and Structures*, vol. 30, n° 7, 2007, p. 582–598.

[POM 09] Pommier S., Lopez-Crespo P., Decreuse P.
A multi-scale approach to condense the cyclic elastic-plastic behaviour of the crack tip region into an extended constitutive model. *Fatigue & Fracture of Engineering Materials & Structures*, vol. 32, n° 11, 2009, p. 899–915.

[PRE 92] Press W. et al.
Numerical recipes in C. Cambridge University Press, 1992.

[RAD 30] Radó T.
The problem of the least area and the problem of Plateau. *Mathematische Zeitschrift*, vol. 32, n° 1, 1930, p. 763–796.

[RAN 09a] Rannou J., Gravouil A., Baietto-Dubourg M.
A local multigrid X-FEM strategy for 3-D crack propagation. *International Journal for Numerical Methods in Engineering*, vol. 77, n° 4, 2009, p. 581–600.

[RAN 09b] Rannou J., Limodin N., Réthoré J., Gravouil A., Ludwig W., Baietto-Dubourg M., Buffière J., Combescure A., Hild F., Roux S.
Three dimensional experimental and numerical multiscale analysis of a fatigue crack. *Computer Methods in Applied Mechanics and Engineering*, vol. 199, n° 21-22, 2009, p. 1307–1325.

[RÉT 10] Réthoré J., Roux S., Hild F.
Hybrid analytical and extended finite element method (HAX-FEM): A new enrichment procedure for cracked solids. *International Journal for Numerical Methods in Engineering*, vol. 81, n° 3, 2010, p. 269–285.

[RIC 68] Rice J.
A path independent integral and the approximate analysis of strain concentration by notches and cracks. *Journal of Applied Mechanics*, vol. 35, n° 2, 1968, p. 379–386.

[RUI 06] Ruiz-Sabariego J., Pommier S.
Modeling environment-assisted fatigue crack propagation. *Fracture of Nano and Engineering Materials and Structures Proceedings of the* 16^{th} *European Conference of Fracture*, July 2006.

[RYC 05a] Ryckelynck D.
A priori hyperreduction method: an adaptive approach. *Journal of Computational Physics*, vol. 202, n° 1, 2005, p. 346–366.

[RYC 05b] Ryckelynck D., Hermanns L., Chinesta F., Alarcon E.
An efficient 'a priori' model reduction for boundary element models. *Engineering Analysis with Boundary Elements*, vol. 29, n° 8, 2005, p. 796–801.

[RYC 06] Ryckelynck D., Chinesta F., Cueto E., Ammar A.
On the *a priori* model reduction: Overview and recent developments. *Archives of Computational Methods in Engineering*, vol. 13, n° 1, 2006, p. 91–128.

[RYC 09] Ryckelynck D.
Hyper-reduction of mechanical models involving internal variables. *International Journal for Numerical Methods in Engineering*, vol. 77, n° 1, 2009, p. 75–89.

[SAM 04] Samareh J.
Aerodynamic shape optimization based on free-form deformation. *10 th AIAA/ISSMO Multidisciplinary Analysis and Optimization Conference*, 2004.

[SCH 97] Schölkopf B., Smola A., Müller K.
Kernel principal component analysis. *Artificial Neural Networks–ICANN'97,*, 1997, p. 583–588.

[SED 86] Sederberg T., Parry S.
Free-form deformation of solid geometric models. *ACM Siggraph Computer Graphics*, vol. 20, n° 4, 1986, p. 151–160.

[SIM 92] Simo J., Laursen T.
An augmented Lagrangian treatment of contact problems involving friction. *Computers & Structures*, vol. 42, n° 1, 1992, p. 97–116.

[SIM 00] Simo J., Hughes T.
Computational inelasticity. Springer, 2000.

[SIR 87] Sirovich L.
Turbulence and the dynamics of coherent structures. I-Coherent structures. II-Symmetries and transformations. III-Dynamics and scaling. *Quarterly of Applied Mathematics*, vol. 45, 1987, p. 561–571.

[SOL 04] Solanki K., Daniewicz S., Newman J. et al.
Finite element analysis of plasticity-induced fatigue crack closure: an overview. *Engineering Fracture Mechanics*, vol. 71, n° 2, 2004, p. 149–171.

[STE 03] Stein K., Tezduyar T., Benney R.
Mesh moving techniques for fluid-structure interactions with large displacements. *Journal of Applied Mechanics*, vol. 70, 2003, Page 58.

[STR 01] Strouboulis T., Copps K., Babuška I.
The generalized finite element method. *Computer Methods in Applied Mechanics and Engineering*, vol. 190, n° 32-33, 2001, p. 4081–4193.

[SUK 01] Sukumar N., Moran B., Semenov A., Belikov V.
Natural neighbour Galerkin methods. *International Journal for Numerical Methods in Engineering*, vol. 50, n° 1, 2001, p. 1–27.

[SUK 08] Sukumar N., Chopp D., Béchet E., Moës N.
Three-dimensional non-planar crack growth by a coupled extended finite element and fast marching method. *International Journal for Numerical Methods in Engineering*, vol. 76, n° 5, 2008, p. 727–748.

[SUN 05] Sunder R.
On the hysteretic nature of variable-amplitude fatigue crack growth. *International Journal of Fatigue*, vol. 27, n° 10-12, 2005, p. 1494–1498.

[SUN 09] Sunder R.
Multi-mechanism model for fatigue crack growth under flight load spectra. *Proceedings of the International Conference on Fatigue Design*, Paris, France, 2009 CETIM.

[SUR 84] Suresh S., Ritchie R.
Propagation of short fatigue cracks. *International Materials Reviews*, vol. 29, n° 1, 1984, p. 445–475.

[TIO 09] Tiong U., Jones R.
Damage tolerance analysis of a helicopter component. *International Journal of Fatigue*, vol. 31, n° 6, 2009, p. 1046–1053.

[VER 03] Veroy K.
Reduced-basis methods applied to problems in elasticity: Analysis and applications. Thèse de doctorat, Massachusetts Institute of Technology, 2003.

[WAN 04] Wang Y., Gu X., Yau S.
Volumetric harmonic map. *Communications in Information and Systems*, vol. 3, n° 3, 2004, p. 191–202.

[WES 39] WESTERGAARD H.
Bearing pressure and cracks. *Journal of Applied Mechanics*, vol. 6, 1939, p. 49–53.

[WHE 72] WHEELER O.
Spectrum load and crack growth. *Transactions of the ASME - Journal of Basic Engineering*, vol. 4, 1972, p. 181–186.

[WIL 57] WILLIAMS M.
On the stress distribution at the base of a stationary crack. *Journal of Applied Mechanics*, vol. 24, 1957, p. 109–114.

[WIL 71] WILLENBORG J., ENGLE R., WOOD H.
A crack growth retardation model using an effective stress concept. rapport, 1971, Air Force Flight Dynamics Laboratory.

[WRO 02] WROBEL L.
The boundary element method. Volume 1, Applications in thermo-fluids and acoustics. Wiley, 2002.

[ZIE 05] ZIENKIEWICZ O., TAYLOR R.
The finite element method for solid and structural mechanics. Elsevier, 2005.

Index

FOLIO ADMINISTRATIF

THÈSE SOUTENUE DEVANT L'INSTITUT NATIONAL DES SCIENCES APPLIQUÉES DE LYON

NOM : GALLAND DATE de SOUTENANCE : 04 Février 2011

Prénoms : Florent, Élisée

TITRE : An adaptive model reduction approach for 3D fatigue crack growth in small scale yielding conditions

NATURE : Doctorat Numéro d'ordre : 2011 – ISAL – 0011

École doctorale : MEGA

Spécialité : Mécanique - Génie Mécanique - Génie Civil

RÉSUMÉ :
Il est connu depuis des décennies que la propagation des fissures de fatigue dans les matériaux élastoplastiques est très sensible à l'histoire du chargement car le comportement non-linéaire du matériau peut avoir une grande influence sur les vitesses de propagation. Cependant, le calcul brut de millions de cycles de fatigue avec des comportements matériaux non-linéaires sur des structures tridimensionnelles réalistes conduirait à des temps de calcul prohibitifs. Ainsi, nous proposons de coupler deux approches de réduction de modèle *a priori* et *a posteriori*, afin de diminuer considérablement le coût de calcul de ce type de problèmes.
Tout d'abord, considérant l'hypothèse de plasticité confinée, une stratégie de réduction de modèle *a posteriori* du comportement plastique de la structure fissurée est proposée. Le modèle réduit ainsi obtenu fournit incrémentalement l'état plastique autour du front de fissure, duquel est déduite la vitesse instantanée de la fissure. De plus, une seconde approche de réduction de modèle, *a priori* cette fois, est aussi mise en place afin d'accélérer encore plus les temps de résolution du problème global. Cette approche *a priori* consiste à construire incrémentalement — et sans calculs préalables — une base réduite spécifique à chaque cas-test, en extrayant de l'information des champs de déplacement de la structure au cours du temps et pendant la propagation éventuelle de la fissure. Ainsi, les champs de déplacement solutions de la géométrie fissurée réactualisée sont vus comme une combinaison linéaire de cette base réduite de vecteurs.
La méthode numérique considérée ici est la méthode des éléments finis. De fait, pendant la propagation de la fissure, la discrétisation spatiale du modèle doit être réactualisée afin d'être conforme avec le front de la fissure. Dans ce but, une technique spécifique de déformation de maillage est utilisée, et permet de discrétiser la géométrie variable du modèle avec des maillages de même topologie. Cette technique de déformation de maillage apparaît comme une étape clé de la stratégie de réduction de modèle.
Finalement, une approche *adaptative* est construite autour de cette stratégie. Elle permet de garantir la qualité des résultats obtenus par rapport à un critère de précision donné. La précision et l'efficacité de cette stratégie globale sont démontrées à travers de nombreux exemples bidimensionnels et tridimensionnels dans le cadre de propagation de fissure en mode I, de même que pour un exemple industriel d'une pièce fissurée d'hélicoptère.

MOTS-CLÉS : Propagation de fissure 3D, Effet de refermeture, Plasticité confinée, Réduction de modèle *a priori*, Déformation de maillage, Méthode des éléments finis

Laboratoire(s) de recherche : Laboratoire de Mécanique des Contacts et des Solides
UMR CNRS 5259 - INSA de Lyon
20, avenue Albert Einstein
69621 Villeurbanne Cedex France

Directeur de thèse : Anthony GRAVOUIL
Co-encadrant : Michel ROCHETTE

Président du jury :

Composition du jury : Amine AMMAR
Alain COMBESCURE
Nicolas MOËS
Michel ROCHETTE
Francisco CHINESTA
Frédéric FEYEL
Sylvie POMMIER
Anthony GRAVOUIL